Neutrino Oscillation Physics
at
Neutrino Factories and Beta Beams

Mark Benjamin Rolinec

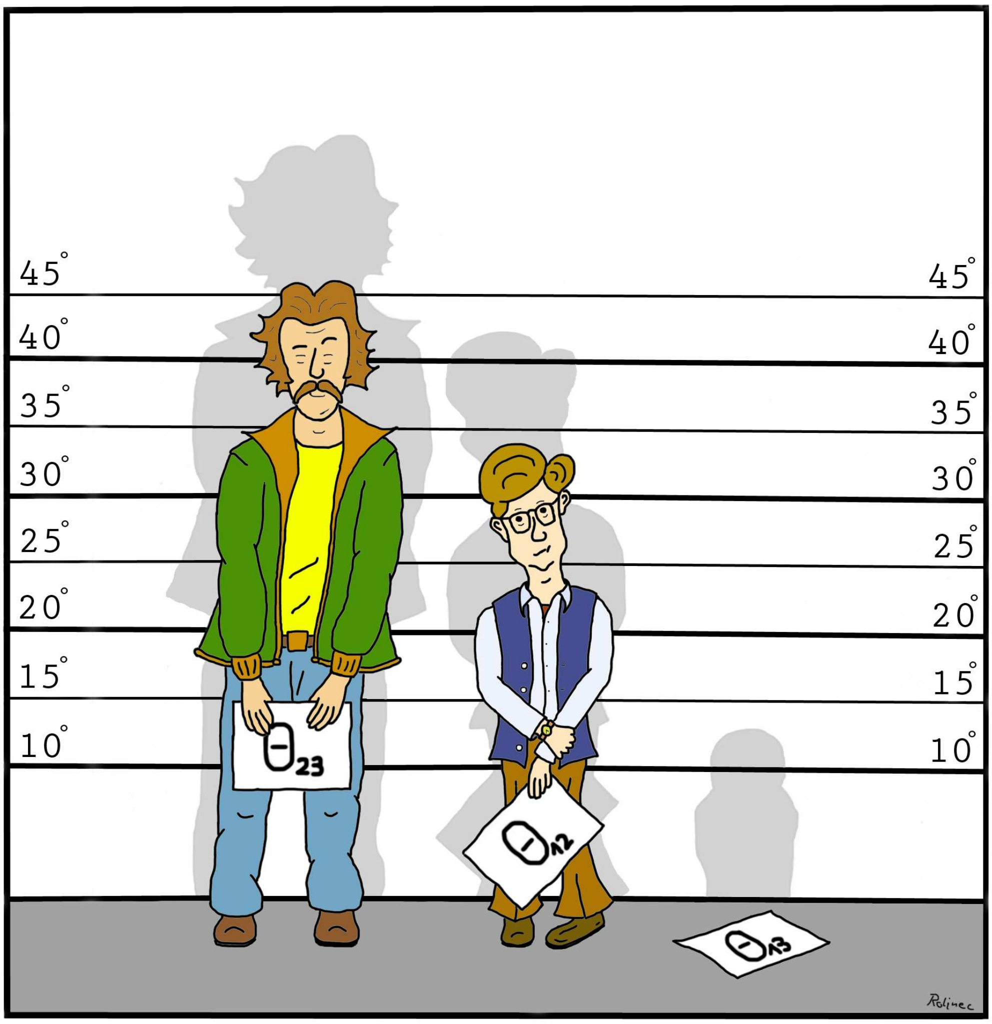

Dissertation
June 2007

Technische Universität München
Physik-Department
Institut für Theoretische Physik T30d
Univ.-Prof. Dr. Manfred Lindner

Neutrino Oscillation Physics at Neutrino Factories and Beta Beams

Dipl.-Phys. Univ. Mark Benjamin Rolinec

Vollständiger Abdruck der von der Fakultät für Physik der Technischen Universität München zur Erlangung des akademischen Grades eines

Doktors der Naturwissenschaften (Dr. rer. nat.)

genehmigten Dissertation.

Vorsitzender:		Univ.-Prof. Dr. Lothar Oberauer
Prüfer der Dissertation:	1.	Univ.-Prof. Dr. Manfred Lindner
	2.	Univ.-Prof. Dr. Andrzej J. Buras

Die Dissertation wurde am 13. Juni 2007 bei der Technischen Universität München eingereicht und durch die Fakultät für Physik am 23. Juli 2007 angenommen.

Wenn wir jetzt Schinken hätten, könnten wir Rührei mit Schinken machen, wenn wir Eier hätten.

Kathrin Passig
Sie befinden sich hier

Contents

1 Introduction **1**

2 The Standard Model **5**

3 Neutrino Masses and Mixing **9**
3.1 Neutrino Mass Terms 9
3.2 Neutrino Mixing 10
3.3 See-Saw Mechanism 12
3.4 Implications 14

4 Neutrino Oscillations **21**
4.1 Two Flavor Oscillations 21
4.2 Matter Effects 23
4.3 Three Flavor Oscillations 29
4.4 Phenomenology of $P_{e\mu}$ and P_{ee} 31

5 Neutrino Data **37**
5.1 Number of Flavors 37
5.2 Absolute Mass Scale 38
5.3 Oscillation Data 42

6 Long Baseline Experiment Scenarios **49**
6.1 Conventional Beam Experiments 50
6.2 Superbeams 51
6.3 Reactor Experiments 52
6.4 Electron Capture Beams 53
6.5 Beta Beams 54
6.6 Neutrino Factories 58

7 Beta Beam Performance **63**
7.1 Beta Beam Simulation 63
7.2 Beta Beam Optimization 68
7.3 Neutrino and Anti-Neutrino Runtime Fraction 81
7.4 Addition of T2K Disappearance Data 82
7.5 γ-Scaling of the Isotope Decays 84
7.6 Performance of the β-Beam Reference Scenarios 86

8 Neutrino Factory Performance **89**
8.1 Neutrino Factory Simulation 89
8.2 Neutrino Factory Optimization 94
8.3 Neutrino and Anti-Neutrino Runtime Fraction 100
8.4 Matter Density Uncertainty 102
8.5 Inclusion of Different Channels 103
8.6 Performance of the Neutrino Factory Reference Scenarios 108

9 The Global Picture **113**
9.1 The Road Map of Neutrino Oscillation Experiments 113
9.2 Promising Future Experiments 115

10 Summary and Conclusions **121**

A The General Long Baseline Experiment Simulator **125**

B Performance Indicators **127**

Acknowledgments **129**

Bibliography **132**

List of Figures

3.1 Diagramatic illustration of the generation of m_L through the See-Saw mechanism. 14
3.2 Mass spectrum of the three neutrino mass eigenstates ν_1, ν_2, and ν_3 for normal and inverted hierarchy. 16
3.3 The diagram of the simplest process leading to neutrino-less double beta decay. 17
3.4 The diagram, leading to an effective Majorana mass in case of a black box process for neutrino-less double beta decay. 18
3.5 The effective neutrino mass parameter $\langle m_{ee} \rangle$ relevant for neutrino-less double beta decay as a function of the lightest neutrino mass. 19
3.6 The tree level and one-loop level Feynman diagrams for the decay of heavy right-handed neutrinos N_i into the Higgs doublet and the lepton doublet, relevant for Leptogenesis. 20

4.1 Neutrino oscillation probability in the two-flavor scenario as a function of the baseline and the neutrino energy. 22
4.2 The Feynman diagrams for coherent forward scattering of neutrinos in matter . 23
4.3 The Neutrino mixing angle in matter for neutrinos involving the Mikheyev-Smirnov-Wolfenstein resonance and for anti-neutrinos as a function of the matter potential parameter A'. 27
4.4 The effective energy eigenvalues in matter and the mass eigenstate composition of the flavor eigenstate $|\nu_\alpha\rangle$ as functions of the matter potential parameter A'. . 29

5.1 Possible neutrino mass spectra with a fourth sterile neutrino and an additional mass-squared difference $\Delta m^2_{\mathrm{LSND}}$. 47

6.1 Schematic illustration of neutrino source, oscillation channels, and detection principles at conventional beam experiments and at Superbeam experiments. . 51
6.2 Schematic illustration of neutrino source, oscillation channels, and detection principles at a neutrino reactor experiment. 53
6.3 Schematic illustration of neutrino source, oscillation channels, and detection principles at a β-Beam experiment. 56
6.4 The energy spectrum of the neutrino flux at a β-Beam experiment. 57
6.5 Schematic illustration of neutrino source, oscillation channels, and detection principles at a Neutrino Factory experiment. 59
6.6 The energy spectrum of the neutrino flux at a Neutrino Factory experiment. . . 60

7.1 The sensitivity limit to $\sin^2 2\theta_{13}$ at a β-Beam (WC) as a function of the baseline L at fixed $\gamma = 150$ and $\gamma = 350$. 69

7.2 The sensitivity limit to $\sin^2 2\theta_{13}$ at a β-Beam (TASD) as a function of the baseline L at fixed $\gamma = 500$ and $\gamma = 1000$. 70

7.3 The sensitivity limit to $\sin^2 2\theta_{13}$ at a β-Beam (WC) as a function of γ at the fixed baselines $L = 130$ km and $L = 730$ km. 71

7.4 The sensitivity limit to $\sin^2 2\theta_{13}$ at a β-Beam (TASD) as a function of γ at the fixed baselines $L = 730$ km and $L = 1500$ km. 73

7.5 The sensitivity to *maximal* CP violation at a β-Beam as a function of the baseline L at fixed a γ. 74

7.6 The sensitivity to *maximal* CP violation at a β-Beam as a function of γ at a fixed baseline L. 75

7.7 The sensitivity to mass hierarchy at a β-Beam as a function of the baseline L at fixed γ. 77

7.8 The sensitivity to mass hierarchy at a β-Beam as a function of γ at a fixed baseline L. 79

7.9 The impact of the ratio of neutrino (^{18}Ne stored) and anti-neutrino (^{6}He stored) runtime at a β-Beam on the sensitivity limit to $\sin^2 2\theta_{13}$, the sensitivity to *maximal* CP violation, and sensitivity to the mass hierarchy. 81

7.10 The impact of the addition of T2K disappearance data to the β-Beam data on the $\sin^2 2\theta_{13}$ discovery reach, the sensitivity to *any* CP violation, and sensitivity to the mass hierarchy. 83

7.11 The impact of the γ-scaling of the number of isotope decays per year at a β-Beam on the $\sin^2 2\theta_{13}$ discovery reach, the sensitivity to *any* CP violation, and sensitivity to the mass hierarchy. 85

7.12 The comparison of the performance of all β-Beam reference scenarios for the performance indicators $\sin^2 2\theta_{13}$ discovery reach, sensitivity to *any* CP violation, and sensitivity to the mass hierarchy. 87

8.1 The sensitivity limit to $\sin^2 2\theta_{13}$ at a Neutrino Factory as a function of the baseline L for a fixed parent muon energy of $E_\mu = 25$ GeV and $E_\mu = 50$ GeV. . 95

8.2 The sensitivity limit to $\sin^2 2\theta_{13}$ at a Neutrino Factory as a function of the parent muon energy for a fixed baseline of $L = 4000$ km and $L = 7500$ km. . 96

8.3 The sensitivity to *maximal* CP violation at a Neutrino Factory as a function of the baseline L for a fixed parent muon energies of $E_\mu = 25$ GeV and $E_\mu = 50$ GeV. 97

8.4 The sensitivity to mass hierarchy at a Neutrino Factory as a function of the baseline L for a fixed parent muon energies of $E_\mu = 25$ GeV and $E_\mu = 50$ GeV. 98

8.5 The impact of the ratio of neutrino and anti-neutrino runtime at a Neutrino Factory on the sensitivity limit to $\sin^2 2\theta_{13}$, the sensitivity to *maximal* CP violation, and sensitivity to the mass hierarchy. 101

8.6 The impact of the matter density uncertainty at a Neutrino Factory on the $\sin^2 2\theta_{13}$ discovery reach, the sensitivity to *any* CP violation, and sensitivity to the mass hierarchy. 103

8.7 The sensitivity gap coverage for a combination of golden and silver channel as a function of the silver channel detector 105

8.8 The impact of the upper platinum CID threshold to the CP violation sensitivity for small, intermediate, and large $\sin^2 2\theta_{13}$. 106

8.9 The comparison of the improvement of the standard and optimistic silver and platinum channel scenarios considering CP violation and mass hierarchy sensitivity for large and intermediate $\sin^2 2\theta_{13}$. 108
8.10 The comparison of the performance of all Neutrino Factory reference scenarios for the performance indicators $\sin^2 2\theta_{13}$ discovery reach, sensitivity to *any* CP violation, and sensitivity to the mass hierarchy. 110

9.1 Possible global evolution of the $\sin^2 2\theta_{13}$ discovery reach as a function of time. . 114
9.2 Summary of the performances of all β-Beam and Neutrino Factory reference scenarios for the performance indicators $\sin^2 2\theta_{13}$ discovery, sensitivity to *any* CP violation, and sensitivity to the mass hierarchy at the true value $\sin^2 2\theta_{13} = 10^{-1}$. 116
9.3 Summary of the performances of all β-Beam and Neutrino Factory reference scenarios for the performance indicators $\sin^2 2\theta_{13}$ discovery, sensitivity to *any* CP violation, and sensitivity to the mass hierarchy at the true value $\sin^2 2\theta_{13} = 10^{-3}$. 118
9.4 Summary of the performances of all β-Beam and Neutrino Factory reference scenarios for the $\sin^2 2\theta_{13}$ reach of the performance indicators $\sin^2 2\theta_{13}$ discovery, sensitivity to *any* CP violation, and sensitivity to the mass hierarchy. 119

List of Tables

2.1 The fermion particle content of the Standard Model. 6
2.2 The Higgs scalar field of the Standard Model 7

3.1 The right-handed neutrinos that are added in the minimal extension of the Standard Model to allow for neutrino masses. 10

7.1 The signal efficiencies and background rejection factors and systematical errors in our description of the Water Cherenkov detector β-Beams. 66
7.2 The signal efficiencies and background rejection factors and systematical errors in our description of the Totally Active Scintillator detector β-Beams. 67
7.3 The listing of all defined β-Beam reference scenarios. 80

8.1 The signal efficiencies and background rejection factors and systematical errors in our description of the standard golden channel at a Neutrino Factory. 90
8.2 The signal efficiencies and background rejection factors and systematical errors in our description of the standard silver channel at a Neutrino Factory. 91
8.3 The signal efficiencies and background rejection factors and systematical errors in our description of the standard platinum channel at a Neutrino Factory. . . . 92
8.4 The listing of all defined Neutrino Factory reference scenarios. 100

Chapter 1

Introduction

Neutrino oscillation physics has clearly entered the era of beam-based long baseline experiments. Already a few years ago in 2002, the first experiment, the K2K in Japan, that uses a collimated ν_μ neutrino beam to search for oscillations at the atmospheric frequency, has confirmed the oscillations that have been observed in data coming from atmospheric neutrinos. At this time the succeeding conventional beam-based neutrinos oscillation long baseline experiments were in the stage of preparation, the MINOS experiment in the United states and the CNGS experiments in Europe.

In 2006 the MINOS collaboration published their highly anticipated results of the first year of operation which was in perfect agreement with the data from atmospheric neutrinos and K2K. Additionally, the MINOS results could already significantly improve the precision in the measurement of the atmospheric parameter $|\Delta m_{31}^2|$. This amazing development followed the extraordinary example of the KamLAND experiment in Japan, where in 2003 the data from a totally earth-based experiment could confirm and even improve the measurements from naturally produced neutrinos, *i.e.* in case of KamLAND the data from solar neutrinos.

Recently, also the CNGS beam delivered the first neutrinos which then could be detected in the Gran Sasso underground laboratories in Italy at the OPERA detector after traveling along the 732 km baseline from their production at CERN in Switzerland. Now, all three beam-based neutrino oscillation long baseline experiment setups are in operation.

However, the first generation of conventional beam-based neutrino oscillation long baseline experiments will mainly contribute to the precision measurements of the leading atmospheric parameters since the experiments do not provide good sensitivities to three-flavor effects because of the relatively small detector dimensions and the relatively small beam powers compared to planned future experiment scenarios. The reason is that three-flavor effects, which would manifest in the appearance of electron neutrinos from the muon neutrino beams at the conventional beam-based oscillation experiments, are suppressed due to the small third mixing angle $\sin^2 2\theta_{13}$ and the hierarchy of the oscillation frequencies $\Delta m_{21}^2/\Delta m_{31}^2$, resulting in an effective decoupling of the atmospheric and solar neutrino oscillations that are so far well explained in an effective two-flavor picture.

It is the goal of future neutrino oscillation experiments to discover three-flavor effects beyond the pure precision measurements of the leading oscillation parameters and various long baseline scenarios have been proposed to shed light on the puzzles of three-flavor oscillations, *i.e.* the question of the actual size of the small mixing angle $\sin^2 2\theta_{13}$, the question of the presence of CP violation in the neutrino sector, and the question of the actual mass ordering of the neutrino mass eigenstates that can be revealed in matter effects of the neutrino oscillations. These questions are to be addressed at future neutrino oscillation experiments, hence the experimental setups have to be optimized for optimal performance in the search for three-flavor effects.

The most obvious advancement from the point of view of the conventional beam-based long baseline experiments is the enhancement of the detector masses and the beam energies to allow for increased statistics. This is the aim of the so-called Superbeam experiments that represent the upgrades of the conventional beam experiments and proposed realizations are the NOνA experiment in the United States, the T2K and T2HK experiments in Japan, and the SPL experiment in Europe. Unfortunately, the conventional beam-based experiments are naturally limited by the intrinsic beam background and flavor pure produced beams are required to be able to observe three-flavor effects for very small $\sin^2 2\theta_{13}$.

At this point the technologies of the sophisticated ideas of conceivable β-Beam experiments and Neutrino Factory experiments come into play. While conventional beam-based experiments use the decay of pions for the neutrino beam production which results in flavor contaminations within the beam and a high energy tail in the neutrino spectrum that enhances the background from neutral-current events, the β-Beam and Neutrino Factory beam production technologies provide neutrino beams with well-known neutrino spectra and definite flavor compositions.

The β-Beam technology is planned to use the decay of accelerated β-decaying isotopes to produce a flavor-pure electron or anti-electron beam depending on the properties of the stored isotopes, *i.e.* if they are β^+ or β^- emitting isotopes. The Neutrino Factory scenarios on the other hand produce the neutrino beam in the decay of accelerated muons or anti-muons. Consequently, as for the β-Beam beam production a neutrino spectrum of well-known shape is produced. In the case of a Neutrino Factory the beam composition is not absolutely flavor pure because electron-flavored neutrinos and muon-flavored neutrinos are contained in the beam at an equal amount. Both technologies are very promising candidates and imply sensitivities to three-flavor effects for large parts of the parameter space.

The aim of this work is to first discuss the phenomenological framework of three-flavor oscillations in light of the current available data and to illustrate the requirements of future neutrino oscillation experiments to be able to observe three-flavor effects and provide excellent sensitivities to the sub-leading parameters $\sin^2 2\theta_{13}$, δ_{CP}, and additionally the mass hierarchy. The main focus is the discussion of possible optimization strategies for β-Beam experiments and Neutrino Factory experiments.

The structure of this work is as follows: First, we will briefly review the Standard Model of elementary particle physics in Chapter 2. There we will focus on the electro-weak part of the Standard Model Lagrangian and briefly discuss the Higgs mechanism where the gauge bosons and the charged fermions acquire their masses. Then in Chapter 3, we will introduce the possibilities to extend the Standard Model in order to introduce neutrino masses. We will additionally discuss the neutrino mixing that can arise in combination with neutrino masses and briefly explain the See-Saw mechanism that gives a natural explanation for the smallness of neutrino masses. Thereafter we will give a short summary of the possible implications of neutrino masses and mixing, *i.e.* neutrino oscillations, neutrino-less double beta decay, and Leptogenesis. Since the main topic of this work is the simulation of future neutrino oscillation long baseline experiments, the phenomenology of neutrino oscillations will be discussed in greater detail in Chapter 4. There we will first discuss vacuum oscillation and matter effects in a two-flavor framework before the three-flavor oscillation framework is explained. In addition we will discuss expansions of the three-flavor oscillation probabilities of the relevant channels that are later discussed for the respective experiments. This discussion will set an analytical basis that allows to understand the numeric results that are discussed in later chapters.

In Chapter 5 the current available neutrino data and the current knowledge about neutrino properties will be presented. This involves a discussion of data that allows a conclusion about the number of neutrino flavors, data that allows constraining the absolute mass scale of neutrinos, and finally the available oscillation data. The latter will be discussed in regard to the data from solar neutrinos, atmospheric neutrinos, and artificially produced neutrinos in reactor cores or in pion decays for the first generation of conventional beam-based experiments. There we will also briefly discuss the results from the neutrino experiment LSND that do not agree with the global data in the three-flavor framework. The next Chapter will give a detailed description of the technologies of proposed or conceivable future neutrino oscillation long baseline experiments, *i.e.* the conventional accelerator beam-based experiments, their possible upgrades, the so-called Superbeam scenarios, reactor experiments, neutrino experiments with a neutrino beam from electron capture, and of course the experiment technologies that will be simulated in the chapters where the main results are presented: β-Beam experiments and Neutrino Factory experiments.

In Chapter 7 we will give a detailed discussion of the performance of β-Beam experiments where we focus on different detector technologies, Water Cherenkov and Totally Active Scintillator, and the three basic categories of β-Beam experiments: low γ, medium γ, and high γ. First the details of the simulation techniques are presented before we give an extensive discussion of the β-Beam optimization in terms of the baseline L and the acceleration factor γ of the stored isotopes. Thereafter, we will concentrate on single technical considerations such as the impact of the ratio of the neutrino and anti-neutrino runtime fractions, the impact of external disappearance data to handle parameter correlations with the leading atmospheric oscillation parameters, and the impact of a possible γ-scaling of the number of isotope decays that affects the potential of medium and high γ scenarios. Finally, we will compare the performances of optimized β-Beam reference scenarios for both detector technologies in terms of the performance indicators: discovery reach in $\sin^2 2\theta_{13}$, sensitivity to *any* CP violation, and sensitivity to the mass hierarchy.

Thereafter in Chapter 8 the main focus will lie on the performance of Neutrino Factory scenarios at very large baselines. Again, we will first introduce the simulation techniques for the Neutrino Factory simulations. Then, as for the β-Beams in the previous chapter a detailed discussion considering the optimization of a golden channel Neutrino Factory experiment in terms of the baseline L and the energy of the stored parent muons E_μ will be presented. Also for the Neutrino Factory experiments we will examine technical considerations such as the impact of the ratio of the runtime fractions in the μ^+-stored and the μ^--stored phase, the impact of the matter density uncertainty along the baseline, and the impact of additional channels: the silver channel $\nu_e \rightarrow \nu_\tau$ and the platinum channel $\nu_\mu \rightarrow \nu_e$. Finally, we will compare the performances of optimized Neutrino Factory reference scenarios including the additional channel scenarios, multiple detector scenarios, and an optimized golden channel scenario with a lower threshold and better energy resolution in terms of the performance indicators: discovery reach in $\sin^2 2\theta_{13}$, sensitivity to *any* CP violation, and sensitivity to the mass hierarchy.

The performance of the optimized reference scenarios, the different β-Beam scenarios from Chapter 7 and the different Neutrino Factory scenarios from Chapter 8 will be compared in Chapter 9 for different regions of true $\sin^2 2\theta_{13}$. The aim is to find the optimal technology in the respective regimes of $\sin^2 2\theta_{13}$ and to discuss the advantages and disadvantages of the different setups. In this Chapter we will also give a discussion of the future road map of future neutrino oscillation experiments of various technologies and expenses in order to classify the β-Beam and Neutrino Factory performances before we give the summary and conclusions.

Chapter 2

The Standard Model

The Standard Model of elementary particle physics describes the interactions of all known elementary particles very successfully up to the high energies at the electroweak scale. The formulation of the electro-weak interactions within the Standard Model goes back to the 1960's [1–3] and the extension including the strong interactions went on to the 1970's [4]. The model has been tested to very accurate precisions and no deviations have been found at the experiments of the collider facilities LEP or Tevatron. Three of the four known fundamental interactions are combined into one theory, the strong interactions of the quarks, the weak interactions of leptons and quarks, and the electromagnetic interactions of charged particles. Only the gravitational force is not included to the Standard Model, but the gravitational interactions are the weakest of the four fundamental forces at the observable energies and thus negligible. However, it is expected that at very high energies, *i.e.* the Planck Scale $M_{Pl} \sim 10^{19}$GeV, the gravitational forces become similarly significant. This is the first indication that, despite the extreme success of the Standard Model, it can only be seen as an effective theory at the observable energies and physics at higher energies has to be expected. Further reasons to believe in new physics beyond the Standard Model are the Hierarchy Problem, *i.e.* the question of stabilization of the Higgs mass against quadratic divergencies, or the puzzles of the origin of Dark Matter and Dark Energy. The evidence for neutrino masses that has been established with the observation of neutrino oscillations is also considered as a hint for physics beyond the Standard Model.

The Standard Model is a local gauge theory with the underlying local gauge symmetry of the group

$$G_{SM} = SU(3)_C \times SU(2)_L \times U(1)_Y, \tag{2.1}$$

where the strong interactions are associated with the local SU(3) symmetry. The unified electro-weak interactions are governed by the SU(2)×U(1) and only the left-handed components of the fermion fields transform under the SU(2) group, hence the right-handed components do not participate in the weak interactions. The particle content of the Standard Model and the associated representations of the Standard Model gauge group are summarized in Table 2.1. We will here only focus on the electro-weak part of the Standard Model since the strong interactions are not relevant for the considerations of this work. The electro-weak interactions are described in the electro-weak part of the Standard Model Lagrangian

$$\mathcal{L}_{SU(2)_L \times U(1)_Y} = \mathcal{L}_G + \mathcal{L}_F + \mathcal{L}_H + \mathcal{L}_Y. \tag{2.2}$$

1st Gen.	2nd Gen.	3rd Gen.	$SU(3)_C$	$SU(2)_L$	Y	Q
$\begin{pmatrix} u \\ d \end{pmatrix}_L$	$\begin{pmatrix} c \\ s \end{pmatrix}_L$	$\begin{pmatrix} t \\ b \end{pmatrix}_L$	$\mathbf{3}$	$\mathbf{2}$	$\frac{1}{3}$	$2/3$ $-1/3$
u_R	c_R	t_R	$\bar{\mathbf{3}}$	$\mathbf{1}$	$\frac{4}{3}$	$2/3$
d_R	s_R	b_R	$\bar{\mathbf{3}}$	$\mathbf{1}$	$-\frac{2}{3}$	$-1/3$
$\begin{pmatrix} \nu_e \\ e \end{pmatrix}_L$	$\begin{pmatrix} \nu_\mu \\ \mu \end{pmatrix}_L$	$\begin{pmatrix} \nu_\tau \\ \tau \end{pmatrix}_L$	$\mathbf{1}$	$\mathbf{2}$	-1	0 -1
e_R	μ_R	τ_R	$\mathbf{1}$	$\mathbf{1}$	-2	-1

Table 2.1: The fermion particle content of the Standard Model and the representations of the gauge groups $SU(3)_C$ and $SU(2)_L$ to which the quark and lepton fields are assigned. Furthermore the respective hypercharge Y and the resulting electric charge Q is given.

Here, $\mathcal{L}_G$ contains the kinetic terms and self-interactions of the gauge bosons, $\mathcal{L}_F$ contains the kinetic terms of the fermionic fields and their interactions with the gauge bosons, $\mathcal{L}_H$ contains the kinetic terms, self-interactions, and interactions with the gauge bosons of a postulated, yet undiscovered scalar field called the Higgs boson, and finally $\mathcal{L}_Y$ contains the interaction terms of the Higgs boson with the fermions. The first part $\mathcal{L}_G$ is built up with the field strength tensors and is written as

$$\mathcal{L}_G = -\frac{1}{4}\sum_{i=1}^{3} F_{i\mu\nu}F_i^{\mu\nu} - \frac{1}{2}G_{\mu\nu}G^{\mu\nu}. \tag{2.3}$$

The field strength tensors contain the partial derivatives of the gauge fields, the SU(2) vector fields W_i^μ and the U(1) scalar field B^μ. Due to the non-commutative structure of the SU(2), self-interactions of the fields W_i^μ occur as is also the case for the gluons which are the SU(3) gauge fields. Since the U(1) transformations commute, no self-interactions appear for the field B^μ. This can be seen if the field strength tensors are explicitly given:

$$F_i^{\mu\nu} = \partial^\mu W_i^\nu - \partial^\nu W_i^\mu + g\varepsilon_{ijk}W_j^\mu W_k^\nu, \qquad G^{\mu\nu} = \partial^\mu B^\nu - \partial^\nu B^\mu. \tag{2.4}$$

The kinematics of the fermion fields is given in $\mathcal{L}_F$

$$\begin{aligned}\mathcal{L}_F \;=\; & i\sum_{\alpha=1}^{3}\left[\overline{l_L}_\alpha\gamma_\mu D^\mu l_{L\alpha} + \overline{e_R}_\alpha\gamma_\mu D^\mu e_{R\alpha} + \overline{q_L}_\alpha\gamma_\mu D^\mu q_{L\alpha}\right.\\ & \qquad\left. + \overline{u_R}_\alpha\gamma_\mu D^\mu u_{R\alpha} + \overline{d_R}_\alpha\gamma_\mu D^\mu d_{R\alpha}\right],\end{aligned} \tag{2.5}$$

Higgs	$SU(3)_C$	$SU(2)_L$	Y	Q
$\phi = \begin{pmatrix} \phi^+ \\ \phi^0 \end{pmatrix}$	**1**	**2**	1	1 0

Table 2.2: The Higgs scalar field of the Standard Model and the representations of the gauge groups $SU(3)_C$ and $SU(2)_L$ to which it is assigned. Furthermore the respective hypercharge Y and the resulting electric charge Q is given.

where the partial derivatives are replaced by the covariant derivatives and the interactions with the gauge fields are introduced to restore the local gauge symmetry. The covariant derivatives are given as

$$D^\mu = \partial^\mu - igT_j W_j^\mu - ig'\frac{Y}{2}B^\mu \tag{2.6}$$

Here, T_j are the generators of the SU(2) gauge group and Y is the hypercharge and the interaction strength is given by the respective coupling constants g and g'.

Up to now, all gauge fields and fermion fields are assumed to be massless which does not match with the experimental evidence of non-vanishing fermion masses since the quarks and charged leptons are known to be massive particles. Furthermore, the gauge bosons of the weak interactions are known to have masses. However, mass terms for the leptons and gauge fields cannot be introduced explicitly to the Lagrangian since this would violate the gauge symmetries. A loophole was found by introducing Spontaneous Symmetry Breaking which required the postulation of a new additional complex scalar field, the Higgs, that transforms as a doublet under the SU(2) of the Standard Model gauge group and evolves a non-vanishing vacuum expectation value. This is the so-called Higgs mechanism [5–8]. The Higgs particle and its assigned gauge representations are given in Table 2.2.

The kinematics of the Higgs field are added to the Standard Model Lagrangian, and as for the fermionic fields, the partial derivative is exchanged with the covariant derivative and interactions with the gauge fields are introduced. Furthermore a potential $V(\phi)$ is introduced:

$$\mathcal{L}_H = (D_\mu\phi)^\dagger(D^\mu\phi) - V(\phi) \tag{2.7}$$

The Higgs potential $V(\phi)$ is chosen as

$$V(\phi) = -\mu^2\phi^\dagger\phi + \lambda(\phi^\dagger\phi)^2, \quad \mu^2 > 0 \tag{2.8}$$

such that the minimum is off the origin and the potential takes the form of a “Mexican Hat”.

This implies a non-zero vacuum expectation value for the Higgs field and a degenerate continuum of minimum eigenstates. The symmetry is broken since only one eigenstate can be occupied. We can choose the gauge such that this minimum state is

$$\langle\phi\rangle = \begin{pmatrix} 0 \\ \frac{1}{\sqrt{2}}v_{EW} \end{pmatrix}, \qquad \text{with} \quad v_{EW} = \sqrt{\frac{\mu^2}{\lambda}}. \tag{2.9}$$

and around the vacuum expectation value the field can be expressed as

$$\phi = \begin{pmatrix} \phi^+ \\ \phi^0 \end{pmatrix} = \begin{pmatrix} G_1^+ + iG_2^+ \\ \frac{1}{\sqrt{2}}(v_{EW} + h + iG^0) \end{pmatrix} \tag{2.10}$$

where the Goldstone bosons G_1^+, G_2^+, and G^0 get "eaten" by inserting this into the Lagrangian and introducing the following linear combinations of the gauge fields:

$$\begin{aligned} W_\mu^\pm &= \frac{1}{\sqrt{2}}(W_\mu^1 \mp W_\mu^2) \\ Z_\mu &= \cos(\theta_W)W_\mu^3 - \sin(\theta_W)B_\mu \\ A_\mu &= \cos(\theta_W)B_\mu + \sin(\theta_W)W_\mu^3. \end{aligned} \tag{2.11}$$

Here, we already introduced the Weinberg angle θ_W that is defined as

$$\cos(\theta_W) = \frac{g}{\sqrt{g^2+g'^2}}, \qquad \sin(\theta_W) = \frac{g'}{\sqrt{g^2+g'^2}}. \tag{2.12}$$

Furthermore, the gauge bosons aquire masses due to the non-vanishing vacuum expectation value v_{EW} because the Higgs part $\mathcal{L}_H$ of the Lagrangian contains the following terms after Spontaneous Symmetry Breaking that can be interpreted as mass terms

$$\mathcal{L}_H \supset \frac{1}{8}v_{EW}^2(g^2+g'^2)Z_\mu Z^\mu + \frac{1}{4}v_{EW}^2 g^2 W_\mu^- W^{+\mu} = \frac{1}{2}m_Z^2 Z_\mu Z^\mu + m_W^2 W_\mu^- W^{+\mu} \tag{2.13}$$

and as can be seen, the masses of the W and the Z bosons are related by the Weinberg angle.

The Higgs mechanism additionally allows to introduce masses for the fermions by adding the so-called Yukawa interactions of the Higgs field with the quark and charged lepton fields to the Lagrangian:

$$\mathcal{L}_Y = -\sum_{\alpha,\beta=1}^{3}\left[(Y_l)_{\alpha\beta}\overline{l_{L\alpha}}\phi e_{R\beta} + (Y_d)_{\alpha\beta}\overline{q_{L\alpha}}\phi d_{R\beta} + (Y_u)_{\alpha\beta}\overline{q_{L\alpha}}(i\sigma_2\phi^*)u_{R\beta}\right] + h.c. \tag{2.14}$$

Here, the Yukawa couplings Y_l, Y_d, and Y_u are 3×3 matrices in flavor space. If one now considers Spontaneous Symmetry Breaking, the fermions aquire masses due to the non-vanishing vacuum expectation value similar to the gauge bosons:

$$\mathcal{L}_Y \xrightarrow{\text{SSB}} -\sum_{\alpha,\beta=1}^{3}\left[(M_l)_{\alpha\beta}\overline{e_{L\alpha}}e_{R\beta} + (M_d)_{\alpha\beta}\overline{d_{L\alpha}}d_{R\beta} + (M_u)_{\alpha\beta}\overline{u_{L\alpha}}u_{R\beta}\right] + h.c. \tag{2.15}$$

where the mass matrices are given by

$$M_u = \frac{1}{\sqrt{2}}v_{EW}Y_u, \quad M_d = \frac{1}{\sqrt{2}}v_{EW}Y_d, \quad M_l = \frac{1}{\sqrt{2}}v_{EW}Y_l. \tag{2.16}$$

Note, that the neutrinos cannot acquire masses in the Standard Model since right-handed neutrinos ν_R are not contained in the Standard Model particle content. These right-handed neutrinos would carry no charge or hypercharge and be singlets under SU(2) and SU(3), hence they would be absolute singlets under the Standard Model gauge transformations and do not interact with any of the Standard Model particles. So, they have not been introduced and neutrinos were believed to be massless particles.

However, the observations of the last decade have established flavor transitions in the neutrino sector and neutrinos have been observed to be massive. So, the Standard Model of elementary particle physics has to be extended in order to allow for neutrino masses.

Chapter 3

Neutrino Masses and Mixing

Within the last Chapter, we briefly discussed the electro-weak part of the Standard Model and the Higgs mechanism where the gauge bosons of the weak interactions and the fermions acquire a mass. It was stated that no masses have been assigned to the neutrinos in this mechanism since no right-handed neutrinos have been introduced to the particle content of the Standard Model. However, the experimental evidence of neutrino oscillations indicates that neutrinos indeed have masses. This requires an extension of the Standard Model and neutrino masses have to be introduced.

3.1 Neutrino Mass Terms

The simplest extension of the Standard Model to incorporate neutrino masses is to introduce right-handed neutrinos to the particle content. These are singlets under the SU(3) and the SU(2). Furthermore neutrinos do not carry electric charge and hence also no Hypercharge as is summarized in Table 3.1. So, the right-handed neutrinos do not contribute to the electro-weak interactions but similar to the other fermions one can introduce Yukawa couplings to the Higgs field that lead to an additional fermionic Dirac mass term after Spontaneous Symmetry Breaking, now for the neutrinos:

$$\mathcal{L}_\nu^{\text{Dirac}} = -\sum_{\alpha,i}(Y_\nu)_{\alpha i}\overline{l_L}_\alpha(i\sigma_2\phi^*)\nu_{Ri} + h.c. \xrightarrow{\text{SSB}} -\sum_{\alpha,i}(m_D)_{\alpha i}\overline{\nu_L}_\alpha\nu_{Ri} + h.c. \tag{3.1}$$

Again, the Yukawa coupling Y_ν is a 3×3 matrix in flavor space and the neutrino Dirac mass matrix is given by the Yukawa coupling and the vacuum expectation value of the Higgs field:

$$m_D = \frac{1}{\sqrt{2}}v_{EW}Y_\nu \tag{3.2}$$

Especially for neutrinos, since they do not carry electric charge, there exists a second way to introduce a Poincare invariant neutrino mass term besides a Dirac type mass term that can be added to the Lagrangian, a so-called Majorana mass term:

$$\mathcal{L}_\nu^{\text{Majorana}} = -\frac{1}{2}\underbrace{\sum_{\alpha,\beta}(m_L)_{\alpha\beta}\overline{\nu_L}_\alpha(\nu_L)^{\mathcal{C}}_\beta}_{\text{not SU(2)}_\text{L}\text{ invariant}} -\frac{1}{2}\sum_{i,j=1}^{3}(M_R)_{ij}\overline{(\nu_R)^{\mathcal{C}}_i}\nu_{Rj} + h.c. \tag{3.3}$$

	$SU(3)_C$	$SU(2)_L$	Y	Q
ν_{Ri}	$\mathbf{1}$	$\mathbf{1}$	0	0

Table 3.1: The right-handed neutrinos that are added in the minimal extension of the Standard Model to allow for neutrino masses and the representations of the gauge groups $SU(3)_C$ and $SU(2)_L$ to which they are assigned.

However, the mass terms that are added to the Lagrangian do not have to only obey Poincare invariance but also the gauge symmetry of the Standard Model and the first term in Eq. (3.3), the Majorana mass term of the left-handed neutrinos, is not invariant under transformations of the SU(2) and cannot be introduced explicitly to the Lagrangian. The Majorana mass term for the right-handed neutrinos on the other hand is invariant under the gauge transformations since it is a total singlet and can be simply added to the Lagrangian. As can be seen from Eq. (3.3), the Majorana mass matrix M_R is symmetric, *i.e.* $(M_R)_{ij} = (M_R)_{ji}$.

In principle a Majorana mass term can also be generated for the left-handed neutrinos by Spontaneous Symmetry Breaking. One could either have an effective coupling of the two neutrino fields to two Higgs doublets to construct a SU(2)-invariant operator, but this would correspond to a 5 dimensional operator and require a suppression factor $1/\Lambda$ of mass dimension -1 where Λ indicates the scale of new physics that give rise to the effective operator. A second possibility is to introduce an additional Higgs field, a SU(2) triplet, to the particle content. This Higgs triplet can also couple to the two neutrino fields and if it develops a non-vanishing vacuum expectation value similar to the Higgs doublet, a Majorana mass for the left-handed neutrinos is generated by Spontaneous Symmetry Breaking. However, the existence of such a Higgs triplet is heavily constrained by electro-weak precision data, especially by the measurement of the ρ-parameter (see *e.g.* [9] for a review). The mass term of the right-handed neutrinos on the other hand is not constrained at all and also not protected by any Standard Model symmetry. Usually the magnitude is naturally expected near the GUT scale $\mathrm{M_{GUT}} \lesssim 10^{16}$ GeV.

3.2 Neutrino Mixing

Parallel to the introduction of neutrino masses to the Standard Model the option of neutrino mixing becomes enabled. In the Standard Model no neutrino masses are present, so that neutrino mass eigenstates are not well defined. In this scenario, the flavor basis of the charged leptons can always be chosen such, that the mass eigenstates of the charged leptons and their weak eigenstates, *i.e.* the interaction eigenstates, are identical and no mixing occurs. However, in this basis also the flavor eigenstates of the neutrinos ν_α are fixed and not necessarily identical to the mass eigenstates ν_i after the introduction of the mass terms.

The flavor eigenstates, *i.e.* the eigenstates of the weak interactions, and the mass eigenstates, *i.e.* the eigenstate basis that provides diagonal mass matrices, are related by a unitary transformation, described by unitary 3×3 matrices in flavor space. This is similar to the Cabibbo-Kobayashi-Maskawa [10, 11] mixing in the quark sector. The mass eigenstates are indicated by Latin indices $i = 1, 2, 3$ and the flavor eigenstates are indicated by Greek indices

$\alpha = e, \mu, \tau$:

$$\begin{aligned} e_{L\alpha} &= \sum_i (U_L^e)_{\alpha i}\, e_{Li} & e_{R\alpha} &= \sum_i (U_R^e)_{\alpha i}\, e_{Ri} \\ \nu_{L\alpha} &= \sum_i (U_L^\nu)_{\alpha i}\, \nu_{Li} & \nu_{R\alpha} &= \sum_i (U_R^\nu)_{\alpha i}\, \nu_{Ri} \end{aligned} \tag{3.4}$$

These so defined unitary matrices diagonalize the mass matrices in flavor space, which reads for the charged leptons as

$$(U_L^e)^*_{\alpha i}(M_l)_{\alpha\beta}(U_R^e)_{\beta j} = m_{li}\delta_{ij}. \tag{3.5}$$

For the neutrinos, one has to discriminate between the two possible underlying mass terms, how to diagonalize the mass matrices:

$$\begin{aligned} \text{Dirac Neutrino Case :} \quad & (U_L^\nu)^*_{\alpha i}(m_D)_{\alpha\beta}(U_R^\nu)_{\beta j} = m_{\nu i}\delta_{ij} \\ \text{Majorana Neutrino Case :} \quad & (U_L^\nu)_{\alpha i}(m_L)_{\alpha\beta}(U_L^\nu)_{\beta j} = m_{\nu i}\delta_{ij} \end{aligned} \tag{3.6}$$

Now, we will focus on the weak interactions of the neutrinos and see how the lepton mixing affects the interactions of neutrinos. The relevant part of the Lagrangian is:

$$\begin{aligned} \mathcal{L}_W^\nu &= -\sum_\alpha \left[\frac{g}{\sqrt{2}}\overline{e_{L\alpha}}\gamma^\mu \nu_{L\alpha} W_\mu^- + \frac{g}{4\cos\theta}\overline{\nu_{L\alpha}}\gamma^\mu \nu_{L\alpha} Z_\mu^0\right] + h.c. \\ &= -\sum_{i,j} \left[\frac{g}{\sqrt{2}}\overline{e_{Li}}(U_L^e)^*_{\alpha i}\gamma^\mu (U_L^\nu)_{\alpha j}\nu_{Lj} W_\mu^- + \frac{g}{4\cos\theta}\overline{\nu_{Li}}(U_L^\nu)^*_{\alpha i}\gamma^\mu (U_L^\nu)_{\alpha j}\nu_{Lj} Z_\mu^0\right] + h.c. \\ &= -\sum_{i,j} \left[\frac{g}{\sqrt{2}}\overline{e_{Li}}\gamma^\mu (U_L^{e\dagger}U_L^\nu)_{ij}\nu_{Lj} W_\mu^- + \frac{g}{4\cos\theta}\overline{\nu_{Li}}\gamma^\mu \nu_{Li} Z_\mu^0\right] + h.c. \end{aligned} \tag{3.7}$$

As can be seen, the unitary matrices cancel out in case of neutral current interaction of the neutrinos due to the unitarity condition. The charged current interactions however are sensitive to leptonic mixing, since the mixing matrices do not cancel. In general, one considers a flavor basis, where the charged lepton eigenstates do correspond to their mass eigenstates and leptonic mixing is shifted to the neutrino sector. In this case only one unitary matrix U merges the mixing of the leptonic sector:

$$U = U_L^{e\dagger} U_L^\nu \tag{3.8}$$

The unitary matrix U is the mixing matrix of neutrinos, sometimes referred to as the Pontecorvo-Maki-Nakagawa-Sakata mixing matrix [12]. Similar to the standard parameterization of the Cabibbo-Kobayashi-Maskawa matrix in the quark sector, the matrix can be parameterized by three Euler angles θ_{12}, θ_{13}, and θ_{23}. Furthermore, U can generally be a complex matrix and six phases remain as free parameters in the parameterization after the nine unitarity constraints are considered. However, three of these phases are unphysical because they can be canceled out by a re-definition of the charged lepton fields, *i.e.* these phases are absorbed. The remaining phases are referred to as the Dirac phase δ_{CP} and the Majorana phases ϕ_1 and ϕ_2. The parameterization has to be defined by the ordering of the three Euler rotations matrices U_{12}, U_{13}, and U_{23}:

$$\begin{aligned} U_{23} &= \begin{pmatrix} 1 & 0 & 0 \\ 0 & c_{23} & s_{23} \\ 0 & -s_{23} & c_{23} \end{pmatrix}, & U_{13} &\begin{pmatrix} c_{13} & 0 & s_{13}e^{-i\delta_{\mathrm{CP}}} \\ 0 & 1 & 0 \\ -s_{13}e^{i\delta_{\mathrm{CP}}} & 0 & c_{13} \end{pmatrix} \\ U_{12} &= \begin{pmatrix} c_{12} & s_{12} & 0 \\ -s_{12} & c_{12} & 0 \\ 0 & 0 & 1 \end{pmatrix}, & P_M &= \begin{pmatrix} e^{i\phi_1/2} & 0 & 0 \\ 0 & e^{i\phi_2/2} & 0 \\ 0 & 0 & 1 \end{pmatrix} \end{aligned} \tag{3.9}$$

Here, the notation is chosen such that $c_{ij} \equiv \cos\theta_{ij}$ and $s_{ij} \equiv \sin\theta_{ij}$. The Majorana phases are contained in the diagonal matrix P_M. In the Dirac case also the Majorana phases are unphysical because they can be canceled out by a re-definition of the right-handed neutrino fields. In this case only one complex phase, the Dirac phase δ_{CP}, remains in the parameterization of U. Depending on the nature of the neutrino mass term, the neutrino mixing matrix U is given as:

$$\begin{aligned} \text{Dirac Neutrino Case :} \qquad & U = U_{23}U_{13}U_{12} \\ \text{Majorana Neutrino Case :} \qquad & U = U_{23}U_{13}U_{12}P_M \end{aligned} \tag{3.10}$$

In the Dirac case the neutrino mixing matrix takes the form

$$U_{23}U_{13}U_{12} = \begin{pmatrix} c_{12}c_{13} & s_{12}c_{13} & s_{13}e^{-i\delta_{\mathrm{CP}}} \\ -s_{12}c_{23} - c_{12}s_{23}s_{13}e^{i\delta_{\mathrm{CP}}} & c_{12}c_{23} - s_{12}s_{23}s_{13}e^{i\delta_{\mathrm{CP}}} & s_{23}c_{13} \\ s_{12}s_{23} - c_{12}c_{23}s_{13}e^{i\delta_{\mathrm{CP}}} & -c_{12}s_{23} - s_{12}c_{23}s_{13}e^{i\delta_{\mathrm{CP}}} & c_{23}c_{13} \end{pmatrix}, \tag{3.11}$$

that is similar to the standard parameterization of the Cabbibo-Kobayashi-Maskawa matrix of the quark sector. The mixing matrix U relates the weak flavor eigenstates ν_e, ν_μ, and ν_τ to the neutrino mass eigenstates ν_1, ν_2, and ν_3:

$$|\nu_\alpha\rangle = \sum_i U^*_{\alpha i}|\nu_i\rangle \tag{3.12}$$

Note that, different than can be naively expected from the last line in Eq. (3.7), the complex conjugate $U^*_{\alpha i}$ enters in the relation between flavor and mass eigenstates. The reason is, that Eq. (3.7) contains fields and here we consider one-particle states that have to be generated out of the vacuum state $|0\rangle$ by applying the conjugate of the field [13].

3.3 See-Saw Mechanism

The observation of neutrino oscillations has given the evidence for massive neutrinos. The absolute scale of the neutrino masses however is not definitively determined yet. But, constraints from Tritium endpoint experiments and cosmology imply an upper bound with $m_\nu \lesssim 1$ eV[1]. In case of Dirac neutrinos where only a Dirac mass term is present, the smallness of neutrino masses is commonly addressed as unnatural. Naively, one would expect the Yukawa couplings of all fermions to be of the same magnitude which would lead to similar masses of all fermions. This expectation is already violated by the charged fermions since the masses, *i.e.* the Yukawa couplings of the lightest charged fermion, the electron, and the heaviest charged fermion, the

---

[1] The details of the measurements and the exact bounds will be given in Chapter 5

top quark, are divided by six orders of magnitude. The smallness of neutrino masses in the Dirac case would have to be achieved by the introduction of even smaller Yukawa couplings, five orders of magnitude smaller than the Yukawa coupling of the electron. The big difference is that the charged fermions follow a strong hierarchy of masses between the generations, but are within one or two orders of magnitude within one generation. The neutrinos on the other hand would additionally introduce a strong hierarchy within the generations.

The so-called See-Saw mechanism is the most popular scenario to provide an explanation for the smallness of neutrino masses. However, the See-Saw mechanism requires the existence of a Dirac and a Majorana mass term simultaneously. The neutrino mass terms in the Lagrangian from Eq. (3.1) and Eq. (3.3) can be merged to a compactified notation:

$$\mathcal{L}_\nu^{Mass} = \begin{pmatrix} \overline{\nu_L} & \overline{(\nu_R)^\mathcal{C}} \end{pmatrix} \underbrace{\begin{pmatrix} m_L & m_D \\ m_D^T & M_R \end{pmatrix}}_{\mathcal{M}} \begin{pmatrix} (\nu_L)^\mathcal{C} \\ \nu_R \end{pmatrix} + h.c. \tag{3.13}$$

The neutrino mass eigenstates are found by diagonalization of the mass matrix $\mathcal{M}$. The single contributions within $\mathcal{M}$ are supposed to follow a hierarchy $m_L \ll m_D \ll M_R$. We stated earlier that m_L is constrained since it arises either from a five dimensional operator or through the vacuum expectation value of a Higgs triplet, constrained by electro-weak precision measurements, and commonly is taken to be $m_L = 0$. The Dirac mass is generated by Spontaneous Symmetry Breaking and expected to be of the order of the electro-weak scale $\Lambda_{EW} \sim 10^2$ GeV or lower while the Majorana mass of the right-handed neutrinos is not constrained by any Standard Model symmetry and is allowed to be as large as the GUT scale $\mathrm{M_{GUT}} \sim 10^{16}$ GeV.

The diagonalization of $\mathcal{M}$

$$\mathcal{M}_{Diag} = V^T \mathcal{M} V = \begin{pmatrix} \tilde{m}_L & 0 \\ 0 & \tilde{M}_R \end{pmatrix} \tag{3.14}$$

can be achieved by approximate block-diagonalization with the matrix

$$V \simeq \begin{pmatrix} 1 & m_D^* M_R^{*\,-1} \\ -M_R{}^{-1} m_D^T & 1 \end{pmatrix} \tag{3.15}$$

which is close to the identity matrix and hence we get

$$\tilde{\nu}_L \simeq \nu_L, \quad \tilde{\nu}_R \simeq \nu_R. \tag{3.16}$$

The block-diagonal matrix $\mathcal{M}_{Diag}$ only connects left-handed neutrinos with their conjugates and right-handed neutrinos with their conjugates and the mass eigenstates are pure Majorana neutrinos after the diagonalization process. The block-entries are given by the famous See-Saw relation:

$$\tilde{m}_L \simeq m_L - m_D M_R^{-1} m_D^T = m_L - \frac{v_{EW}^2}{2} Y_\nu M_R^{-1} Y_\nu^T, \qquad \tilde{M}_R \simeq M_R \tag{3.17}$$

Here, the right-handed neutrino masses are still at the GUT scale but the left-handed neutrino masses are suppressed by the GUT scale through M_R^{-1} and the smallness can be explained. If $m_L = 0$ is assumed, it is referred to as the See-Saw mechanism of Type-I, while a non-zero m_L leads to the denotation of See-Saw Type-II. In case of See-Saw Type-I, although $m_L = 0$, the effective low energy neutrinos are left-handed Majorana neutrinos and the non-zero mass is generated by the See-Saw mechanism. This effect is schematically shown in the diagram of Fig. 3.1.

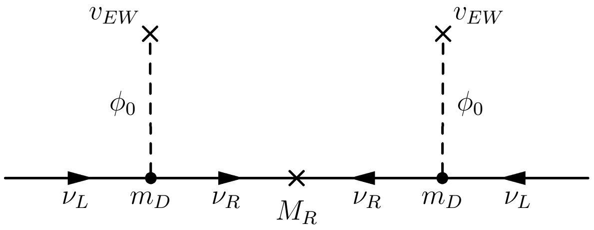

Figure 3.1: Diagramatic illustration of the generation of an effective left-handed majorana mass operator m_L of light neutrinos through the See-Saw mechanism involving the Dirac mass term and the Majorana mass term of the heavy right-handed neutrinos ν_R.

3.4 Implications

The presence of neutrino masses and neutrino mixing implies additional phenomenological consequences compared to the Standard Model. We will review in this section the three most interesting possible implications of neutrino masses. Neutrino oscillations have already been established and confirm that neutrinos indeed do have a mass and there is mixing between the neutrino flavor eigenstates. For the oscillation mechanism to work, the nature of neutrino masses, *i.e.* if they are Majorana or Dirac particles, is not relevant and hence this cannot be observed in neutrino oscillations. The further discussed possible implications of masses and mixing are the famous neutrino-less double beta decay, in abbreviation $0\nu\beta\beta$, and Leptogenesis, *i.e.* the mechanism to explain the baryon asymmetry of our universe by the decay of heavy right-handed neutrinos in the early universe.

Neutrino Oscillations

Here, we will only briefly discuss the framework of neutrino oscillations as they are implications of non-zero neutrino masses and neutrino mixing. Since neutrino oscillations are the topic of this work, a more detailed introduction to the framework is given in the next chapter. Neutrino oscillations can be understood in a complete quantum mechanical framework. The first description of neutrino oscillations was given in [14] but for $\nu \leftrightarrow \overline{\nu}$, whereas the first discussion of neutrino oscillations between the flavor eigenstates was given in [15, 16]. The starting point is the neutrino mixing described by the unitary mixing matrix as introduced in Eq. (3.12):

$$|\nu_\alpha\rangle = \sum_i U^*_{\alpha i}|\nu_i\rangle$$

The time evolution of the neutrino states is described by the Schrödinger equation, here formulated for neutrino mass eigenstates in the rest frame of the neutrinos:

$$i\frac{\partial}{\partial\tau_i}|\nu_i\rangle \;=\; \hat{\mathbf{H}}|\nu_i\rangle \;=\; m_i|\nu_i\rangle \tag{3.18}$$

Thus, the time evolution of the neutrino mass eigenstates is described by a time dependent complex phase factor:

$$|\nu_i(\tau_i)\rangle \;=\; e^{-im_i\tau_i}|\nu_i(0)\rangle. \tag{3.19}$$

However, the time evolution is required to be described in the laboratory frame where the measurements take place. We will only consider relativistic neutrinos since the neutrino mass is very small and all considered neutrino energies throughout this work will satisfy the condition $E_\nu \gg m_\nu$. The phase exponent in the time evolution of the neutrino mass eigenstates in the laboratory system is expressed in terms of neutrino energy E_i and momentum p_i as

$$\begin{aligned} m_i\tau_i = E_i t - p_i x &= E_i t - \sqrt{E_i^2 - m_i^2}x \\ &\simeq Et - Ex + \frac{m_i^2}{2E}x \\ &\simeq \frac{m_i^2}{2E}x = \frac{m_i^2}{2E}L \end{aligned} \tag{3.20}$$

where we have used the expansion of the square root and the relativistic approximation $x \approx t$. Furthermore, we have introduced the baseline L, *i.e.* the distance between the location of neutrino production and detection. It can be seen that the phase factor can be approximated and expressed in terms of squared neutrino masses[2].

Now, the relevant aspect leading to neutrino oscillations is that neutrinos can only be produced or detected in charged current weak interaction processes where only neutrino flavor eigenstates participate. Between production and detection the neutrinos propagate as superposition of neutrino mass eigenstates with different evolutions of the phase factors and flavor transitions become possible, *i.e.* the detection of a neutrino of different flavor as the flavor of the initially produced neutrino. The probability $P_{\alpha\beta}$ of such a flavor transition from flavor α to flavor β is again calculated in the simple quantum mechanical picture:

$$|\nu(t=0)\rangle = |\nu_\alpha\rangle = \sum_k U^*_{\alpha k}|\nu_k\rangle \tag{3.21}$$

$$\begin{aligned} P_{\alpha\beta} = |\langle\nu_\beta|\nu(t)\rangle|^2 &= \left|\sum_k U^*_{\alpha k} e^{-i\frac{m_k^2}{2E}L}\langle\nu_\beta|\nu_k\rangle\right|^2 \\ &= \left|\sum_{k,j} U_{\beta j}U^*_{\alpha k} e^{-i\frac{m_k^2}{2E}L}\langle\nu_j|\nu_k\rangle\right|^2 \\ &= \left|\sum_k U_{\beta k}U^*_{\alpha k} e^{-i\frac{m_k^2}{2E}L}\right|^2 \\ &= \sum_{k,j} U_{\beta k}U^*_{\alpha k}U^*_{\beta j}U_{\alpha j} e^{-i\frac{m_k^2-m_j^2}{2E}L} \end{aligned} \tag{3.22}$$

It arises that the transition probability has indeed an oscillatory behavior since it is 2π-periodic in the parameter L/E, *i.e.* for a fixed neutrino energy the probability oscillates with the distance from the location of neutrino production. Besides, it is obvious that a non-zero transition probability between the different flavors $\alpha \neq \beta$ can only be obtained if neutrino mixing *and* non-zero neutrino masses are present simultaneously. If only one is present, *i.e.* either neutrino mixing of massless neutrinos or no mixing of massive neutrinos, no neutrino oscillations can occur:

---

[2] Note, that this is similar to the equal energy approximation (all mass eigenstates have equal energies $E_i = E$) which is in principle not the correct assumption but gives the right result as does the opposed equal momenta approximation (all mass eigenstates have equal momenta $p_i = p$). In general, the kinematics of the process where the neutrino is produced has to be taken accurately into account. See [17] or the review [18] for details of the discussion.

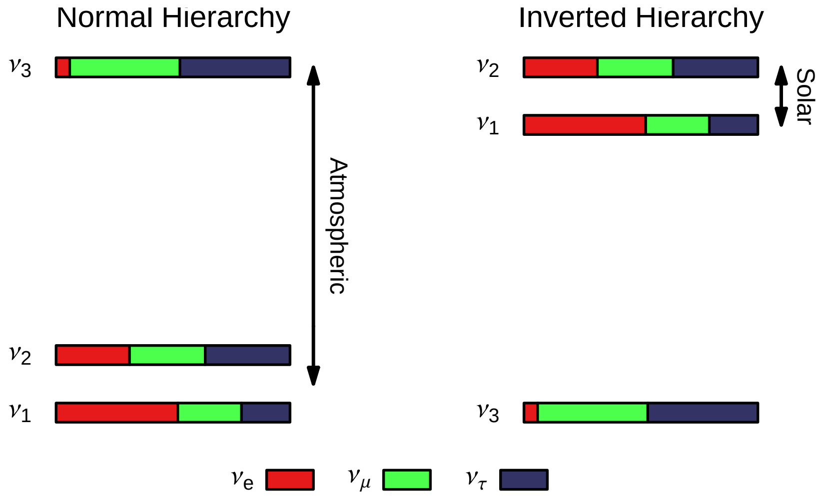

Figure 3.2: The mass spectrum of the three neutrino mass eigenstates ν_1, ν_2, and ν_3 in case of normal hierarchy (left) and inverted hierarchy (right). The single mass eigenstates are separated into the respective contributions coming from the three flavor eigenstates ν_e (red), ν_μ (green), and ν_τ (blue). The contribution of ν_e to ν_3 is given by $|U_{e3}|^2$ and would vanish in case of $\sin^2 2\theta_{13} = 0$. Here a value of $\sin^2 2\theta_{13} = 10^{-2}$ is chosen.

No neutrino masses ($m_i = 0$)

$$P_{\alpha\beta} = \sum_k U_{\beta k} U^*_{\alpha k} \sum_j U^*_{\beta j} U_{\alpha j} = (UU^\dagger)_{\beta\alpha} (U^\dagger U)_{\beta\alpha} = \delta_{\alpha\beta} \tag{3.23}$$

No neutrino mixing ($U_{\alpha i} = \delta_{\alpha i}$)

$$P_{\alpha\beta} = \sum_{k,j} \delta_{\beta k}\delta_{\alpha k}\delta_{\beta j}\delta_{\alpha j} e^{-i\frac{m_k^2 - m_j^2}{2E}L} = \delta_{\beta\alpha}\delta_{\beta\alpha} e^{-i\frac{m_\beta^2 - m_\alpha^2}{2E}L} = \delta_{\alpha\beta} \tag{3.24}$$

Furthermore, Eq. (3.22) shows that not the absolute neutrino mass scale or absolute neutrino mass differences enter the oscillation probabilities but the difference of the squared neutrino masses $\Delta m^2_{kj} \equiv m_k^2 - m_j^2$, the so-called mass-squared differences. It should be mentioned that in the Majorana case the introduced Majorana phases ϕ_1 and ϕ_2 do not enter the oscillation probability and neutrino oscillations do not distinguish phenomenologically between the Dirac and the Majorana case. So, neutrino oscillations do not provide any possible insight to this important puzzle of neutrino physics and the Majorana phases are the only parameters in the neutrino mixing matrix that cannot be addressed in neutrino oscillations.

The masses and mixing of neutrinos is illustrated in Fig. 3.2. The horizontal bars represent the neutrino mass eigenstates ν_1, ν_2, and ν_3 with increasing mass from bottom to top. The mass eigenstates are linear combinations of the flavor eigenstates ν_e, ν_μ, and ν_τ indicated by the colored contributions to the bars. The three neutrino framework allows to combine neutrino masses to three mass squared differences Δm^2_{21}, Δm^2_{31}, and Δm^2_{32}. However, only two out of the three mass squared differences are independent. From neutrino oscillation observations, that will be presented in detail in Chapter 5, it is known that one mass squared difference Δm^2_{21}, the so-called solar mass squared difference since it appears in flavor transitions of solar neutrinos, is two orders of magnitude smaller than the other two mass squared differences Δm^2_{31} and Δm^2_{32}, the so-called atmospheric mass squared differences since they

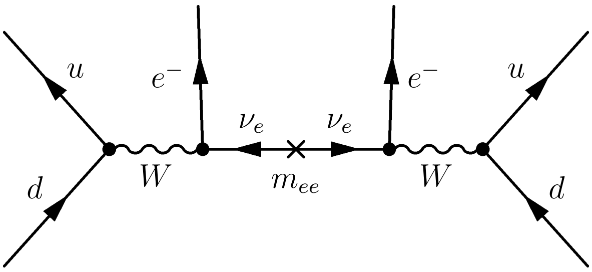

Figure 3.3: The simplest diagram leading to neutrino-less double beta decay ($0\nu\beta\beta$) in case of a non-vanishing Majorana mass term for the left-handed neutrinos ν_L. Lepton number L_e is violated by two units since two electrons are emitted. The amplitude is proportional to the 11-element of the neutrino mass matrix m_{ee}

appear in the neutrino oscillations of neutrinos produced in the Earth's atmosphere. This is illustrated in Fig. 3.2 by the hierarchical ordering in the figure. But since the sign of the atmospheric mass squared differences is not known yet there exist two possible mass hierarchy ordering scenarios for the neutrinos, one where the third mass eigenstate ν_3 is heavier than the other two which is called the normal neutrino mass hierarchy (left-hand side) and the opposite mass ordering where ν_3 is the lightest neutrino mass eigenstate which is called the inverted neutrino hierarchy (right-hand side)[3]. Note, that the absolute mass scale is not known and there only exist upper bounds that still allow for a so-called quasi-degenerate neutrino mass spectrum, where the absolute mass scale of the neutrinos is considerably larger than the mass differences between the single neutrinos and all three neutrino mass eigenstates have very similar masses.

Neutrino-less Double Beta Decay

Within the last subsection we stated that neutrino oscillations cannot distinguish between the Dirac neutrino case and the Majorana neutrino case. One of the most promising processes that could shed light to this very important puzzle of neutrino physics is the process of neutrino-less double beta decay. If neutrinos are of Majorana type, *i.e.* have non-vanishing Majorana masses, lepton number violating processes become possible with one of them being this famous neutrino-less double beta decay ($0\nu\beta\beta$) where a nucleus decays to another nucleus with the atomic number Z increased by two units and accompanied by the emission of two electrons

$$(A, Z) \to (A, Z+2) + 2e^-, \tag{3.25}$$

hence the lepton number L_e is violated by two units. This can only be observable for nuclei that already allow normal double beta decay where single beta decays are energetically forbidden but two beta decays simultaneously accompanied with the emission of two electrons and two anti-neutrinos are allowed. The spectrum of the electron energy sum of the conventional

---

[3] Here, the terms "normal" and "inverted" refer to the prejudice that neutrinos should fit into the usual picture of mass orderings as is true for the other fermions, since for the charged leptons and up- and down-type quarks the mass differences increase between 1st/2nd and 2nd/3rd generation. However, neutrinos are known to allow for surprises, since due to a similar prejudice it was expected that neutrino mixing should be small as in the quark sector.

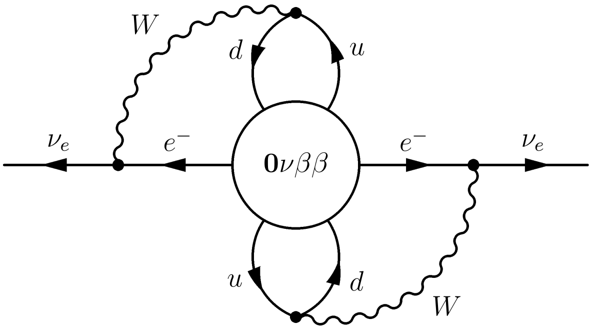

Figure 3.4: The diagram of the black box argument that shows that the presence of neutrino-less double beta decay automatically implies the existence of an effective Majorana mass term [19].

double beta decay is continuous due to the emission of the undetectable neutrinos but the neutrino-less double beta decay must give a discrete peak. The decay width of the process is proportional to the squared of the absolute value of the 11-element $\langle m_{ee} \rangle$ of the neutrino mass matrix in the flavor basis as can be understood from the tree level Feynman diagram of the process illustrated in Fig. 3.3. Additionally nuclear matrix elements enter the decay amplitude and introduce a further limiting factor additionally to the long half-time of the decay since the nuclear matrix elements are associated with large uncertainties.

However, neutrino-less double beta decay only is allowed for Majorana neutrinos. Thus, the process is directly related to the Majorana character of the neutrinos and an observation of neutrino-less double beta decay is a clear signature for the Majorana character of neutrinos. Not only a Majorana mass term makes neutrino-less double beta decay possible but also in the other direction every black box neutrino-less double beta decay process directly implies an effective Majorana mass term for the neutrinos [19] as can be seen from the diagram in Fig. 3.4. Unfortunately, the argument cannot be twisted because from the non-observation the neutrino-less double beta decay cannot exclude the Majorana character of neutrinos. This can be understood from the formula for the 11-element of the mass matrix $\langle m_{ee} \rangle$:

$$\langle m_{ee} \rangle = \left| \sum_{j=1}^{3} U_{ej}^2 \, m_j \right| = \left| c_{13}^2 \, c_{12}^2 \, m_1 \, e^{i\phi_1} + c_{13}^2 \, s_{12}^2 \, m_2 \, e^{i\phi_2} + s_{13}^2 \, m_3 \, e^{i2\delta} \right| \tag{3.26}$$

As can be seen, the relevant mass matrix element contains three terms where all three phases enter here. Thus, three complex numbers are summed and cancellation can occur for a proper combination of phases. Such a cancellation could lead to a vanishing $\langle m_{ee} \rangle$ although neutrinos are Majorana particles and neutrino-less double beta decay cannot be observed. However such a cancellation is only possible if neutrino masses are of normal hierarchy as is illustrated in Fig. 3.5. There, the mass matrix element $\langle m_{ee} \rangle$ is given as a function of the mass m of the lightest neutrino mass eigenstate for normal hierarchy (left-hand side, with $m = m_1 = m(\nu_1)$) and inverted hierarchy (right-hand side, with $m = m_3 = m(\nu_3)$). The bands indicate variations of the input parameters θ_{12}, Δm_{21}^2, Δm_{31}^2, θ_{13} and the phases δ_{CP}, ϕ_1, and ϕ_2 that enter the formula of $\langle m_{ee} \rangle$. The innermost dark bands only take a variation of the phases into account while the other parameters are fixed to their best-fit values. The next brighter region uses the variation of the phases and the other parameters besides θ_{13} within their 3σ allowed ranges while $\theta_{13} = 0$ is kept fixed. The brightest largest region also takes

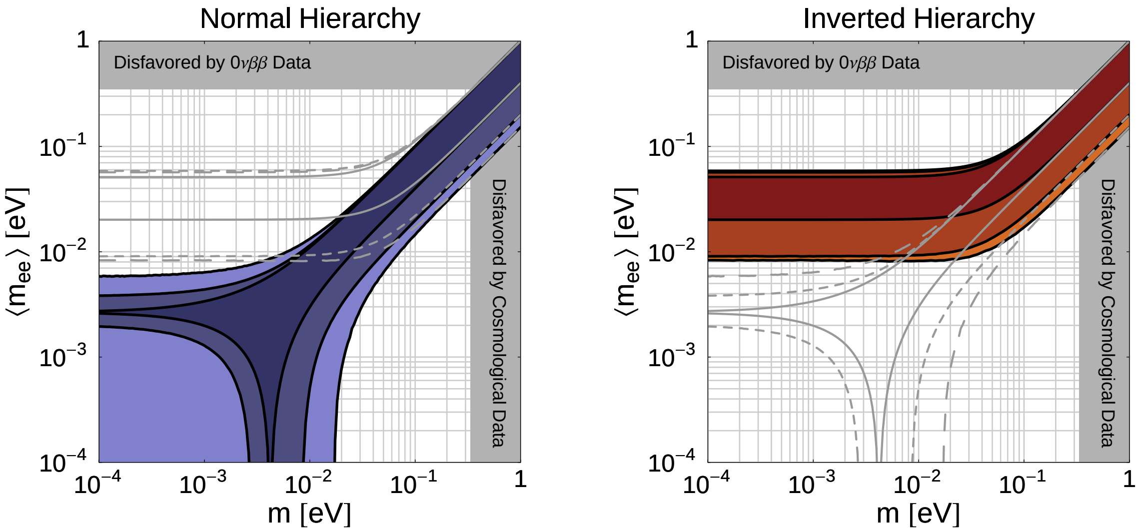

Figure 3.5: The possible values of the effective neutrino mass $\langle m_{ee}\rangle$ relevant in $0\nu\beta\beta$ decay as a function of the lightest neutrino mass m for the normal mass hierarchy $m = m_1 < m_2 < m_3$ (left) and the inverted mass hierarchy $m = m_3 < m_1 < m_2$ (right). The inner (darkest) regions are obtained with the best-fit values of the oscillation parameters and only the CP phases ϕ_1, ϕ_1, and δ are kept free. The next brighter region is obtained by the variation of the phases *and* the oscillation parameters θ_{12}, Δm^2_{21}, and Δm^2_{31} within the allowed 3σ ranges while θ_{13} is fixed to be zero. The outmost brightest region is obtained by a variation of all relevant parameters in $\langle m_{ee}\rangle$ within their allowed 3σ ranges.

into account a variation of θ_{13} within the allowed 3σ range. In case of normal hierarchy we observe that for intermediate neutrino masses 10^{-2} eV $< m < 10^{-3}$ eV indeed a cancellation of $\langle m_{ee}\rangle$ is possible while for inverted hierarchy this is never the case and $\langle m_{ee}\rangle \gtrsim 10^{-2}$ eV holds independent of the magnitude of neutrino masses. Thus, neutrino-less double beta decay could provide a possibility for the discrimination between normal and inverted hierarchy of neutrinos.

Leptogenesis

Extensions of the Standard Model that include neutrino masses additionally offer a promising explanation for the baryon asymmetry of our universe. The amount of the observed present baryon asymmetry is generally described with the quantity

$$\frac{n_{\mathrm{b}} - n_{\overline{\mathrm{b}}}}{n_\gamma} = 6.15 \pm 0.25 \cdot 10^{-10} \tag{3.27}$$

that relates the difference in the number density of baryons and anti-baryons to the present number density of photons in the universe. This number is obtained from observations of the fluctuations in the Cosmic Microwave Background at WMAP [20] and shows that only a tiny asymmetry, *i.e.* a tiny excess of matter over anti-matter, is required at the time the photons decouple to explain the very large asymmetry we observe today. It was found that any mechanism that can provide an explanation for the baryon asymmetry of the universe must fulfill the three Sakharov conditions [21] that are baryon number violation, C and CP violation, and a deviation from thermal equilibrium. In principle these conditions can be fulfilled in the Standard Model but it is still not able to explain the observed asymmetry.

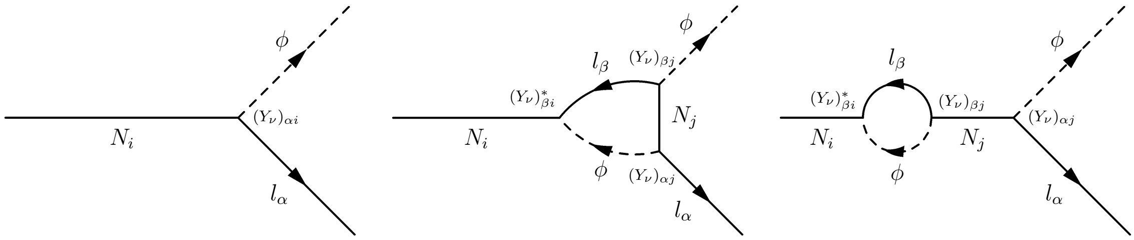

Figure 3.6: The Feynman diagrams for the decay of heavy right-handed neutrinos N_i into a Higgs doublet (containing the neutral scalar ϕ_0 and the charged Higgs scalar) and a lepton doublet (containing the charged leptons and the light left-handed neutrinos) at tree level and at one-loop level. The interference of these diagrams is relevant for Leptogenesis.

It is also not possible to explain the asymmetry with an initially imposed asymmetry since it would have been washed out during inflation. Thus, the observed asymmetry has to be generated dynamically. One scenario where this can be achieved within a See-Saw scenario is the famous mechanism of Leptogenesis [22] where the asymmetry is generated in the lepton sector due to the out-of-equilibrium decays of the heavy right-handed Majorana neutrinos. The relevant processes are shown in Fig. 3.6. This asymmetry in the lepton sector is then transfered to the baryon sector via the (B+L) violating sphaleron processes [23] that are present in the dynamics of the Standard Model.

Usually the framework of Leptogenesis is discussed in a scenario with hierarchical right-handed neutrinos and the asymmetry is generated by the decays of the lightest right-handed Majorana neutrinos ν_{R1}, that are thermally produced during the reheating after the epoch of inflation, the so-called "Thermal Leptogenesis" scenario. Since the number of parameters in the See-Saw mechanism is considerably larger than the number of measurable quantities in low energy neutrino experiments[4], it was questionable if low energy parameters, as for instance the CP phases in light neutrino mixing ϕ_1, ϕ_2, and δ_{CP}, are connected to the mechanism of Leptogenesis. A large number of studies considering the mechanism of Leptogenesis were performed in the so-called "one-flavor" approximation, where flavor effects were neglected and the CP violating decay of the lightest right-handed neutrinos ν_{R1} produced a total lepton number asymmetry. In this scenario the asymmetry was generated due to the CP violation from the right-handed sector and no connection to low energy observables was found.

However, recently it has been discussed that flavor effects can play an important role in scenarios with neutrino masses with $M_{R1} \lesssim 10^{12}$ GeV since at temperatures $T \sim 10^{12}$ GeV the Yukawa couplings of the tau leptons and at $T \sim 10^9$ GeV the Yukawa couplings of the muons get into equilibrium and flavor becomes distinguishable [24, 25]. It was found that in these scenarios low energy parameters can be linked to the mechanism of Leptogenesis and the low energy CP violation from the left-handed neutrinos can contribute to the produced asymmetry. Even in case of absolute CP conservation in the right-handed sector of the See-Saw mechanism the baryon asymmetry of the universe can be dynamically generated by Leptogenesis only due to ϕ_1, ϕ_2, and δ_{CP} [25–32]. Thus, finding CP violation in low energy neutrino experiments as for instance in neutrino oscillation experiments would clearly support the idea of Leptogenesis.

---

[4] Here, the term "low energy" refers to energies much smaller than the natural masses of the right-handed neutrinos within the See-Saw mechanism.

Chapter 4

Neutrino Oscillations

In the last chapter, we already introduced neutrino oscillations alongside the implications of neutrino masses and neutrino mixing. There it has been shown that both, masses and mixing, is required to allow the oscillatory flavor transitions between the neutrinos. In this chapter, we will review the phenomenology of neutrino oscillations in greater detail since we will focus on neutrino oscillation experiments in later chapters. First, we will address the simple framework of two flavor oscillations because the framework is most comprehensible and further phenomenological consequences such as the matter effect can already be discussed in a two flavor scenario. After that, we will switch to the three flavor framework and the additional three flavor effects compared to the two flavor framework will become apparent.

4.1 Two Flavor Oscillations

In the two flavor framework we will work in a two dimensional flavor space. *i.e.* there are two flavor eigenstates $|\nu_\alpha\rangle$ and $|\nu_\beta\rangle$ and two mass eigenstates $|\nu_1\rangle$ and $|\nu_2\rangle$. These states are again related by the neutrino mixing matrix, now called $\tilde{U}$:

$$|\nu_\alpha\rangle = \sum_{i=1}^{2} \tilde{U}^*_{\alpha i}\ |\nu_i\rangle \tag{4.1}$$

This neutrino mixing matrix is now a unitary 2×2 matrix and in this case only one mixing angle is sufficient for the parameterization of the matrix:

$$\begin{pmatrix} |\nu_\alpha\rangle \\ |\nu_\beta\rangle \end{pmatrix} = \begin{pmatrix} \cos\theta & \sin\theta \\ -\sin\theta & \cos\theta \end{pmatrix} \begin{pmatrix} |\nu_1\rangle \\ |\nu_2\rangle \end{pmatrix} \tag{4.2}$$

We will now address the calculation of the disappearance probability for a neutrino that is produced as a flavor eigenstate $|\nu_\alpha\rangle$ and after propagation over the distance of the baseline L it is detected as a neutrino flavor eigenstate $|\nu_\beta\rangle$, *i.e.* a flavor transition has been occurred. The propagation is described by the Schrödinger equation with a Hamiltonian that is diagonal in the basis of mass eigenstates $|\nu_1\rangle$ and $|\nu_2\rangle$ and the propagation of mass eigenstates can be described by a complex phase factor as given in Chapter 3.4, but the initial neutrino is produced as a flavor eigenstate $|\nu(t=0)\rangle = |\nu_\alpha\rangle$. The oscillation probability is calculated by

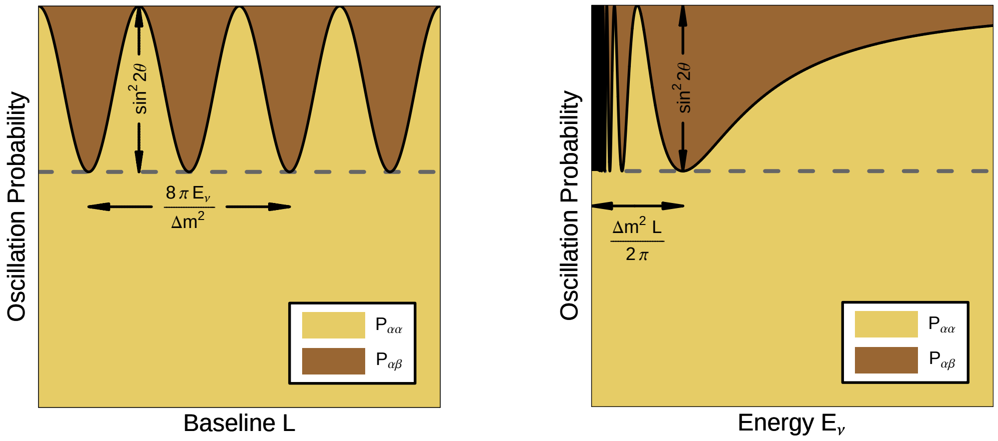

Figure 4.1: The oscillation probabilities $P_{\alpha\alpha}$ (disappearance) and $P_{\alpha\beta}$ (appearance) in the two-flavor scenario as a function of the baseline L, *i.e.* the distance from the source (left), and the neutrino energy E_ν (right). At every baseline L in the left figure and at every neutrino energy E_ν in the right figure the two neutrino oscillation probabilities, disappearance and appearance, add up to unity due to unitarity reasons, *i.e.* $P_{\alpha\alpha} + P_{\alpha\beta} = 1$.

the square of the amplitude:

$$\begin{aligned}
P_{\alpha\beta} &= |\langle \nu_\beta | \nu(t) \rangle|^2 \\
&= \left| \Big(-\sin\theta \langle \nu_1 | + \cos\theta \langle \nu_2 | \Big) \Big(\cos\theta e^{-i\frac{m_1^2}{2E}L} |\nu_1\rangle + \sin\theta e^{-i\frac{m_2^2}{2E}L} |\nu_2\rangle \Big) \right|^2 \\
&= \sin^2\theta \cos^2\theta \left| e^{-i\frac{m_2^2}{2E}L} - e^{-i\frac{m_1^2}{2E}L} \right|^2 \\
&= \frac{1}{4} \sin^2 2\theta \left[2 - 2\cos\left(\tfrac{m_2^2 - m_1^2}{2E} L \right) \right] \\
&= \sin^2 2\theta \, \sin^2\left(\frac{m_2^2 - m_1^2}{4E} L \right) \qquad (4.3)
\end{aligned}$$

This is the famous two-flavor oscillation probability for neutrinos propagating in vacuum. The amplitude of the oscillations is given by the mixing angle parameter $\sin^2 2\theta$ and the oscillation is periodic in the parameter L/E where the frequency is fixed by the mass squared difference of the neutrinos. Note, that the mass ordering of the neutrinos is irrelevant in this formula. The calculation of the related disappearance probability for a neutrino of the flavor α can be calculated similarly. However, the unitarity of the neutrino mixing matrix leads to the unitarity conditions of the oscillation probabilities that is for instance the disappearance and appearance probability adding up to unity:

$$P_{\alpha\alpha} + P_{\alpha\beta} = 1. \qquad (4.4)$$

Thus, the disappearance does not have to be calculated like above but is just given as

$$P_{\alpha\alpha} = 1 - P_{\alpha\beta} = 1 - \sin^2 2\theta \, \sin^2\left(\frac{m_2^2 - m_1^2}{4E} L \right). \qquad (4.5)$$

The unitarity of the oscillation probabilities is also illustrated in Fig. 4.1. The oscillation probabilities in the two-flavor case are shown for neutrino oscillations as a function of the baseline

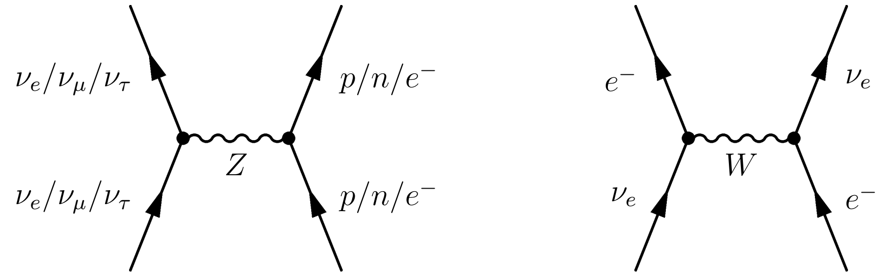

Figure 4.2: The relevant Feynman diagrams for coherent forward scattering of neutrinos traveling through matter. Independently of the flavor, all neutrinos can scatter through neutral-current reactions with the matter neutrons, protons, and electrons (left). Additionally the coherent forward scattering of the ν_e gets contributions from charged-current reactions with the matter electrons (right).

L for neutrinos of a fixed energy (left-hand side) and as a function of the neutrino energy E_ν for a fixed baseline (right-hand side). While the left plot illustrates the periodic oscillatory behavior of the neutrino oscillations, *i.e.* the fact that the initial state is periodically restored, the right plot shows the relevant information for the understanding of the phenomenology at beam-based neutrino oscillation experiments. For the later discussed beam-based oscillation experiments the baseline L between the neutrino source and the detector is usually fixed but the neutrino beam spectrum is continuous and a wider range of neutrino energies is contained. The neutrino beam energy spectrum and the baseline L have to be chosen such that the first oscillation maximum is optimally covered by the beam spectrum. Fig. 4.1 also shows that the amplitude of the oscillations is given by the mixing angle and the frequency is determined by the mass squared difference.

4.2 Matter Effects

The oscillations of neutrinos in vacuum are quite different from oscillations where the neutrinos travel through matter along the baseline. Different than for the propagation of neutrinos in vacuum, the propagation through matter allows for the so-called coherent forward scattering of the neutrinos via weak interactions with the particles of the matter along the path of the neutrinos. While the neutral-current interactions are flavor-blind and do not distinguish between the flavors, the charged-current forward scattering only becomes possible with the corresponding charged leptons that are contained in matter. But since the matter only contains electrons coherent forward scattering is only possible for electron neutrinos. This effect is illustrated in Fig. 4.2. The left-hand side shows the diagram for neutral-current coherent forward scattering with the protons, neutrons, and electrons of the matter that is possible for all flavors while the diagram of the right-hand side is only possible for electron neutrinos.

We will now derive the changes of the oscillation phenomenology in matter. The starting point is the Hamiltonian of neutrino propagation of two flavors in vacuum, now written in the flavor basis while in former discussions it was more convenient to discuss the Hamiltonian in the basis of mass eigenstates. Since in the latter basis the Hamiltonian was diagonal the now discussed Hamiltonian in the flavor basis is not in a diagonal form. The Schrödinger equation is:

$$i\frac{\partial}{\partial t}\begin{pmatrix} |\nu_\alpha\rangle \\ |\nu_\beta\rangle \end{pmatrix} = \frac{1}{2E}\left[\tilde{U}\begin{pmatrix} m_1^2 & 0 \\ 0 & m_2^2 \end{pmatrix}\tilde{U}^\dagger\right]\begin{pmatrix} |\nu_\alpha\rangle \\ |\nu_\beta\rangle \end{pmatrix} \tag{4.6}$$

and the Hamiltonian is a 2×2 matrix that also contains the mixing matrix:

$$\hat{\mathbf{H}}_{\mathrm{VAC}} = \frac{1}{2E}\left[\tilde{U}\begin{pmatrix} m_1^2 & 0 \\ 0 & m_2^2 \end{pmatrix}\tilde{U}^\dagger\right] \tag{4.7}$$

For the discussion of matter effects it is convenient to rewrite the Hamiltonian. Subtracting or adding contributions that are proportional to the identity matrix $\mathbb{1}_{2\times 2}$ do shift the eigenvalues of the Hamiltonian but the dynamics of oscillations between the flavors are not affected by such a transformation since this is only leading to an overall phase shift while neutrino oscillations are the outcome of phase differences[1]. By making use of this effect the derivation of matter effects becomes more convenient.

First, the Hamiltonian of vacuum oscillations is written explicitely in the flavor basis and some trigonometric identities are used. Here, we already have subtracted a matrix proportional to the identity matrix to extract all dimensional quantities out of the matrix. The modified Hamiltonian in Vacuum becomes:

$$\hat{\mathbf{H}}_{\mathrm{VAC}} = \frac{\Delta m_{21}^2}{2E}\left[\tilde{U}\begin{pmatrix} 0 & 0 \\ 0 & 1 \end{pmatrix}\tilde{U}^\dagger\right] = \frac{\Delta m_{21}^2}{4E}\begin{pmatrix} 1-\cos 2\theta & \sin 2\theta \\ \sin 2\theta & 1+\cos 2\theta \end{pmatrix} \tag{4.8}$$

Furthermore, we can again safely subtract all contributions that are proportional to the identity matrix and end up with the further modified Hamiltonian in vacuum in the flavor basis of the two neutrino states:

$$\hat{\mathbf{H}}_{\mathrm{VAC}} = \frac{\Delta m_{21}^2}{4E}\begin{pmatrix} -\cos 2\theta & \sin 2\theta \\ \sin 2\theta & +\cos 2\theta \end{pmatrix} \tag{4.9}$$

Again, the eigenvalues have been shifted by the values that have been subtracted from the diagonal elements but the dynamics is still the same oscillation phenomenology that has been derived in the last section. Now, if a propagation through matter is considered, the mentioned coherent forward scattering adds contributions to the Hamiltonian that are the so-called effective matter potentials. We will here identify the flavor $|\nu_\alpha\rangle$ with the electron neutrino and the flavor $|\nu_\beta\rangle$ with the muon neutrino or the tau neutrino. As could be read off from Fig. 4.2, the neutrinos of flavor α can undergo neutral-current and charged-current coherent forward scattering while the neutrinos of flavor β are only sensitive to neutral-current coherent forward scattering. The relevant effective matter potential can be derived from the weak interaction part of the Lagrangian and are found to be:

$$A_{CC} = A_{CC}(t) = \sqrt{2}G_F N_E(t), \quad A_{NC} = A_{NC}(t) = \frac{1}{\sqrt{2}}G_F N_n(t) \tag{4.10}$$

The effective matter potential for charged current scattering A_{CC} is proportional to the electron number density N_e and the effective coupling constant of the weak interactions, the Fermi constant G_F. The effective matter potentials for the neutral-current coherent forward scattering A_{NC} is also proportional to the Fermi constant and additionally to the number density of the neutrons[2]. These effective matter potential are now inserted to the Hamiltonian in

---

[1] Note, that this argument is independent of the basis and the subtractions can be performed in the flavor basis and in the mass eigenstate basis.

[2] The scattering involves the protons, neutrons, and electrons of the matter but the contributions of protons and electrons cancel out [33].

the flavor basis on the respective diagonal elements since no flavor transitions are governed directly by the forward scattering and one ends up with the Hamiltonian in matter:

$$\hat{\mathbf{H}}_{\mathrm{MAT}} = \frac{\Delta m^2_{21}}{4E}\begin{pmatrix} -\cos 2\theta & \sin 2\theta \\ \sin 2\theta & +\cos 2\theta \end{pmatrix} + \begin{pmatrix} A_{CC} + A_{NC} & 0 \\ 0 & A_{NC} \end{pmatrix} \tag{4.11}$$

Again, the contributions proportional to the identity matrix can be split off

$$\hat{\mathbf{H}}_{\mathrm{MAT}} = \frac{\Delta m^2_{21}}{4E}\begin{pmatrix} -(\cos 2\theta - A') & \sin 2\theta \\ \sin 2\theta & \cos 2\theta - A' \end{pmatrix} + \begin{pmatrix} \frac{A_{CC}}{2} + A_{NC} & 0 \\ 0 & \frac{A_{CC}}{2} + A_{NC} \end{pmatrix} \tag{4.12}$$

and only the first term is relevant for the dynamics of neutrino oscillations. The only remaining contribution from the matter through coherent forward scattering is coming from charged-current interactions of the neutrinos of flavor α. The effective matter potential A_{CC} is hidden in the dimensionless variable A':

$$A' \equiv \frac{2E}{\Delta m^2_{21}} A_{CC} \tag{4.13}$$

Now, the new eigenvalues of the Hamiltonian in matter can be easily calculated:

$$\lambda_{1/2} = \mp \frac{\Delta m^2_{21}}{4E}\sqrt{\sin^2 2\theta + (\cos 2\theta - A')^2} \tag{4.14}$$

With an educated guess and this eigenvalues in mind one can rewrite the Hamiltonian in matter as

$$\begin{aligned} \hat{\mathbf{H}}_{\mathrm{MAT}} &= \frac{\Delta m^2_{21}\sqrt{\sin^2 2\theta + (\cos 2\theta - A')^2}}{4E}\begin{pmatrix} -\frac{(\cos 2\theta - A')}{\sqrt{\sin^2 2\theta + (\cos 2\theta - A')^2}} & \frac{\sin 2\theta}{\sqrt{\sin^2 2\theta + (\cos 2\theta - A')^2}} \\ \frac{\sin 2\theta}{\sqrt{\sin^2 2\theta + (\cos 2\theta - A')^2}} & \frac{\cos 2\theta - A'}{\sqrt{\sin^2 2\theta + (\cos 2\theta - A')^2}} \end{pmatrix} \\ &= \frac{\Delta m^2_{\mathrm{M}}}{4E}\begin{pmatrix} -\cos 2\theta_{\mathrm{M}} & \sin 2\theta_{\mathrm{M}} \\ \sin 2\theta_{\mathrm{M}} & +\cos 2\theta_{\mathrm{M}} \end{pmatrix} \end{aligned} \tag{4.15}$$

which after introducing the new parameters Δm^2_{M}, $\sin 2\theta_{\mathrm{M}}$, and $\cos 2\theta_{\mathrm{M}}$ takes again the form of the vacuum Hamiltonian of Eq. (4.9). Thus the derived Hamiltonian in matter shows the same phenomenology of neutrino oscillations as the Hamiltonian in vacuum but the vacuum parameters are modified by the matter potential parameter A':

$$\begin{aligned} \Delta m^2_{\mathrm{M}} &= \Delta m^2_{21}\sqrt{\sin^2 2\theta + (\cos 2\theta - A')^2} \\ \sin 2\theta_{\mathrm{M}} &= \frac{\sin 2\theta}{\sqrt{\sin^2 2\theta + (\cos 2\theta - A')^2}} \\ \cos 2\theta_{\mathrm{M}} &= \frac{\cos 2\theta - A'}{\sqrt{\sin^2 2\theta + (\cos 2\theta - A')^2}} \end{aligned} \tag{4.16}$$

In the case of anti-neutrinos traveling through the matter the sign of the effective matter potential has to be reversed and the oscillation parameters for anti-neutrinos in matter become:

$$\begin{aligned} \Delta \overline{m}^2_{\mathrm{M}} &= \Delta m^2_{21}\sqrt{\sin^2 2\theta + (\cos 2\theta + A')^2} \\ \sin 2\overline{\theta}_{\mathrm{M}} &= \frac{\sin 2\theta}{\sqrt{\sin^2 2\theta + (\cos 2\theta + A')^2}} \\ \cos 2\overline{\theta}_{\mathrm{M}} &= \frac{\cos 2\theta + A'}{\sqrt{\sin^2 2\theta + (\cos 2\theta + A')^2}} \end{aligned} \tag{4.17}$$

Constant Matter Density Profile

If the neutrinos travel through matter with constant matter density along the baseline, *i.e.* the effective matter potential parameter A' stays constant and the oscillation parameters stay constant along the baseline the new neutrino oscillation probabilities can be easily determined. Since the Hamiltonian is of the same form as the Hamiltonian in vacuum, the formulas for the oscillation probabilities stay the same as derived in the vacuum case. However, the oscillation frequency and the oscillation amplitude are modified due to the presence of the matter potential. Without further calculation we can use the formulas from the last section and find for the oscillation probabilities for neutrinos traveling along a baseline of constant matter density profile:

$$\begin{aligned}
P_{\alpha\alpha} &= 1-\sin^2 2\theta_{\mathrm{M}}\ \sin^2\left(\frac{\Delta m^2_{\mathrm{M}}}{4E}L\right)\\
P_{\alpha\beta} &= \sin^2 2\theta_{\mathrm{M}}\ \sin^2\left(\frac{\Delta m^2_{\mathrm{M}}}{4E}L\right)\\
P_{\bar\alpha\bar\alpha} &= 1-\sin^2 2\overline{\theta}_{\mathrm{M}}\ \sin^2\left(\frac{\Delta \overline{m}^2_{\mathrm{M}}}{4E}L\right)\\
P_{\bar\alpha\bar\beta} &= \sin^2 2\overline{\theta}_{\mathrm{M}}\ \sin^2\left(\frac{\Delta \overline{m}^2_{\mathrm{M}}}{4E}L\right)
\end{aligned} \tag{4.18}$$

We find that different than in vacuum two-flavor oscillations the probabilities for neutrinos and anti-neutrinos differ since the effect of the matter potential is reversed for neutrinos and anti-neutrinos. Thus, a form of CP violation is introduced with the matter along the baseline. This has to be carefully distinguished from intrinsic CP violation that is introduced on an elementary basis since here the CP violation, *i.e.* different probabilities for neutrinos and anti-neutrinos is a consequence of the composition of the matter that is only containing matter and no anti-matter. This externally introduced CP violation is sometimes referred to as extrinsic CP violation. Intrinsic CP violation is, as we will see in the case of three-flavor oscillations, a possible consequence of a complex mixing matrix however in the two-flavor scenario the mixing matrix is always real.

Mikheyev-Smirnov-Wolfenstein Resonance

A further important consequence of the matter potential is the so-called Mikheyev-Smirnov-Wolfenstein resonance. The oscillation parameters in matter differ from the original oscillation parameters in vacuum as described in Eq. (4.16) for neutrinos and Eq. (4.17) for anti-neutrinos. There can occur a resonant enhancement of the mixing angle in matter depending on the value of the dimensionless matter potential parameter A'. For special choices of A' maximal mixing, *i.e.* a mixing angle of $\sin^2 2\theta_{\mathrm{M}} = 1$, can occur even for very small mixing in vacuum, *i.e.* a small vacuum mixing angle $\sin^2 2\theta$. The conditions are

$$\cos 2\theta - A' = 0 \rightarrow \sin^2 2\theta_{\mathrm{M}} = 1 \tag{4.19}$$

for neutrinos and

$$\cos 2\theta + A' = 0 \rightarrow \sin^2 2\overline{\theta}_{\mathrm{M}} = 1 \tag{4.20}$$

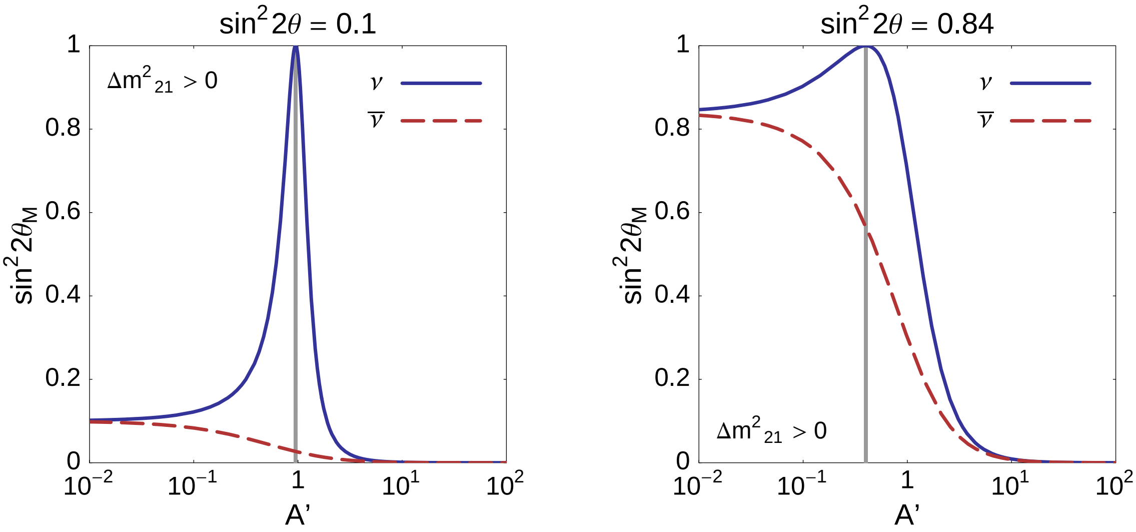

Figure 4.3: The neutrino mixing angle in matter $\sin^2 2\theta_{\mathrm{M}}$ for neutrinos and anti-neutrinos as a function of the matter potential parameter A' for a large vacuum mixing angle $\sin^2 2\theta = 0.84$ (corresponding to the solar mixing angle $\sin^2 2\theta_{12}$) on the left-hand side and a small vacuum mixing angle $\sin^2 2\theta = 0.1$ on the right-hand side. Since $\Delta m^2_{21} > 0$ is assumed, the Mikheyev-Smirnov-Wolfenstein resonance appears for neutrinos at $A' = \cos 2\theta$.

for anti-neutrinos. As we can see, A' has to be compared with $\cos 2\theta$. When A' is explicitely written

$$\cos 2\theta = \begin{cases} +\dfrac{2\sqrt{2}N_e G_F E}{\Delta m^2_{21}} & \text{for } \nu \\[2ex] -\dfrac{2\sqrt{2}N_e G_F E}{\Delta m^2_{21}} & \text{for } \overline{\nu} \end{cases} \tag{4.21}$$

we can read off that for a given energy E and a given mixing angle $\cos 2\theta$ the Mikheyev-Smirnov-Wolfenstein resonance can either occur for neutrinos or anti-neutrinos, depending on the sign of the mass squared difference. This means that the observation of matter effects of neutrinos and anti-neutrinos can discriminate between different mass orderings of neutrinos since it is sensitive to the question which neutrino mass eigenstate is lighter than the other. This is a big difference to vacuum oscillations, where the sign of the Δm^2 did not have any impact.

The Mikheyev-Smirnov-Wolfenstein resonance is illustrated in Fig. 4.3 where the mixing angle in matter $\sin^2 2\theta$ is given as a function of the matter potential parameter A'. Smaller A' is for a lower mass density and larger A' indicates a larger matter density since A' is proportional to the electron density of the matter N_e. The resonance is shown for two cases, small vacuum mixing angle $\sin^2 2\theta = 0.1$ (left-hand side) and large vacuum mixing angle $\sin^2 2\theta = 0.84$ (right-hand side). The matter mixing angle is shown for neutrinos (solid curve) and anti-neutrinos (dashed curve) and since a positive Δm^2 is assumed, the resonance only appears for neutrinos and maximal mixing is obtained. We can also read off from the plots that for very high matter densities (right edges of the plots) the mixing angle vanishes completely independent of the vacuum value. This can be understood in terms of the Hamiltonian in Eq. (4.11). For large matter densities, *i.e.* large potentials A_{CC} and A_{NC}

the first part of the Hamiltonian can be neglected and only the second matrix forms the Hamiltonian but this matrix is diagonal in the flavor-basis. Thus, the basis that provides a diagonal Hamiltonian, *i.e.* the basis of mass eigenstates, is already given in the flavor basis. So, for very high matter densities flavor and mass eigenstates are identical and no mixing occurs. This effect is of importance for the understanding of the solar neutrino puzzle since solar neutrinos are produced in the interior of the sun at very high densities of $\rho \sim 150$ g/cm^3. This will be described in the next chapter in the context of the phenomenology of an adiabatic matter density profile.

Adiabatic Matter Density Profile

Up to now we have only discussed neutrino propagation through constant matter denitiy profiles. However some scenarios like the propagation of solar neutrinos cannot be approximated with a constant matter density profile. Solar neutrinos are produced in the middle of the sun at very high matter densities $\rho \sim 150$ g/cm^3 and then propagate outwards until they leave the sun. From the middle of the sun to the outer regions the matter density decreases continously until zero matter density, *i.e.* vacuum is reached. This can be approximated by the so-called adiabatic matter density profile, where the matter density ρ, and thus also the matter density parameter A', changes adiabatically. Adiabatically here means that the change of matter density is very slow and the system can adjust adequately during the propagation. For a neutrino that is produced as a mass eigenstate at very high densities above the resonance this implies that the neutrino remains the same mass eigenstate during propagation through the adiabatically decreasing matter density and transitions between the mass eigenstates is suppressed. The eigenvalues of the Hamiltonian changes as a function of the matter density, *i.e.* the matter density parameter A'. The eigenvalues are

$$E_{1/2} = \frac{\Delta m_{21}^2}{4E} \left[A' \mp \sqrt{\sin^2 2\theta + (\cos 2\theta - A')^2} \right] \tag{4.22}$$

and the evolution as a function of A' is given in the left-hand side of Fig. 4.4. Note, that these eigenvalues are not the eigenvalues $\lambda_{1/2}$ of the first term in the Hamiltonian in Eq. (4.12) but shifted with $A_{CC}/2$ that is the diagonal part of the charged current matter potential that was neglected for the calculation of $\lambda_{1/2}$. But since we here are interested in the eigenvalues this part is not neglected and $E_{1/2}$ describe the full effect of the charged current coherent forward scattering. The dashed lines in Fig. 4.4 appear for a vanishing mixing angle $\sin^2 2\theta = 0$ and cross at the resonance, but if even a small mixing is introduced the curves avoid crossing. However, if the neutrino is produced at higher densities as a mass eigenstate and remains that state during the propagation through the adiabatically decreasing matter density, the flavor composition of this mass eigenstate changes due to the matter effect and an adiabatic conversion of flavors happens. This effect has to be distinguished from neutrino oscillations. The flavor conversion is illustrated in the right-hand side of Fig. 4.4. At the right edge the neutrino is produced as a ν_α identical with the mass eigenstate ν_2 at high matter densities. The neutrino state ν_2 propagates to smaller matter densities and passes the resonance condition (maximal mixing thus $|\langle \nu_2 | \nu_\alpha \rangle|^2 = |\langle \nu_2 | \nu_\beta \rangle|^2$=0.5). For even smaller matter densities the contribution of the flavor ν_β even increases. Since the flavor composition of ν_α in the propagating mass eigenstate ν_2 in vacuum is given by the vacuum mixing $|\langle \nu_2 | \nu_\alpha \rangle|^2 = \sin^2 \theta$ for very small mixing angles the mass eigenstate ν_2 can even be completely conversed adiabatically from flavor ν_α to flavor ν_β.

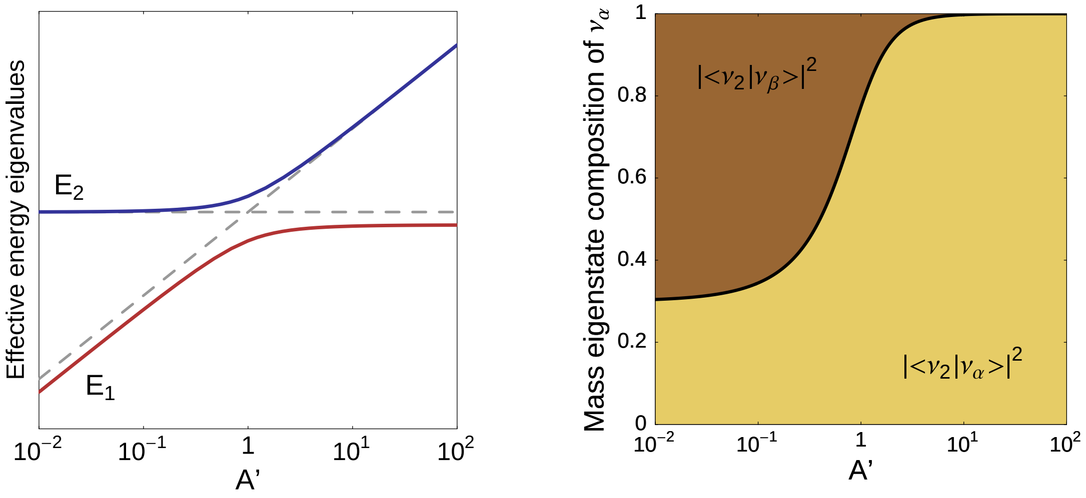

Figure 4.4: The effective energy eigenvalues $E_{1/2}$ in matter (left, logarithmic scaling) and the mass eigenstate compositions $|\langle\nu_2|\nu_\beta\rangle|^2 = \cos^2\theta_\mathrm{M}$ and $|\langle\nu_2|\nu_\alpha\rangle|^2 = \sin^2\theta_\mathrm{M}$ of the flavor eigenstate $|\nu_\alpha\rangle$ (right) as functions of the matter potential parameter A'. The dashed lines in the left-hand side plot illustrate the behavior of the energy eigenvalues in the case of no mixing. The horizontal grey dashed line corresponds to the value of the larger vacuum energy eigenvalue $E_2(A' \ll 0) = \Delta m^2_{21}/2E$ whereas the diagonal grey dashed line corresponds to the larger energy eigenvalue in the limit of very high matter densities $E_2(A' \gg 0) = \Delta m^2_{21}A'/2E$.

4.3 Three Flavor Oscillations

The framework of neutrino oscillations with three flavors is slightly more complicated compared to the two-flavor framework. The unitary mixing matrix contains four instead of only one parameter, that is three mixing angles θ_{12}, θ_{13}, θ_{23}, and the phase δ_CP. The parameterization of the mixing matrix was given in Chapter 3.2[3]. However the basic principles are the same. We begin with calculating the oscillation probabilities, now in the three-flavor framework.

Oscillation Probabilities

The starting point is Eq. (3.22) from the last chapter where an expression for the oscillation probability was found independent of the number of flavors. Here, we assume a summation over the three indices of the three-dimensional flavor space (Latin indices sum over 1,2,3 and indicate mass eigenstates, Greek indices sum over the three flavors of the flavor eigenstates e, μ, τ).

$$
\begin{aligned}
P_{\alpha\beta} &= \sum_{k,l} U_{\beta k} U^*_{\alpha k} U^*_{\beta l} U_{\alpha l} e^{-i\frac{m_k^2 - m_l^2}{2E}L} \\
&= \sum_{k} U_{\beta k} U^*_{\alpha k} U^*_{\beta k} U_{\alpha k} + 2\sum_{k>l} \mathrm{Re}\left[U_{\beta k} U^*_{\alpha k} U^*_{\beta l} U_{\alpha l}\, e^{-i\frac{m_k^2 - m_l^2}{2E}L}\right]
\end{aligned}
$$

---

[3] We will now neglect the Majorana phases ϕ_1 and ϕ_2 because neutrino oscillations are not sensitive to these parameters and the Majorana neutrino case cannot be distinguished from the Dirac neutrino case.

$$
\begin{aligned}
&= \delta_{\alpha\beta} - \sum_{i,j} U_{\beta i} U^*_{\alpha i} U^*_{\beta j} U_{\alpha j} + \sum_k U_{\beta k} U^*_{\alpha k} U^*_{\beta k} U_{\alpha k} \\
&\quad +2 \sum_{k>l} \Big[\mathrm{Re}\left[U_{\beta k} U^*_{\alpha k} U^*_{\beta l} U_{\alpha l}\right] \cos(2\Delta_{kl}) - \mathrm{Im}\left[U_{\beta k} U^*_{\alpha k} U^*_{\beta l} U_{\alpha l}\right] \sin(2\Delta_{kl}) \Big] \\
&= \delta_{\alpha\beta} - 4 \sum_{k>l} \mathrm{Re}\left[U_{\beta k} U^*_{\alpha k} U^*_{\beta l} U_{\alpha l}\right] \sin^2(\Delta_{kl}) \\
&\quad -2 \sum_{k>l} \mathrm{Im}\left[U_{\beta k} U^*_{\alpha k} U^*_{\beta l} U_{\alpha l}\right] \sin(2\Delta_{kl}) \qquad (4.23)
\end{aligned}
$$

This is the famous general formula of neutrino oscillations. We have used the abbreviation $\Delta^2_{kl} \equiv \Delta m^2_{kl} L/2E$. This expression holds for neutrinos and if anti-neutrinos are considered the conjugated elements of the mixing matrix have to be taken. This transformation does not affect the first two terms of the expression however the third term switches the sign. So, if three-flavor oscillations are considered, a complex mixing matrix introduces differences in the oscillation probabilities for neutrinos and anti-neutrinos, hence CP violation becomes possible. Since a complex phase was absent in the two-flavor scenario, CP violation could not arise for two flavors and intrinsic CP violation is a genuine effect for oscillations with more than two flavors.

CP Violation

Intrinsic CP violation in vacuum oscillations arises not until three flavors are considered and thus is called a genuine tree-flavor effect. Note that in the discussion of the matter effect in the two-flavor scenario a difference in the oscillation probabilities of neutrinos and anti-neutrinos was obtained but this effect was due to the CP asymmetric composition of the matter along the baseline that is only containing matter and no anti-matter. This CP violation is called extrinsic CP violation while the genuine CP violation that can arise even for vacuum oscillations in the three-flavor framework is referred to as intrinsic. CP violation in three-flavor vacuum oscillations is given in the case of differing oscillation probabilities:

$$P(\nu_\alpha \to \nu_\beta) \neq P(\overline{\nu}_\alpha \to \overline{\nu}_\beta). \qquad (4.24)$$

In Eq. (4.23) the CP violation arises due to the third term with the imaginary part of the product of neutrino mixing matrix entries. So, CP violation can only arise if the phase δ_{CP} is not realized at one of the CP conserving values, *i.e.*:

$$\delta_{\mathrm{CP}} \neq 0, \quad \text{and} \quad \delta_{\mathrm{CP}} \neq \pi. \qquad (4.25)$$

If δ_{CP} deviates from these values the mixing matrix becomes complex and neutrino and anti-neutrino oscillation probabilities deviate. It can be derived that all CP violating quantities can be expressed with a parameter J_{CP} that is similar to the Jarlskog parameter in the quark sector [34–36]. J_{CP} is given as

$$J_{CP} = \frac{1}{8} \sin\delta_{\mathrm{CP}} \cos\theta_{13} \; \sin 2\theta_{12} \sin 2\theta_{13} \sin 2\theta_{23} \qquad (4.26)$$

In the parameterization of the mixing matrix the CP phase δ_{CP} is closely connected to the mixing angle $\sin\theta_{13}$ and in case of $\sin\theta_{13} = 0$ the parameter δ_{CP} is unphysical and CP violation is not possible. While this might appear to be a artificial preference of $\sin\theta_{13}$ over the other mixing parameters, the parameter J_{CP} shows that this is not the case since every CP violating quantity is proportional to J_{CP} and thus vanishes for either of the three mixing angles equal to zero. So, three non-vanishing mixing angles are the requirement for CP violation to be possible.

Furthermore, CP violation can only be observed in appearance channels. The disappearance channels cannot show CP violating effects because of the CPT theorem:

$$P_{\alpha\alpha} \overset{CP}{\rightarrow} P_{\bar{\alpha}\bar{\alpha}} \overset{T}{\rightarrow} P_{\bar{\alpha}\bar{\alpha}} \tag{4.27}$$

So, the relevant oscillation channels at future neutrino oscillation experiments for the search of CP violation will be the appearance channels like for instance the golden channel at a Neutrino Factory, the oscillation channel $\nu_e \rightarrow \nu_\mu$.

Matter Effects in Three Flavors

Matter effects occur in the three flavor framework as well. The electron neutrinos can undergo charged current and neutral current coherent forward scattering while the other flavors ν_μ and ν_τ only can scatter via neutral currents. As already in the two-flavor framework, the matter effect can be described by adding an additional effective matter potential to the ee-element in the Hamiltonian in the flavor basis. This corresponds to the framework with two flavors. The non-diagonal Hamiltonian is given as:

$$i\frac{\partial}{\partial t}\begin{pmatrix} |\nu_e\rangle \\ |\nu_\mu\rangle \\ |\nu_\tau\rangle \end{pmatrix} = \frac{\Delta m^2_{31}}{2E}\left[U\begin{pmatrix} 0 & 0 & 0 \\ 0 & \alpha & 0 \\ 0 & 0 & 1 \end{pmatrix}U^\dagger + \begin{pmatrix} \hat{A} & 0 & 0 \\ 0 & 0 & 0 \\ 0 & 0 & 0 \end{pmatrix}\right]\begin{pmatrix} |\nu_e\rangle \\ |\nu_\mu\rangle \\ |\nu_\tau\rangle \end{pmatrix}. \tag{4.28}$$

As in the two-flavor scenario the contributions from the neutral current coherent forward scattering has been neglected since terms proportional to the identity matrix $\mathbb{1}_{3\times3}$ do not contribute to the oscillation phenomenology but only shift the eigenvalues. Additionally, all dimensional parameters have been extracted from the matrix by introducing the parameters

$$\hat{A} \equiv \frac{2E}{\Delta m^2_{31}}A_{CC}, \qquad \text{and} \qquad \alpha \equiv \frac{\Delta m^2_{21}}{\Delta m^2_{31}}. \tag{4.29}$$

The oscillation parameters in matter can now be obtained by a re-diagonalization of the new Hamiltonian and the original form of the vacuum Hamiltonian can be restored by switching to new parameters, the mixing parameters in matter $\Delta m^2_{21,\mathrm{M}}$, $\Delta m^2_{31,\mathrm{M}}$, $\sin\theta_{12,\mathrm{M}}$, $\sin\theta_{13,\mathrm{M}}$, $\sin\theta_{23,\mathrm{M}}$, and $\delta_{\mathrm{CP,M}}$. Different to the two-flavor framework not only one Mikheyev-Smirnov-Wolfenstein resonance is present since two frequencies Δm^2_{21} and Δm^2_{31} are introduced. The explicit full formulas of the neutrino oscillation probabilities in matter have been derived and can be found in [37, 38]

4.4 Phenomenology of $P_{e\mu}$ and P_{ee}

The explicit full expressions for the neutrino oscillation probabilities in the three-flavor framework are quite extended and do not provide enough analytical insight to understand the relevant phenomenology. Thus, if one wants to understand the phenomenology of the performance of future and present beam based neutrino long baseline experiments, it has turned out helpful to use expansions of the full neutrino oscillation probabilities in small parameters. The two small parameters that can be used for these expansions are the small mixing angle $\sin 2\theta_{13}$ and the hierarchy parameter α of the two independent mass squared differences, that was introduced in the last subsection. The derivation of the here presented expansions and more is given in [39, 40].

Expansion of $P_{e\mu}$

The most important oscillation channel for future beam-based long baseline oscillation experiments is the appearance channel $\nu_e \to \nu_\mu$. This is the so-called "golden channel" at a Neutrino Factory, which is also the relevant channel at a β-Beam. The T reversed channel $\nu_\mu \to \nu_e$ is the relevant appearance channel at future Superbeam experiments. Since this is an appearance channel it allows for an observation of the intrinsic CP violation that would be governed by δ_{CP} while CP violation cannot be observed at the corresponding disappearance channels. However, this requires the measurements with neutrinos and anti-neutrinos in this channel.

The most convenient expansion of $P_{e\mu}$ for analytical understanding of the experiment phenomenology is the simultaneous expansion in $\sin 2\theta_{13}$ and α up to second order. All higher orders are neglected. It turns out that no first order terms survive and the probability $P_{e\mu}$ appears not until the second order in both parameters. The expansion is given by three terms, one proportional to $\sin^2 2\theta_{13}$, one proportional to α^2, and one proportional to the product of $\sin 2\theta_{13}$ and α:

$$P_{e\mu} \simeq \sin^2 2\theta_{13}\, T_1 + \alpha\, \sin 2\theta_{13}\, (T_2 + T_3) + \alpha^2\, T_4. \tag{4.30}$$

Here, the middle term proportional to the product of $\sin 2\theta_{13}$ and α is split into two terms T_2 and T_3. This splitting is helpful since it will turn out that the CP phase will enter in T_2 and T_3, once CP odd and once CP even.

In Vacuum

First, the expression is given for vacuum oscillations:

$$T_1 = \sin^2\theta_{23}\, \sin^2\Delta \tag{4.31}$$

$$T_2 = \sin\delta_{\mathrm{CP}}\, \sin 2\theta_{12}\, \sin 2\theta_{23}\, \sin^3\Delta \tag{4.32}$$

$$T_3 = \cos\delta_{\mathrm{CP}}\, \sin 2\theta_{12}\, \sin 2\theta_{23}\, \cos\Delta\, \sin^2\Delta \tag{4.33}$$

$$T_4 = \cos^2\theta_{23}\, \sin^2 2\theta_{12}\, \sin^2\Delta \tag{4.34}$$

Here, the abbreviation

$$\Delta \equiv \frac{\Delta m^2_{31}}{4E} L \tag{4.35}$$

is used. This approximation breaks down when the contribution from the solar oscillation frequency cannot longer linearly approximated and thus the expansion is only valid for baselines

$$L \lesssim 8000\ \mathrm{km} \left(\frac{10^{-4}\mathrm{eV}^2}{\Delta m^2_{21}}\right)\left(\frac{E_\nu}{\mathrm{GeV}}\right). \tag{4.36}$$

As can be seen from Eq. (4.34), all mixing parameters enter this expression leading to parameter correlations and if information of one parameter is to be extracted the uncertainties on all other parameters come into play. For large $\sin^2 2\theta_{13}$ the first term containing T_1 is the dominating term. For intermediate $\sin^2 2\theta_{13}$ however all four terms contribute with similar magnitudes. Only for small or vanishing $\sin^2 2\theta_{13}$ the last term T_4 dominates. It is apparent that even for vanishing $\sin^2 2\theta_{13}$ the oscillation probability $P_{e\mu}$ does not vanish because of $T_4 \neq 0$.

However, the parameter correlations are not the only limiting factor if information on single parameters is to be extracted from oscillation data of this channel. It was observed that the oscillation probability $P_{e\mu}$ is invariant under a certain set of three independent transformations leading to the so-called "eight-fold degeneracy" [41]. This set of degeneracies is given by the following transformations:

- Intrinsic (θ_{13},δ_{CP}) degeneracy with (θ_{13},δ_{CP}) $\rightarrow$ (θ'_{13},δ'_{CP}) [42]
- Sign-degeneracy with $\Delta m^2_{31} \rightarrow -\Delta m^2_{31}$ [43]
- Octant-degeneracy with $\theta_{23} \rightarrow \pi/2 - \theta_{23}$ [44]

All of these parameter transformation and all combinations of these parameter transformations lead to a degenerate solution in parameter space. In total there are eight combinations of parameter transformations thus the name of the eight-fold degeneracy. The intrinsic (θ_{13},δ_{CP})-degeneracy is of continuous character. Given a true set of parameters with a true value of δ_{CP} the identical value for the oscillation probability can be obtained by *any* value for δ_{CP} by adjusting the value of $\sin 2\theta_{13}$ appropriately. The sign-degeneracy appears for the opposite sign of the atmospheric mass squared difference Δm^2_{31}, *i.e.* $\Delta \rightarrow -\Delta$. Note, that only the sign of the second term T_2 is changed by this transformation and this can be exactly compensated by a simultaneous sign change of the phase $\delta_{\mathrm{CP}} \rightarrow -\delta_{\mathrm{CP}}$. The octant degeneracy is given by the transformation of the atmospheric mixing angle $\theta_{23} \rightarrow \pi/2 - \theta_{23}$. This transformation corresponds to $\sin 2\theta_{23} \rightarrow \sin 2\theta_{23}$ and $\cos 2\theta_{23} \rightarrow -\cos 2\theta_{23}$ thus leaving the oscillation probability $P_{e\mu}$ invariant.

In Matter

The expression of the oscillation probability $P_{e\mu}$ in matter has the similar structure than the expression in vacuum but now the dimensionless parameter $\hat{A}$ that describes the effective matter potential because of the coherent forward scattering is additionally introduced:

$$T_1 = \sin^2\theta_{23} \frac{\sin^2[(1-\hat{A})\Delta]}{(1-\hat{A})^2} \tag{4.37}$$

$$T_2 = \sin\delta_{\mathrm{CP}}\ \sin 2\theta_{12}\ \sin 2\theta_{23}\ \sin\Delta\ \frac{\sin(\hat{A}\Delta)}{\hat{A}}\ \frac{\sin[(1-\hat{A})\Delta]}{(1-\hat{A})} \tag{4.38}$$

$$T_3 = \cos\delta_{\mathrm{CP}}\ \sin 2\theta_{12}\ \sin 2\theta_{23}\ \cos\Delta\ \frac{\sin(\hat{A}\Delta)}{\hat{A}}\ \frac{\sin[(1-\hat{A})\Delta]}{(1-\hat{A})} \tag{4.39}$$

$$T_4 = \cos^2\theta_{23}\ \sin^2 2\theta_{12}\ \frac{\sin^2(\hat{A}\Delta)}{\hat{A}^2} \tag{4.40}$$

The validity of this expansion depends on the baseline and is given as in Eq. (4.36) but since the solar resonance is not covered by the expansion further restrictions for the neutrino energies are introduced to guarantee the validity of the expansion:

$$E_\nu \gtrsim 0.45 \text{ GeV} \left(\frac{\Delta m^2_{21}}{10^{-4}\text{eV}^2}\right)\left(\frac{2.8\text{g cm}^{-3}}{\rho}\right). \tag{4.41}$$

This condition is slightly violated by the later discussed low γ β-Beam experiments, however the approximation still holds and can be considered because of the small baselines where matter effects do not contribute significantly.

Still all oscillation parameters enter the expression in Eq. (4.40) and a big impact of parameter correlations is expected. The intrinsic (θ_{13},δ_{CP})-degeneracy and the octant degeneracy are still present unchanged but the sign degeneracy is not exact anymore. This means that the sign of the mass squared difference gets accessible through the matter effects in this channel. This is not surprising since already the two-favor matter effect discussion has shown that matter effects discriminate the mass ordering of the mass eigenstates. However, phenomenologically the sign degeneracy is still hard to resolve and especially for small or vanishing θ_{13} it becomes impossible to determine the sign of Δm^2_{31} in the regime where the term T_4 dominates the probability $P_{e\mu}$, since T_4 is invariant under the transformation $\Delta m^2_{31} \to -\Delta m^2_{31}$. The expression of the oscillation probability shows again that the physical meaning of δ_{CP} is connected with a non-zero $\sin^2 2\theta_{13}$ since for $\theta_{13} = 0$ only the last term contributes and no CP violation, at least no intrinsic CP violation can be observed.

The main goals in measurements of the appearance channel $\nu_e \to \nu_\mu$ at future neutrino long baseline experiments are the measurement of a non-zero $\sin^2 2\theta_{13}$, the search for intrinsic CP violation, and the determination of the underlying mass hierarchy, *i.e.* the sign of Δm^2_{31}. However, we have seen that parameter correlations and degeneracies spoil the possibility to extract information from the appearance measurement of the relevant appearance channel. So, the main problem for the optimization of future experiments is to resolve the parameter correlations and degenerate solutions as good as possible. The neutrino beam itself already provides the possibility to not only measure the appearance rates that are related to the oscillation probability at one single neutrino energy but for the neutrino energies covered by the energy spectrum of the neutrino flux in the beam. However, this requires very good abilities in energy resolution and further strategies to resolve parameter correlations and degeneracies have to be utilized.

Magic Baseline

A very promising strategy to resolve the sign-degeneracy in the golden appearance channel is the possibility to locate a detector at the so-called “magic baseline” [45]. The magic baseline is a very unique baseline for the phenomenology of the appearance probability $P_{e\mu}$. The oscillation probability in matter contains the parameter product $\hat{A}\Delta$ which is given explicitely as

$$\hat{A}\Delta = \frac{1}{\sqrt{2}} G_F N_E L. \tag{4.42}$$

It can be seen that it is absolutely independent of any oscillation parameters and only fixed by the experiment baseline L and the matter density along the baseline. Now, the magic baseline is the distance L that gives $\hat{A}\Delta = \pi$ and is found to be approximately at $L = 7250$ km. If this baseline is inserted into the expression of the oscillation probability we find that the second, third and fourth terms cancel

$$\hat{A}\Delta \equiv \pi \to \sin(\hat{A}\Delta) = 0 \to T_1 = T_2 = T_3 = 0 \tag{4.43}$$

and only the first term T_1 remains in the oscillation probability:

$$P_{e\mu} \simeq \sin^2 2\theta_{13}\ T_1 = \sin^2 2\theta_{13}\ \sin^2\theta_{23}\ \frac{\sin^2[(1-\hat{A})\Delta]}{(1-\hat{A})^2} \tag{4.44}$$

Thus, the impact of parameter correlations is enormously reduced and a clean measurement of the mixing angle $\sin^2 2\theta_{13}$ and the determination of the sign of Δm^2_{31} becomes possible. The effect of the (θ_{13},δ_{CP})-degeneracy is dropped out completely since the terms T_2 and T_3 containing the parameter δ_{CP} have vanished. On the other hand this implies that measurements of δ_{CP} become impossible if the detector is located at the magic baseline. So, it is not advisable to only use a detector at the magic baseline since the observation of possible CP violation is one of the main goals. But, a two detector scenario involving the magic baseline is a preferable strategy to resolve the correlations and degeneracies.

Related Oscillation Channels

Another strategy to resolve the parameter correlations and degeneracies in the appearance measurements is the combination of different channels. For instance all future experiments from Superbeam experiments to β-Beams or a Neutrino Factory plan to do neutrino running and anti-neutrino running. The corresponding expression for the oscillation probability for anti-neutrinos is given by the transformations $\delta_{\mathrm{CP}} \to -\delta_{\mathrm{CP}}$ and $\hat{A} \to -\hat{A}$ leading to a change of the sign of the term containing T_2:

$$\begin{aligned} P_{\bar{e}\bar{\mu}} &= P_{e\mu}(\delta_{\mathrm{CP}} \to -\delta_{\mathrm{CP}}, \hat{A} \to -\hat{A}) = & (4.45)\\ &\simeq \sin^2 2\theta_{13}\ T_1(\hat{A} \to -\hat{A}) - \alpha\ \sin 2\theta_{13}\ T_2(\hat{A} \to -\hat{A}) \\ &+ \alpha\ \sin 2\theta_{13}\ T_3(\hat{A} \to -\hat{A}) + \alpha^2\ T_4(\hat{A} \to -\hat{A}) & (4.46) \end{aligned}$$

This means that for the combination of neutrino and anti-neutrino running the (θ_{13},δ_{CP})-degeneracy can to a certain extend be resolved because the two oscillation probabilities show a different behavior with δ_{CP}. For only one channel the equi-probability curve in the (θ_{13},δ_{CP}) parameter plane is a continuous line covering all values of δ_{CP}. If also the anti-neutrino channel is considered only two intersection points remain, the true solution and one degenerate solution in parameter space. If also spectral data is used, the degenerate solution can be disfavored and for most of the parameter space even excluded. So, the combination of neutrino and anti-neutrino channels provides good abilities to resolve the (θ_{13},δ_{CP})-degeneracy.

Additionally it was proposed for Neutrino Factory experiments to use an additional channel, the so-called silver channel, *i.e.* the appearance $\nu_e \to \mu_\tau$. This channel requires high enough neutrino energies above the τ threshold, so that the τ leptons can be produced in charged current interactions at the detector. The expansion of the respective oscillation probability $P_{\mu\tau}$ is given as

$$\begin{aligned} P_{e\tau} &= P_{e\mu}(s^2_{23} \leftrightarrow c^2_{23}, \sin 2\theta_{23} \to -\sin 2\theta_{23}) = & (4.47)\\ &\simeq \sin^2 2\theta_{13}\ T_1 - \alpha\ \sin 2\theta_{13}\ T_2 \\ &- \alpha\ \sin 2\theta_{13}\ T_3 + \alpha^2\ T_4. \end{aligned}$$

The phenomenology is quite similar and compared to $P_{e\mu}$ the sign of the second and third term is changed. A combination of golden channel and silver channel should provide further potential to resolve the correlations and degeneracies, but technical difficulties arise. The detection of the τ leptons requires a detector technology that can reconstruct the decay of the τ lepton.

The third channel that is intrinsically available at Neutrino Factory experiments is the so-called platinum channel. This channel is the T reversed channel of the golden channel, *i.e.* the appearance $\nu_\mu \rightarrow \nu_e$. Since it is the T reversed channel, the oscillation probability is derived from $P_{e\mu}$ by the transformation $\delta_{\mathrm{CP}} \rightarrow -\delta_{\mathrm{CP}}$:

$$\begin{aligned} P_{\mu e} &= P_{e\mu}(\delta_{\mathrm{CP}} \rightarrow -\delta_{\mathrm{CP}}) = \\ &\simeq \sin^2 2\theta_{13}\, T_1 \;-\; \alpha\, \sin 2\theta_{13}\, T_2 \\ &+ \alpha\, \sin 2\theta_{13}\, T_3 \;+\; \alpha^2\, T_4 \end{aligned} \tag{4.48}$$

This channel is especially very interesting for a combination with the golden channel in neutrino and anti-neutrino mode since then the original golden channel is compared with the CP conjugated channel, once with changed matter effect (anti-neutrinos, $\hat{A} \rightarrow -\hat{A}$) and without changed matter effect (platinum channel). This allows to separate clearly the intrinsic (governed by δ_{CP}) and the extrinsic (governed by the matter effect) contributions to possible CP violating effects.

Expansion of P_{ee}

Degeneracy resolving potential lies also in the synergetical combination of different experiment technologies. Such a synergetical effect is present in the combination of appearance data of beam based long baseline experiments and future reactor experiments. Reactor experiments measure the disappearance of $\overline{\nu}_e$ that are produced in the core of a reactor and if this disappearance is measured at relatively low baselines $\mathcal{O}(1\text{ km})$ a clean measurement of the small mixing angle $\sin^2 2\theta_{13}$ becomes possible.

The relevant oscillation probability expansion is

$$P_{ee} \;\simeq\; 1 \;-\; \sin^2 2\theta_{13}\; \sin^2\Delta \;-\; \alpha^2\Delta^2\; \cos^4\theta_{13}\; \sin^2 2\theta_{12} \tag{4.49}$$

and no dependency of the parameter δ_{CP} is found. This is not surprising, since CP violation cannot be observed in disappearance measurements due to the CPT theorem[4]. Also, the parameter correlations do not have a big impact on P_{ee} since the composition is rather simple and not all parameter enter the probability. However, the reach for this kind of reactor experiments is limited by systematical uncertainties and is only helpful in the regime of large $\sin^2 2\theta_{13}$.

---

[4] Note, that disappearance channels in general can show a dependency in the parameter δ_{CP}, but only CP even, *i.e.* depending on $\cos\delta_{\mathrm{CP}}$.

Chapter 5

Neutrino Data

In this chapter we will review the current data that exists for the properties of neutrinos. The main focus is on the confirmation of neutrino oscillations and the status of measurements of the neutrino oscillation parameters. But before this is discussed also different experimental results of measurements of neutrino properties are briefly discussed.

5.1 Number of Flavors

The LEP collider experiment has provided various precision measurements of weak interaction processes. One of the famous measurements involved the decay width of the Z^0 boson. The measurement of electron positron collisions with a center of mass energy a at the resonance of the Z^0 did not only allow for a determination of the Z^0 mass but also a measurement of the number of neutrino flavors that are active in the weak interactions and couple to the Z^0. The measured total decay width Γ_{tot} was compared to the partial width of the Z^0 decay into the charged leptons and quarks, the so-called visible width Γ_{vis}. The missing part of the decay width that was invisible to the detector $\Gamma_{\text{inv}} = \Gamma_{\text{tot}} - \Gamma_{\text{vis}} = 498 \pm 4.2$ MeV could be compared with the expected Standard Model decay width of the decay into neutrinos $Z^0 \to \nu_\alpha \overline{\nu}_\alpha$ and the number of light neutrino flavors α that participate at the weak couplings to the Z^0 boson could be estimated in a global fit of the data of all four LEP experiments [46]:

$$N_\nu = 2.994 \pm 0.012. \tag{5.1}$$

There exist further data from the LEP experiments from studies of the single γ decays $e^+ + e^- \to \gamma + \nu + \overline{\nu}$ where the above result for the number of light neutrino flavors could be confirmed [47–50].

There also exist indirect estimates of the number of light neutrino species from cosmological considerations. The mechanism of Big Bang Nucleosynthesis is closely related with the number of light neutrino species that would have been relativistic at the time of Big Bang Nucleosynthesis. Different than the considerations from above this number would include so-called sterile neutrinos, *i.e.* SU(2) singlets that do not participate with the weak interactions. The comparison of Big Bang Nucleosynthesis predictions and measurements of the abundances of primordial light elements constrains the number of neutrino species. The newest estimates at the 2σ confidence level are $N_\nu < 3.3$ [51] and $N_\nu < 4.4$ [52][1]. Due to the large uncertainties in measurements of the primordial light elements these numbers are less reliable and as can be seen from the last number, the existence of sterile neutrinos cannot be excluded.

5.2 Absolute Mass Scale

As was pointed out in the last chapter, neutrino oscillation experiments are only sensitive to mass squared differences Δm^2 of neutrino mass eigenstates. So, although non-zero neutrino masses are established by the observation of neutrino oscillation, no insight is gained in the question of the absolute mass scale of neutrinos. However, different experimental techniques have addressed the absolute mass scale and provided upper mass bounds while neutrino oscillation measurements allow for lower bounds on the mass of the heaviest neutrino mass eigenstate via the relation $m_\nu \geq \sqrt{\Delta m^2}$. In this section we summarize the efforts to constrain the absolute mass scale of neutrinos.

Tritium Decay

The most sensitive technique for a direct search of the effective electron based neutrino mass[2] is the measurement of the electron spectrum of the electrons produced in the beta decay of Tritium near the endpoint of the decay. In the case of a non-vanishing neutrino mass the well-known beta spectrum is distorted and the statistically most significant distortion appears very close to the endpoint. However, collecting enough statistics near the endpoint is very difficult since only a tiny fraction of all beta decays happens close to the endpoint. The choice of Tritium as the source is connected to the fact that Tritium is the isotope with the second lowest endpoint energy E_0 of all known unstable beta decaying isotopes with $E_0 = 18.6$ keV and the fraction of beta decays close to the endpoint is proportional to $1/E_0^3$, so low E_0 is preferable. The relevant process is

$$^3H \;\rightarrow\; ^3He^+ \, e^- \;+\; \overline{\nu}_e \tag{5.2}$$

and the effective electron based neutrino mass is given as

$$m_{\nu_e}^2 = \sum_k |U_{ek}|^2 m_k^2. \tag{5.3}$$

From this formula it can be read off that the effective electron based neutrino mass is independent of the question whether neutrinos are Dirac or Majorana particles.

The first measurements in the early 1990's observed an enhancement of beta decays near the endpoint rather than the expected reduction due to a non-zero neutrino mass and the measurement provided unphysical results with $m_{\nu_e}^2 < 0$. However, this problem is almost disappeared at newer experiments due to a better understanding of the systematical uncertainties and improved experimental setups, mainly by an improvement of the spectrometry.

---

[1] The latter number is based on a reanalysis of the data of the measurements of the abundance of primordial ^4He that indicate a higher statistical uncertainty and a shift of the best-fit value [53].

[2] Note, that the here discussed mass bounds have been obtained in the kinematics of interactions of the neutrino flavor eigenstates and flavor eigenstates do not have distinct masses because the mass eigenstates do. Although it is often used in a loose terminology, it is in principle not meaningful to discuss an "electron neutrino mass" since neutrino mixing turned out to be large.

The current best bounds are provided by the MAINZ [54] and TROITSK [55] experiments. These still get negative $m^2_{\nu_e}$ as best-fit values but the uncertainty of the measurement is well in agreement with physical values but no hint for a non-zero m_{ν_e} could be found. The current bounds are

MAINZ: $m_{\nu_e} < 2.2$ eV at the 95% confidence level

TROITSK: $m_{\nu_e} < 2.5$ eV at the 95% confidence level

An improvement of this bound can be expected from the KATRIN [56] experiment that is planned to gain one order of magnitude in sensitivity to m_{ν_e}, which is even two orders of magnitude improvement in the actual observable $m^2_{\nu_e}$. This increase in sensitivity is accomplished by an enhancement of the luminosity of the Tritium source and an improved resolution of the spectrometer.

Kinematical Test

The effective muon and tau based neutrino masses have been investigated directly in the kinematics of weak decays where all charged decay products have been observed and measured. The effective masses are given as

$$\begin{aligned} m^2_{\nu_\mu} &= \sum_k |U_{\mu k}|^2 m^2_k \\ m^2_{\nu_\tau} &= \sum_k |U_{\tau k}|^2 m^2_k. \end{aligned} \tag{5.4}$$

The best bound for the effective muon based neutrino mass was obtained by the measurements of pion decays at rest $\pi^+ \rightarrow \mu^+ \nu_\mu$ at PSI [57]

$$m_{\nu_\mu} < 190 \text{ keV} \qquad \text{at the 90\% confidence level} \tag{5.5}$$

and the best bound for the effective tau based neutrino mass is coming from the observation of tau decays into pions $\tau^- \rightarrow 2\pi^- \pi^+ \nu_\tau$ and $\tau^- \rightarrow 3\pi^- 2\pi^+ \nu_\tau$ at the ALEPH detector of the LEP collider experiment [58]. The obtained bound is:

$$m_{\nu_\tau} < 18.2 \text{ MeV} \qquad \text{at the 95\% confidence level.} \tag{5.6}$$

Cosmology

In the early universe at temperatures $T \gtrsim 1$ MeV the neutrinos were in thermal equilibrium with the baryon-photon plasma via the weak interactions. When the temperature dropped below this value, the weak interaction froze out and the neutrinos decoupled from the plasma. While the temperature of the early universe was decreasing further, it shortly after that dropped below the electron mass $m_e = 0.511$ MeV and the electrons and positrons annihilated transferring their entropy to the photon gas. Thus the temperature of the photons is increased compared to the temperature of the neutrinos. The relation between the neutrino and photon temperatures is given by [59][3]:

$$\frac{T_\gamma}{T_\nu} = \left(\frac{11}{4}\right)^{\frac{1}{3}} \approx 1.40 \tag{5.7}$$

---

[3] Note added in proof: This relation is only true in the limit of vanishing neutrino masses.

The photons that were produced at that time represent the famous Cosmic Microwave Background that has been discovered in 1965 [60, 61]. The present spectrum of the relic photons has been measured in the observation of the Cosmic Microwave Background by COBE [62] and has been found to be a perfect black body spectrum with a mean temperature of $T_{\text{CMB}} = 2.725 \pm 0.002$ K [63]. Thus, the present temperature of the relic neutrinos is known to be $T_\nu = 1.96$ K, *i.e.* approximately $2 \cdot 10^{-4}$ eV, and at least one neutrino species is extremely non-relativistic[4] at present. The contribution of the neutrinos to the present day matter density of the universe can be expressed by the sum of the masses of light neutrino species[5]

$$\Omega_\nu h^2 = \frac{\sum_i m_i}{94 \text{ eV}} \tag{5.8}$$

and in order not to over close the universe the so-called Cowsik-McClelland bound [64, 65] was obtained:

$$\sum_i m_i \lesssim 94 \text{ eV } h^2 \tag{5.9}$$

with $h = 0.72 \pm 0.08$ at the 68% confidence level [66].

In this case neutrinos were considered to be a good candidate for dark matter. They would contribute to the so-called Hot Dark Matter since they were still relativistic at decoupling, while heavy weakly massive particles (WIMPs) that would be non-relativistic at freeze out of the thermal equilibrium are referred to as candidates for the so-called Cold Dark Matter. However, neutrinos as a dominant contribution to the dark matter content of the universe would highly affect the structure formation of the universe. The reason is the large free streaming length of the relativistic neutrinos that would suppress the amplitudes and wash out matter fluctuations at small scales while Cold Dark Matter does not suppress the small scale fluctuations at early stages. The matter fluctuations at the relevant scales were measured in the anisotropies of the Cosmic Microwave Background at small angles, *i.e.* high multipole moments, at the Wilkinson Microwave Anisotropy Probe WMAP [67]. The presence of the fluctuations at the small scales and the amplitudes ruled out the Hot Dark Matter to form the main contribution of Dark Matter and instead the so-called ΛCDM[6] model was established and the neutrino mass was constrained [68]. The structure amplitudes at similar physical scales but from a very different epoch of the universe can be analyzed in the Large Scale Structure surveys. The 2dF Galaxy Redshift Survey collected the spectra and measured the redshift of about 150 000 galaxies to analyze structure formation [69] and the neutrino masses could be constrained [70]. Especially the combination of WMAP and 2dfGRS data is a powerful tool to break parameter degeneracies associated with the Cosmic Microwave Background and especially the sum of light neutrino masses is impressively constrained [71] to:

$$\sum_i m_i < 1.0 \text{ eV} \qquad \text{at the 95\% confidence level.} \tag{5.10}$$

---

[4] Due to the knowledge of the atmospheric mass squared difference, at least one neutrino mass eigenstate has a mass $m \gtrsim \sqrt{|\Delta m^2_{31}|} \approx 0.05$ eV.

[5] The term “light neutrinos” in this context means, that they are relativistic at decoupling.

[6] The ΛCDM model is characterized by a flat universe with $\Omega = 1$ where about 70% of the overall energy density comes from a Cosmological Constant Λ and the rest comes from matter energy density, approximately 25% Cold Dark Matter and 5% baryonic matter.

There exist even stronger limits that are obtained by additionally including the Lyman-α forest data. But since the interpretation of the data is still controversial [72], the above given limit is conservative and can be regarded as robust. Note, that the above given limit still allows for a quasi-degenerate mass ordering of neutrino mass eigenstates if the data from neutrino oscillations, that is discussed in the next section, is considered. It should be mentioned, that there exists an estimate of a possible future detection for $\sum_i m_i \gtrsim 0.05$ eV at the 95% confidence level in the combination of future CMB data and Large Scale Structure surveys at low and high redshift [73].

Neutrino-less Double Beta Decay

The mechanism of neutrino-less double beta decay has been briefly discussed in Chapter 3. There has been large effort to observe $0\nu\beta\beta$ processes in the last two decades using the high-purity sources with enriched parent isotopes as for instance ^{100}Mo, ^{116}Cd, ^{130}Te, or ^{136}Xe. The best sensitivities however could be achieved in experiments that used the germanium isotope ^{76}Ge as a source. The source serves simultaneously as the detector and has to be shielded against possible background sources like for instance unidentified external γ radiation. The search for $0\nu\beta\beta$ decay results in practice in the search for the decay spectrum, a sharp peak at the known Q value of the used isotope that is in the case of ^{76}Ge a value of $Q = 2039$ keV. The sensitivity of the experiment is given by the size of the source, its purity and the level of background suppression. The best lower limit for the half-life of $0\nu\beta\beta$ is currently provided from the data of the Heidelberg-Moscow experiment that used a 11 kg germanium source with an enrichment of 86% ^{76}Ge (the natural abundance is 7.8%). The data taking took place in the Gran Sasso laboratories in the years 1990-2003 leading to an exposure of 53.9 kg yrs and no positive signal at the expected peak position could be found and an upper limit for the half-life was obtained [74, 75]:

$$T_{1/2} > 1.9 \cdot 10^{25} \text{ yrs} \qquad \text{at the 90\% confidence level.} \tag{5.11}$$

This can be translated into an upper bound on the effective neutrino mass matrix entry $\langle m_{ee} \rangle$ by the use of the nuclear matrix elements from [76] to

$$\langle m_{ee} \rangle < 0.35 \text{ eV} \qquad \text{at the 90\% confidence level} \tag{5.12}$$

where the uncertainties associated with the nuclear matrix elements have been taken into account. A similar limit was obtained at the ^{76}Ge experiment IGEX [77].

There exists a claim of parts of the Heidelberg-Moscow collaboration that neutrino-less double beta decay could be observed in the expanded data set of 71.7 kg yrs. It is pretended that a peak has been found at the expected Q value with a 4.2σ significance [78] and the obtained life-time is

$$T_{1/2} = 1.19^{+2.99}_{-0.50} \cdot 10^{25} \text{ yrs} \tag{5.13}$$

which implies the evidence of neutrino-less double beta decay with the effective neutrino mass

$$\langle m_{ee} \rangle = 0.44^{+0.14}_{-0.20} \text{ eV} \tag{5.14}$$

In this case neutrinos are Majorana particles and as can be seen from Fig. 3.5 the neutrino mass ordering would be quasi-degenerate. Not only does this claim of evidence dissent former results of Heidelberg-Moscow and IGEX but additionally the possible parameter space for the smallest neutrino mass in the claimed region for $\langle m_{ee} \rangle$ is strongly constrained from the mass bound coming from cosmology as can be read off Fig. 3.5. The claim of the evidence is very controversially discussed [79–84]. There exist various proposals for future $0\nu\beta\beta$ experiments with source strengths of $\sim$ 100 kg that will be able to test the claim with different isotopes used as for instance CUORE (^{130}Te) [85], GERDA (^{76}Ge) [86,87], and MAJORANA (^{76}Ge) [88]. A good review of the topic, including a discussion of the claim of evidence and details of future experiments can be found in [89].

5.3 Oscillation Data

There has been a huge progress in our knowledge of neutrino properties in the last years coming from observations of neutrino oscillations from neutrinos coming from natural sources as the sun and the earth's atmosphere and also from artificially produced neutrinos in completely earth-based experiments. In this section we will briefly review the status of the neutrino data that has been obtained from neutrino oscillation data.

Solar Data

Nuclear fusion reactions in the interior of the sun are the driving processes of the thermal energy of the sun. The main process is the fusion of Hydrogen to Helium with a net reaction

$$4p^+ \; + \; 2e^- \; \to \; {}^4He \; + \; 2\nu_e. \tag{5.15}$$

This net reaction is driven by various single reactions that form a reaction chain. The dominating reaction chain with a contribution of $\sim$ 98% to the sun's energy is the so-called *pp* cycle. In the chain of the *pp* cycle five single reactions produce electron neutrinos ν_e of different energies, the *pp*, *pep*, *hep*, ^7Be and ^8B neutrinos. Since all reactions in the sun are fusion reaction no anti-neutrinos are produced and additionally no muon or tau neutrinos appear in the reactions, so that the sun is a pure ν_e source. The neutrino energies in the neutrino spectrum of the sun are relatively small and do not exceed 11 MeV. The *pep* and ^7Be neutrinos have discrete energies whereas the other neutrinos form continuous spectra. The *pp* neutrinos give the main contribution to the neutrino spectrum of the sun and appear at very low energies $E_\nu \lesssim 0.4$ MeV. The theoretical predictions of the solar neutrino fluxes is given in the so-called Standard Model of the sun SSM [90, 91] and the theoretical spectrum of the solar neutrino flux can be found amongst further details in [92].

The first experiment that measured the neutrino flux from the sun was the Homestake [93] chlorine experiment and the neutrinos were detected in the reaction

$$\nu_e \; + \; {}^{37}Cl \; \to^{37} Ar \; + \; e^-. \tag{5.16}$$

However, the detection was not direct but after data taking the amount of produced ^{37}Ar was estimated by radiochemical methods. The threshold of the process is 0.814 MeV and only the ^7Be, *pep*, and ^8B neutrinos could be measured where the latter gave the main contribution. The *pp* neutrinos could be detected at different radiochemical experiments SAGE [94], GALLEX [95], and GNO [96] using ^{71}Ga in the reaction

$$\nu_e \; + \; {}^{71}Ga \; \to^{71} Ge \; + \; e^-. \tag{5.17}$$

The reaction has a threshold of 0.234 MeV and is thus also sensitive to the low energy *pp* neutrinos. Due to the small cross sections the observed neutrino rates were so small that a new unit had been introduced to describe the low rates, the Solar Neutrino Unit SNU$\equiv 10^{-36}$ ν captures per target atom and second. The Homestake experiments reported a detection of $2.56 \pm 0.16 \pm 0.16$ SNUs [97, 98] and the later gallium experiments could collect more statistics, *i.e.* $66.9^{+3.9+3.6}_{-3.8-3.2}$ SNUs at SAGE [94,99] and $66.9^{+3.9+3.6}_{-3.8-3.2}$ SNUs at GALLEX/GNO [95, 96, 100].

Direct measurements of solar neutrinos could be achieved at the Water Cherenkov detectors Kamiokande and later Super-Kamiokande [101] using the neutrino electron scattering reaction

$$\nu_\alpha \ + \ e^- \to \ \nu_\alpha \ + \ e^- \tag{5.18}$$

with no physical threshold. The Water Cherenkov experiments require an energy cut $E_\nu \gtrsim$ 5 MeV so that they are only sensitive to the ^8B neutrinos of the solar neutrino flux. The nice feature of the Water Cherenkov technology was the possibility of directional information and it was found that the measured neutrinos indeed are coming from the direction of the sun, while the radiochemical experiments could not confirm the initial source. The data sets indicated a neutrino flux deficit compared to the predictions of the solar flux from the SSM which was referred to as the Solar Neutrino Problem. However, the obtained ratio of detected to expected neutrino rates was different at the different experiments and hinted to an energy dependent reduction of the ν_e flux because the experiments were sensitive to different energy ranges of the solar flux. Besides the discussion about the reliability of the theoretical predictions of the SSM the possible flavor transitions of the ν_e neutrinos was a popular attempt to explain the Solar Neutrino Problem and the most natural mechanism was neutrino oscillations. The predictions of the SSM could be confirmed at the detector of the Sudbury Neutrino Observatory SNO where not only charged-current or quasi-elastic neutrino reactions, but also the neutral-current reactions could be detected [102–104]. Since the observed amount of neutral current reactions is sensitive to the total flux of all flavors $\phi_{\nu_e} + \phi_{\nu_\mu} + \phi_{\nu_\tau}$ the SNO results could confirm the flux prediction of the SSM in the total flux of all flavors. So, flavor transitions of ν_e to ν_μ or ν_τ were established as the cause of the Solar Neutrino Problem and furthermore, the flavor transition into a sterile neutrino in solar neutrino transitions could be heavily constrained. But still, the fit to the global solar data allowed for different separated allowed regions in the $\sin^2 2\theta$-Δm^2 parameter plane including vacuum oscillations and matter enhanced solutions with MSW effect. It was the later described KamLAND data [105, 106] that selected the true solution, the so-called MSW Large Mixing Angle (LMA) solution and resolved the ambiguity. The best-fit values of the solar parameters from the combination of all available solar neutrino data in a two-flavor framework are [107]:

$$\sin^2 2\theta_{\rm sol} = 0.83 \qquad \Delta m^2_{\rm sol} = 6.0 \cdot 10^{-5} \ {\rm eV}^2. \tag{5.19}$$

Atmospheric Data

A second natural source of neutrinos are the atmospheric neutrinos that are produced in the upper atmosphere of the earth due to scattering of cosmic rays (mainly protons). Pions are produced in the interactions with the cosmic rays and in the decay chain of these pions the atmospheric neutrinos are produced:

$$\begin{array}{rllll} \pi^- & \rightarrow & \mu^- & + \overline{\nu}_\mu & \\ & & \mu^- & \rightarrow e^- + \nu_\mu + \overline{\nu}_e & \\ \pi^+ & \rightarrow & \mu^+ & + \nu_\mu & \\ & & \mu^+ & \rightarrow e^+ + \overline{\nu}_\mu + \nu_e . & \end{array} \tag{5.20}$$

Atmospheric neutrinos have been studied at the Water Cherenkov detector of Super-Kamiokande. The Water Cherenkov technology cannot distinguish neutrinos from anti-neutrinos but neutrino flavored neutrinos can be discriminated from muon neutrinos with quite good accuracy. The flavor identification is performed by a shape analysis of the Cherenkov ring of the charged current produced charged lepton, electron or muon. Since the lighter electrons are affected more by scattering with the detector medium, the Cherenkov ring of electrons appears more fuzzy than the Cherenkov ring of a muon. On the other hand is it not possible to distinguish neutrinos from anti-neutrinos at a Water Cherenkov detector. As can be seen from the reaction chain above, the atmospheric neutrinos should obey a distinct ratio of 2:1 muon neutrino events to electron events in case of a no oscillation hypothesis. The Water Cherenkov detector allows for a direction measurement of the incoming neutrinos and the zenith angle dependence of the atmospheric neutrino flux was measured. The electron-like events showed the expected behavior and upward going and downward going neutrino flux was observed to be similar. The muon-like events however showed a different behavior and while the downward going neutrino flux was in agreement with the expectations a significant deficit was observed in the upward going neutrino flux. This can be explained by flavor transitions $\nu_\mu \rightarrow \nu_\tau$ that occur while the neutrinos are traveling through the earth until observed in the detector and tau neutrinos cannot be detected. This resulted in the famous evidence for atmospheric neutrino oscillations in 1998 by the Super-Kamiokande experiment [108] that can also be confirmed by the Soudan [109] and MACRO [110, 111] experiments. In a newer analysis the L/E dependence was analyzed carefully and a oscillatory dip was found which gave a clear signature for neutrino oscillations and other explanations of the flavor transitions like scenarios involving decoherence or neutrino decay were disfavored [112]. The atmospheric neutrino oscillations can be explained in a two-flavor framework and the obtained best-fit values in a fit to the Super-Kamiokande atmospheric data are [107]:

$$\sin^2 2\theta_{\mathrm{atm}} = 1.0 \qquad \Delta m^2_{\mathrm{atm}} = 2.0 \cdot 10^{-3}\ \mathrm{eV}^2. \tag{5.21}$$

KamLAND

The solar data alone could not solve the ambiguities and various separated alternative allowed regions in the parameter space survived. These regions involved pure vacuum oscillations, matter enhanced neutrino oscillations with a small or a large mixing angle. The true solution could be established at the reactor neutrino experiment KamLAND in Japan. The KamLAND detector, a 1 kt Liquid scintillator detector is located at the Kamiokande site and measures the neutrino flux of 53 surrounding nuclear power plants at distances between 80 and 350 km, which sums up to an average baseline of about 180 km. Thus, the $\overline{\nu}_e$ disappearance of the reactor neutrinos is measured at a baseline where the LMA solution of the fit to the solar neutrino data can be probed in a vacuum oscillation framework. In case of no oscillations an event number of 356.2 ± 23.7 would have been expected in the data taking period from

March 2002 to January 2004 and a total of 258 events has been actually observed which is in very good agreement with two-flavor neutrino oscillations due to the solar LMA parameters [105, 106]. Furthermore, a spectral distortion could be found that indicates oscillatory L/E dependence [106]. The position of the KamLAND detector is not optimal since it is located at a too large baseline, slightly of the oscillation maximum and hence it is not very sensitive to the oscillation amplitude and the precision for $\sin^2 2\theta_{\rm sol}$ could not be increased compared to the precision from solar data. The precision on $\Delta m^2_{\rm sol}$ on the other hand could be significantly improved. The KamLAND contribution to the Solar Neutrino Problem is very important because before KamLAND the alternative allowed regions for the solar oscillation parameters could not be ruled out. The best-fit values for the oscillation parameters in a two-flavor fit to the KamLAND data are given as [107]:

$$\sin^2 2\theta_{\rm sol} = 0.83 \qquad \Delta m^2_{\rm sol} = 8.1 \cdot 10^{-5}\ {\rm eV}^2. \tag{5.22}$$

CHOOZ

The third mixing angle $\sin^2 2\theta_{13}$ has been addressed in the measurements of the CHOOZ reactor experiment [113]. The 5 t Liquid Scintillator detector was placed at a distance of L=1 km to the reactor cores of the Chooz reactor site. The reactor cores provide a large flux of $\overline{\nu}_e$ and only the disappearance channel of the electron anti-neutrinos could be performed since the energies of reactor neutrinos are to small to produce the heavy muon or tau leptons in charged-current reactions. However, in the data taking phase between April 1997 and July 1997 no hints for any neutrino oscillations could be found and an upper limit for the parameter $\sin^2 2\theta_{13}$ was published [114]. The obtained limit is strongly dependent on the chosen value of the atmospheric $\Delta m^2_{\rm atm}$ and for $\Delta m^2_{\rm atm} < 10^{-3}\ {\rm eV}^2$ no limit can be obtained at all. The authors [115] of performed a global fit of the CHOOZ data with the atmospheric data to include the constraints on $\Delta m^2_{\rm atm}$ into the CHOOZ limit and the obtained upper limit for $\sin^2 2\theta_{13}$ is [107]:

$$\sin^2 2\theta_{13} < 0.11\ (0.25) \qquad \text{at the 90\% } (3\sigma) \text{ confidence level.} \tag{5.23}$$

The period of data taking might seem very low and one might wonder if a longer period could not have improved the limit by an increased statistics. But, as will be pointed out later in Chapter 6.3 reactor experiments are mainly limited by systematical uncertainties and not the collected statistics.

K2K and MINOS

The first confirmation of the atmospheric neutrino oscillation in an earth-based experiment was provided by the K2K [116] experiment in Japan. At K2K a conventionally produced ν_μ beam was produced at the accelerator complex of KEK and lead to the Super-Kamiokande Water Cherenkov detector at a baseline of L=250 km. The mean energy of the neutrinos in the beam was 1.3 GeV and oscillation due to the atmospheric parameters should evolve. The mechanism of conventional beam production will be discussed in Chapter 6.1. The full data sample was taken in the period from June 1999 to November 2004 and 112 ν_μ events have been observed whereas in case of no oscillations $158^{+9.2}_{-8.6}$ events would have been expected [117, 118]. The fit in a two-flavor framework implied an allowed region for $\sin^2 2\theta_{\rm atm}$ and $\Delta m^2_{\rm atm}$ that was very well in agreement with the atmospheric neutrino data however no significant improvement in the precision could be achieved.

In 2006 the MINOS experiment [119] in the United States published the first year results of the measurement of ν_μ neutrinos [120–123]. The experiment uses a conventionally produced ν_μ beam at a mean energy of 3 GeV that is produced at the FermiLab accelerator complex and directed towards the 5.4 kt Magnetized Iron Calorimeter MINOS detector located in the Soudan mine 735 km north of FermiLab. The MINOS experiment is still ongoing and a five year run is planned [124]. The first observed event sample contains 122 ν_μ events whereas in case of no oscillations 239 ± 17 events would have been expected. The MINOS experiment provides the slightly better statistical significance and better energy reconstruction capabilities than K2K and thus the precision on $\Delta m^2_{\mathrm{atm}}$ has slightly improved by the inclusion of the MINOS data. Furthermore the best-fit value has shifted to slightly higher values as will be seen in the next subsection where a global fit to all available data will be presented.

Global Fit

In the last subsections we have discussed the available data on neutrino oscillation parameters from measurements of the solar neutrino flux, the atmospheric neutrino flux, the measurement of reactor neutrinos at various baselines, and finally the most recent data from the first generation of conventional neutrino beam experiments. Up to now, all single data sets can be interpreted in a two-flavor framework with only two parameters, one oscillation amplitude $\sin^2 2\theta$ and a corresponding oscillation frequency Δm^2. The reason why no three-flavor effects have been observed so far is the smallness of two quantities, $\sin^2 2\theta_{13}$ and the hierarchy of the solar and atmospheric mass squared differences $\alpha = \Delta m^2_{\mathrm{sol}}/\Delta m^2_{\mathrm{atm}}$. Nevertheless there have been various studies that try to fit all available data sets simultaneously in a global fit in the complete three-flavor framework of neutrino oscillations [107, 125–127]. Note, that by switching from the two-flavor frameworks to the three-flavor framework the correspondences are:

$$\begin{aligned} \sin^2 2\theta_{\mathrm{sol}} &\mathrel{\hat{=}} \sin^2 2\theta_{12} \qquad & \Delta m^2_{\mathrm{sol}} &\mathrel{\hat{=}} \Delta m^2_{21} \\ \sin^2 2\theta_{\mathrm{atm}} &\mathrel{\hat{=}} \sin^2 2\theta_{23} \qquad & \Delta m^2_{\mathrm{atm}} &\mathrel{\hat{=}} |\Delta m^2_{31}|. \end{aligned} \tag{5.24}$$

The global fit studies are updated when new data sets get available and so represent the global knowledge of neutrino oscillation parameters. Here, we will only make use of the global fit from [107] and the global fit best-ft values and the allowed 3σ regions are given as:

$$\begin{aligned} \sin^2 2\theta_{12} &= 0.84^{+0.12}_{-0.11} \qquad & \Delta m^2_{21} &= 7.9^{+1.0}_{-0.8} \cdot 10^{-5}\ \mathrm{eV}^2 \\ \sin^2 2\theta_{23} &= 1.00^{+0.00}_{-0.13} \qquad & |\Delta m^2_{31}| &= 2.6^{+0.6}_{-0.6} \cdot 10^{-3}\ \mathrm{eV}^2 \\ \sin^2 2\theta_{13} &= 0.000^{+0.154}_{-0.000} \qquad & \delta_{\mathrm{CP}} &= 0^{+\pi}_{-\pi} \end{aligned} \tag{5.25}$$

If not stated otherwise, we will adopt the best-fit values of Eq. (5.25) as the true input values for the oscillation parameters used in the experiment simulations in later chapters of this work.

LSND

A controversial result that has not been considered in the global fit given above is the data [128] of the LSND [129] experiment being the first experiment to report the observation of neutrino oscillation appearance. In the neutrinos coming from pion decays at rest and a Liquid

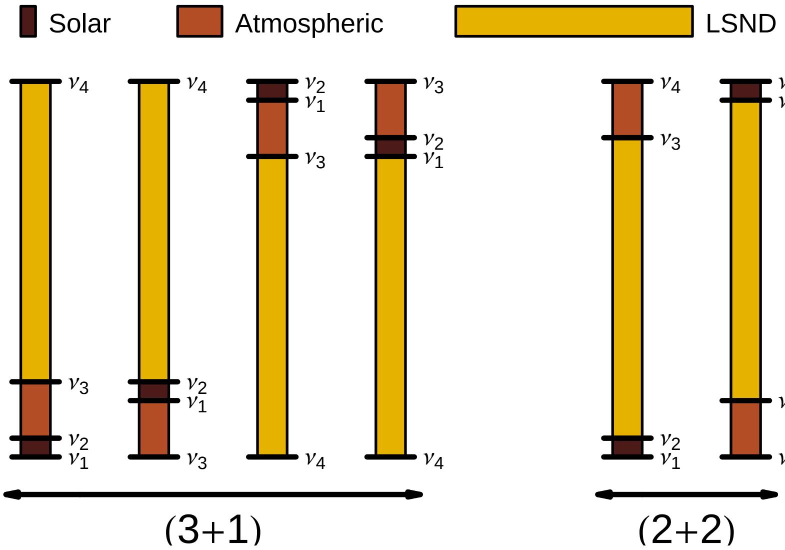

Figure 5.1: The different possible neutrino mass spectra in case of a four neutrino scheme with an additional mass-squared difference $\Delta m^2_{\mathrm{LSND}} \sim 1\ \mathrm{eV}^2$ to explain the data from the LSND experiment. The different mass spectra can be divided into two classes, the four possible (3+1) scenarios (left) and the two (2+2) scenarios (right).

Scintillator detector at a very small baseline the appearance of electron anti-neutrinos in the channel $\overline{\nu}_\mu \rightarrow \overline{\nu}_e$ is reported indicating towards neutrino oscillations at a large $\Delta m^2 \sim 1$ eV that is not compatible with the global data discussed above in the three-flavor framework. The KARMEN experiment however has constrained the LSND solution and only small parts were still allowed [130].

As the LSND result cannot be included to the global three-flavor framework additional scenarios have been proposed. One is the addition of at least one sterile neutrino to the neutrino mass spectrum. The resulting classes of mass ordering scenarios are referred to as (2+2) and (3+1) scenarios depending on the location of the large mass splitting as illustrated in Fig. 5.1. In the (3+1) mass spectra the large mass splitting is decoupled from the two mass splittings of active neutrinos but for (2+2) mass spectra the sterile neutrino cannot be decoupled and must appear in either solar or atmospheric oscillations. Thus, the (2+2) scenario can be completely ruled out by atmospheric and solar data after SNO and KamLAND [107]. Although (3+1) were still not ruled out it could be shown that this kind of scenario was also highly disfavored by disappearance data from small baseline measurements [107]. Another possible explanation could be provided by the rather provoking assumption of CPT violation with different mass splittings in the neutrino and anti-neutrino sector. However, global data without LSND favors CPT conservation [107] and the assumption of CPT violation does not provide a satisfactory explanation [131, 132].

Recently, the MiniBooNE [133] collaboration has published the first results [134] of a $\nu_\mu \rightarrow \nu_e$ appearance search at a similar L/E as LSND and no appearance could be found. This disfavors (3+1) sterile neutrino even more[7], but if a second sterile neutrino is added to form a (3+2) mass scheme, the combination of MiniBooNE and LSND data is very well compatible due to the possibility of CP violation [135]. Summarizing, the puzzle of the LSND

---

[7] In a (3+1) scenario the two experiments are incompatible at the 98% confidence level [135].

result is not resolved by the recent MiniBooNE data and the $\overline{\nu}_\mu \to \overline{\nu}_e$ data of MiniBooNE is required for the final conclusion. The LSND result will not be considered for the simulations throughout this work and we will only operate in a three-flavor framework with the assumption of CPT conservation.

Chapter 6

Long Baseline Experiment Scenarios

The first cognitions in neutrino oscillation physics came from the detection of neutrinos from natural neutrino sources like neutrinos produced in the fusion reactions in the sun's interior or neutrinos produced in the earth's upper atmosphere. This resulted in pinning down the leading oscillation parameters. However, observing three-flavor effects in oscillations of neutrinos from these natural sources is hardly achievable[1]. So, the future of neutrino oscillation physics will be dominated by artificially produced "man-made" neutrinos in present and future experiments. The era of neutrino oscillation long baseline experiments has already been initiated with the first generation of conventional neutrino beam experiments that are currently ongoing or finished data taking. However, these experiments were mainly planned to measure and confirm the former measurements of the leading oscillation parameters. Although, it was shown that already the conventional beam experiments have some potential to discover three flavor effects such as the observation of a non-zero $\sin^2 2\theta_{13}$ if it is just around the corner slightly below the Chooz bound [136–141], the conventional beam experiments cannot constrain the parameter space of the CP phase or determine the underlying neutrino mass hierarchy. So, new classes of experiments have been proposed to address these issues in the future, going from Superbeam experiments that are upgrades of the conventional technology to even more dedicated technologies such as β-Beam or Neutrino Factory experiments. In this chapter we will introduce the possible different configurations of technologies, beginning with the concept of the conventional beam based experiments and their possible upgrade scenarios, the Superbeam experiments. The most sophisticated scenarios of β-Beam experiments and Neutrino Factory experiments will be described in greater detail since their performance and optimization issues are the main topic of the following chapters where we present the main results. Furthermore the basic principles of reactor oscillation experiments are reviewed because reactor experiments can play an important role, when the global picture of future neutrino oscillation physics is discussed in Chapter 9. Additionally we will give a brief description of the rather novel idea of neutrino beam experiments with monochromatic neutrinos from electron capture processes since the technology is related to the principles of β-Beam experiments.

---

[1] However, there is some potential to extract information on $\sin^2 2\theta_{13}$ from atmospheric neutrino data [17].

6.1 Conventional Beam Experiments

The conventional beam experiments are already ongoing. They can be seen as the first generation of beam based neutrino oscillation experiments. The first conventional beam experiment was the K2K experiment in Japan. The neutrino beam was produced in the accelerator complex of KEK and lead towards the Super-Kamiokande Water Cherenkov detector at a baseline of $L = 250$ km. The data taking period at the K2K experiment is already finished and the fit to the data confirmed the best-fit allowed region for the leading atmospheric parameters $\sin^2 2\theta_{23}$ and $|\Delta m^2_{31}|$ that was obtained from the atmospheric neutrino data at the Super-Kamiokande detector. While the global precision of the atmospheric parameter measurements could not be significantly improved, this was the first confirmation of neutrino oscillations at the atmospheric oscillation length by artificially produced neutrinos. The second conventional beam experiment is the MINOS experiment in the United States. The neutrino beam is produced at the accelerator complex of FermiLab in the so-called NuMI beamline. The detector is a 5.4 kt Magnetized Iron calorimeter detector located in the Soudan mine 732 km north of the FermiLab site. The first neutrino events from the NuMI beam have been observed in 2005 and the first results from a fit to the MINOS data was published in mid 2006 [120–123] and is in perfect agreement with atmospheric and K2K data. Also the European conventional neutrino beam produced at the CERN accelerator complex, the CNGS beam has been switched on recently and the first neutrino events could have been detected at the OPERA detector at a distance of $L = 735$ km in the Gran Sasso laboratories [142].

The basic principles of the beam production are similar for all the three mentioned conventional neutrino beams. The neutrinos are produced in the decay of secondary mesons, mostly pions but also rarely kaons:

$$\begin{aligned}
\pi^+/K^+ &\rightarrow \mu^+ + \nu_\mu \qquad (> 99\%)\\
\pi^+/K^+ &\rightarrow e^+ + \nu_e \qquad (< 1\%)\\
\\
\pi^-/K^- &\rightarrow \mu^- + \overline{\nu}_\mu \qquad (> 99\%)\\
\pi^-/K^- &\rightarrow e^- + \overline{\nu}_e \qquad (< 1\%)
\end{aligned} \tag{6.1}$$

The secondary mesons are created by protons that are accelerated towards a fixed target. The neutrino beam mostly consists of muon neutrinos ν_μ or $\overline{\nu}_\mu$ depending on the polarization of the magnetic horns that selects either negative or positive charged mesons that then decay in a straight decay pipe. Due to the decay properties of pions and kaons not only muon neutrinos are produced but also a small contamination of $\sim 0.5\%$ electron neutrinos or antineutrinos. This contribution from electron neutrinos is the limiting factor in the search for the appearance channel $\nu_\mu \rightarrow \nu_e$ that is suppressed by the small mixing angle $\sin^2 2\theta_{13}$. However, the main goal for conventional beam experiments is to measure the disappearance channel $\nu_\mu \rightarrow \nu_\mu$ and increase the precision of the leading atmospheric oscillation parameters. The schematic illustration of the neutrino production and the detection of different channels is illustrated in Fig. 6.1.

It should be mentioned that the neutrino energy of the CNGS beam is too large for the respective baseline and the neutrino spectrum is off the first oscillation maximum. Thus measurements are less sensitive to the oscillation amplitude $\sin^2 2\theta_{23}$ in the disappearance channel and the current knowledge coming from atmospheric data cannot be improved and also the sensitivity to $|\Delta m^2_{31}|$ is strongly limited. However, the main purpose of the CNGS

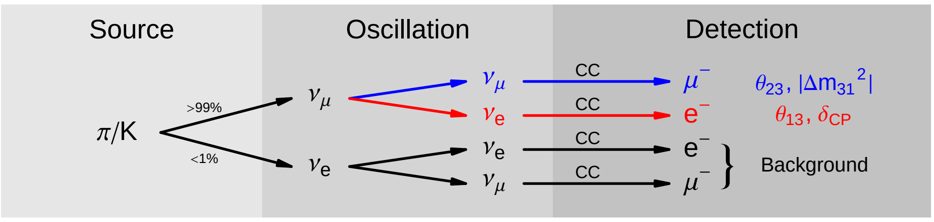

Figure 6.1: The schematic illustration of neutrino source, oscillation channels, and detection principles at a Superbeam experiment. The neutrino beam consists mainly of $\nu_\mu(\bar{\nu}_\mu)$ coming from the decay of secondary pions and more rarely also kaons. Due to the decay properties of the kaons, a small contamination of $\nu_e(\bar{\nu}_e)$ is contained in the neutrino beam. The measurement involves ν_μ-disappearance and ν_e-appearance.

detectors of the OPERA [143] and ICARUS [144] detectors are optimized for the detection and reconstructions of the τ leptons from the appearance channel $\nu_\mu \to \nu_\tau$. The relatively high energy of the CNGS neutrino beam is chosen such that τ leptons are produced in charged current reactions at a reasonable amount. This would give the first direct experimental confirmation of the flavor transition $\nu_\mu \to \nu_\tau$ in leading atmospheric oscillations while all former results rely on the disappearance of muon neutrinos.

6.2 Superbeams

Superbeam experiments are the upgrade scenarios of the conventional beam experiments. While the principles of neutrino beam production are identical to the conventional beams, the neutrino beam flux is increased by an increased power of the initial protons that hit the target and the discussed detectors use a larger fiducial volume. Thus, the statistics at a Superbeam upgrade is increased compared to the conventional neutrino experiments. This means that the precision of the leading atmospheric parameters is further improved and the appearance of electron neutrinos becomes accessible for large and intermediate $\sin^2 2\theta_{13} \gtrsim 10^{-2}$. The basic principles are still as illustrated in Fig. 6.1. Different than for conventional beam experiments the appearance measurement due to the large statistics provides good abilities to measure the small mixing angle $\sin^2 2\theta_{13}$, constrain the phase δ_{CP}, and even determine the mass hierarchy for large $\sin^2 2\theta_{13}$. However, due to the intrinsic beam background coming from the flavor contamination of $\sim 0.5\%$ electron neutrinos in the beam that cannot be distinguished from appearance electron neutrinos, the performance of Superbeam experiments is naturally limited to relatively large $\sin^2 2\theta_{13} \gtrsim 10^{-3}$. A second limiting factor is the background coming from inelastic neutral current events with an associated production of π_0 mesons that can be misidentified as electrons, *i.e.* be misidentified signal event candidates. The neutral current events are usually reconstructed at much lower energies as the incident neutrino energy since the surviving neutrino carries away invisible energy, *i.e.* missing energy. For Superbeam experiments it is planned to locate the detector slightly off the beam line, which is the so-called off-axis scenario. The relativistic kinematical decay properties of the initial pions offer this possibility with the effect that the long tail of the neutrino beam spectrum at high energies is strongly suppressed. This results in an decrease of overall statistics but additionally the signal-over-background ratio is improved because the background form neutral current events is more significantly reduced and the overall performance can be improved.

As a first generation of Superbeam experiments the upgrades of the NuMI beam with the

Superbeam experiment NOνA [145] in the United States and the T2K [146] experiment in Japan are proposed. The second generation of Superbeam experiments is planned to even increase the performance of Superbeams by further increasing statistics and neutrino energies. So, it is proposed to use a megaton Water Cherenkov detector such as the possible to be built Hyper-Kamiokande detector [146] in Japan or MEMPHYS [147] in Europe. The respective Superbeam experiments are the T2HK experiments and the SPL Superbeam [148]. Also at the FermiLab it is proposed to upgrade the first generation Superbeam experiment NOνA with an upgraded proton driver [149].

6.3 Reactor Experiments

It was already mentioned that the observation of $\overline{\nu}_e$ disappearance in the neutrino flux produced in fission reactions (mainly ^{235}U fission processes) in the core of a reactor provides the opportunity to examine neutrino oscillation properties. The neutrinos are detected in the inverse beta decay

$$\overline{\nu}_e + p \rightarrow e^+ + n \tag{6.2}$$

with a threshold of approximately 1.8 MeV and a significant signal signature that allows to reconstruct the incident neutrino energy due to the coincidence of three photons, the two prompt photons from the incident annihilation of the positron and the a delayed photon from the capture of the neutron.

The first observation of neutrino events was performed at a early reactor experiment in 1956 and was followed by neutrino oscillation experiments at very low baseline $L \lesssim 100$ m that did not find any hints for $\overline{\nu}_e$ disappearance at this distances. The most important were the experiments at Gösgen [150], Bugey [151], Palo Verde [152], and CHOOZ [113].

If the detector is located at a distance $L \sim 100$ km the measurement is sensitive to the leading solar parameters $\sin^2 2\theta_{12}$ and Δm^2_{21}. The ongoing KamLAND experiment in Japan measures the $\overline{\nu}_e$ disappearance at a 1 kt Liquid Scintillator detector that are coming from 53 surrounding power plants at an average distance of L$\sim$ 180 km. Although this distance is slightly of the solar oscillation maximum, the KamLAND data [105, 106] established a disappearance that was consistent with the LMA-MSW solution of the solar neutrino data. Due to the inefficient location of the detector, KamLAND is less sensitive to the oscillation amplitude $\sin^2 2\theta_{23}$ but could provide a good measurement of Δm^2_{21}. For precision measurements of both parameters it has been proposed to use a very large Liquid Scintillator detector like for instance the LENA [153, 154] detector (50 kt) at a baseline of $L \sim 60$ km to perform precision measurements of the solar parameters at the percent level.

The Liquid Scintillator can also be located at the first atmospheric oscillation maximum $L \sim 1.3$ km to search for $\overline{\nu}_e$ disappearance in oscillations at the atmospheric frequency. This oscillation channel is driven by the small mixing angle $\sin^2 2\theta_{13}$ at this baselines and a clean measurement of $\sin^2 2\theta_{13}$ becomes possible because only few parameter correlations spoil this oscillation channel compared to the appearance channels at beam based experiments. The limiting factor at $\sin^2 2\theta_{13}$ reactor experiments is the issue of systematical uncertainties [155]. In this close distance from the reactor core statistics is not that kind of a problem because the neutrino flux is extremely high. But systematical uncertainties such as the uncertainties in cross sections, the uncertainty of the normalization of the neutrino flux, and the uncertainty of the fiducial mass of the detector can easily destroy the sensitivity to $\sin^2 2\theta_{13}$. It is crucial to keep the overall systematical uncertainties below the level of 1% which can be achieved by a

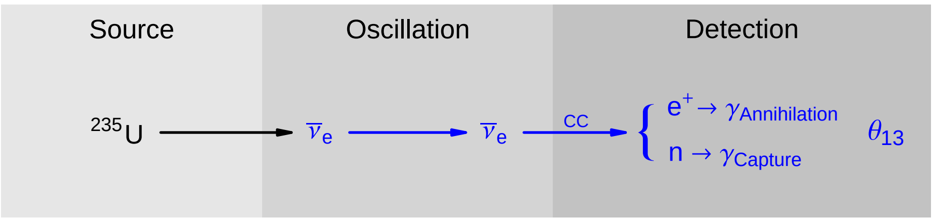

Figure 6.2: The schematic illustration of neutrino source, oscillation channels, and detection principles at a neutrino reactor experiment. The $\bar{\nu}_e$ are produced in the fission reactions of nuclei (mainly ^{235}U) in a reactor core. The disappearance of the $\bar{\nu}_e$ is measured.

combined measurement at a near and a far detector so that associated uncertainties cancel out. The schematic illustration of this kind of neutrino oscillation experiment is shown in Fig. 6.2.

Still, the CHOOZ bound gives the current upper limit (slightly improved by solar data) for $\sin^2 2\theta_{13}$ but no hint for disappearance could be observed. However, the CHOOZ experiment only used a far detector and was highly limited by the systematical uncertainties. All future planned reactor experiments are proposed as multi-detector setups to increase the $\sin^2 2\theta_{13}$ sensitivities to smaller values of $\sin^2 2\theta_{13}$. The first of the new generation of $\sin^2 2\theta_{13}$ reactor experiments is DoubleCHOOZ [156] with two detectors at the same Chooz reactor complex as the initial CHOOZ experiment. The total exposure of a reactor experiment is proportional to and can be described by the product of the runtime, the detector mass, and the thermal power of the reactor core, *i.e.* the so-called integrated luminosity. The exposure of the DoubleCHOOZ experiment is planned as 5 yrs $\times$ 10.16 t $\times$ 8.4 GW $\sim$ 430 GW t yrs. However, to even improve the sensitivity to $\sin^2 2\theta_{13}$ even larger reactor experiments have been proposed with an integrated Luminosity of the order of 10^4 GW t yrs [157]. For such experiments at this high exposure the handling of bin-to-bin uncorrelated systematical uncertainties have to be carefully addressed to further improve the sensitivity to $\sin^2 2\theta_{13}$. This is discussed for a typical scenario in [155] there called Reactor-II scenario. Possible realizations are the proposed reactor experiments Daya Bay [158] in China, RENO [159] in Korea, KASKA-II [160] in Japan, or even an upgrade at the Chooz site TripleCHOOZ [161].

6.4 Electron Capture Beams

Recently, another idea has been proposed, which makes use of a neutrino beam with neutrinos coming from electron capture processes [162–168]. The electron neutrinos that are emitted from such electron capture processes would have a definite monochromatic energy Q in the rest frame of the mother nuclei. Therefore by accelerating the mother nuclei to a Lorentz factor γ the neutrino energy E_ν can be completely controlled, since the energy of the neutrinos that are boosted exactly towards the direction of the detector is $E_\nu = 2\gamma Q$. The challenge from a technological point of view is that simultaneously a beam of electrons has to be accelerated at the same γ and coincide in the decay ring at one point with the accelerated nuclei so that both are in the same rest frame and the electron capture process can occur.

In such a scenario, the γ factor and the baseline length L have to be chosen respectively to the Q value of the electron capture process, the location of the oscillation maximum, and the minimal energy observable at the detector, *e.g.* above the Cherenkov threshold of muons at a Water Cherenkov detector. For example, if Q is relatively large ($\mathcal{O}(1\text{ MeV})$), γ can be chosen to be of the order $\mathcal{O}(100)$. In this case the neutrino beam can be viewed as exactly monoenergetic in the detector [162–169]. On the contrary, if Q is relatively small ($\mathcal{O}(100\text{ keV})$) the γ must be chosen quite high ($\mathcal{O}(1000)$), but the necessary choice of the baseline leads to the effect that the neutrinos now have a wider energy range at the detector. While the maximal energy of $E_\nu = 2\gamma Q$ is reached by the neutrinos in the beam axis, the energy of the neutrinos becomes smaller off the axis and the minimal energy of the neutrinos depends on the detector size and the baseline.

$$E_\nu(R) = \frac{Q}{\gamma}\left[1 - \frac{\beta}{\sqrt{1+(R/L)^2}}\right]^{-1} \approx \frac{2\gamma Q}{1+(\gamma R/L)^2}. \tag{6.3}$$

In this scenario, the neutrino energy can be reconstructed from the measurement of the vertical position R relatively to the beam axis within the detector and a superb energy resolution can be achieved [162, 163, 170][2]. This case seems interesting since only with one acceleration factor γ a wide range of neutrino energy can be covered simultaneously with a very accurate neutrino energy determination. On the other hand only neutrino running is available and no comparison with the anti-neutrino channel is possible, hence parameter correlations and especially the eight-fold degeneracy is hard to be resolved. The lack of the anti-neutrino channel has to be compensated by the extraordinary energy resolution available and enough statistics has to be collected, *i.e.* a very large fiducial mass such as at a megaton Water Cherenkov detector is preferable. The performance of such high γ electron capture beam experiments was analyzed in [170] and the requirements for being competitive to a standard Neutrino Factory experiment was estimated. The considered electron capture process was

$${}^{110}_{50}Sn + e^- \rightarrow {}^{110}_{49}In + \nu_e. \tag{6.4}$$

with a rest frame neutrino energy of $Q = 267$ keV at a lifetime of 4.11 h. It was found that in principle the very good energy resolution abilities can provide the potential to resolve the eight-fold degeneracy and measurements of $\sin^2 2\theta_{13}$ and δ_{CP} in a very large part of the parameter space can be possible. Even a competitiveness to a Neutrino Factory or β-Beams could be given however the requirements turned out to be extreme. The acceleration factor is required to be $\gamma \gtrsim 2000$ which would need a very powerful accelerator complex of the size of the LHC and the high statistics to gain from the superb energy resolution capabilities would require a very high number of electron capture decays per year $\sim 10^{18}$ which is hardly feasible considered that the lifetime is 4.11 h in the rest frame of the process[3].

6.5 Beta Beams

The idea of producing a flavor pure electron neutrino beam in the beta decay of accelerated mother nuclei was first proposed in [175]. In the last years this idea has gained a reasonable popularity and is discussed as the neutrino source of a possible future neutrino oscillation experiment, the so-called β-Beam. Various papers have been published discussing different

---

[2] The position reconstruction of the initial vertex at a Water Cherenkov detector is possible at least at a resolution of 30 cm [171]

[3] The rate of electron capture processes clearly requires enhancement which could be achieved by a laser irradiation as discussed in [172–174].

β-Beam scenarios and their performance compared to other established beam technologies as Superbeams and Neutrino Factory experiments, *e.g.* [176–188].

The basic principle is the acceleration of bunches of ionized beta decaying isotopes into a decay ring to relativistic energies at a relativistic Lorentz factor γ. The accelerated isotopes that decay in the straight sections of the designed decay ring produce electron neutrinos or anti-neutrinos, depending on the chosen isotope. In the rest frame of the decay the spacial momentum distribution is isotropic however in the laboratory system the neutrinos are boosted in the direction of the straight sections and form a collimated neutrino beam. The energy of the neutrinos can be accurately tuned by the acceleration of the mother nuclei, *i.e.* the γ factor. In this work, the considered isotopes for the production of the neutrino beam are ^{18}Ne for the neutrino beam and ^{6}He for the anti-neutrino beam. The relevant beta decay processes are:

$$\begin{aligned} ^{18}Ne &\rightarrow {}^{18}F + e^+ + \nu_e \\ ^{6}He &\rightarrow {}^{6}Li + e^- + \overline{\nu}_e. \end{aligned} \tag{6.5}$$

The produced neutrinos constitute a flavor pure neutrino beam that consists either of electron neutrinos or electron anti-neutrinos. Hence, the first obvious advantage compared to the conventional neutrino beam production in the decay of pions at conventional beam experiments or their Superbeam upgrades is the complete absence of a intrinsic beam contamination of neutrinos of a different flavor. The relevant oscillation channels are the disappearance channels $\nu_e \rightarrow \nu_\mu$ and $\overline{\nu}_e \rightarrow \overline{\nu}_\mu$. The signal events are very clean and have a clear signature, the produced muon that is easily distinguished from the electrons/positrons coming from the disappearance events. The schematic illustration of neutrino production and detection of the appearance channels at a β-Beam is given in Fig. 6.3. In principle, the disappearance channels $\nu_e \rightarrow \nu_e$ and $\overline{\nu}_e \rightarrow \overline{\nu}_e$ can also be measured at a β-Beam experiment but these channels can be compared to the measurements at a reactor experiment and so, the usefulness of the disappearance channels is only given if the systematical uncertainties in the spectral normalization can be kept below the 1% level which is hardly achievable at a beam-based experiment.

Let us consider the relevant appearance channels. The main possible background sources are coming from inelastic neutral current events with an associated single charged pion production, *e.g.*:

$$\begin{aligned} \text{Signal}: \quad & \nu_\mu \, + \, n \, \rightarrow \, p \, + \, \mu^- \\ \text{Background}: \quad & \nu_x \, + \, n \, \rightarrow \, p \, + \, \nu_x \, + \pi^-, \end{aligned} \tag{6.6}$$

where the charged pion is misidentified as a muon and the event is classified as signal event, because the further pion decay remains undetected, possibly because it happens outside the fiducial volume of the detector. A further possible source of background is due to atmospheric neutrinos. However, this source of background is not time-dependent as the incoming neutrino beam bunches and the magnitude and spectral distribution of atmospheric neutrinos is well known from the detector operation in the absence of the operating beam. It is expectable that the neutral current single pion background is the dominating background source since atmospheric neutrinos can be effectively rejected due to direction information and the direction of the incoming beam is known.

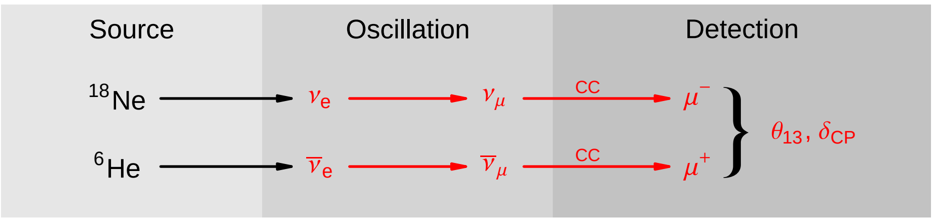

Figure 6.3: The schematic illustration of neutrino source, oscillation channels, and detection principles at a β-Beam experiment. The neutrinos are produced in the beta decay of the *boosted* and stored isotopes ^{18}Ne (ν_e) and ^{6}He ($\bar{\nu}_e$). The appearance of ν_μ, respectively $\bar{\nu}_\mu$ is measured.

The further advantage compared to conventional beam production is the well-known spectra of beta decay. In the rest frame of the beta decay the neutrino energy spectrum is continuous up to a well-known endpoint energy depending on the chosen mother nuclei. The energy spectra is boosted to higher energies due to the relativistic acceleration of the mother nuclei but the spectral form remains similar and is exactly known. Thus the energy dependent bin-to-bin systematical uncertainties of the spectrum are reduced to the minimum and only the overall normalization uncertainty has to be controlled by a near detector while for conventional beams the complete spectrum is required to be probed over all available neutrino energies. Above the endpoint energy no neutrino flux is present at a β-Beam and the flux is centered around the mean energy while for conventionally produced beams the high energy tail far off the mean energy resulted in increased background from neutral current event that are reconstructed at smaller energies.

The formula for the boosted β-Beam neutrino spectrum of the beam flux as a function of the incident neutrino energy E_ν in the exact direction of the beam-line (θ=0) is given as [179]:

$$\left.\frac{d\phi}{dE_\nu}\right|_{\theta=0} = C_\beta \, \frac{E_\nu^2}{\gamma} \left(1 - \frac{E_\nu}{2\gamma(E_0+m_e)}\right) \sqrt{\left(1 - \frac{E_\nu}{2\gamma(E_0+m_e)}\right)^2 - \left(\frac{m_e}{E_0+m_e}\right)^2} \,. \tag{6.7}$$

Here, the rest frame endpoint point energies E_0 enter. The considered isotopes ^{18}Ne and ^{6}He do provide a further advantage, that is their endpoint energies being very similar with $E_0(^{18}Ne) = 3.4$ MeV and $E_0(^{6}He) = 3.5$ MeV. So, both isotopes can be accelerated at the same γ factor resulting in similar beam energies. For a given accelerator complex the achievable acceleration is limited and using isotopes with similar endpoint energies makes sure that the acceleration complex cannot only be optimized for one of the isotopes. Due to different exited states in the mother nuclei, in principle different endpoint energies can combine to the overall spectrum of neutrinos. However, for the here considered isotopes the mentioned endpoint energies dominate and only small contributions below the 1% level to the spectrum are present from other endpoint energies. So, the different excited states are neglected throughout this work since the impact is absolutely negligible for the considered isotopes.

In the above formula of the β-Beam neutrino spectrum in the laboratory frame an energy independent pre-factor C_β appears:

$$C_\beta = \frac{N_\beta}{\pi L^2} \, \frac{15}{2 \; g(y_e) \; (E_0+m_e)^3} \tag{6.8}$$

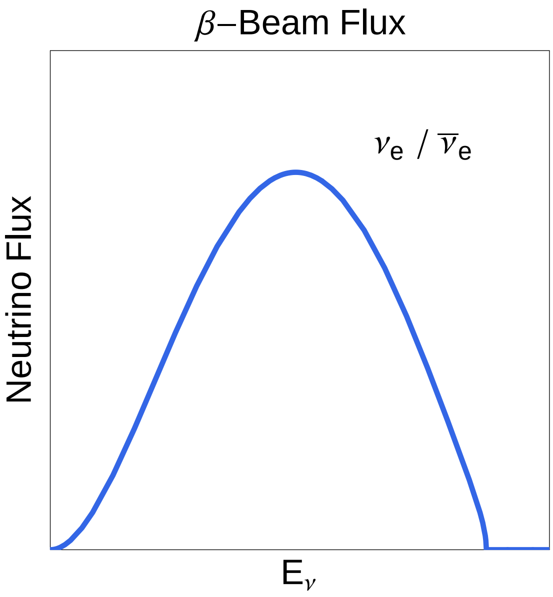

Figure 6.4: The energy spectrum of the neutrino flux at a β-Beam experiment. The neutrino flux is absolutely flavor-pure and contains only of ν_e for stored ^{18}Ne isotopes or $\overline{\nu}_e$ for stored ^{6}He isotopes. The maximal energy is $E_{\max} \approx 2\gamma E_0$.

It contains the number of isotope decays in the storage ring N_β per units of time (typically per year) and the geometric baseline suppression factor of $1/L^2$ and also a factor $g(y_e)$ that depends on the chosen isotope:

$$g(y_e) = \sqrt{1-y_e^2}\left[2-9y_e^2-8y_e^4\right] + 15y_e^4 \log\left[\frac{y_e}{1-\sqrt{1-y_e^2}}\right]. \tag{6.9}$$

Summarizing, the neutrino beam of a β-Beam scenario is absolutely flavor pure and contains only of electron or anti-electron neutrinos and the spectrum is very well known. The β-Beam spectrum of the neutrino flux is illustrated in Fig. 6.4.

We will discuss two different detector technologies suitable for a β-Beam experiment. The β-Beam detector requires excellent capabilities in electron/muon separation but no charge separation and no magnetized detector material is needed. So, the Water Cherenkov detector seems well suitable also due to the large statistics that can be collected at a possible future megaton Water Cherenkov detector. However, Water Cherenkov detectors only provide very good detector properties at lower neutrino energies $E_\nu \lesssim 1$ GeV in the quasi-elastic regime of charged-current interactions. For higher energies the energy reconstruction becomes difficult in the regime of dominating inelastic interactions since the hadronic components that are below the Cherenkov threshold cannot be measured. Furthermore, for increasing neutrino energies the neutral-current background due to single pion production becomes the limiting factor. Thus, for higher neutrino energy β-Beams we will also discuss the technology of Totally Active Scintillator detector to be suitable which provides a better energy resolution and better handling of the neutral current backgrounds. The details of the detector simulation will be presented in Chapter 7. Depending on the choice of the acceleration factor γ the β-Beam scenarios are usually classified as either "low γ" β-Beam, "medium γ" β-Beam, or "high γ" β-Beam. The classification follows the dimension of the accelerator that is required to accelerate the respective isotopes to the respective γ which depends also on the isotope choice. For the here discussed isotopes ^6He and ^{18}Ne the classes are approximately given as follows: "low γ" for $\gamma \lesssim 150-200$[4], "medium γ" for $150-200 \lesssim \gamma \lesssim 600-800$[5], and "high γ" for $\gamma \gtrsim 600-800$[6].

6.6 Neutrino Factories

The idea of a Neutrino Factory experiment has been first discussed almost ten years ago [189] and the performance of the scenario have been widely discussed, *e.g.* in [42, 190–198]. It was pointed out that the conventional neutrino beam production is based on the decay of pions, β-Beam neutrino production is based on the beta decay of accelerated isotopes, and the idea for Neutrino Factory experiments is to produce the neutrino beam in the decay of muons that are accelerated and then stored in a storage ring just as the isotopes at a β-Beam facility. The muons decaying in the straight sections of the storage ring form a boosted collimated neutrino beam. The difference to the beam of a β-Beam experiment is that the Neutrino Factory neutrino beam contains not only one flavor since the decay of a muon results in a muon neutrino and electron anti-neutrino. The respective anti-neutrino beam can be produced if anti-muons are stored in the storage ring. The relevant decays are:

$$\begin{aligned} \mu^- &\rightarrow e^- + \nu_\mu + \overline{\nu}_e \\ \mu^+ &\rightarrow e^+ + \overline{\nu}_\mu + \nu_e . \end{aligned} \tag{6.10}$$

The Neutrino Factory neutrino beam provides the possibility to perform precision measurements of the leading atmospheric oscillation parameters $\sin^2 2\theta_{23}$ and $|\Delta m^2_{31}|$ in the disappearance channels $\nu_\mu \rightarrow \nu_\mu$ and $\overline{\nu}_\mu \rightarrow \overline{\nu}_\mu$ and additionally measurements in the so-called golden channel, *i.e.* the appearance channels $\nu_e \rightarrow \nu_\mu$ and $\overline{\nu}_e \rightarrow \overline{\nu}_\mu$. The golden channels provide access to three-flavor effects in terms of measurements of $\sin^2 2\theta_{13}$, δ_{CP}, and the sign of Δm^2_{31}. The schematic illustration of neutrino production and detection is shown in Fig. 6.5.

A significant background contribution is coming from neutral-current events as was the case for the β-Beam. But, as can be seen from Fig. 6.5 the phenomenology at a Neutrino Factory is added an additional possible background source. Different than the β-Beam neutrino beam, the Neutrino Factory neutrino beam is not flavor pure but consists of 50% ν_μ and 50% $\overline{\nu}_e$ (50% $\overline{\nu}_\mu$ and 50% ν_e in case of μ^+ stored). The large amount of charged-current events at the detector will be the disappearance events with the signature of a produced muon μ^- (μ^+ in case of μ^+ stored) while the signature of the $\sin^2 2\theta_{13}$ suppressed golden channel is a produced anti-muon μ^+ (μ^- in case of μ^+ stored). The detection of the golden channel events thus requires an effective charge separation of the muons. This is the origin of the term wrong-sign muon, *i.e.* the disappearance channel produced muons are the so-called wrong-sign muons if the golden channel is to be measured. The charge separation can only performed at a magnetized detector, where the track of the muons can be reconstructed and the curvature of the muons can be measured relatively to the magnetic field. In this procedure a new cut is required, the CID (charge identification) cut, which is a cut to the minimum transverse muon momentum. The selection of the cut requirements affect the

---

[4] This isotope acceleration requires an accelerator complex of comparable size to the SPS [180].

[5] This isotope acceleration requires an accelerator complex of comparable size to a Super-SPS [185].

[6] For such high acceleration factors an accelerator complex of comparable size of the LHC itself is required.

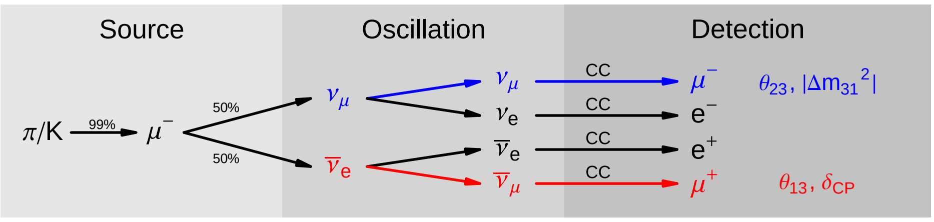

Figure 6.5: The schematic illustration of neutrino source, oscillation channels, and detection principles at a Neutrino Factory experiment. The neutrinos are produced in the decay of *boosted* and stored μ^- or μ^+. Both, a measurement of disappearance and appearance of muon neutrinos is possible. However, the appearance measurement involves the detection of the so-called *wrong sign muons* as can be seen from the illustration. Hence, a magnetized detector has to be used in order to allow for charge identification of the muons.

signal efficiency as well as the background level (see the appendix of [198] for a detailed discussion). The usually discussed detector technology is a Magnetized Iron Calorimeter comparable to the detectors of MINOS [119] or MONOLITH [199]. Due to the CID cut, very high neutrino energies are required at a Neutrino Factory scenario with $E_\nu \gtrsim 20$ GeV. Thus, the discussed baselines for a Neutrino Factory experiment are also very high, at several thousands of kilometers but still it is hard to achieve a Neutrino Factory to be operated at the first oscillation maximum and the discussed Neutrino Factory baselines are slightly off. That is the reason why a Neutrino Factory experiment suffers the most from parameter correlations and the eight-fold degeneracy compared to other experiment technologies and additional strategies like multi-baseline detector locations are required to resolve the degeneracies. Strategies that involve different baselines, *i.e.* one detector at the magic baseline and one detector at a baseline optimized for measurements of $\delta_{\rm CP}$ can be realized by the arrangement of the storage ring architecture. Since the neutrino beam is produced at the straight sections of the storage ring, the assembling of different straight sections in one storage ring allows to lead neutrino beams to different beam lines and different detectors at different baselines. Note, that the construction of a Neutrino Factory storage ring is very demanding since the straight sections have to be tilt down. For instance a beam-line towards a detector at the magic baseline requires an angle of approximately 37 degrees into the ground.

As for the beta decay of the isotopes at a β-Beam facility, the muon decay provides a very well-known spectrum in the rest frame of the decay and the formula for the boosted spectrum of the neutrino flux in the laboratory frame as a function of the neutrino energy in the laboratory frame E_ν in the exact direction of the beam-line ($\theta = 0$) is given as:

$$\left.\frac{d\phi_{\nu_\mu}}{dE_\nu}\right|_{\theta=0} = \frac{4\ N_\mu}{\pi L^2\ m_\mu^3}\ E_\nu^2 \left[3 - 4\ \gamma(1-\beta)\ \frac{E\nu}{m_\mu}\right]$$

$$\left.\frac{d\phi_{\nu_e}}{dE_\nu}\right|_{\theta=0} = \frac{24\ N_\mu}{\pi L^2\ m_\mu^3}\ E_\nu^2 \left[1 - 2\ \gamma(1-\beta)\ \frac{E\nu}{m_\mu}\right] \qquad (6.11)$$

Here, the acceleration of the muons is described by the relativistic γ factor and the corresponding $\beta = \sqrt{1 - 1/\gamma^2}$. However, different than for the discussion of β-Beams, in case of Neutrino Factory experiments the discussions in the literature do not describe the muon acceleration in terms of γ but in terms of the parent energy of the stored muons in the storage ring E_μ. The relevant relation for the above formula is $\gamma = E_\mu/m_\mu$. The shape of the

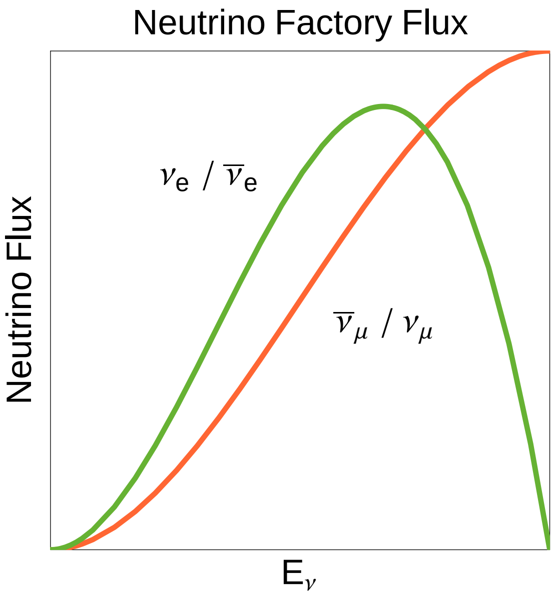

Figure 6.6: The energy spectrum of the neutrino flux at a Neutrino Factory experiment. The neutrino flux consists either of ν_μ and $\overline{\nu}_e$ for stored μ^- or $\overline{\nu}_\mu$ and ν_e for stored μ^+. The maximal energy is $E_{\text{max}} = E_\mu$, the energy of the parent muons in the storage ring.

neutrino flux at a Neutrino Factory is illustrated in Fig. 6.6. The electron neutrino and muon neutrino contributions follow different behaviors and the maximal flux for electron neutrinos is obtained at neutrino energies smaller than E_μ while the maximal muon neutrino flux is obtained at the highest possible energy, the initial energy of the stored parent muon E_μ.

The technology of conventional beam production and beam production at a Neutrino Factory is not as disconnected as it may seem, because the muons for the decay in the storage rings are to be produced in the decay of pions just as the neutrinos in conventional beam production. The storage selection of either muons or anti-muons is performed by the selection of the π^+ or π^- at the target by the polarization of the magnetized horns. The main challenge for the further handling of the produced muons in the decays of the pions is the issue of muon cooling. The initially produced muons have a wide distribution in momentum space but are required to be cooled down to allow for a further clean acceleration [193, 200–204]. The most promising technology for the required muon cooling is the so-called ionization cooling [205, 206] since all existing cooling technologies do not work for muons. The feasibility of this technology is to be proved at the MICE experiment [207–209]. It should be mentioned that a successful technology for the muon cooling is not only required for neutrino oscillation physics at a Neutrino Factory but is also a very important issue for the feasibility of a possible future muon collider experiment [210, 211].

It should be noted, that a Neutrino Factory experiment is not only a very good tool for standard three-flavor oscillations but is also sensitive to possible deviations from the “standard physics” and “new physics” would be observable, as for instance the possibility of the so-called non-standard interactions of neutrinos that mediate additional flavor transition contributions and interfere with the oscillation. These have been addressed in [212–219]. Since we will not implement non-standard interactions to the simulations in this work, it should be kept in mind that the optimization arguments discussed in this work do not correspond to the optimization with respect to all physical motivations but only to the standard three-flavor oscillation.

Chapter 7

Beta Beam Performance

The aim for this Chapter is to estimate and optimize the performance of a possible β-Beam experiment for measurements of $\sin^2 2\theta_{13}$, the phase δ_{CP}, and the sign of Δm^2_{31}. First, we introduce the simulation methods that have been used to analyze the physics potential of the β-Beam. Next, the possible optimization in terms of neutrino energy, *i.e.* the isotope acceleration factor γ, and the experiment baseline L are addressed. Thereafter single technical aspects and possible impacts on the physics potential are discussed, before optimized reference scenarios with different ambitious detector effort and technology are defined and the potential is compared. Furthermore, the performance of these reference setups is related to optimized Neutrino Factory reference scenarios in Chapter 9.

7.1 Beta Beam Simulation

All β-Beam simulations throughout this work are performed with the GLoBES software [220, 221] that is briefly introduced in the appendix. For all discussed β-Beam scenarios we assume a total runtime of 8 years data taking. The endpoint of the spectrum of the neutrino flux is determined by the tuned γ acceleration factor and the endpoint energy E_0 of the used isotopes, here ^{18}Ne (ν_e-beam) and ^6He with endpoint energies $E_0 = 3.4$ MeV for ^{18}Ne and $E_0 = 3.5$ MeV for ^6He. The endpoint energies of the two nuclei are very similar and we assume the same acceleration factors for both, *i.e.* $\gamma(^{18}Ne) = \gamma(^6He)$, so that the neutrino energies in the anti-neutrino and neutrino modes are very similar. In principle, the γ's can be chosen differently, however there is no obvious gain in increasing one with respect to the other (*cf.*, Ref. [180]). We neglect the fact that there exist different excited states in the daughter nuclei of the decay, which additionally lead to negligible small contributions to the spectra with different endpoint energies. We assume $2.9 \cdot 10^{-18}$ ^6He and $1.1 \cdot 10^{-18}$ ^{18}Ne isotope decays per year in the storage rings. This assumes a concurrent neutrino and anti-neutrino runtime with both isotopes operated over the absolute runtime of 8 years and corresponds to the standard assumption for β-Beams in the literature [176–187] . The same statistics can also be obtained by a consecutive neutrino and anti-neutrino runtime of 4 years each with the double numbers of the decays per year. However, these numbers are based on estimates for low γ with the acceleration factors $\gamma(^{18}Ne) = 100$ and $\gamma(^6He) = 60$ and it has not been demonstrated that the numbers of decays can be maintained for medium or high γ. Basically, we assume that this is the case but the impact of a γ-scaling of the isotope decays is addressed in Section 7.5 since the assumption might not be justified for technical considerations.

An important difference of a β-Beam experiment to Superbeams or Neutrino Factory experiments is the missing information on the leading atmospheric oscillation parameters in the disappearance data. In principle Δm^2_{31} is accessible while $\sin^2 2\theta_{23}$ is not, however this would require systematical uncertainties below the 1% level which is hardly achievable. So, a β-Beam experiment itself cannot measure the leading parameters and is not able to contribute to the desirable precision measurements of the atmospheric parameters as would be the case for Superbeams or a Neutrino Factory. Here, we are mainly interested in the performance of the appearance measurements to determine $\sin^2 2\theta_{13}$, $\delta_{\rm CP}$, and the neutrino mass hierarchy. But as was pointed out earlier, the leading parameters also affect this performance via parameter correlations. So, we add the simulated disappearance data of the Superbeam experiment T2K[1] (8 years assumed) to minimize the parameter correlations with the leading atmospheric oscillation parameters. At the time a β-Beam starts operation this data will be available to constrain the parameters. However, we do not include the T2K appearance data in order to analyze the performance of the β-Beam appearance measurements alone. The impact of the inclusion of the T2K disappearance data is addressed in Section 7.4. We will apply the same technique in the simulations of the Neutrino Factory experiments and for the simulation of T2HK since these experiments will have the ability to measure the atmospheric parameters by far best from their own disappearance data that is included to the simulation.

The solar oscillation parameters are constrained with a precision of 5% for each independently to the best-fit values by GLoBES internal priors with pull terms in the χ^2 calculation. Eventually, we assume a constant matter density profile with a 5 % uncertainty on the value of the baseline-averaged matter density, where the uncertainty takes into account matter density uncertainties as well as matter density profile effects [224–226]. If the baseline of an experiment is changed, we also re-compute and use the average matter density for this baseline.

Detector technologies

A general requirement for any β-Beam detector is to have good muon-electron separation capabilities and to have an efficient neutral-current rejection. At the same time, the technology must be available and cost effective to allow in time a scaling to large detectors. For lower values of γ, certainly Water Cherenkov detectors fulfill these criteria [175, 176, 179, 180, 182, 183]. However, at higher γ values, the lack of background discrimination in Water Cherenkov detectors becomes a huge problem and other detector types, such as calorimeters or TPCs (Time Projection Chambers) are more suitable [179, 227]. The precise value of γ where this turnover happens seems to be an unresolved question and different views can be found in the literature [176, 179]. Our choice for large values of γ is the so-called Totally Active Scintillator detector for reasons which will be discussed below. The two detector technologies used in this study, namely Water Cherenkov and Totally Active Scintillator, are described in more detail in the following subsections.

Water Cherenkov Detector

Water Cherenkov detectors are well suited to distinguish muon neutrinos from electron neutrinos by analyzing the topology of the detected Cherenkov ring. However, background rejection

---

[1] See Refs. [198, 222, 223] for details of the T2K description within GLoBES. The corresponding experiment describing file is provided with the GLoBES 3.0 software. The here used file is a modified version of `T2K.glb`.

can be a problem in using a Water Cherenkov detector in combination with a β-Beam. The main source of background to the muon neutrino appearance search will be the flavor-blind neutral-current events which are mistaken for muon neutrino charged-current events. The most critical neutral-current events are those where one or several energetic pions are involved, which implies that there is basically no background below the pion production threshold around 200 MeV. Therefore, one solution would be to tune γ to a low value where most of the neutrinos in the beam are below this threshold [176]. In that case there would be no energy information, since the Fermi-motion of the nucleons would induce an energy smearing of about 100 MeV. This would reduce the β-Beam to a mere counting experiment, which would have only a very limited physics reach [179]. Above the pion threshold, the feasibility of using a Water Cherenkov detector depends on the ability to correctly identify pions and to reject neutral-current events. The pion identification works, in principle, by identifying its decay process and it seems to be possible up to some level. There are very different statements in the literature how well this can be done [176, 179]. The different results can to a large extent be attributed to the different level of detail used in the detector simulation.

In order to describe the energy response of the detector in our study, we divide the signal events into samples of quasi-elastic events (QE) and inelastic events (IE). Only for the QE sample, it is possible to accurately reconstruct the neutrino energy from the charged lepton. For IE events, the reconstructed energy will always lie below the true (incident) neutrino energy because the hadronic component of the interaction cannot be seen by a Water Cherenkov detector. Since the separation of those two event samples is fraud with a large error, we will use the same technique as described in Ref. [198]. This means that the total rates number of all IE + QE events is taken into account and in addition the spectrum of the QE event sample is used to obtain spectral information. In order to avoid double counting of events, the QE event sample is taken only with a free normalization. In this approach, no particular assumption about the event by event separation has to be made, because this approach is purely statistical. In fact, the real experiment might even perform better since there actually could be some event by event separation. For the spectral analysis, we assume that the Fermi-motion is the main component of the resulting energy resolution function. Therefore, a constant width of 85 MeV [146] in a Gaußian energy resolution function is taken, in order to describe the energy reconstruction of the QE sample. For the background distribution, we make the assumption that every neutrino which interacts via neutral-currents is reconstructed with an energy distribution which is flat from zero up to the true neutrino energy. In this way we obtain a background which is peaked at low energies. We do not take into account any other background source, since in Ref. [180] it was shown that atmospheric neutrinos only give a very small contribution.

In order to be able to use γ values in the range from 50 to 500, the energy range is chosen as $0.2 - 3.0$ GeV and is divided into bins of 100 MeV width, such that the total number of bins is 28. All efficiencies are constant with exception of the first bin where they are only 1/2 of the value given in the signal/background table to account for threshold effects. The numbers for the disappearance channel could be quite different (in fact, the efficiencies might be much higher), but we checked that the final results do not depend on this assumption. Therefore, because of simplicity, we take the same numbers as for the appearance channels. We also include systematic uncertainties on the normalization of signal and background events as given in Table 7.1, where all errors are assumed to be fully uncorrelated. This is a conservative approximation and does not affect the result from the appearance measurement. The disappearance measurement, on the other hand, would require a total absolute error of less than

Disappearance – ^{18}Ne stored		σ_{norm}	σ_{cal}
Signal	$0.55 \otimes (\nu_e \to \nu_e)_{\mathrm{QE}}$	0.025	10^{-4}
Background	$0.003 \otimes (\nu_e \to \nu_x)_{\mathrm{NC}}$	0.05	10^{-4}
Appearance – ^{18}Ne stored – Spectrum			
Signal	$0.55 \otimes (\nu_e \to \nu_\mu)_{\mathrm{QE}}$	10.0	10^{-4}
Background	$0.003 \otimes (\nu_e \to \nu_x)_{\mathrm{NC}}$	0.05	10^{-4}
Appearance – ^{18}Ne stored – Total Rates			
Signal	$0.55 \otimes (\nu_e \to \nu_\mu)_{\mathrm{CC}}$	0.025	10^{-4}
Background	$0.003 \otimes (\nu_e \to \nu_x)_{\mathrm{NC}}$	0.05	10^{-4}
Disappearance – ^{6}He stored			
Signal	$0.75 \otimes (\bar{\nu}_e \to \bar{\nu}_e)_{\mathrm{QE}}$	0.025	10^{-4}
Background	$0.0025 \otimes (\bar{\nu}_e \to \bar{\nu}_x)_{\mathrm{NC}}$	0.05	10^{-4}
Appearance – ^{6}He stored – Spectrum			
Signal	$0.75 \otimes (\bar{\nu}_e \to \bar{\nu}_\mu)_{\mathrm{QE}}$	10.0	10^{-4}
Background	$0.0025 \otimes (\bar{\nu}_e \to \bar{\nu}_x)_{\mathrm{NC}}$	0.05	10^{-4}
Appearance – ^{6}He stored – Total Rates			
Signal	$0.75 \otimes (\bar{\nu}_e \to \bar{\nu}_\mu)_{\mathrm{CC}}$	0.025	10^{-4}
Background	$0.0025 \otimes (\bar{\nu}_e \to \bar{\nu}_x)_{\mathrm{NC}}$	0.05	10^{-4}

Table 7.1: The signal efficiencies and background rejection factors together with the associated systematical errors for the various signals and backgrounds used in our description of the performance of a Water Cherenkov detector β-Beam. The normalization errors are the normalization error σ_{norm} and the energy calibration error σ_{cal}. This corresponds to the `BBvar_WC.glb` file that is provided with GLOBES 3.0.

1% to yield any information on θ_{13} [155,228,229]. This number, however, seems very difficult to be reached, if at all, for any experiment which involves neutrino-nucleus cross-sections at low energies. Our parameterization has been calibrated against low γ scenarios from earlier literature ($\gamma = 150$, [180]). Therefore using different values of γ involves some extrapolation. Our parameterization should nevertheless be reliable from γ 100 up to 350, and it should additionally reproduce the qualitative features of the γ-scaling within a range from 50 to 500. The experiment description is similar to the one from [186] and is provided with the newest version of GLoBES 3.0 [220,221].

Totally Active Scintillator Detector

For even larger values of γ, a detector which can also measures the hadronic energy deposition is required. The reason is that the fraction of inelastic events in the whole event sample increases with increasing γ, because the neutrino spectra are extended to higher energies. The techniques which have traditionally been used for that purpose are tracking calorimeters and TPCs (such as a large liquid Argon TPC as described in Ref. [227]). The latter technology has certainly a great potential in neutrino physics, but given the fact that background issues are not the primary concern, we will discuss the more traditional and better understood option of a tracking calorimeter. Basically, there exist three different approaches:

- magnetized iron plates, interleaved with scintillator bars

Disappearance – ^{18}Ne stored		σ_{norm}	σ_{cal}
Signal	$0.2 \otimes (\nu_e \rightarrow \nu_e)_{\text{CC}}$	0.025	10^{-4}
Background	$0.001 \otimes (\nu_e \rightarrow \nu_x)_{\text{NC}}$	0.05	10^{-4}
Appearance – ^{18}Ne stored			
Signal	$0.8 \otimes (\nu_e \rightarrow \nu_\mu)_{\text{CC}}$	0.025	10^{-4}
Background	$0.001 \otimes (\nu_e \rightarrow \nu_x)_{\text{NC}}$	0.05	10^{-4}
Disappearance – ^{6}He stored			
Signal	$0.2 \otimes (\bar{\nu}_e \rightarrow \bar{\nu}_e)_{\text{CC}}$	0.025	10^{-4}
Background	$0.001 \otimes (\bar{\nu}_e \rightarrow \bar{\nu}_x)_{\text{NC}}$	0.05	10^{-4}
Appearance – ^{6}He stored			
Signal	$0.8 \otimes (\bar{\nu}_e \rightarrow \bar{\nu}_\mu)_{\text{CC}}$	0.025	10^{-4}
Background	$0.001 \otimes (\bar{\nu}_e \rightarrow \bar{\nu}_x)_{\text{NC}}$	0.05	10^{-4}

Table 7.2: The signal efficiencies and background rejection factors together with the associated systematical errors for the various signals and backgrounds used in our description of the performance of a Totally Active Scintillator detector β-Beam. The normalization errors are the normalization error σ_{norm} and the energy calibration error σ_{cal}. This corresponds to the `BBvar_TASD.glb` file that is provided with GLOBES 3.0.

- low-Z material (such as particle board), interleaved with scintillator bars
- all active detector made of liquid scintillator and plastic tubes

The big advantage of a (magnetized) iron calorimeter is usually the ability to determine the charge of muons, but this is pointless for a β-Beam since there is no appearance of wrong sign muons like at a Neutrino Factory. For the other options, the advantages and disadvantages have been very carefully addressed in the preparation of the NOνA proposal [230]. We decided to use for our study the same technology as in the NOνA proposal, which is the so-called Totally Active Scintillator Detector. The totally active design provides a superior energy resolution and background rejection at reasonable efficiencies. For our parameterization, we follow closely the work done by the NOνA collaboration, the only problem being that all studies have been done for ν_e appearance, whereas we look for ν_μ appearance. The latter should be much easier because the muon track is much more difficult to be confused with a neutral-current event. Therefore, our parameterization is on the conservative side, which does not affect our conclusions since the Totally Active Scintillator detector very effectively rejects backgrounds. The numbers we use for efficiencies and systematical errors are given in Table 7.2 and are taken from Refs. [230–233].

The energy window reaches from 0.5 GeV up to the endpoint of the neutrino spectrum and is divided into 20 bins. The energy resolution is given by a Gaußian with a width of 3% $\sqrt{E}$ for muon neutrinos and 6% $\sqrt{E}$ for electron neutrinos. The background is assumed to have the same shape as the signal. But note that the shape of the background is not much of an issue in the case of a Totally Active Scintillator detector detector since the background is very small. We checked that a background of the same total magnitude which is distributed like E_ν^{-1} gives basically the same results. The experiment description is similar to the one from [186] and is provided with the newest version of GLoBES 3.0 [220, 221].

7.2 Beta Beam Optimization

In this section, we will focus on the optimization of a β-Beam experiment in terms of optimizing the baseline L or the neutrino energy E_ν by tuning the isotope acceleration γ. Such an optimization attempt was already performed in [186] for a slightly different set of true oscillation parameter values. There, the optimization process involved a tuning of γ by fixing the ratio L/γ so that higher γ also implies a larger baseline. As outcome for both scenarios, Water Cherenkov and Totally Active Scintillator, the simple rule "the larger γ, the better" was found, however slightly more effective for the latter. We will not repeat this discussion and focus on the single optimization of either baseline L for a selected fixed γ or the isotope acceleration γ for a selected fixed baseline L. We will discuss the optimization for the three performance indicators: sensitivity limit to $\sin^2 2\theta_{13}$, sensitivity to *maximal* CP violation, and sensitivity to mass hierarchy. These performance indicators will be shortly described when first discussed, however a list of all performance indicators together with the exact definition and further useful comments is given in the appendix. The performance indicators will be introduced to describe the abilities of the considered experiment scenarios in measurements of $\sin^2 2\theta_{13}$, δ_{CP}, and the mass hierarchy[2].

For the discussion of the optimization issues concerning the baseline L we discuss a low γ β-Beam with a Water Cherenkov ($\gamma = 150$), two medium γ β-Beams, one Water Cherenkov ($\gamma = 350$) and one Totally Active Scintillator detector scenario ($\gamma = 500$), and finally a high γ scenario with a Totally Active Scintillator detector ($\gamma = 1000$). For the discussion of the optimization issues concerning the isotope acceleration factor γ we try to stick to realistic baselines. For that reason a Water Cherenkov β-Beam is discussed at the CERN-Frejus baseline of L=130 km. So, the CERN-MEMPHYS baseline scenario is included [187, 234]. A second baseline is discussed for a Water Cherenkov detector at a distance of L=730 km. This baseline can be associated with the distance between the CERN and the Gran Sasso underground laboratories in Italy or to the baseline between the FermiLab and the Soudan mine, *i.e.* the actual MINOS baseline. This baseline is large enough for β-Beam energies where already a Totally Active Scintillator detector can be installed so we will also discuss this possibility and additionally also a Totally Active Scintillator detector scenario at an even larger baseline of L=1500 km.

Sensitivity to θ_{13}

The sensitivity limit to $\sin^2 2\theta_{13}$ describes the ability of an experiment to set a lower bound to $\sin^2 2\theta_{13}$ in the worst-case scenario[3] of a vanishing true value $\sin^2 2\theta_{13} = 0$. It is given by the largest fit value of $\sin^2 2\theta_{13}$ that can be excluded at the chosen confidence level, that is here and throughout this work 3σ, under the simulation assumption $\sin^2 2\theta_{13}^{\mathrm{true}} = 0$.

First, we concentrate on the optimization of the baseline for a low $\gamma = 150$ and a medium $\gamma = 350$ β-Beam with a megaton Water Cherenkov detector. The respective sensitivity limits to $\sin^2 2\theta_{13}$ as a function of the baseline L are shown in Fig. 7.1. In order to allow comparison of the results with results from the corresponding discussion in [186] the upper x-axis is labeled

---

[2] For reasons of intuitive lucidity a color coding has been introduced to the screen version and selected print versions in the chapters where the main results are presented, that is each parameter corresponds to its own color. All performance indicators involving $\sin^2 2\theta_{13}$ are indicated with blue colors, the ones involving δ_{CP} are shown in red colors, and the sensitivity to mass hierarchy is always associated with green colors.

[3] Here, the term worst-case scenario is used from a view point of the experiment, since $\sin^2 2\theta_{13} = 0$ would effect in a non-observation of three-flavor effects at the experiment.

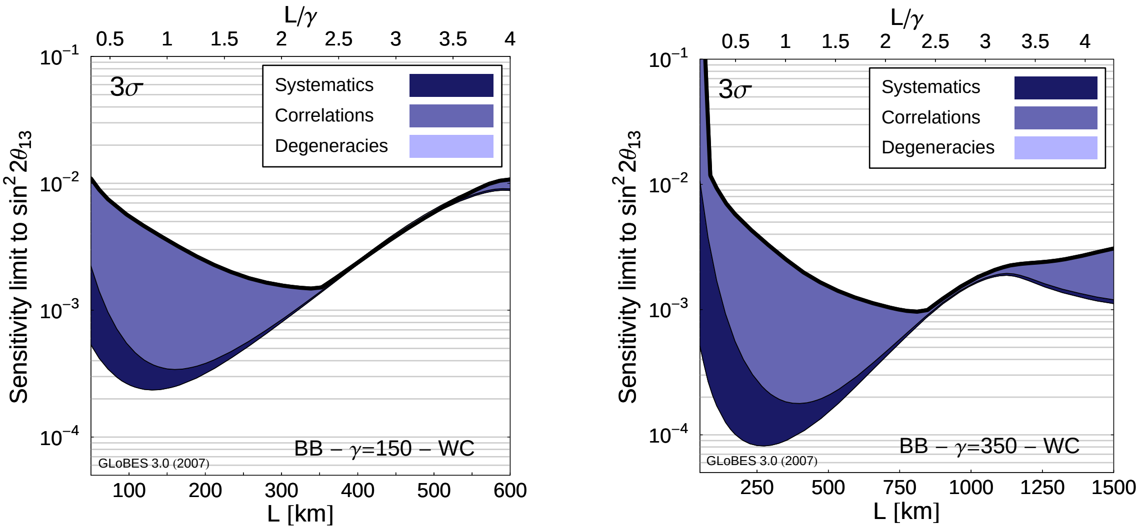

Figure 7.1: The sensitivity limit to $\sin^2 2\theta_{13}$ at a β-Beam at the 3σ confidence level as a function of the baseline L for fixed $\gamma = 150$ (left) and $\gamma = 350$ (right). The plots are for a megaton Water Cherenkov detector with a fiducial mass of 500 kt. The bands indicate the influence of systematics, correlations, and degeneracies and the final sensitivity limit is indicated by the uppermost thick black line.

with the parameter L/γ. Systematics, correlations and degeneracies are taken into account an their effect is indicated by the colored bands. The lowest curve indicates the pure statistical sensitivity limit. The dark blue/grey band shows the effect of switching on the systematical uncertainties. For both Water Cherenkov detector scenarios one can establish an optimal baseline at a ratio $L/\gamma \sim 1$ (L ~150 km in the left plot for $\gamma = 150$ and L~ 300km in the right plot for $\gamma = 350$). In this baseline range the highest event rates (which determine the pure statistical limit) can be achieved. Note, that obtaining the maximal number of events is a tuning problem where more factors are involved. Typically, the highest event rates are achieved if the position of the first oscillation maximum in E_ν (given by L/E_ν, *i.e.* by the chosen baseline L) coincides with the peak of the convolution of cross section and neutrino flux with the reducing factor $1/L^2$. If the baseline is too small, the oscillation maximum is located at too low energies where cross sections and neutrino flux decrease. If the baseline is increased, the location of the first oscillation maximum travels to higher energies, until the neutrino flux decreases again. In the right plot one can observe an improved statistical sensitivity limit for baselines $L > 1200$ km where the second oscillation maximum travels towards the maximum of the convolution of cross section and neutrino flux. However, the best statistical sensitivity limit is still achieved with the first oscillation maximum. But, if also correlations (indicated by the medium bright grey/blue band) and degeneracies (indicated by the bright grey/blue band, but here for the Water Cherenkov detector scenarios it has no visible effect) are considered, the sensitivity limit becomes worse by one order of magnitude. This effect is mainly due to the correlation with the phase δ_{CP}. The final sensitivity limit to $\sin^2 2\theta_{13}$ is highlighted by the uppermost thick black curve in the plots of Fig. 7.1 and we observe that it shows a different behavior as a function of the baseline L than the statistical and systematical limits due to the effect of correlations and degeneracies. At a baseline of L ~350 km for $\gamma = 150$ and L ~800 km, in both cases at $L/\gamma \sim 2.5$, the final sensitivity limit is at its optimal value. There, the effect of correlations and degeneracies vanishes, *i.e.* the

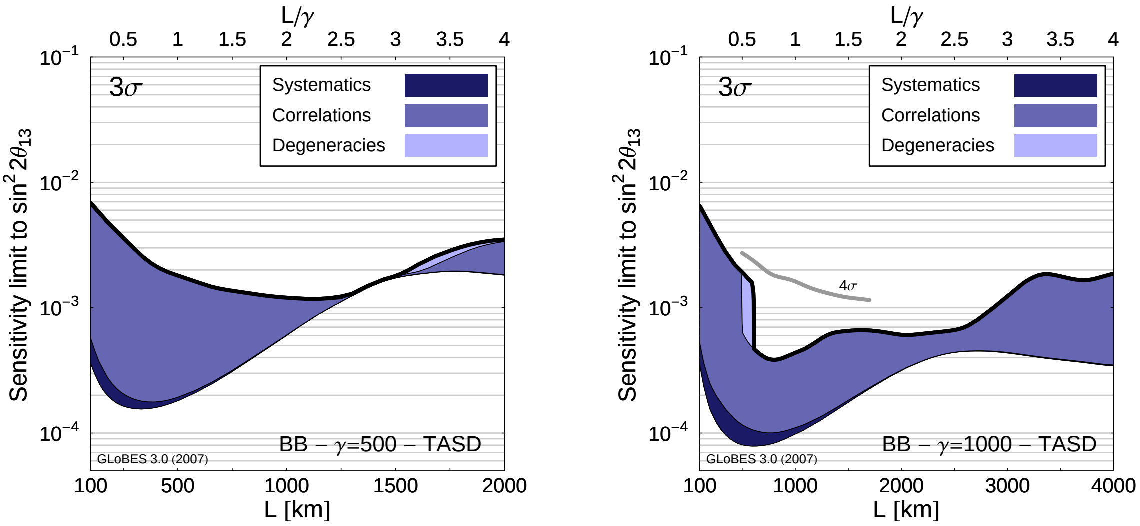

Figure 7.2: The sensitivity limit to $\sin^2 2\theta_{13}$ at a β-Beam at the 3σ confidence level as a function of the baseline L for fixed $\gamma = 500$ (left) and $\gamma = 1000$ (right). The plots are for a Totally Active Scintillator detector with a fiducial mass of 50 kt. The bands indicate the influence of systematics, correlations, and degeneracies and the final sensitivity limit is indicated by the uppermost thick black line.

correlations and degeneracies can be completely resolved and the final limit is found extremely close to the pure statistical and systematical limit. This result was already observed in [186]. The reason is, that not only the first oscillation maximum deviates from the maximum of the convolution of cross sections and neutrino flux but the second oscillation maximum enters the analysis window from lower energies and events from both, the first *and* the second oscillation maximum can be observed at once and correlations and degeneracies are resolved at a very powerful level. In the appendix of [186] this is visualized on a binned event rate level of the analysis window. At even larger baselines the first oscillation maximum leaves the neutrino energies of the neutrino flux and only events from the second oscillation maximum can be observed. Hence, the impact of correlations and degeneracies becomes visible again which can be seen at $L \sim 550$ km for the $\gamma = 150$ scenario and at $L \sim 1100$ km for the $\gamma = 350$ scenario. Note, that the rule "the larger γ, the better" at a fixed L/γ is true for Fig. 7.1 if the left and right plot are compared at the same L/γ.

Now let us switch the detector technology and discuss the baseline optimization for the Totally Active Scintillator detector scenarios at medium $\gamma = 500$ and $\gamma = 1000$. In Fig. 7.2 the sensitivity limit to $\sin^2 2\theta_{13}$ is given as a function of the baseline L. Again, the uppermost thick black curve indicates the final sensitivity limit and the bands illustrate the effect of switching on systematical uncertainties, correlations, and degeneracies. The left plot for the case $\gamma = 500$ shows the same qualitative behavior as the discussed Water Cherenkov scenarios. However, since the Totally Active Scintillator detector offers the better energy resolution and also the lower background (with 5% associated systematical normalization uncertainty), the impact of systematics is less visible than for the Water Cherenkov detector. Also, if the final sensitivity limit is compared to the Water Cherenkov scenario with $\gamma = 350$, one can see that they share almost the same behavior although the huge Water Cherenkov detector delivers much higher statistics, *i.e.* the better statistical limit. So, the Totally Active Scintillator detector can indeed compensate the much lower statistics by the improved energy resolution

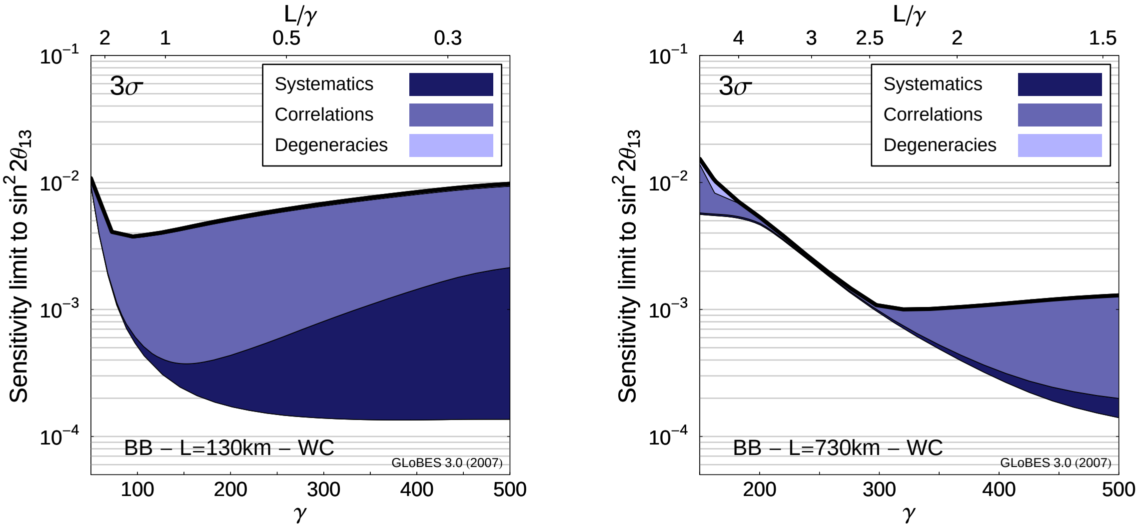

Figure 7.3: The sensitivity limit to $\sin^2 2\theta_{13}$ at a β-Beam at the 3σ confidence level as a function of γ for the fixed baselines $L = 130$ km (left) and $L = 730$ km (right). The plots are for a Water Cerenkov detector with a fiducial mass of 500 kt. The bands indicate the influence of systematics, correlations, and degeneracies and the final sensitivity limit is indicated by the uppermost thick black line.

and signal/background ratio when it comes to resolving the correlations and degeneracies.

By regarding the right plot of Fig. 7.2, a slightly different behavior of the sensitivity limit can be observed. First, the correlations and degeneracies have a remaining effect at baselines, where events from both, the first and second oscillation maximum can be observed. However, still the effect is much smaller than for other baselines and the combination of first and second oscillation maximum helps in resolving the correlations and degeneracies. The second visual difference is the behavior at the first oscillation maximum at $L \sim$800 km where now the optimal final sensitivity limit can be obtained due to a jump by half an order of magnitude at $L \sim$600 km. This behavior is well known from the simulation of Neutrino Factory experiments and will also occur in the next chapter when these are discussed. The effect arises from the phenomenology of the $(\theta_{13}, \delta_{\rm CP}$-degeneracy) that appears at larger fit values of $\sin^2 2\theta_{13}$ as a local minimum in the χ^2-distribution while the global minimum is located at the true value $\sin^2 2\theta_{13} = 0$. For two example scenarios, this local degenerate minimum in the χ^2-distribution can be nearly identical but once slightly above and once slightly below the chosen confidence level, *i.e.* it can or cannot be excluded at that confidence level. Consequently the two example scenarios, although almost identical in the performance, would be attributed with quite different $\sin^2 2\theta_{13}$ sensitivity limits separated by half or more of an order of magnitude. Thus, the visible jump at $L \sim$600 km in the right plot of Fig. 7.2 has to be treated very carefully when it comes to interpretation. In order to illustrate this effect, the sensitivity limit at the 4σ confidence level is also indicated in the plot by the thick grey line between 500 km$\lesssim L \lesssim$2000 km. It is obvious, that the huge improvement of the final limit at the 3σ level is not robust and vanishes already at 4σ. Hence, the interpretation has to be, that the true performance of the $\gamma = 1000$ scenario does indeed not change so dramatically in that range as could be naively deduced from the 3σ curve.

As already mentioned, not only the baseline can be optimized at a β-Beam experiment but additionally the γ can be tuned to an optimal value for fixed baselines. This issue will now be discussed, since there exist selected baselines that have been proposed for β-Beam experiments due to existing or planned cavities that could accommodate the detector in relation to already existing accelerator infrastructure. This can for instance be the $L = 130$ km CERN-Frejus baseline where a low γ β-Beam already is suggested and discussed since Frejus is considered as a possible location of a megaton Water Cherenkov detector. Also, the distance between the CERN and the Gran Sasso laboratories of $L = 730$ km was already discussed for a β-Beam experiment. The authors of [179] suggested a medium γ β-Beam with a Water Cherenkov detector to be a very promising candidate. We will adopt this baseline, since it is also the approximate distance between the FermiLab and the Soudan mine, *i.e.* the baseline of the operating MINOS experiment.

The sensitivity limit to $\sin^2 2\theta_{13}$ as a function of the γ for these two baselines is illustrated in Fig. 7.3 with a considered Water Cherenkov detector. Again, the parameter L/γ is labeled at the upper x-axis. The effect of systematics, correlations and degeneracies is visualized by the colored bands and the final sensitivity limit that takes these into account is the uppermost thick black line. As can be seen for the left $L = 130$ km scenario, the optimal limit is achieved at $\gamma \sim 100$, which is indeed the planned and discussed γ-value for the so-called CERN β-Beam baseline scenario (CERN-MEMPHYS, [187, 234]). A further observation from the left plot of Fig. 7.3 is the effect, that the statistical limit remains constant for increasing $\gamma > 200$. The reason is, that the expected increasing number of events (higher cross sections) is exactly compensated by the decrease of the oscillation probability at higher energies. However, the effect of systematical uncertainties increases dramatically for higher γ values due to the fact that the neutral-current background with 5% associated normalization uncertainty increases due to the higher cross sections at higher energies but is not affected by the oscillation probability. As a result also the final sensitivity limit becomes worse again for larger values of γ. The $L = 730$ km scenario in the right plot of Fig. 7.3 reaches its optimal sensitivity limit at $\gamma \sim 300$ but although it gets slightly worse for larger values it essentially qualitatively stays the same although the statistical optimum is not present until $\gamma \sim 500$ where the reliability of our β-Beam description in the simulation decreases. For values of $200 \lesssim \gamma \lesssim 300$ the correlations and degeneracies loose their impact. This is the same effect as in the baseline optimization plots, because here when adjusting γ, *i.e.* to smaller values, the events from the second oscillation maximum can be observed together with events from the first oscillation maximum. Note, that the ordering of the oscillation maxima is mirrored in comparison to the baseline optimization plots. The region, where second and first oscillation maximum events coincide can also be observed in the corresponding illustration for the Totally Active Scintillator detector scenarios in Fig. 7.4 for smaller γ ($\gamma < 300$ for $L = 730$ km and $\gamma < 600$ for $L = 1500$ km, both at $L/\gamma > 2.5$). Here, again, the CERN-Gran Sasso baseline of $L = 730$ km is discussed and also an even higher baseline of $L = 1500$ km where a better sensitivity to mass hierarchy can be expected in later discussions. For the $L = 730$ km scenario, the final limit stays almost independent of γ at $\sin^2 2\theta_{13} \sim 10^{-3}$ in the range $300 \lesssim \gamma \lesssim 800$. For even higher values of γ, the limit improves smoothly by half an order of magnitude. Here, the (θ_{13},δ_{CP})-degeneracy gets resolved (since not disconnected from the true solution, it is treated as correlation in the plot)[4]. However, the resolving of the

---

[4] The change-over is smooth because the $(\theta_{13}, \delta_{\mathrm{CP}})$-degeneracy for this β-Beam scenario does not appear as a second local minimum in the $\Delta\chi^2$ distribution at a larger fit value of $\sin^2 2\theta_{13}$ but rather turns out to appear in the shape of a plateau that is located at higher $\Delta\chi^2$ values for higher γ scenarios. Consequently there is no jump in the $\sin^2 2\theta_{13}$ limit like it is observed for most long baseline scenarios as for instance at Neutrino

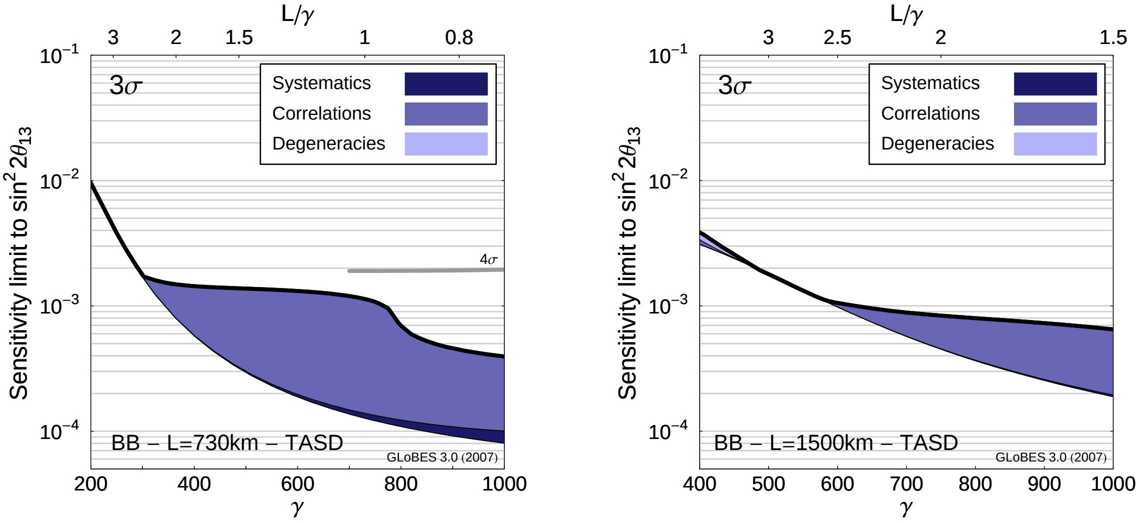

Figure 7.4: The sensitivity limit to $\sin^2 2\theta_{13}$ at a β-Beam at the 3σ confidence level as a function of γ for the fixed baselines $L = 730$ km (left) and $L = 1500$ km (right). The plots are for a Totally Active Scintillator detector with a fiducial mass of 50 kt. The bands indicate the influence of systematics, correlations, and degeneracies and the final sensitivity limit is indicated by the uppermost thick black line.

$(\theta_{13}$,$\delta_{\mathrm{CP}})$-degeneracy is not very robust as was already the case for the right plot of Fig. 7.2. If one considers the 4σ confidence level the effect vanishes and the final limit does not change significantly for increasing γ up to $\gamma = 1000$. This can be seen from the thick grey line in the left plot of Fig. 7.4 in the range $700 < \gamma < 1000$ which indicates the sensitivity limit to $\sin^2 2\theta_{13}$ at the 4σ confidence level.

The discussion of the optimization of the sensitivity limit to $\sin^2 2\theta_{13}$ resulted in the insight that usually the best performance is gained at a ratio of $1.5 \lesssim L/\gamma \lesssim 2.5$. There the final sensitivity stays nearly the same, so that for the optimization in terms of θ_{13} the exact value of L/γ seems not to be enormously crucial. Only for very high γ scenarios there exists the possibility to achieve better performances at lower $L/\gamma \sim 1$ since the $(\theta_{13}, \delta_{\mathrm{CP}})$-degeneracy can partially be resolved. However, this effect is not very robust in terms of the confidence level and vanishes at the 4σ confidence level. We observed that the low γ regime with a Water Cherenkov detector at baselines $L \sim 100 - 300$ km seems most suitable to reach sensitivity limits at $\sin^2 2\theta_{13} \sim (1 - 2.5) \cdot 10^{-3}$, while the medium γ scenarios could achieve robust sensitivity limits down to $\sin^2 2\theta_{13} \sim 10^{-3}$ independent of the used detector technology. The Totally Active Liquid Scintillator detector could compensate the disadvantage of considerable less statistics by the better background rejection and energy resolution. In order to push the sensitivity limit below $\sin^2 2\theta_{13} \sim 10^{-3}$ a high γ scenario is required.

Sensitivity to CP violation

The discovery of CP violation in the lepton sector is widely considered as one of the most important goals to be achieved at future neutrino oscillation experiments. Hence, optimizing in terms of best sensitivity to CP violation, *i.e.* the phase δ_{CP}, is a very important issue.

Factory experiments.

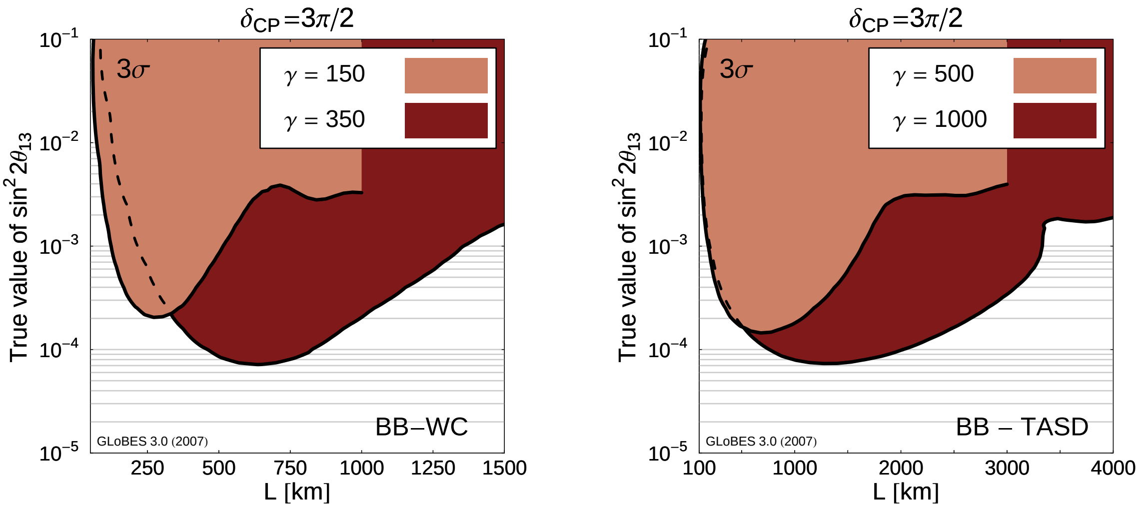

Figure 7.5: The sensitivity to *maximal* CP violation at a β-Beam at the 3σ confidence level as a function of the baseline L for the assumed true value $\delta_{\rm CP} = 3\pi/2$. The left-hand side is for a 500 kt Water Cerenkov detector at the fixed values $\gamma = 150$ and $\gamma = 350$. The right-hand side is for a 50 kt Totally Active Scintillator detector at the fixed values $\gamma = 500$ and $\gamma = 1000$. Systematics, correlations and degeneracies are taken into account.

In principle, CP violation is present in neutrino oscillation as soon as the neutrino mixing matrix U is complex, *i.e.* the parameter $\delta_{\rm CP}$ is not realized at the values $\delta_{\rm CP} = 0$ or $\delta_{\rm CP} = \pi$. Consequently, an experiment optimized in terms of CP violation should be able to exclude the values $\delta_{\rm CP} = 0$ or $\delta_{\rm CP} = \pi$ in a largest possible extent in the true parameter space (here: the true $(\sin^2 2\theta_{13}, \delta_{\rm CP})$-plane, since the other true values are chosen at their best-fit values). To avoid the huge computational effort that would be required by a scanning of the full true $(\sin^2 2\theta_{13}, \delta_{\rm CP})$-plane, we will stick to the optimization of the sensitivity to *maximal* CP violation. Sensitivity to *maximal* CP violation is defined as the interval of true values of $\sin^2 2\theta_{13}$, where the maximal CP violating values $\delta_{\rm CP} = \pi/2$ and $\delta_{\rm CP} = 3\pi/2$ can be excluded at the 3σ confidence level including systematics, correlations, and degeneracies. Sensitivity to *maximal* CP violation however gives already a good hint for the overall performance considering the search for CP violation. The most important questions that arise are, to which smallest true values of $\sin^2 2\theta_{13}$ maximal CP violation can be established and if degeneracies spoil the sensitivity to *maximal* CP violation at intermediate true values of $\sin^2 2\theta_{13}$. As in the previous subsection we will focus on the optimization of either the baseline L or the isotope acceleration γ while the respective other parameter is kept fixed at a selected value.

First, we consider the sensitivity to *maximal* CP violation optimization in terms of baseline for the Water Cerenkov β-Beam scenarios with low $\gamma = 150$ and $\gamma = 350$ and the Totally Liquid Scintillator β-Beam scenarios at medium $\gamma = 500$ and high $\gamma = 1000$. This is illustrated in Fig. 7.5 for the true value assumption $\delta_{\rm CP} = 3\pi/2$. The corresponding sensitivity to *maximal* CP violation with the assumption of true $\delta_{\rm CP} = \pi/2$ is not shown here, since the behavior is very similar to the plots shown in Fig. 7.5. The most remarkable observation is, that neither of the considered scenarios suffers from degeneracies at intermediate true values of $\sin^2 2\theta_{13}$ and sensitivity to *maximal* CP violation is established in a connected interval from $\sin^2 2\theta_{13} = 10^{-1}$ down to a respective minimal value. Furthermore, for each of the considered

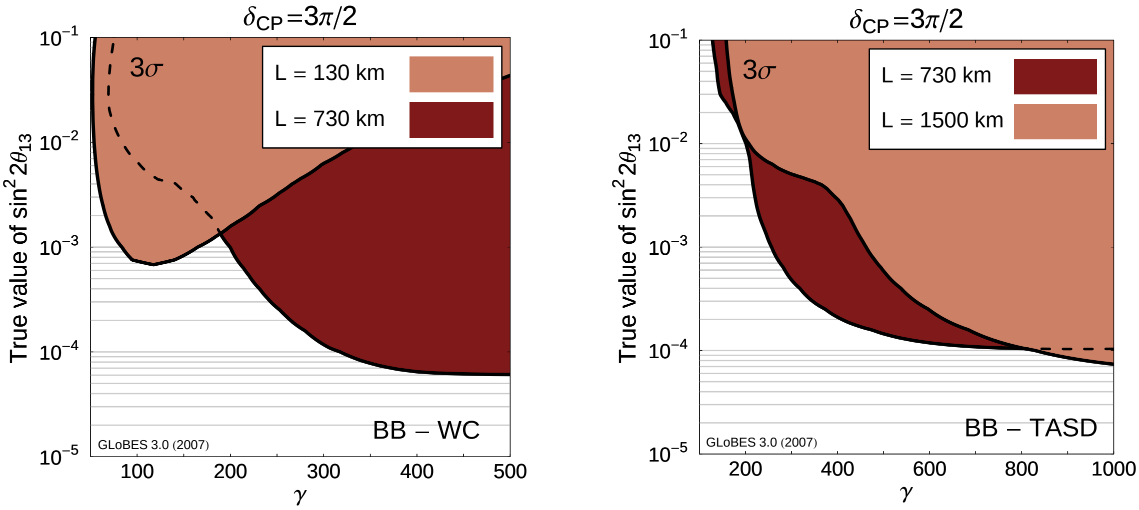

Figure 7.6: The sensitivity to *maximal* CP violation at a β-Beam at the 3σ confidence level as a function of γ for normal hierarchy assumed and the true value $\delta_{\mathrm{CP}} = 3\pi/2$. The left-hand side is for a 500 kt Water Cerenkov detector at the fixed baselines $L = 130$ km and $L = 730$ km. The right-hand side is for a 50 kt Totally Active Scintillator detector at the fixed baselines $L = 730$ km and $L = 1500$ km. Systematics, correlations and degeneracies are taken into account.

scenarios there is a clear optimal baseline for the discussed values of γ. The β-Beam with a Water Cherenkov detector gives the best sensitivity at L$\sim$250 km in case of $\gamma = 150$ and L$\sim$600-700 km in case of $\gamma = 350$, both at L/$\gamma \sim 1.7$. The Totally Active Scintillator detector scenarios achieve the best performance at slightly smaller values of L/$\gamma \sim 1.3 - 1.4$, at L$\sim$ 700 km for $\gamma = 500$ and L$\sim$ 1300 km for $\gamma = 1000$. Note, that the optimal potential by also considering correlations and degeneracies lies, as was also the case for the sensitivity limit to $\sin^2 2\theta_{13}$, slightly beyond the baselines where the best statistical performance can be achieved (L/$\gamma \sim 1$ in case of the sensitivity limit to $\sin^2 2\theta_{13}$). The effects of the second oscillation maximum can be observed for the $\gamma = 150$ scenario at a baseline of L$\sim$ 800 km where a local best performance can be read off. However, the first oscillation maximum provides a much better sensitivity by one order of magnitude.

Now, we will address the optimization of the sensitivity to *maximal* CP violation in terms of γ at the same selected fixed baselines as in the last subsection. This is illustrated in Fig. 7.6 for both detector technologies, Water Cherenkov (left-hand side) and Totally Active Scintillator detector (right-hand side). Again, we only show the sensitivity for the true value assumption of $\delta_{\mathrm{CP}} = 3\pi/2$ since the sensitivity under the assumption $\delta_{\mathrm{CP}} = \pi/2$ follows nearly the same evolution. As could already be seen for the sensitivity to θ_{13}, the increasing γ improves the sensitivity to δ_{CP} up to certain values and then seems to stay at one particular level without significant modifications where the higher cross sections at higher γ are compensated by the decrease of the oscillation probability. This means, that the minimal acceleration that should be realized would be $\gamma \gtrsim 350$ for the Water Cherenkov detector at L=730 km, and for the Totally Active Scintillator detectors $\gamma \gtrsim 400$ for L=730 km and $\gamma \gtrsim 800$ for L=1500 km. For these three scenarios, the effect of the second oscillation maximum can be observed as a plateau at lower γ. Only the Water Cherenkov scenario at the CERN-Frejus baseline shows a clear optimum sensitivity to δ_{CP} at $\gamma \sim 100 - 150$.

For larger acceleration values the sensitivity deteriorates again. The reason is, as could already be observed for the θ_{13} sensitivity, the increasing neutral-current background that is independent of the oscillation probabilities since they are flavor blind. Note, that also with varied baseline for none of the considered β-Beam scenarios arises a problem with degeneracies at medium true values of $\sin^2 2\theta_{13}$ that could spoil the sensitivity to *maximal* CP violation.

It turned out, that the question of β-Beam optimization in terms of $\delta_{\rm CP}$ sensitivity does not deviate significantly from the optimization in terms of $\sin^2 2\theta_{13}$, so that there is no trade-off needed to optimize in respect of both parameters, $\delta_{\rm CP}$ and $\sin^2 2\theta_{13}$. Of course, this does not appear to be very surprising since for both performances, resolving the same $(\theta_{13}, \delta_{\rm CP})$-degeneracy is the important issue in case of a β-Beam experiment. The low γ Water Cherenkov detector scenario covers the sensitivity range down to true $\sin^2 2\theta_{13} \sim 10^{-3}$ and is therefore a direct competitor of possible upgraded Superbeam experiments such as for example the possible T2K-upgrade T2HK that also involves a megaton Water Cherenkov detector which was found to also cover a $\delta_{\rm CP}$ sensitivity range down to values $\sin^2 2\theta_{13} \sim 10^{-3}$ [198]. However, since the β-Beam does not suffer from beam intrinsic backgrounds it should provide a slightly better performance. A comparison with the T2HK experiment will be presented in later sections. The medium and high γ scenarios will be able to establish sensitivity to *maximal* CP violation down to $\sin^2 2\theta_{13} \sim 10^{-4}$, which is the performance level of a dedicated Neutrino Factory experiment as will be revealed in the next chapter. The gain from the medium γ scenarios going to a high γ scenario is not significant and it can be expected that medium γ scenarios are completely satisfactory for measurements of θ_{13} and $\delta_{\rm CP}$ and going to a less feasible high γ is not justified until a β-Beam is required to also enable considerable abilities when it comes to the determination of the mass hierarchy that requests larger baselines.

Sensitivity to Mass Hierarchy

The third important goal at a future neutrino oscillation experiment is the determination of the mass ordering of the neutrino mass eigenstates, *i.e.* normal or inverted mass hierarchy. We will discuss the optimization of the sensitivity to mass hierarchy of the β-Beam scenarios in terms of the baseline L and γ. The sensitivity to mass hierarchy is given for a pair of true values $\sin^2 2\theta_{13}$ and $\delta_{\rm CP}$, if the sign-degenerated solution, *i.e.* the solution fitted with the wrong $\Delta m^2_{31} < 0$ since normal hierarchy is assumed, can be excluded at the chosen confidence level. The possibility to determine the mass hierarchy is connected to the matter effect and hence it is expected that larger baselines are required to establish an adequate sensitivity to mass hierarchy. In further discussions the whole parameter plane of true $\sin^2 2\theta_{13}$ and $\delta_{\rm CP}$ will be scanned, but for the optimization discussion we will concentrate on the selected true values $\delta_{\rm CP} = \pi/2$ and $\delta_{\rm CP} = 3\pi/2$ and only true $\sin^2 2\theta_{13}$ will be scanned to keep the computational effort at a reasonable level. The most important question will be, as for the last subsection, to which smallest true values of $\sin^2 2\theta_{13}$ the mass hierarchy can be determined and if degeneracies spoil the sensitivity to the sign of Δm^2_{31} at intermediate true values of $\sin^2 2\theta_{13}$.

The optimization issue of the baseline L is illustrated in Fig. 7.7 where the sensitivity to mass hierarchy at the 3σ confidence level is shown for the Water Cherenkov low $\gamma = 150$ and medium $\gamma = 350$ scenarios in the upper row and the Totally Active Scintillator scenarios with medium $\gamma = 500$ and high $\gamma = 1000$ in the lower row. The left column is for $\delta_{\rm CP} = \pi/2$ and the right column is for $3\delta_{\rm CP} = \pi/2$, since different evolutions can be observed. It

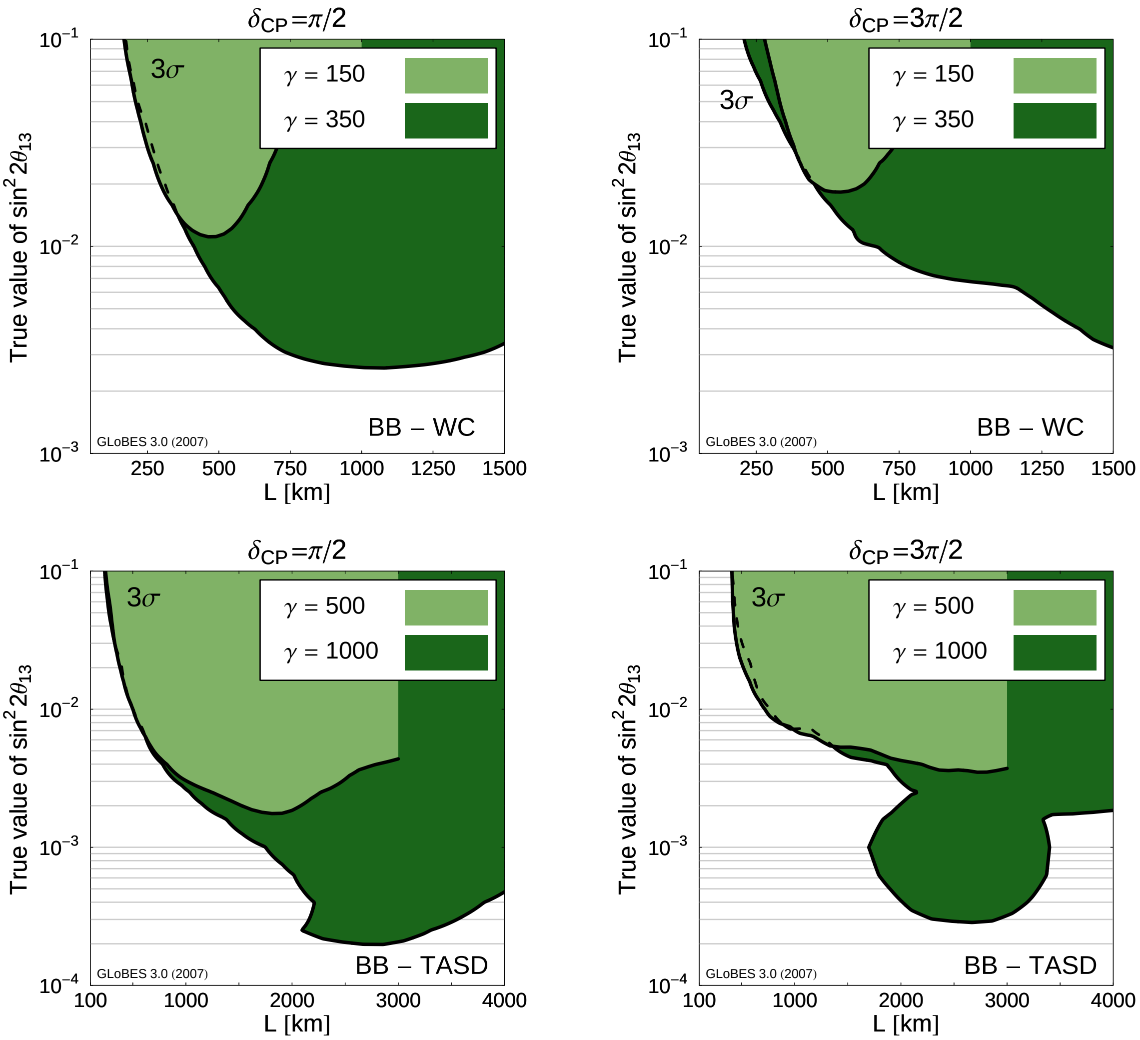

Figure 7.7: The sensitivity to mass hierarchy at a β-Beam at the 3σ confidence level as a function of the baseline L for fixed γ and the assumed true values $\delta_{\rm CP} = \pi/2$ (left column) and $\delta_{\rm CP} = 3\pi/2$ (right column). The upper row plots are for a megaton Water Cherenkov detector with a fiducial mass of 500 kt at fixed $\gamma = 150$ and $\gamma = 350$. The lower row plots are for a Totally Active Scintillator detector with a fiducial mass of 50 kt at fixed $\gamma = 500$ and $\gamma = 1000$.

can be read off, that the low γ scenario does not possess good abilities to determine the mass hierarchy and only a small window of baselines at L$\sim$ 500 km (L/γ $\sim$ 3.3) allows a determination to still very large values of $\sin^2 2\theta_{13} \sim 10^{-2}$ which is not competitive to the medium or high γ scenarios. Again, we observe, that the performance of the medium γ scenarios share a similar performance and the higher statistics at a Water Cherenkov detector cannot outperform a Totally Active Scintillator detector with better background rejection and energy resolution abilities. Also, it can be observed, that there is no striking optimal baseline since the optimization depends on the true value of $\delta_{\rm CP}$. However, it can be deduced, that at least baselines above L/γ $\sim 1.6 - 1.7$ should be chosen (L$\gtrsim$ 600 km for $\gamma = 350$ and L$\gtrsim$ 800 km for $\gamma = 500$). We observe that no correlations or degeneracies spoil the sensitivity to mass hierarchy at intermediate true values $\sin^2 2\theta_{13}$. This picture changes if the high γ scenario is investigated. Here only a smaller window of baselines is favored: 2500 km $\lesssim$ L $\lesssim$ 3500 km. The evolution as a function of γ is not smooth anymore and there appear regions, where sensitivity is lost due to correlations and degeneracies. It appears, that in the range 1000 km $\lesssim$ L $\lesssim$ 2000 km the sensitivity is lost in small parts of the $\sin^2 2\theta_{13}$ parameter space. At baselines L$\sim$2000km the sensitivity to mass hierarchy acquires a gap of sensitivity loss for intermediate $\sin^2 2\theta_{13} \sim 2 \cdot 10^{-3}$ whereas it is restored again for smaller values of $\sin^2 2\theta_{13}$ in the case of $\delta_{\rm CP} = 3\pi/2$ (lower right plot in Fig. 7.7). For this choice of $\delta_{\rm CP}$ the sensitivity gets lost again for baselines L$\gtrsim$ 3500 km for the smallest true values of $\sin^2 2\theta_{13}$. However, in the favored baseline window 2500 km $\lesssim$ L $\lesssim$ 3500 km this scenario can establish sensitivity to mass hierarchy down to $\sin^2 2\theta_{13} \sim (2-3) \cdot 10^{-4}$. This window translates to 2.5 $\lesssim$ L/γ $\lesssim$ 1.5 which is unfortunately far off the optimal baseline range for measurements of $\delta_{\rm CP}$. Hence, in order to have optimal abilities in both, search for $\delta_{\rm CP}$ and the mass hierarchy, a two detector scenario with Totally Active Scintillator detectors at two different baselines should turn out as the optimal scenario. Scenarios with only one detector cannot be able to optimize performance for both performance aspects.

Finally, we will address the γ optimization for the sensitivity to mass hierarchy in Fig. 7.8. Now, the dependency of the sensitivity to the sign of Δm^2_{31} on the isotope acceleration factor γ is illustrated for selected baselines. The upper row shows the performance of the Water Cherenkov detector scenarios at $L = 130$ km and $L = 730$ km while the Totally Active Scintillator detector scenarios at $L = 730$ km and $L = 1500$ km are considered in the lower row. The $L = 130$ km scenario suffers from a total lack of sensitivity to the mass hierarchy at any chosen value of γ, so this scenario is only able to provide information on $\sin^2 2\theta_{13}$ and $\delta_{\rm CP}$. Hence, it can be optimized just with respect to these two parameters. Furthermore, if the upper and lower row plots are compared, the medium baseline scenarios share a very similar performance independent of the detector technology as turned out to be true already for the performances if considering θ_{13} and $\delta_{\rm CP}$. The higher baseline of $L = 1500$ km only provides a small increase in the performance which is not surprising, because it was observed in Fig. 7.7 that only in the window of 2500 km $\lesssim$ L $\lesssim$ 3500 km very good sensitivities to the mass hierarchy can be achieved.

When it comes to a comparison of the performance of β-Beam scenarios with Neutrino Factory experiments, the sensitivity to mass hierarchy will be crucial point for the most dedicated[5] β-Beam scenarios to compete with the Neutrino Factory that provides for very good abilities in determining the mass hierarchy due to the very high baselines of several thousands of kilometers. It is clear, that low γ β-Beam scenarios cannot compete at all with a Neutrino Factory on this issue and have to be seen as very powerful alternatives to upgraded Superbeams such as T2HK in the search for $\sin^2 2\theta_{13}$ and $\delta_{\rm CP}$. While medium γ scenarios provide at least some moderate capabilities in determining the mass hierarchy, the ultimate β-Beam optimization in that respect involves a detector at very large baselines 2500 km $\lesssim$ L $\lesssim$ 3500 km which collides for the realistic range of γ with the optimization with respect to $\delta_{\rm CP}$, so a two detector scenario is preferable to assure optimal performance in both aspects.

---

[5] in terms of cost intensiveness

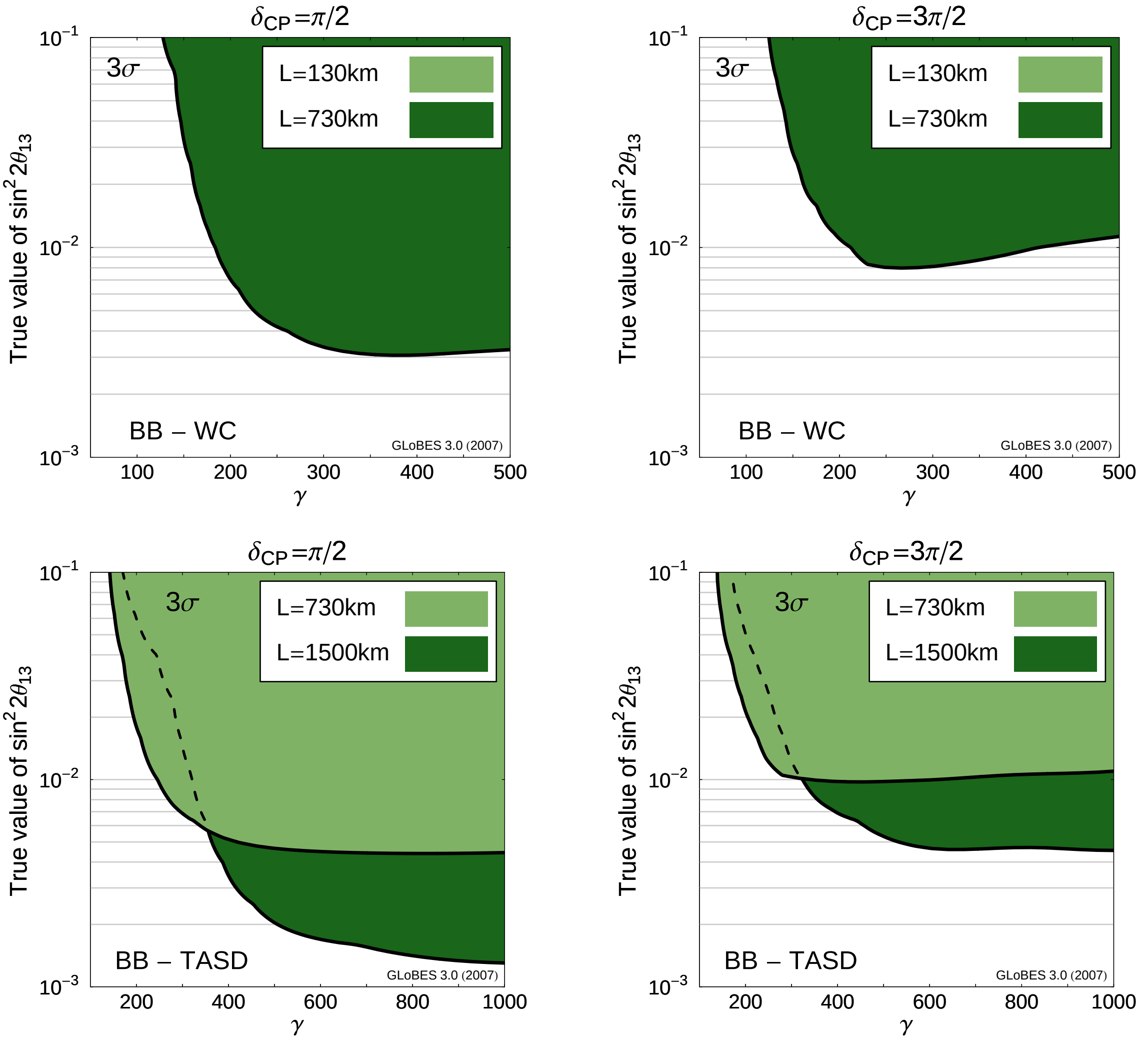

Figure 7.8: The sensitivity to mass hierarchy at a β-Beam at the 3σ confidence level as a function of γ for a fixed baseline L and the assumed true values $\delta_{CP} = \pi/2$ (left column) and $\delta_{CP} = 3\pi/2$ (right column). Normal Hierarchy is assumed. The upper plots are for a megaton Water Cherenkov detector with a fiducial mass of 500 kt at fixed $L = 130$ km and $L = 730$ km. The lower row plots are for a Totally Active Scintillator detector with a fiducial mass of 50 kt at fixed $L = 730$ km and $L = 1500$ km.

β-Beam Reference Scenarios

The last subsections focused on the independent optimization of different β-Beam scenarios in terms of baseline L and γ. We will now assign defined reference setups that follow the suggestions from the optimization discussions and provide the possibility to study the properties and performances in a greater detail. Furthermore, these defined reference setups and their abilities can be comfortably compared to reference setups of different technologies, *e.g.* Neutrino Factory setups or the Superbeam upgrade T2HK. These reference setups shall cover all three ranges of γ, low, medium and high, and the two discussed detector technologies in the compatible γ range. The definition of the reference setups is based slightly more upon the discussion of γ-optimization since the selected baselines that were discussed there are

Label	L [km]	γ	Detector	Mass (fid.) [kt]
BB100@130km	130	100	WC	500
BB150@300km	300	150	WC	500
BB350@730km	730	350	WC	500
BB500@730km	730	500	TASD	50
BB1000@730km	730	1000	TASD	50
BB1000@1500km	1500	1000	TASD	50
BB1000@2D1L	730	1000	TASD	100
BB1000@2D2L	730/3000	1000	TASD	2×50

Table 7.3: The listing of all defined reference β-Beam scenarios with low γ, medium γ, and high γ. The lowest two scenarios involve a double detector effort. The label in the left column are used throughout this work for account for the respective scenarios. The β-Beam scenarios involve two detector technologies: Water Cherenkov (WC) and Totally Active Scintillator (TASD).

based on more realistic baseline scenarios between already existing accelerator complexes and underground laboratories or at least possibilities for those. Additionally, a scenario will be introduced that makes use of two 50 kt Totally Active Scintillator at two different baselines in order to allow for Neutrino Factory competitive performance with respect to δ_{CP} *and* the determination of the mass hierarchy. Such a scenario has not been discussed in the literature, however we introduce that setup since the discussion of the optimal Neutrino Factory experiment setup will also contain considerations of scenarios with a double detector effort with two 50 kt Magnetized Iron detectors at different baselines, even with a triple detector effort[6].

We choose two low γ scenarios BB100@130km with a megaton Water Cherenkov detector at the CERN-Frejus baseline of $L = 130$ km with an optimal $\gamma = 100$ and a second low γ scenario BB150@300km with a megaton Water Cherenkov detector at a baseline of $L = 300$ km at the optimal $\gamma = 150$. Note, that $\gamma = 150$ is discussed as the maximal achievable γ for the isotopes ^{18}Ne and ^{6}He at a SPS-like accelerator machine [180]. The last choice accounts for a conceivable scenario, where a β-Beam isotope accelerator machine could included to the infrastructure at J-PARC in Japan and use a possible Hyper-Kamiokande detector. Hence it also is not to be considered as a green-field scenario. As medium γ scenarios we introduce one for each detector technology: BB350@730km locates a megaton Water Cherenkov detector at a baseline $L = 730$ km and $\gamma = 350$ and the corresponding medium γ scenario with a 50 kt Totally Active Scintillator detector at a baseline of $L = 730$ km and $\gamma = 500$ is called BB500@730km. The high γ reference scenarios share the acceleration factor $\gamma = 1000$ and only the Totally Active Scintillator detector technology is discussed, once at a baseline $L = 730$ km and once at $L = 1500$ km. The two detector high $\gamma = 1000$ scenario BB1000@2D2L is defined with two detectors at two different baselines $L = 730$ km and $L = 3000$ km where the latter shall provide optimal abilities to determine the mass hierarchy. In order to address the improvement of the second baseline properly, a second double detector scenario BB1000@2D1L is defined that centers the double detector effort at one baseline $L = 730$ km and the same $\gamma = 1000$. The complete listing of all defined reference β-Beam scenarios and their main features is resumed in Table 7.3.

---

[6] Note, that recently it was suggested to utilize a β-Beam at the magic baseline with different parent isotopes [188] which also gives the opportunity to improve the sensitivity the the mass hierarchy. This scenario would also imply a two-detector scenario to additionally provide sensitivity to CP violation.

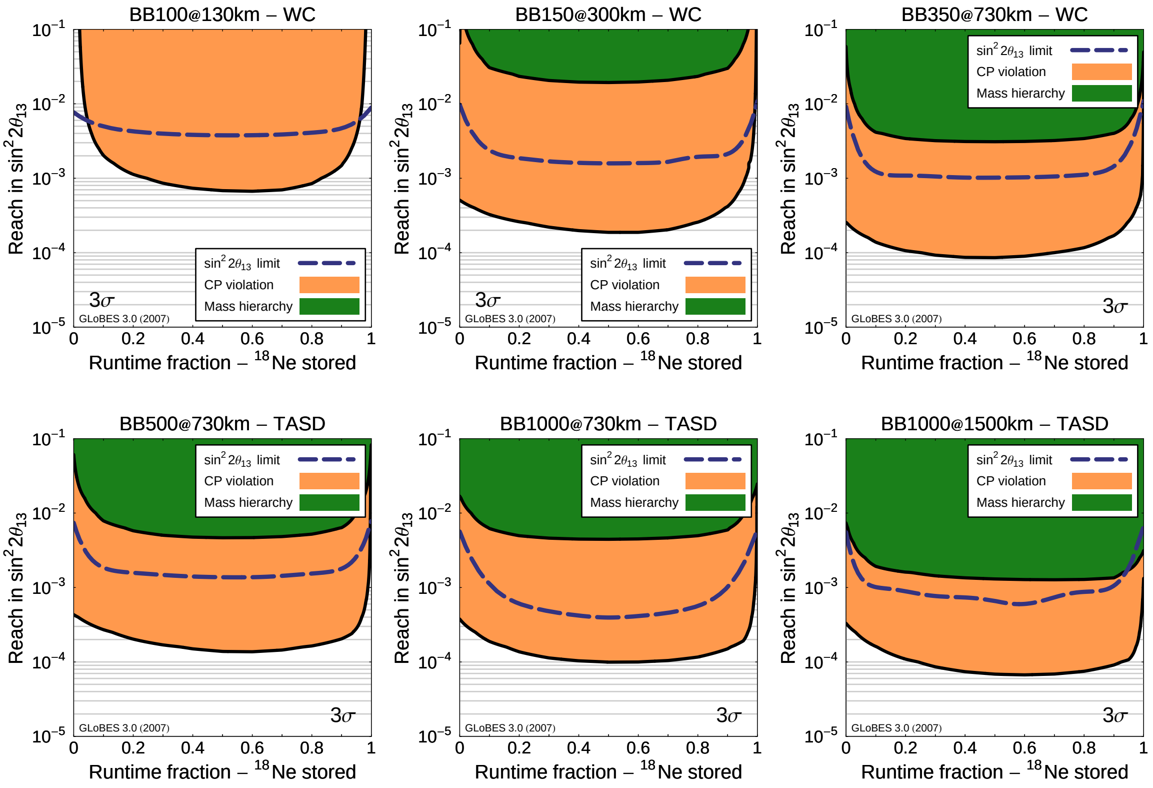

Figure 7.9: The impact of the ratio of neutrino and anti-neutrino runtime at a β-Beam on the sensitivity limit to $\sin^2 2\theta_{13}$ (left), the sensitivity to *maximal* CP violation (middle), and sensitivity to the mass hierarchy (right) at the 3σ confidence level respectively. The total runtime is 8 years and divided into a runtime fraction of ^{18}Ne stored (labeled on the x-axis) and the runtime fraction of ^{6}He stored. In each plot the right edge represents neutrino running only and the left edge represents anti-neutrino running only. The upper row is for the β-Beam scenarios with a 500kt Water Cherenkov detector BB100@130km, BB150@300km, and BB350@730km. The lower row is for the β-Beam scenarios with a 50kt Totally Active Liquid scintillator detector BB500@730km, BB1000@730km, and BB1000@1500km.

7.3 Neutrino and Anti-Neutrino Runtime Fraction

Up to now, we have only discussed β-Beam scenarios with an equal splitting into neutrino and anti-neutrino runtime. Since the cross sections are higher for neutrinos, this results in a higher amount of event rates for neutrinos compared to anti-neutrinos. So the question arises, if the performance of β-Beam experiments can be optimized by modifying the ratio of the runtime fraction of neutrinos and anti-neutrinos. The total runtime of the experiment still is assumed to be 8 years. Clearly, the comparison of neutrino and anti-neutrino rates is required to observe CP violation or determine the neutrino mass hierarchy. Also, for the sensitivity to $\sin^2 2\theta_{13}$ the comparison is used to resolve the parameter correlations and degeneracies. So it is expected, that pure neutrino or anti-neutrino running should give the worst performances.

The dependence of the neutrino/anti-neutrino runtime ratio when considering the performance indicators sensitivity limit to $\sin^2 2\theta_{13}$, sensitivity to *maximal* CP violation, and sensitivity to mass hierarchy is shown in Fig. 7.9 for all six optimized β-Beam scenarios, Water Cherenkov (upper row) and Totally Active Scintillator detector (lower row). The x-axis indicates the neutrino runtime fraction $f(^{18}Ne)$, *i.e.* the fraction of the phase with ^{18}Ne isotopes stored in the storage rings compared to the total runtime of the experiment. The anti-neutrino runtime fraction $f(^{6}He)$, *i.e.* the phase with ^{6}He isotopes stored in the storage ring is the given by $f(^{6}He) = 1 - f(^{18}Ne)$. Thus, the left edge of the respective plots describes the performance with anti-neutrino running only and the right edge describes the performance with pure neutrino running. The middle position of each plot with $f(^{18}Ne) = f(^{6}He) = 0.5$ corresponds to the scenarios discussed up to now with an equal amount of runtime for neutrinos and anti-neutrinos. As expected the performance drops visibly to the outer regions of the respective plots. However, for neutrino runtime fraction $0.2 \lesssim f(^{18}Ne) \lesssim 0.8$ the performances for all three discussed performance indicators are approximately independent of the actual ratio between neutrino and anti-neutrino runtime. There could be a slight individual optimization for the scenarios, but it turns out that appointing an equal runtime of neutrinos and anti-neutrinos is on average the best choice and has not to be modified. Consequently, throughout the rest of this work we will stick to the assumption of $f(^{18}Ne) = f(^{6}He) = 0.5$ and keep the equal runtimes for neutrinos and anti-neutrinos.

The results from Fig. 7.9 can also interpreted in such a way, that the performance of the β-Beam does not depend so crucially on the requirement that the number of isotope decays per year has to be achieved as planned. If, for some reason, for one of the isotopes the planned number of decays per year can not be technically feasible and a lower number turns out to be realistic, this could be compensated by an increase of the number of decays of the other isotope (see [235] for issues of feasibility).

7.4 Addition of T2K Disappearance Data

It was mentioned before, that the leading atmospheric parameters $\sin^2 2\theta_{23}$ and Δm^2_{31} cannot be measured at a β-Beam experiment itself. This clearly distinguishes a β-Beam experiment from a Neutrino Factory or even Superbeams where information on the leading atmospheric parameters can be obtained by the observation of the ν_μ-disappearance, whereas at a β-Beam experiment only the disappearance of ν_e could be measured in addition to the appearance data. Since the corresponding disappearance is driven by the parameters $\sin^2 2\theta_{13}$ and Δm^2_{31} there cannot be extracted any information on $\sin^2 2\theta_{23}$. Furthermore, since the amplitude is $\sin^2 2\theta_{13}$, which is known to be small, the usefulness of the ν_e-disappearance data depends crucially on the systematical uncertainties. This effect is known very well from reactor experiments where $\overline{\nu}_e$-disappearance is observed and the achievable sensitivity to $\sin^2 2\theta_{13}$ is limited by the systematical uncertainties concerning for instance the reactor flux normalization, the cross sections, the fiducial volumes of the detector or even bin-to-bin errors like uncertainties in the reactor flux spectrum. It is well known, that these uncertainties have to be kept at the order of 1% or below to improve the current limits on $\sin^2 2\theta_{13}$ [155]. However, at beam experiments like at a β-Beam it is hardly achievable to arrive at such low systematical uncertainties. In fact, the assumption of 2.5% uncertainty on the number of signal events has already to be viewed as slightly optimistic. Consequently, it is not to be expected that the performance of a β-Beam is affected by the inclusion of the disappearance data. Although this is not explicitly shown in this work, we checked that indeed all later discussed β-Beam scenarios arrive at the same $\sin^2 2\theta_{13}$, δ_{CP}, and mass hierarchy sensitivities, whether the disappearance data is included or not.

Thus, neither $\sin^2 2\theta_{23}$ nor Δm^2_{31} can be measured at a β-Beam experiment. It was previ-

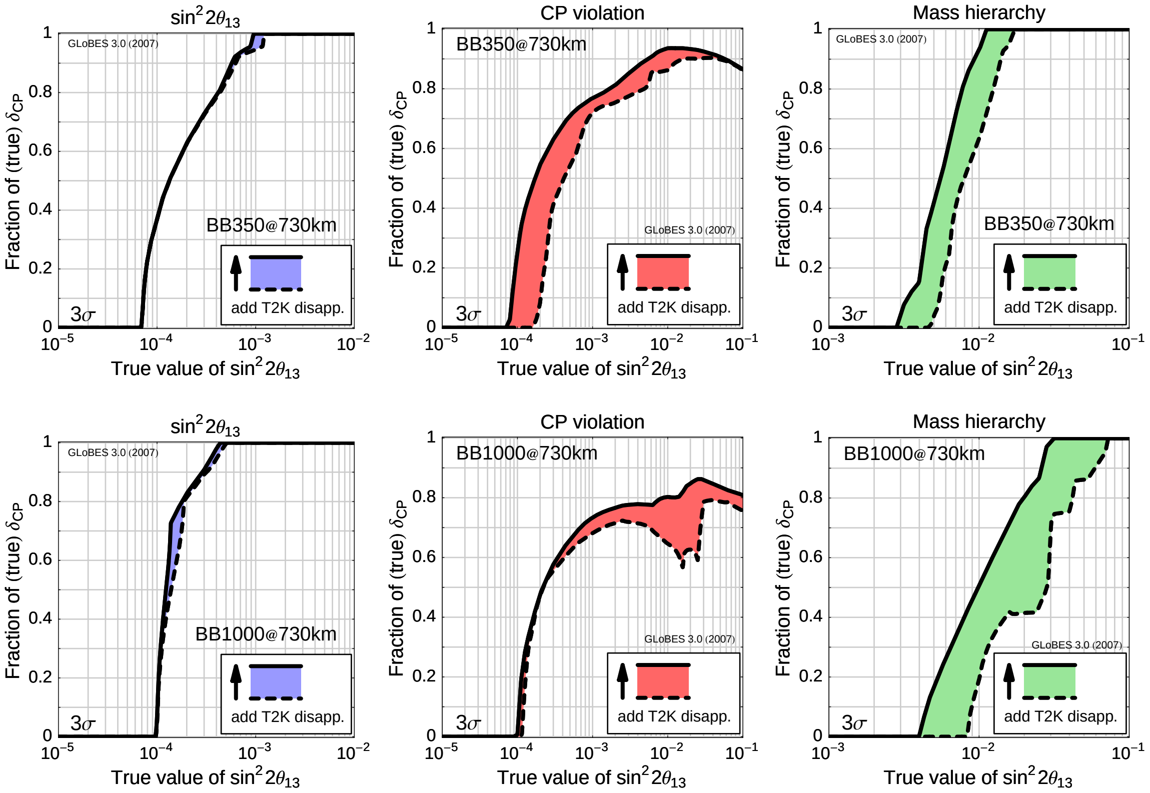

Figure 7.10: The impact of the addition of T2K disappearance data to the β-Beam data on the $\sin^2 2\theta_{13}$ discovery reach (left), the sensitivity to *any* CP violation (middle), and sensitivity to the mass hierarchy (right). The fraction of the true values of δ_{CP} of all possible values in the interval $[0, 2\pi[$ where the respective sensitivity is given at the 3σ confidence level is displayed as a function of the true value of $\sin^2 2\theta_{13}$. The dashed line represents the respective sensitivities *without* the T2K disappearance data included and the solid line represents the respective sensitivities *with* the T2K disappearance data included. The T2K appearance data is neglected so the impact is solely caused by the higher precision on the leading atmospheric parameters, *i.e.* correlations with $\sin^2 2\theta_{23}$ and Δm^2_{31} are reduced. The upper row is for the β-Beam scenarios with a 500 kt Water Cherenkov detector BB100@130km, BB150@300km, and BB350@730km. The lower row is for the β-Beam scenarios with a 50 kt Totally Active Liquid scintillator detector BB500@730km, BB1000@730km, and BB1000@1500km.

ously shown, that the $\nu_e \to \nu_\mu$ appearance channel suffers from correlations and degeneracies if information on the parameters $\sin^2 2\theta_{13}$ and δ_{CP} is to be extracted. The parameter correlations also involve the leading atmospheric parameters. Hence, the fact that they cannot be measured at a β-Beam experiment also limits the ability to measure $\sin^2 2\theta_{13}$, δ_{CP}, and the mass hierarchy. However, at the time, the β-Beam data will be analyzed the leading atmospheric parameters will be known at a better precision than today, since the disappearance data of Superbeam experiments like T2K or NOνA will improve the measurements from atmospheric data of Super-Kamiokande or the conventional beam experiments like MINOS or the CNGS experiments. Therefore we include the T2K disappearance data to all β-Beam simulations. For the simulation of the T2Kdisappearance data, a modified version of the pre-defined experiment describing file `T2K.glb` of the GLoBES package is used[7]. The appearance data of

---

[7] The modification involves only the exclusion of the appearance data. All other properties of `T2K.glb` are kept unchanged.

T2K is excluded so that all sensitivities to $\sin^2 2\theta_{13}$, δ_{CP}, and the mass hierarchy are solely obtained from the β-Beam appearance data. The same technique has already been used in the β-Beam simulations in ([186, 236]).

The impact of the inclusion of the T2K disappearance data is exemplary shown in Fig. 7.10 for the discovery reach in $\sin^2 2\theta_{13}$ (left plot), sensitivity to *any* CP violation (middle plot), and sensitivity to mass hierarchy (right plot) for the a selected β-Beam scenario with a Water Cherenkov detector in the upper row (BB350@730km) and one with a Totally Active Scintillator detector in the lower row (BB1000@730km). In each plot, the dashed line depicts the performance for the β-Beam scenarios alone without the T2K disappearance data. The improvement of the inclusion of the T2K disappearance data is indicated by the grey shaded area up to the solid line that indicates the performance of the β-Beam scenarios if the T2K disappearance data is included to the analysis. The discovery reach in $\sin^2 2\theta_{13}$ turns out to be quite robust for both the considered β-Beam scenarios, but the sensitivities to *any* CP violation and mass hierarchy are indeed strongly improved by the inclusion of the T2K disappearance data.

7.5 γ-Scaling of the Isotope Decays

We have already mentioned that the number of decays per year is most likely not constant in γ. In order to include this effect, we use the following power law parameterization, which should be justified for a certain γ-range, to describe this scaling with γ ($i = 1$ for ^{18}Ne: neutrinos, $i = 2$ for ^{6}He: anti-neutrinos):

$$N^i = N_0^i \cdot \left(\frac{\gamma_0^i}{\gamma}\right)^n \tag{7.1}$$

Here N_0^i is determined by our reference point at $\gamma_0^1 = 100$, $\gamma_0^2 = 60$. We can now discuss different cases for n, which leads to different optimization strategies:

- $n = 0$: The number of decays per year is fixed. This implies that the accelerator and storage ring has to scale appropriately with γ in a non-trivial manner.
- $0 < n < 1$: This seems to be the most likely range of realistic cases. The number of decays per year becomes constrained with increasing γ by the geometry of the accelerator and decay ring and γ increased lifetime of the isotopes in the laboratory system.
- $n \sim 1$: This case corresponds to a fixed setup constraining the performance. A realistic constraint for the SPS would be, for example, $n \sim 1$ from the number of merges in the decay ring and the number of ions per bunch [235].
- $n > 1$: In this case, it clearly does not make sense to go to higher γ's, since the event rate decreases with γ if we stay in the oscillation maximum
- $n < 0$: The number of decays per year increases with γ. This hypothetical (but technologically unlikely) possibility requires that the accelerator and decay ring over-proportionally scale with γ.

We further on consider the range $0 \lesssim n \lesssim 1$ to be realistic. However, it is conceivable that, for a given setup, the performance will scale with $n \simeq 0$ in the beginning, and change into an

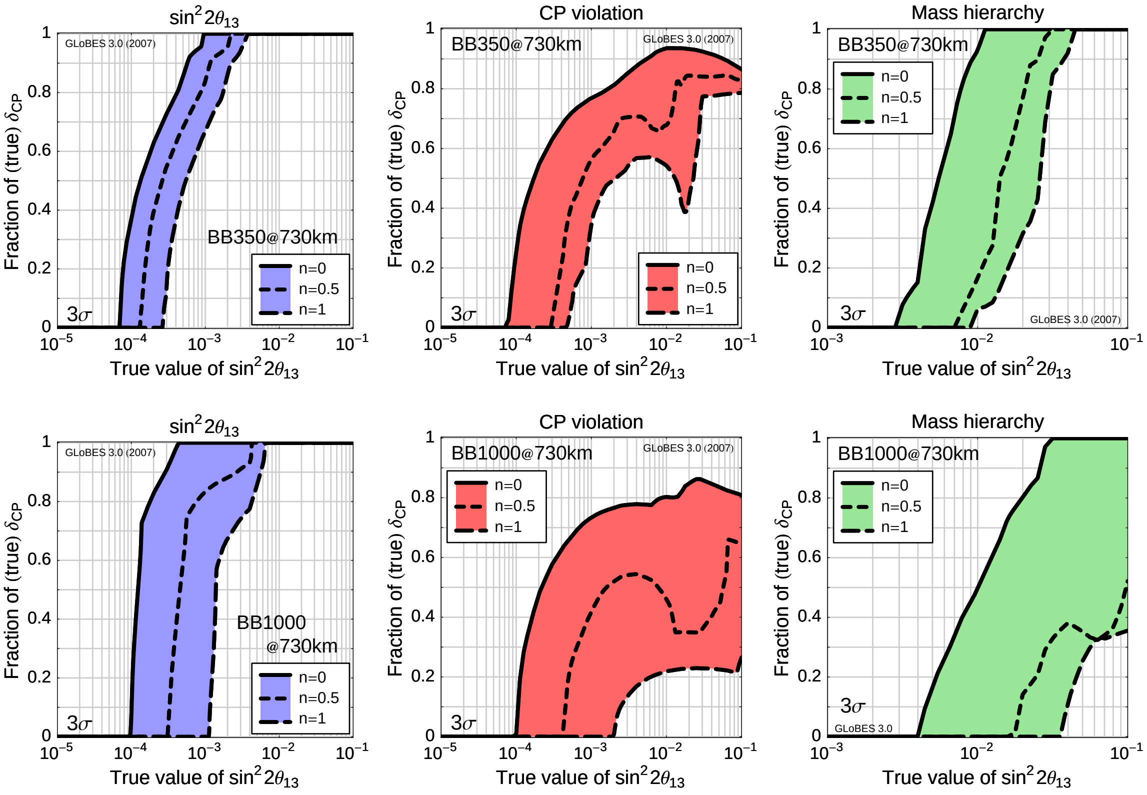

Figure 7.11: The impact of the γ-scaling of the number of isotope decays per year at a β-Beam on the $\sin^2 2\theta_{13}$ discovery reach (left), the sensitivity to *any* CP violation (middle), and sensitivity to the mass hierarchy (right). The fraction of the true values of δ_{CP} of all possible values in the interval $[0, 2\pi[$ where the respective sensitivity is given at the 3σ confidence level is displayed as a function of the true value of $\sin^2 2\theta_{13}$. The number of isotope decays per year is not treated as constant but as a function of γ. It is effectively described by an exponent n so that the number of isotope decays scales with $(1/\gamma)^n$ (see text for details). The band indicates the impact of the γ-scaling where the exponent n is varied from $n = 0$ (solid line, standard assumption) over $n = 0.5$ (short-dashed line) to $n = 1$ (long-dashed line). The upper row is for the β-Beam scenarios with a 500 kt Water Cherenkov detector BB100@130km, BB150@300km, and BB350@730km. The lower row is for the β-Beam scenarios with a 50 kt Totally Active Liquid scintillator detector BB500@730km, BB1000@730km, and BB1000@1500km.

$n \simeq 1$ scaling in the saturation regime. In case of $n \sim 1$ the γ-scaling would counteract the effect of higher statistics due to higher cross sections at higher energies. The cross sections increase linearly with the neutrino energies that are proportional to γ but the number of isotope decays would exactly compensate the effect by the scaling with $1/\gamma$. In this case only low γ β-Beams are conceivable since medium and high γ β-Beams additionally require larger baselines to cover the oscillation maximum and introduce an effective loss in statistics due to the additional baseline scaling of the events with $1/L^2$.

We show in Fig. 7.11 the γ-scaling of the performance indicators discovery reach in $\sin^2 2\theta_{13}$ (left), sensitivity to *any* CP violation (middle), and sensitivity to the mass hierarchy (right) for the medium γ Water Cherenkov β-Beam BB350@730km (upper row) and the high γ Totally Active Scintillator β-Beam BB1000@730km (lower row). The bands indicate the impact of the γ-scaling describing parameter $0 \leq n \leq 1$. The solid upper curves are for $n = 0$ which corresponds to the assumption throughout the rest of this work, while the dashed lines imply a γ scaling with $n = 0.5$ (short-dashed curves) and $n = 1$ (long-dashed curves). The low γ β-Beams are not shown here, because it can be expected that the γ-scaling has no big impact since the discussed values of γ are close to the reference values γ_0^i. The effect that the impact of a possible γ-scaling increases with γ can also be observed in Fig. 7.11 by comparing the upper and lower rows. Clearly, the high γ scenario BB1000@730km suffers more severe from the γ-scaling than the medium γ scenario BB350@730km. However, also the performance of BB350@730km is strongly limited if the number of isotope decays cannot be guaranteed by either injecting a larger number of parent isotopes into the storage ring or adjust the architecture of the storing ring.

7.6 Performance of the β-Beam Reference Scenarios

The aim of this section is to compare the performance of the optimized reference β-Beam scenarios that have been introduced in Section 7.2. We will focus on the respective abilities to discover a non-zero θ_{13}, CP violation, and determine the mass hierarchy in the range from large $\sin^2 2\theta_{13}$ to very small $\sin^2 2\theta_{13}$. The goal is to compare the abilities of the possible β-Beam scenarios that involve low, medium, and high γ acceleration of the stored isotopes and different detector technologies. The performances of the reference setups are shown in Fig. 7.12. The left column represents the discovery reach in $\sin^2 2\theta_{13}$, the middle column represents the sensitivity to *any* CP violation, and the right column represents the sensitivity to mass hierarchy, each at the 3σ confidence level. The rows correspond to different detector efforts. The first row involves a megaton Water Cherenkov detector and the optimized low and medium γ scenarios. The second row involves a 50 kt Totally Active Scintillator detector that allows for higher neutrino energies and compares the optimized meed medium and high γ scenarios. The lowest row represents β-Beam scenarios that involve a double detector effort, *i.e.* two 50 kt Totally Active Scintillator detectors. The performance is furthermore compared with the performance of an upgraded Superbeam experiment T2HK*[8] that is indicated by the grey area in the plots. Note, that the comparison with T2HK* is most interesting for the Water Cherenkov β-Beam scenarios in the first row, since the detector effort is the same since also T2HK* involves a megaton Water Cherenkov detector, in case of BB150@300km actually at a similar baseline.

So, let us first discuss the Water Cherenkov β-Beam scenarios in the first row of Fig. 7.12. It can be observed that the scenarios BB100@130km and BB150@300km do not have significant abilities to determine the neutrino mass hierarchy due to the relatively small baselines. Also T2HK* does not show better sensitivity to the sign of Δm^2_{31}. The medium γ scenario BB350@730km on the other hand is able to determine the mass hierarchy in the large regime of $\sin^2 2\theta_{13} > 10^{-2}$ for 100% of all possible values of δ_{CP}. If one considers the sensitivity to CP violation the performance of the β-Beams increases with γ and the medium γ scenario BB350@730km shows excellent sensitivity. For $\sin^2 2\theta_{13} \sim 10^{-2}$ this scenario can establish CP violation already for more than 90% of all possible values of δ_{CP}. Note, that 100% cannot be reached since CP violation cannot be excluded for values near the CP conserving values $\delta_{\mathrm{CP}} = 0$ and $\delta_{\mathrm{CP}} = \pi$. So, BB350@730km is able to perform δ_{CP} measurements at very

---

[8] The simulation is performed with the GLoBES experiment file `T2HK.glb` provided with the GLoBES 3.0 package [220] but the fiducial volume is modified to 500 kt instead of 440 kt to be comparable at a fair with the β-Beam scenarios that involve a Water Cherenkov detector. The modification is indicated by the star following the notation from [186] since this is the same scenario that was used there. Further details of the experiment description are given in the GLoBES manual [223].

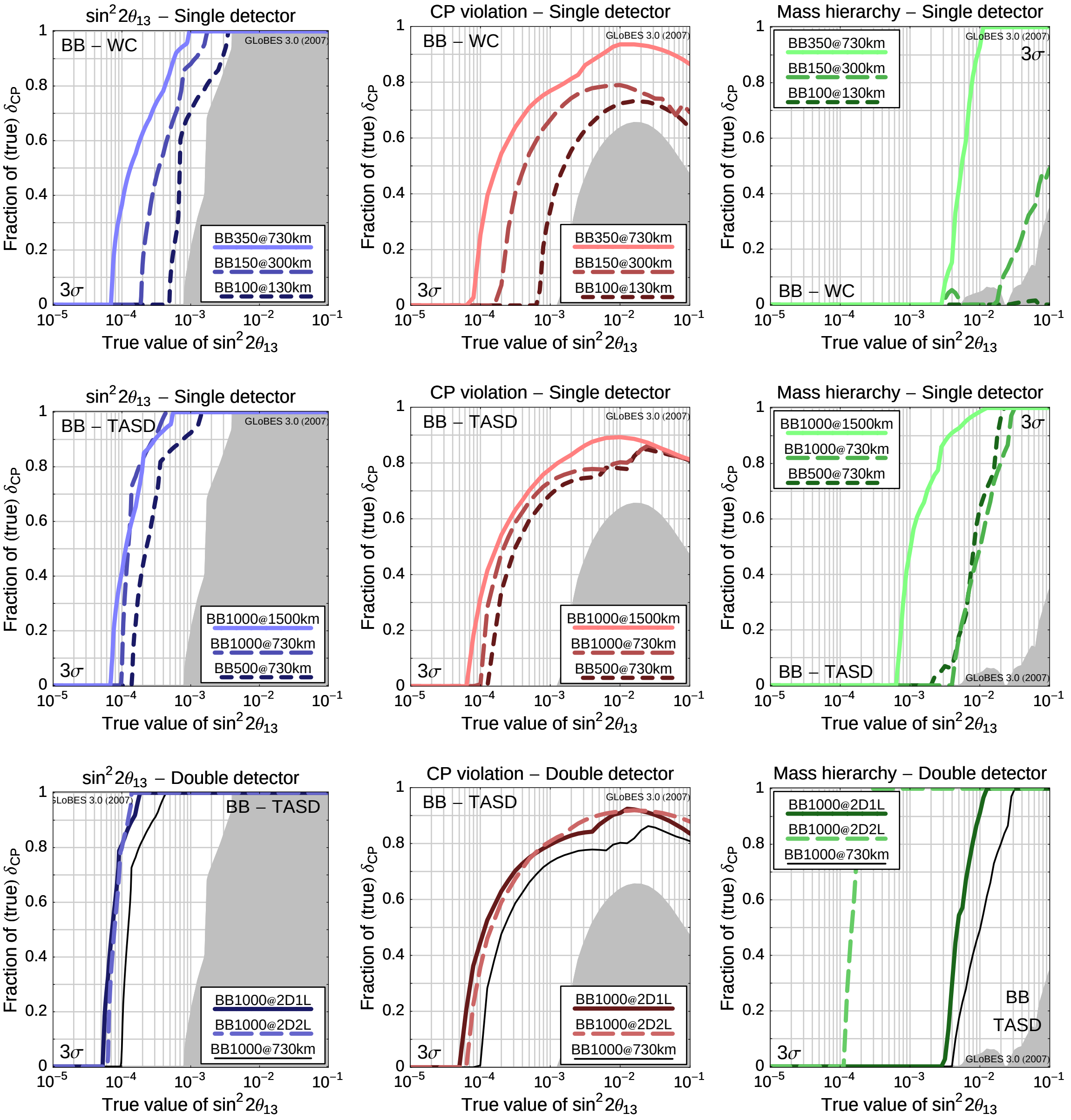

Figure 7.12: The comparison of the performance of all β-Beam reference scenarios for the performance indicators $\sin^2 2\theta_{13}$ discovery reach (left column), sensitivity to *any* CP violation (middle column), and sensitivity to the mass hierarchy (right column). The fraction of the true values of δ_{CP} of all possible values in the interval $[0, 2\pi[$ where the respective sensitivity is given at the 3σ confidence level is displayed as a function of the true value of $\sin^2 2\theta_{13}$. The upper row is for the β-Beam scenarios with a 500 kt Water Cherenkov detector, the middle row is for the β-Beam scenarios with a 50 kt Totally Active Scintillator detector and the lower row is for the β-Beam scenarios with a double detector effort (only Totally Active Scintillator detector technology assumed). The grey area indicates the respective performance of the upgraded Superbeam scenario T2HK* for reasons of comparison.

good accuracy. The ability to establish CP violation at this scenario reaches down to values $\sin^2 2\theta_{13} \sim 10^{-4}$. The low γ scenarios show better performance than the Superbeam upgrade T2HK* since they are not limited by the intrinsic beam background. The same picture manifests for the discovery reach in $\sin^2 2\theta_{13}$. Also here, the performance apparently improves for increasing γ and all scenarios outperform the upgraded Superbeam. The outcome is, that already the low γ β-Beams show better performances than an upgraded Superbeam like T2HK* although they utilize the exact same detector effort. Also, we can conclude that a low γ β-Beam that involves a megaton Water Cherenkov detector is more justified to be placed at a baseline at about L=300 km, since the same detector is used and going from $\gamma = 100$ to $\gamma = 150$ is no huge leap and can already be achieved at an accelerator machine of the size of the SPS.

The second row of Fig. 7.12 deals with the performance of medium and high γ β-Beams and a Totally Active Scintillator detector. The main difference to the first row is that the Totally Active Scintillator lacks a lot of statistics compared to the Water Cherenkov detector, but with better energy resolution and background rejection. If one considers the discover reach in $\sin^2 2\theta_{13}$ going from medium to high γ does only slightly improve the performance and the different baselines of BB500@730km and BB1000@730km do not change the picture significantly. Also for the sensitivity to CP violation the three Totally Active Scintillator detector scenarios do not differ to great extend. Only around $\sin^2 2\theta_{13} \sim 10^{-2}$ BB1000@730km covers approximately 10% more of the $\delta_{\rm CP}$ parameter space. A very important observation is that the high γ scenario does not perform better in CP violation measurements than the medium γ scenario BB350@730km in the first row. Hence, the optimization of a β-Beam in terms of $\delta_{\rm CP}$ sensitivity does not necessarily require a high γ scenario and a medium γ β-Beam can already achieve the very similar performance. Only the mass hierarchy determination requires the high γ scenarios at large baseline. However, the L=1500 km still does not provide the performance for a determination for $\sin^2 2\theta_{13} < 10^{-3}$.

As was found in Section 7.2, excellent abilities in determining the mass hierarchy require a baseline L∼3000 km which on the other hand is not optimal for $\delta_{\rm CP}$ measurements. So, a β-Beam scenario that is optimized in both aspects involves two baselines. This is shown in the lower row of Fig. 7.12. There the performance of the high γ scenario BB1000@2D2L with two 50 kt Totally Active Scintillator detectors at L=1500 and L=3000 km is illustrated. To highlight the synergetical effects, in addition a double detector scenario BB1000@2D1L has been introduced that involves the double detector effort at the same baseline L=1500 km and the improvement in the performance is only due to doubled statistics. Thus, wherever the scenario BB1000@2D2L performs better, true synergetical effects are observed that cannot be attributed to the higher statistics of the double detector effort. The thin black line shows the corresponding single detector scenario BB1000@730km in order to show the improvement by adding a second detector. It turns out that for the discovery reach in $\sin^2 2\theta_{13}$ and the sensitivity to CP violation, the improvement of the second baseline allows for no synergies and the effect is very similar to just a doubled statistics at the same baseline. But the sensitivity to mass hierarchy is significantly pushed. BB1000@2D2L allows for a determination of the sign of Δm^2_{31} in 100% of the $\delta_{\rm CP}$ parameter space down to $\sin^2 2\theta_{13} \sim 2 \cdot 10^{-4}$. So, this β-Beam scenario is optimized for excellent abilities in measurements of $\delta_{\rm CP}$ and the mass hierarchy, while the single detector scenarios have to undergo a trade-off. The performance of BB1000@2D2L will be competitive in terms of mass hierarchy determination to the Neutrino Factory scenarios that will be discussed in the next chapter.

Chapter 8

Neutrino Factory Performance

The goal for this Chapter is to estimate and optimize the performance of a possible Neutrino Factory experiment for measurements of $\sin^2 2\theta_{13}$, the phase δ_{CP}, and the sign of Δm^2_{31}. First, we will introduce the simulation methods that have been used to analyze the physics potential of the Neutrino Factory. Next, the possible optimization in terms of neutrino energy and the experiment baseline L are addressed. Thereafter single technical aspects and possible impacts on the physics potential are discussed, before optimized reference scenarios with different ambitious detector effort are defined and the potential is compared. Furthermore, the performance of these reference setups is compared to optimized β-Beam reference scenarios in Chapter 9. Note, that we do not discuss the abilities of a Neutrino Factory experiment to find deviations from maximal atmospheric mixing $\sin^2 2\theta_{23} = 1$. A detailed study on this topic can be found in [237].

8.1 Neutrino Factory Simulation

All Neutrino Factory simulations throughout this work are performed with the GLoBES software [220] that is briefly introduced in the appendix.

Standard Golden Channel

As our "standard neutrino factory", we use the definition NuFact-II from Ref. [198] with some modifications that we will discuss below. This setup uses $1.06 \cdot 10^{21}$ useful muon decays per year and a total running time of four years in each polarity (corresponding to $5.3 \cdot 10^{20}$ useful muon decays per year and polarity for a simultaneous operation with both polarities). The detector is a Magnetized Iron detector with a fiducial mass of 50 kt located in a distance L from the source. We allow the baseline L and the muon energy E_μ to vary within a reasonable range. In the standard setup, we only include the ν_μ appearance and disappearance channels (for neutrinos and anti-neutrinos), where we assume that the best information on the leading atmospheric parameters is determined from the experiment's own disappearance channels.

Compared to the NuFact-II setup from Ref. [198], we split the raw dataset into two samples: One with charge identification (CID), the other without, where the dataset with charge identification is used for the appearance channel and modeled according to Ref. [198]. It turns out to be useful *not* to use the CID information for the disappearance channels (*cf.*, Ref. [238]). This allows to use also the low energy bins with full efficiency, which maximizes

Disappearance – μ^+-stored			σ_{norm}	σ_{cal}
Signal	$0.9 \otimes (\bar{\nu}_\mu \to \bar{\nu}_\mu)_{\mathrm{CC}}$	$0.9 \otimes (\nu_e \to \nu_\mu)_{\mathrm{CC}}$	0.025	10^{-4}
Background	$1.0 \cdot 10^{-5} \otimes (\bar{\nu}_\mu \to \bar{\nu}_x)_{\mathrm{NC}}$		0.2	10^{-4}
Appearance – μ^+-stored				
Signal	$0.45 \otimes (\nu_e \to \nu_\mu)_{\mathrm{CC}}$		0.025	10^{-4}
Background	$5.0 \cdot 10^{-6} \otimes (\bar{\nu}_\mu \to \bar{\nu}_x)_{\mathrm{NC}}$	$5.0 \cdot 10^{-6} \otimes (\bar{\nu}_\mu \to \bar{\nu}_\mu)_{\mathrm{CC}}$	0.2	10^{-4}
Disappearance – μ^--stored				
Signal	$0.9 \otimes (\nu_\mu \to \nu_\mu)_{\mathrm{CC}}$	$0.9 \otimes (\bar{\nu}_e \to \bar{\nu}_\mu)_{\mathrm{CC}}$	0.025	10^{-4}
Background	$1.0 \cdot 10^{-5} \otimes (\nu_\mu \to \nu_x)_{\mathrm{NC}}$		0.2	10^{-4}
Appearance – μ^--stored				
Signal	$0.35 \otimes (\bar{\nu}_e \to \bar{\nu}_\mu)_{\mathrm{CC}}$		0.025	10^{-4}
Background	$5.0 \cdot 10^{-6} \otimes (\nu_\mu \to \nu_x)_{\mathrm{NC}}$	$5.0 \cdot 10^{-6} \otimes (\nu_\mu \to \nu_\mu)_{\mathrm{CC}}$	0.2	10^{-4}

Table 8.1: The signal efficiencies and background rejection factors together with the associated systematical errors for the signal and backgrounds used in our description of the performance of the standard golden channel measurement. The normalization errors are the normalization error σ_{norm} and the energy calibration error σ_{cal}. This corresponds to the golden channel in the `NFvar.glb` file that is provided with GLOBES 3.0.

the oscillatory signal. The price one has to pay for that is that the neutrino and antineutrino rates have to be added in this case, which is not a major problem for the disappearance channel [239]. However, as pointed out in Ref. [238], the higher event rates at low energies may lead to relatively fast oscillations especially for long baselines, which can lead to problems for large muon energies and small bin numbers. Therefore, we change the binning and use 43 bins in total.[1] In addition, we use the filter feature from GLoBES in order to average any fast oscillations already on the probability level over a width of 150 MeV.[2] We have tested that this choice appropriately describes the low energy range where the first significant events enter in order to allow muon energies up to about 100 GeV in combination with baselines up to about 9000 km. Since we do not use CID in the disappearance channel, we use the MINOS efficiencies and threshold from Refs. [119, 140] in this channel. Note that we now have two different energy threshold functions. The fact that there are almost no events below about 4 GeV in the appearance channel is appropriately modeled.[3] Finally, we choose 2.5% for the signal normalization errors, 20% for the background normalization errors, and $\sigma_E = 0.15\, E_\nu$ for the energy resolution. The signal efficiencies and background rejection factors that are used in our description of the standard golden channel are summarized in Table 8.1. There, additionally the assumptions of the systematical uncertainties are given.

---

[1] We use 43 variable bins from 1 GeV to E_μ: 18 bins of $\xi \times 500\,\mathrm{MeV}$, 10 bins of $\xi \times 1\,\mathrm{GeV}$, and 15 bins of $\xi \times 2\,\mathrm{GeV}$ from the lowest to the highest energy, where $\xi = (E_\mu - 1)/49$ is an overall scale factor ($\xi = 1$ correspond to the "canonical" 50 GeV neutrino factory).

[2] We use the energy resolution type 2 to compensate for this additional energy smearing; *cf.*, GLoBES manual [223].

[3] For details on the shape of the appearance channel threshold function, the efficiencies, and model of the energy resolution, see the appendix of Ref. [198].

τ-Appearance – μ^+-stored			σ_{norm}	σ_{cal}
Signal	$0.096 \otimes (\nu_e \rightarrow \nu_\tau)_{\mathrm{CC}}$		0.15	10^{-4}
Background	$3.1 \cdot 10^{-8} \otimes (\nu_e \rightarrow \nu_e)_{\mathrm{CC}}$	$2.0 \cdot 10^{-8} \otimes (\nu_e \rightarrow \nu_\mu)_{\mathrm{CC}}$	0.2	10^{-4}
	$3.7 \cdot 10^{-6} \otimes (\bar{\nu}_\mu \rightarrow \bar{\nu}_\mu)_{\mathrm{CC}}$	$1.0 \cdot 10^{-3} \otimes (\bar{\nu}_\mu \rightarrow \bar{\nu}_\tau)_{\mathrm{CC}}$	0.2	10^{-4}
	$7.0 \cdot 10^{-7} \otimes (\bar{\nu}_\mu \rightarrow \bar{\nu}_x)_{\mathrm{NC}}$	$7.0 \cdot 10^{-7} \otimes (\nu_e \rightarrow \nu_x)_{\mathrm{NC}}$	0.2	10^{-4}

Table 8.2: The signal efficiencies and background rejection factors together with the associated systematical errors for the signal and backgrounds used in our description of the performance of the standard silver channel measurement in the μ^+-stored phase. The normalization errors are the normalization error σ_{norm} and the energy calibration error σ_{cal}. This corresponds to the silver channel in the `NF_GoldSilver.glb` file that is provided with GLOBES 3.0. For the optimistic setup five times the signal efficiency and three times the background rejection factors are taken.

Silver Channel

For the silver channel, the tau neutrinos are detected which are oscillating from the electron neutrinos in the beam. Since the neutrino energies at a neutrino factory are above the tau production threshold, tau leptons can be produced in charged-current reactions. The detection of these tau leptons from the $\nu_e \rightarrow \nu_\tau$ oscillation is called "silver channel" and was already discussed in the literature [240, 241]. The observation of the produced tau leptons is not possible at the "golden" detector, which means that a second OPERA-like Emulsion Cloud Chamber (ECC) detector is assumed for the measurement. This kind of detector is capable of distinguishing the tau lepton events from other events by the observation of the decay topology of the tau decay. Our description of the silver channel follows Ref. [241]. The discussed OPERA-like ECC detector is capable of observing the decay of the charged-current produced tau leptons into muons. We incorporate an energy dependent threshold for the decay-produced muon identification. The evolution of this threshold was taken from Figure 7 in Ref. [241]. The energy resolution is assumed to be 20% $\times E$, which is also an optimistic choice. We assume silver channel data taking only during the μ^+-stored phase. We define two setups representing the current "standard" assumptions that are currently considered to be realistic and a setup based on very optimistic assumptions to show the maximal improvement potential of the additional silver channel.

- **Standard Silver Channel**
  We assume the ECC detector to have a fiducial mass of 5 kt as in Ref. [241]. In addition, we apply an overall signal efficiency of approximately 10%, which was chosen to reproduce the signal event numbers from Table 4 in Ref. [241]. The background rejection factors are taken from Ref. [241] as well, and are summarized in Table 8.2.

- **Optimistic Silver Channel**
  In the standard scenario, it was assumed, that only leptonic tau decays can be observed. But, in principle, all the other decay channels of the tau lepton might be analyzed as well, this increases the signal by a factor of five. At the same time, we assume that those improvements necessary for identifying hadronic tau decays will allow to reduce the background somewhat and hence we take only three time the value of the standard setup. Furthermore, we assume a fiducial detector mass of 10 kt which is to be considered as very demanding for the ECC technology.

Appearance – μ^+-stored			σ_{norm}	σ_{cal}
Signal	$0.2 \otimes (\bar{\nu}_\mu \rightarrow \bar{\nu}_e)_{\text{CC}}$		0.025	10^{-4}
Background	$10^{-3} \otimes (\bar{\nu}_\mu \rightarrow \bar{\nu}_\mu)_{\text{CC}}$	$5.0 \cdot 10^{-2} \otimes (\bar{\nu}_\mu \rightarrow \bar{\nu}_\tau)_{\text{CC}}$	0.2	10^{-4}
	$10^{-2} \otimes (\bar{\nu}_\mu \rightarrow \bar{\nu}_x)_{\text{NC}}$	$10^{-2} \otimes (\nu_e \rightarrow \nu_x)_{\text{NC}}$	0.2	10^{-4}
	$10^{-2} \otimes (\nu_e \rightarrow \nu_e)_{\text{CC}}$		0.2	10^{-4}

Appearance – μ^--stored			σ_{norm}	σ_{cal}
Signal	$0.2 \otimes (\nu_\mu \rightarrow \nu_e)_{\text{CC}}$		0.025	10^{-4}
Background	$10^{-3} \otimes (\mu_\mu \rightarrow \nu_\mu)_{\text{CC}}$	$5.0 \cdot 10^{-2} \otimes (\nu_\mu \rightarrow \nu_\tau)_{\text{CC}}$	0.2	10^{-4}
	$10^{-2} \otimes (\nu_\mu \rightarrow \nu_x)_{\text{NC}}$	$10^{-2} \otimes (\bar{\nu}_e \rightarrow \bar{\nu}_x)_{\text{NC}}$	0.2	10^{-4}
	$10^{-2} \otimes (\bar{\nu}_e \rightarrow \bar{\nu}_e)_{\text{CC}}$		0.2	10^{-4}

Table 8.3: The signal efficiencies and background rejection factors together with the associated systematical errors for the signal and backgrounds used in our description of the performance of the standard platinum channel measurement. The normalization errors are the normalization error σ_{norm} and the energy calibration error σ_{cal}.

Platinum Channel

Besides the previously considered channels, the neutrino beam of a neutrino factory allows to observe neutrino oscillations from the $\nu_\mu/\bar{\nu}_\mu \rightarrow \nu_e/\bar{\nu}_e$ channel, which is often called "platinum channel". This is the T-conjugated oscillation channel to the golden channel, and corresponds to the CP-conjugated golden channel with different matter effect. Therefore, it should allow to resolve the correlations and degeneracies of the golden channel measurements as well. Again, as for the silver channel, we define two different scenarios, one conservative and one optimistic. For the description of the platinum channel, we roughly follow the ν_e-appearance performance of the MINOS detector, which has been estimated in Ref. [136]. However, since we require charge identification to establish the ν_e ($\bar{\nu}_e$) appearance against the $\bar{\nu}_e$ (ν_e) disappearance from the beam, we add an extra background from these disappearance neutrinos. We assume the background after the CID selection to be 1% of all electron neutrino disappearance neutrinos. We apply a lower energy detection threshold at 0.5 GeV. Electron charge ID so far has been only studied for a magnetized liquid Argon TPC and the numbers above roughly match the ones indicated in [242]. In the same Ref. it was also pointed out that electron charge ID may have an upper threshold beyond which it may no longer be possible to measure the charge. Electrons/positrons at higher energies tend to shower early, which means that the track is too short and the curvature is hardly measurable. Therefore, the CID of electrons and positrons most likely is only possible up to a certain energy threshold.

For the platinum channel, we will always assume the same baseline as for the golden channel, since it is at least in principle conceivable to use the same detector for both golden and platinum channel. We define two setups:

- **Standard Platinum Channel**
  We assume a platinum channel detector with a fiducial mass of 15 kt, which may be the largest magnetizable volume for a liquid argon TPC. The signal efficiency is taken to be 20% [242], and the background rejection factors are summarized in Table 8.3. Furthermore, the energy resolution is assumed to be 15% $\times E$. The upper threshold for the electron/positron CID is assumed to be 7.5 GeV. The CID background is assumed to be 1% [242] and the other backgrounds are taken from Ref. [136].

- **Optimistic Platinum Channel**
  We assume a platinum channel detector with a fiducial mass of 50 kt. This choice is inspired by the possibility (at least in principle) to use the same, improved detector than for the golden channel. The signal efficiency is 40%. The background rejection factors of Ref. [136] are extrapolated to higher energies. The CID background is the same than for the standard setup. Electron/positron CID is assumed to be possible to the highest energies and no upper threshold is imposed.

Hybrid Detector for the Optimized Golden Channel

The main limitation of a neutrino factory compared to other advanced neutrino facilities comes from the fact the standard detector has a relatively high neutrino energy threshold (necessary for charge identification), which makes the first oscillation maximum basically inaccessible (*cf.*, Ref. [243]). All measurements have therefore to be performed in the high energy tail of the oscillation probability off the oscillation maximum. In different words, a neutrino factory is optimized for high statistics in the appearance channel, not for operation at the oscillation maximum. This is the reason why it seems to be the experiment most affected by the eightfold degeneracy [41, 198]. A number of solutions to this degeneracies problem has been proposed, amongst them it has been studied what a better detector in terms of a better neutrino energy threshold could achieve [198]. We will pick up this starting point and discuss improvements in the detection threshold and energy resolution in this section.

The high neutrino energy threshold in Ref. [243] is the result from optimizing for the purest possible sample of wrong sign muons, which clearly puts the emphasis on events with a high energy muon. The lower the muon energy is, the higher the likelihood to misidentify the muon charge or the nature of the event (CC vs NC) becomes. Thus the background increases with decreasing neutrino energy, since the average muon energy will decrease with the neutrino energy. The background fraction scales with the neutrino energy such as a power law with a spectral index around -2. Our background model assumes that whatever happens with the threshold will only affect events below the threshold, but not events above, *i.e.*, there is only down-feeding of background but no up-feeding. The reason behind this assumption is that a mis-identified NC event always should have a reconstructed energy which is lower than the true energy, since there is missing energy in every NC event. In order to roughly match the total background obtained in Ref. [243], we use a background fraction βE_ν^{-2} with $\beta = 10^{-3}$. Integrating this background fraction from $4\,\mathrm{GeV}$ to $50\,\mathrm{GeV}$ yields an average background fraction of $5 \cdot 10^{-6}$. We assume this background fraction separately for the background from neutral currents and wrong sign muons.

Achieving a lower threshold probably requires a finer granularity of the detector, *i.e.*, a higher sampling density in the calorimeter. This should at the same time improve the energy resolution of the detector. We use a parameterization $\sigma_E\,[\mathrm{GeV}] = \sigma\,\sqrt{E_\nu\,[\mathrm{GeV}]} + 0.085\,\mathrm{GeV}$ with $\sigma = 0.15$ for the energy resolution (as compared to $\sigma_E = 0.15\,E_\nu$ before, corresponding to $\sigma \simeq 0.5$), where the constant part models a lower limit from Fermi motion.[4] For definiteness, we take the neutrino energy threshold to be $1\,\mathrm{GeV}$, and the efficiency to be constant 0.5 for all appearance neutrino events above threshold. Similar numbers are quoted for the NOνA detector [145], which is a totally active calorimeter[5].

---

[4] For the neutrino factory, this lower limit turns out to be of secondary importance because there are practically no events in the relevant energy range.

[5] Using an air coil system similar to the one in ATLAS, it should be possible to magnetize a detector like

8.2 Neutrino Factory Optimization

After discussing the optimization of β-Beam experiments in greater detail in the last chapter we will here present the corresponding discussion considering Neutrino Factory experiments. The main properties that can be arranged are the baseline L between neutrino source and detector and secondly the associated neutrino energy that is set by the parent energy E_μ of the stored muons in the storage ring. The optimal settings are to be explored, such that the sensitivity limit to $\sin^2 2\theta_{13}$, the sensitivity to *maximal* CP violation, and the sensitivity to the mass hierarchy are most effectively optimized. Such an optimization was already performed in [236] for slightly different assumptions for the set of neutrino oscillation parameters. The main focus of this section will however lie on the baseline optimization, since the analysis in [236] showed that tuning the neutrino energy by E_μ does not lead to significant improvement of the respective sensitivities beyond parent muon energies $E_\mu \gtrsim 20 - 30$ GeV. The widely discussed standard value is $E_\mu = 50$ GeV, however a lower parent muon energy could be an effective tool to reduce the costs of the complete project and hence is also very worthwhile to be discussed. For the optimization of the Neutrino Factory setup we only consider the standard golden channel.

Sensitivity to θ_{13}

The first performance indicator that will be discussed is the sensitivity limit to $\sin^2 2\theta_{13}$ as a function of the baseline. The range of the baseline is modified between $L = 500$ km and $L = 10000$ km, so that also the magic baseline at $L \sim$7500 km is covered. Note, that even the largest discussed baseline of $L = 10000$ km still does not strike the outer core of the earth that starts approximately in a depth of 3000 km and so the neutrinos still only travel through the earth's mantle. The final sensitivity is strongly affected by systematical uncertainties and even more by the parameter correlations and degeneracies as can be seen from Fig. 8.1. As in the corresponding discussion for the β-Beam in the last chapter, these effects are indicated by the bands. The dark grey/blue band displays the impact of the systematical uncertainties to the pure statistical limit that is given by the lowermost curve. Effects of correlations are indicated by the medium grey/blue band and finally if also the degeneracies are considered, the bright grey/blue band gives the modification to the final sensitivity limit that is given by the thick black curve. The left plot of Fig. 8.1 is for a low energy Neutrino Factory scenario with a parent muon energy $E_\mu = 25$ GeV and the right plot is for a standard scenario with $E_\mu = 50$ GeV. It was checked, that an even higher energy Neutrino Factory scenario with $E_\mu = 80$ GeV gives a very similar evolution of the final sensitivity limit compared to the $E_\mu = 50$ GeV scenario. The best statistical sensitivity to θ_{13} is achieved for smaller baselines at $L \sim 2000$ km for $E_\mu = 25$ GeV and $L \sim 3000 - 4000$ km for the $E_\mu = 50$ GeV scenario. A further outcome is, that the effect of the systematical uncertainties is small compared to the effect of the parameter correlations and the degeneracies. These can spoil the final sensitivity limit by more than two orders of magnitude in $\sin^2 2\theta_{13}$ compared to the systematics only limit. For both considered parent muon energies the magic baseline and its effect is clearly visible at $L \sim$7500 km where the final limit can be pushed almost down to $\sin^2 2\theta_{13} \sim 10^{-4}$. The low energy scenario achieves the unambiguously best sensitivity to θ_{13} at the magic baseline. For the higher energy scenario with $E_\mu = 50$ GeV there exists a second baseline range, where a clearly better sensitivity can be obtained at $L \sim 4000$ km. In this small energy range the

---

this.

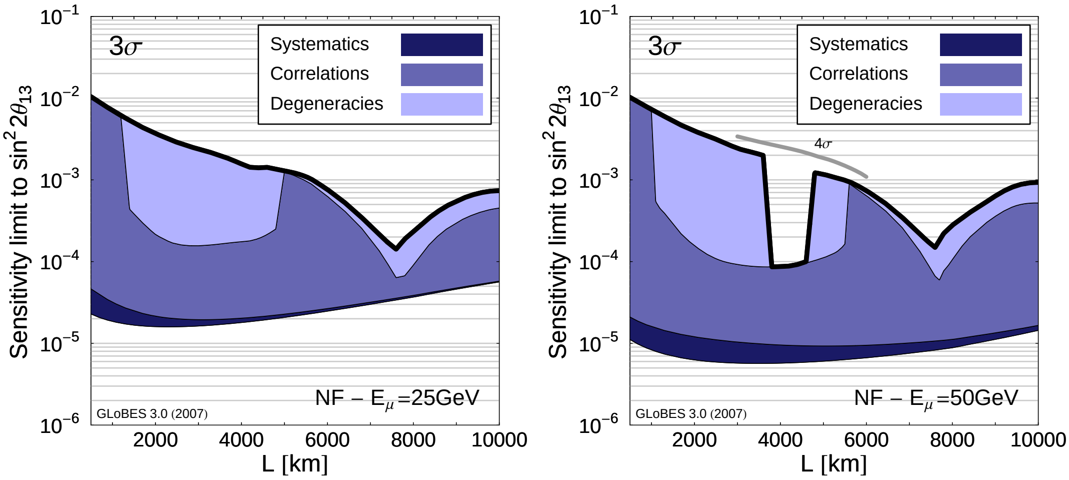

Figure 8.1: The sensitivity limit to $\sin^2 2\theta_{13}$ at a Neutrino Factory at the 3σ confidence level as a function of the baseline L for a fixed parent muon energy $E_\mu = 25$ GeV (left) and $E_\mu = 50$ GeV (right). The bands indicate the influence of systematics, correlations, and degeneracies and the final sensitivity limit is indicated by the uppermost thick black line. In the right plot the degeneracies can be resolved around a baseline of 4000 km at 3σ and the sensitivity limit to $\sin^2 2\theta_{13}$ improves by one order of magnitude. However, already at the 4σ confidence level the degeneracies cannot be resolved anymore as indicated by the grey line.

degeneracies can be resolved. This can be understood as the following. In the baseline range $1000 \text{ km} \lesssim L \lesssim 6000$ km the effect of the correlations drops by one order of magnitude because in this range the local minimum in the $\Delta\chi^2$ distribution at higher fit values of $\sin^2 2\theta_{13}$ due to the $(\sin^2 2\theta_{13}, \delta_{\rm CP})$-degeneracy gets disconnected from the true solution (global minimum at a fit value of $\sin^2 2\theta_{13} = 0$ as there the true value is set) at the considered confidence level of 3σ. For baselines $L \sim 4000$ km and $E_\mu = 50$ GeV this local minimum is shifted above $\Delta\chi^2 = 9$ and hence can be excluded. However this exclusion is not very robust and already at a chosen confidence level of 4σ the resolution of the $(\sin^2 2\theta_{13}, \delta_{\rm CP})$-degeneracy disappears as is indicated by the thick grey line in the right plot of Fig. 8.1 that indicates the evolution of the final sensitivity limit at 4σ. So, it is obvious that the $L \sim 4000$ km Neutrino Factory is not as extremely unique as could be concluded from the evolution of the sensitivity at 3σ. It is worthwhile to mention that the huge impact of switching on the parameter degeneracies at these baselines is almost only due to the $(\sin^2 2\theta_{13}, \delta_{\rm CP})$-degeneracy while the small impact of parameter degeneracies at the magic baseline is solely caused by the sign-degeneracy as the parameter $\delta_{\rm CP}$ does not enter the appearance probability at this baseline.

In Fig. 8.2 the parent muon energy dependency of the sensitivity limit to $\sin^2 2\theta_{13}$ is illustrated for the fixed baselines $L = 4000$ km (left plot) and $L = 7500$ km (right plot) that were the two most promising baselines in the previous discussion. It was mentioned before, that lower parent muon energies could be a very interesting option since directly connected to the cost effort that has to be expended. We observe that the ability to exclude the $(\sin^2 2\theta_{13}, \delta_{\rm CP})$-degeneracy at the 3σ confidence level that was already found in case of $E\mu = 50$ GeV is already present for parent muon energies $E_\mu > 30$ GeV and for even higher energies there cannot be deduced any significant improvement in the final sensitivity limit to $\sin^2 2\theta_{13}$ although the statistical limit still sees some kind of improvement due to the higher

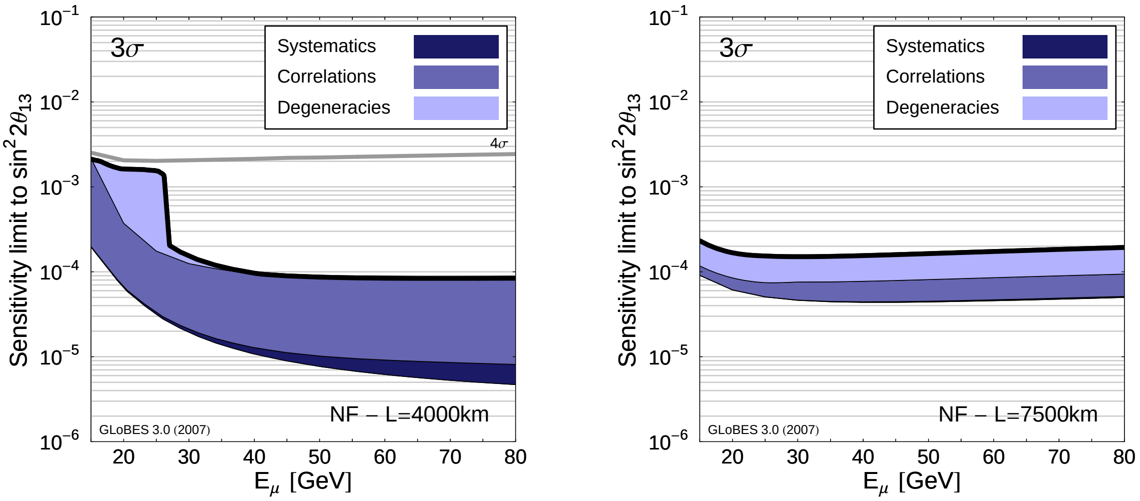

Figure 8.2: The sensitivity limit to $\sin^2 2\theta_{13}$ at a Neutrino Factory at the 3σ confidence level as a function of the parent muon energy E_μ for a fixed baseline of $L = 4000$ km (left) and $L = 7500$ km (right). The bands indicate the influence of systematics, correlations, and degeneracies and the final sensitivity limit is indicated by the uppermost thick black line. In the left plot the degeneracies can be resolved for $E_\mu \gtrsim 25$ GeV at 3σ and the sensitivity limit to $\sin^2 2\theta_{13}$ improves by one order of magnitude. However, already at the 4σ confidence level the degeneracies cannot be resolved anymore as indicated by the grey line.

cross sections at higher energies, *i.e.* higher event rates. Also, the sensitivity limit at 4σ is again indicated by the thick grey curve and it can be seen that even for very high energies up to $E_\mu = 80$ GeV the impact of the $(\sin^2 2\theta_{13}, \delta_{\rm CP})$-degeneracy at this confidence level cannot be avoided anymore. This already implies that there is no reason at all to actually consider higher values than the standard value $E_\mu = 50$ GeV. Still, the impression settles that slightly smaller parent muon energies do not lead to significant loss of sensitivity unless it remains larger than $E_\mu \gtrsim 30$ GeV. This is also observed in the right plot of Fig. 8.2 for the scenario with a detector at the magic baseline. For this baseline a slight optimum of the final sensitivity limit can be obtained at $E_\mu \sim$25 GeV, however the overall limit does only get affected to a minimal extend over the whole range of considered parent muon energies.

Sensitivity to CP violation

Now, we will consider the issue of optimizing the Neutrino Factory baseline for the sensitivity to *maximal* CP violation. As it was found in [236] that the performance of a Neutrino Factory is nearly unattached for a variation of the parent muon energy E_μ as long it is kept above $E_\mu \gtrsim 25$ GeV we will not introduce the discussion of optimal neutrino energy to this subsection and consider only the baseline optimization for two scenarios with $E_\mu = 25$ GeV and $E_\mu = 50$ GeV. This observation from [236] is also supported by the results of the last subsection. Since the sensitivity to *maximal* CP violation at a Neutrino Factory is different for the two assumptions of true $\delta_{\rm CP} = \pi/2$ and $\delta_{\rm CP} = 3\pi/2$, both assumptions will be discussed in the following. Opposite to the β-Beam scenarios discussed in the last chapter the Neutrino Factory is suffering from the sign-degeneracy at intermediate $\sin^2 2\theta_{13}$ where sensitivity to *maximal* CP violation is lost for $\delta_{\rm CP} = 3\pi/2$.

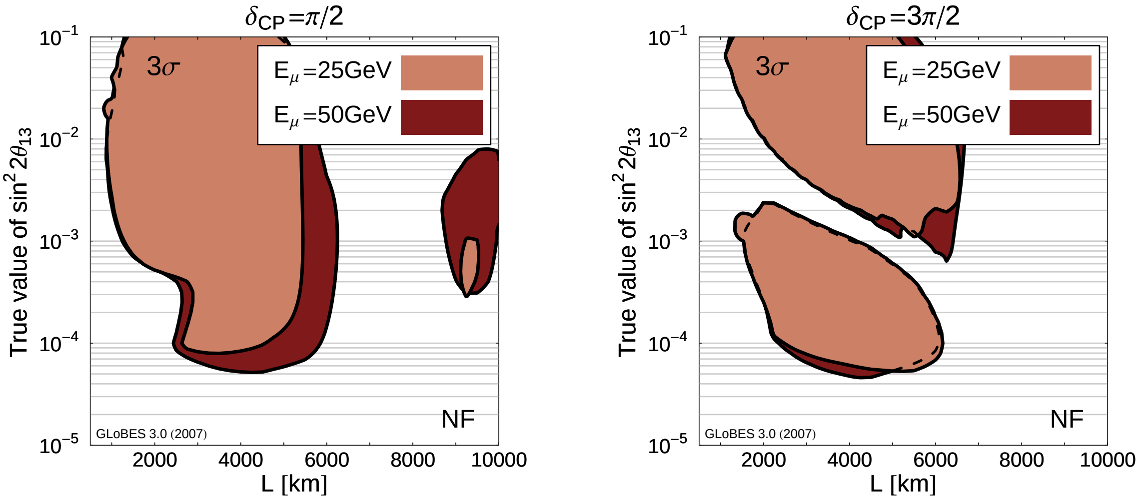

Figure 8.3: The sensitivity to *maximal* CP violation at a Neutrino Factory at the 3σ confidence level as a function of the baseline L for fixed parent muon energies $E_\mu = 25$ GeV and $E_\mu = 50$ GeV for the assumed true values $\delta_{\rm CP} = \pi/2$ (left) and $\delta_{\rm CP} = 3\pi/2$ (right). Systematics, correlations, and degeneracies are taken into account.

This effect can be noticed in the right plot of Fig. 8.3 where the $\sin^2 2\theta_{13}$ range where sensitivity to *maximal* CP violation can be established is shown for the case $\delta_{\rm CP}$ as a function of the baseline in the range 500 km $\lesssim L \lesssim$ 10000 km. We find a considerable large range of true $\sin^2 2\theta_{13}$ to values below 10^{-4} in the window of baselines between $L \sim 2000$ km and $L \sim 6000$ km for both assumptions for E_μ. However for intermediate true values $\sin^2 2\theta_{13} \sim (2-3) \cdot 10^{-3}$ the sensitivity vanishes and a sensitivity gap arises. The reason is that the sign-degenerate solution manifests as a local minimum in the $\Delta\chi^2$ distribution with Δm^2_{31} but also the other oscillation parameter fit values can be shifted away from the assumed true values. In [198] it was shown that the fit value of $\delta_{\rm CP}$ in the local minimum of the sign-degeneracy moves continously by adjusting the true value of $\sin^2 2\theta_{13}$ from $\delta_{\rm CP} = 3\pi/2$ ($\sin^2 2\theta_{13} = 0$) to $\delta_{\rm CP} \sim 3\pi/2$ for higher $\sin^2 2\theta_{13}$ under the assumption of true $\delta_{\rm CP} = 3\pi/2$. During this traveling of the fit value of $\delta_{\rm CP}$ at the local minimum of the sign-degeneracy the value of $\delta_{\rm CP} = \pi$ is passed and then the underlying CP violation cannot be distinguished from CP conservation. Consequently, the sensitivity to *maximal* CP violation gets lost. This effect is the so-called “π-transit” [198] and appears for true values $\sin^2 2\theta_{13} \sim (2-3) \cdot 10^{-3}$ at the discussed scenarios. However, under the assumption of true $\delta_{\rm CP} = \pi/2$ this “π-transit” does not occur and sensitivity to *maximal* CP violation can be established also at intermediate values of $\sin^2 2\theta_{13}$ as can be seen in the left plot of Fig. 8.3. Another effect can be observed from Fig. 8.3 which is the missing sensitivity to CP violation for baselines 6000 km $\lesssim L \lesssim$ 9000 km which is not surprising at all, since the magic baseline at L ~7500 km does not provide any information for $\delta_{\rm CP}$. So, the optimal baselines for a search of $\delta_{\rm CP}$ at a Neutrino Factory clearly suggest baselines in the range 3000 km $\lesssim L \lesssim$ 6000 km with a slight optimum at L ~4000 km. Furthermore, it can also be seen in Fig. 8.3 that there is no significant difference in the performances of the standard and the low parent muon energy scenarios. Only for $\delta_{\rm CP} = 3\pi/2$ the higher energy scenario can reach the sensitivity to slightly smaller values of $\sin^2 2\theta_{13}$ but for both energies sensitivity to *maximal* CP violation can be established for true

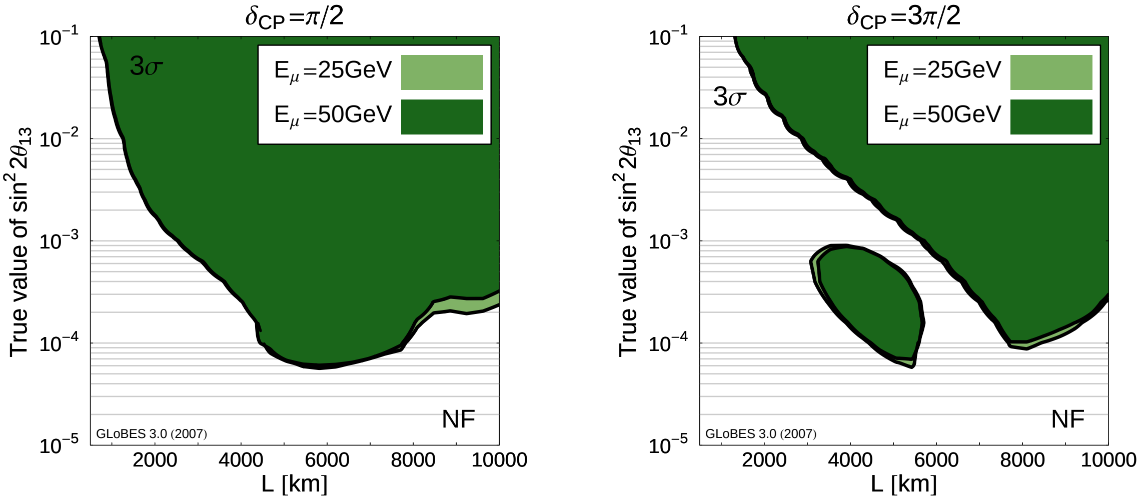

Figure 8.4: The sensitivity to mass hierarchy at a Neutrino Factory at the 3σ confidence level as a function of the baseline L for fixed parent muon energies $E_\mu = 25$ GeV and $E_\mu = 50$ GeV for normal hierarchy assumed and the true values $\delta_{\mathrm{CP}} = \pi/2$ (left) and $\delta_{\mathrm{CP}} = 3\pi/2$ (right). Systematics, correlations, and degeneracies are taken into account.

values of $\sin^2 2\theta_{13}$ smaller than 10^{-4}.

Sensitivity to mass hierarchy

Due to the very high baselines of several thousands of kilometers a Neutrino Factory will have excellent capabilities to determine the mass hierarchy of the neutrino mass eigenstates, *i.e.* exclude the sign-degenerate solution in parameter space. We will now focus on the baseline optimization with regards to the sensitivity to mass hierarchy at the 3σ confidence level for the two scenarios with a parent muon energy of $E_\mu = 25$ GeV and $E_\mu = 50$ GeV. We will not discuss further energy optimization issues, since as for the sensitivities to θ_{13} and δ_{CP} the evolution with E_μ is rather marginal for energies $E_\mu > 25$ GeV (*cf.* [236]). In fact, higher parent muon energies than 50 Gev are slightly disfavored for some regions in the δ_{CP} parameter space since the matter resonance appears at smaller neutrino energies.

The baseline dependent evolution of the range of true $\sin^2 2\theta_{13}$ where the neutrino mass hierarchy can be determined (normal hierarchy assumed) is illustrated in Fig. 8.4 for two selected true values $\delta_{\mathrm{CP}} = \pi/2$ (left) and $\delta_{\mathrm{CP}} = 3\pi/2$ (right). It can be read off that the two scenarios $E_\mu = 25$ GeV and $E_\mu = 50$ GeV indeed share essentially the same performance and the differences are hardly visible in Fig. 8.4. As expected, larger baselines are favored and the magic baseline L ~7500 km is able to provide extremely good sensitivity to mass hierarchy for both assumptions of true δ_{CP}. At intermediate baselines the sensitivity to mass hierarchy is spoiled by the $(\sin^2 2\theta_{13}, \delta_{\mathrm{CP}})$-degeneracy for δ_{CP} and a baseline in the range 6000 km $\lesssim L \lesssim$ 7500 km is completely disqualified. For baselines in the range 3000 km $\lesssim L \lesssim$ 6000 km the degeneracies spoil the sensitivity at intermediate $\sin^2 2\theta_{13} \sim 10^{-3}$ and at smaller $\sin^2 2\theta_{13}$ the sensitivity is restored again. As was already the case for the β-Beam scenarios it turns out that optimization of the experiment in terms of δ_{CP} and the mass hierarchy collides since the optimal baseline for sensitivity to the sign of Δm^2_{31} provides no sensitivity to CP violation at all. However a baseline of $L \sim$4000 km seems to offer a good compromise however the resolving of the degeneracies at intermediate $\sin^2 2\theta_{13}$ is the challenge that has to be addressed. For that reason we will in the following also discuss performances of Neutrino Factory scenarios with more than one detector involved.

Neutrino Factory Reference Scenarios

The last subsections focused on the independent optimization of different Neutrino Factory scenarios in terms of baseline L and the energy of the parent muons in the storage ring E_μ. We will now assign defined reference setups, as was already done in the last chapter for β-Beams. These follow the suggestions from the optimization discussions and provide the possibility to study the properties and performances in a greater detail. Furthermore, these defined reference setups and their abilities can be comfortably compared to the performance of the β-Beam reference setups and to each other. The definition of the reference setups is based slightly more upon the discussion of the baseline optimization since the dependence of the performance on the variation of the energy turned out to be of secondary importance. So, we will stick to the standard choice $E_\mu = 50$ GeV and only introduce one low energy scenario with $E_\mu = 30$ GeV to further investigate if a lower energy Neutrino Factory can be justified. Additionally, we will also introduce scenarios that involve two or even three detectors partially located at different baselines to cover optimal performances in all three performance indicators: discovery reach of $\sin^2 2\theta_{13}$, sensitivity to *any* CP violation, and sensitivity to mass hierarchy.

The standard Neutrino Factory scenario with $E_\mu = 50$ GeV at a baseline of $L = 4000$ km will be labeled NF50@4000km. It makes use of a 50 kt Magnetized Iron detector to allow for the charge identification of the detected muons to separate the wrong-sign muons. NF30@4000km is basically the same setup as NF50@4000km however run at a lower energy $E_\mu = 30$ GeV of the stored parent muons. The single detector scenario at $E_\mu = 50$ GeV with the 50 kt Magnetized Iron detector located at $L = 7500$ km, *i.e.* approximately at the magic baseline is introduced as NF50@7500km. Furthermore, we introduce double detector scenarios to allow for an improved potential in degeneracy resolving. Since we are interested in the improvement of these double detector scenarios that is not only governed by the increased statistics due to the second detector, we additionally introduce a scenario that involves just a simple doubled detector. This scenario is essentially identically to NF50@4000km with an increased detector volume of 100 kt and it is labeled NF50@2D1L. The next simplest double detector scenario involves two 50 kt Magnetized Iron detectors, one located at $L = 4000$ km and the other at the magic baseline $L = 7500$ km. Since the problems of degeneracy resolving at a Neutrino Factory result from the high energy threshold due to the muon momentum cut we also introduce a hybrid detector scenario NF50@2DIT that shows the same high energy behavior than the usually discussed detector, but with a lower energy threshold and a higher energy resolution. The lower threshold should make the first oscillation maximum accessible and allow for better handling of the parameter degeneracies[6]. Another possibility to improve the abilities of resolving the degeneracies could be provided by the inclusion of additional channels that require different detector technologies. The silver channel is included for the scenario NF50@2DGS by the addition of a 10 kt Emulsion Cloud Chamber detector of the OPERA type at the same baseline $L = 4000$ km as the Magnetized Iron detector that allows

---

[6] In [236] it was found that the better performance of this scenario is mainly caused by the lower energy threshold and only on a secondary basis by the higher energy resolution.

Label	L [km]	E_μ [GeV]	Detector	Mass (fid.) [kt]
NF50@4000km	4000	50	MID	50
NF30@4000km	4000	30	MID	50
NF50@7500km	7500	50	MID	50
NF50@2D1L	4000	50	MID	2×50
NF50@2D2L	4000/7500	50	MID/MID	50
NF50@2DIT	4000	50	Hybrid	50
NF50@2DGS	4000/4000	50	MID/ECC	50/10
NF50@2DGP	4000	50	opt. MID	50
NF50@3D	4000/7500	50	Hybrid/MID	50/50

Table 8.4: The listing of all defined reference Neutrino Factory scenarios. the 4th trough the 8th scenarios involve a two detector effort and the last scenario even involves three detectors. The label in the left column are used throughout this work for account for the respective scenarios. The detector technologies involve a Magnetized Iron detector (MID), a Hybrid detector optimized for higher energy resolution and a lower energy threshold, an OPERA-like Emulsion Cloud Chamber detector (ECC), and an optimized Magnetized Iron Detector for the Platinum Channel (opt. MID).

for the golden channel measurements[7]. The scenario that includes the platinum channel is NF50@2DGP that assumes an optimized 50 kt Magnetized Iron detector that allows charge identification of electrons and positrons. This scenario is counted as a double effort scenario since the optimization of the main detector is very ambitious and it can easily turn that the platinum channel measurement require a second detector of different technology. Note, that both reference scenarios that involve an additional channel are based on the optimistic channel scenarios. The last Neutrino Factory scenario that is introduced is a triple detector scenario NF50@3D that combines the hybrid detector at $L = 4000$ km with a normal Magnetized Iron detector at the magic baseline $L = 7500$ km. The complete listing of all defined reference Neutrino Factory scenarios and their main features is resumed in Table 8.4.

8.3 Neutrino and Anti-Neutrino Runtime Fraction

The total runtime of a Neutrino Factory experiment is planned to contain a period when μ^+ are stored in the storage ring and the opposed period when polarity is changed and μ^- are stored in the storage ring to allow for comparison of neutrinos and anti-neutrinos. As was pointed out earlier, this comparison helps in resolving the parameter correlations and degeneracies in the appearance measurements. In the previous simulations all Neutrino Factory experiments were assumed to share an equally split runtime for both, μ^- stored and μ^+ stored. However, as already discussed for β-Beam experiments, one can try to improve the performance by modifying the ratio of the two runtime fractions. The difference to β-Beams is that at Neutrino Factory experiments the terms neutrino and anti-neutrino running cannot be unambiguously attributed to the storage phases μ^- stored and μ^+ anymore since the neutrino beam at a Neutrino Factory does not contain only neutrinos or anti-neutrinos. The stored muons decay to electron and muon neutrinos, *e.g.* $\mu^- \rightarrow e^- + \overline{\nu}_e + \nu_\mu$, and thus the

---

[7] Actually the second detector could be located at a different baseline as the main detector. However, in [236] it was shown that the silver channel detector is most suitable if located at the same baseline as the golden detector in order to help resolving the degeneracies at intermediate $\sin^2 2\theta_{13}$. So, the possibility to locate the silver detector at a different baseline is omitted here.

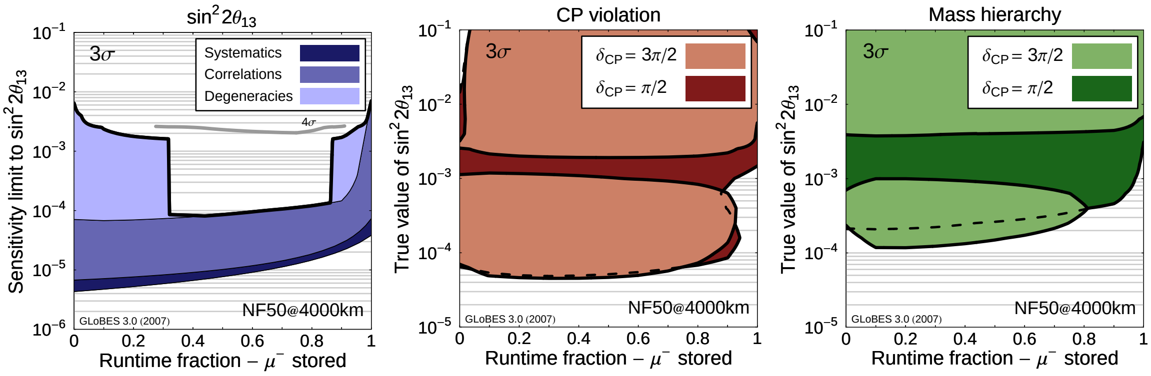

Figure 8.5: The impact of the ratio of neutrino and anti-neutrino runtime at a Neutrino Factory (NF50@4000km scenario) on the sensitivity limit to $\sin^2 2\theta_{13}$, the sensitivity to *maximal* CP violation, and sensitivity to the mass hierarchy at the 3σ confidence level respectively. The total runtime is 8 years and divided into a runtime fraction of μ^--stored (labeled on the x-axis) and the runtime fraction of μ^+-stored. In each plot the right edge represents neutrino running only ($\nu_\mu/\overline{\nu}_e$) and the left edge represents anti-neutrino running only ($\overline{\nu}_\mu/\nu_e$).

neutrino runtime in the disappearance channel, *e.g.* $\nu_\mu \to \nu_\mu$, coincides with the anti-neutrino running in the respective appearance channel, *e.g.* $\overline{\nu}_e \to \overline{\nu}_\mu$. Since the measurements in the appearance channel focus on the sub-leading parameters θ_{13}, δ_{CP} and the sign of Δm^2_{31} that are the main focus of this work, we will use the terms neutrino or anti-neutrino running at a Neutrino Factory following the mode of the neutrinos in the appearance channel, so neutrino running is associated with the μ^+ stored phase and anti-neutrino running is associated with the μ^- stored phase.

In Fig. 8.5 the performance of the standard Neutrino Factory scenario NF50@4000km in terms of the sensitivity limit to $\sin^2 2\theta_{13}$ (left plot), sensitivity to *maximal* CP violation (middle plot), and sensitivity to mass hierarchy (right plot), each at the 3σ confidence level is shown as a function of the runtime fraction of the μ^- stored phase, *i.e.*the anti-neutrino running. The middle of the plots (0.5 runtime fraction) corresponds to the standard assumption of the last subsections of an equally split runtime in 4 years neutrino and 4 years anti-neutrino running. The total runtime is always assumed to be 8 years, the left edge corresponds to pure neutrino running and the right edge corresponds to pure anti-neutrino running. The statistical sensitivity limit to $\sin^2 2\theta_{13}$, indicated as the lowermost curve in the left plot, reaches to the smallest possible values of $\sin^2 2\theta_{13}$ for a pure neutrino running which is related to the fact that the cross sections for neutrinos are larger than the cross sections for anti-neutrinos and 8 years of pure neutrino running could collect the maximal number of event rates in the appearance channel. However, the inclusion of anti-neutrinos is needed to resolve the correlations and degeneracies and improve the final sensitivity limit significantly. The final sensitivity limit that takes systematics, correlations and degeneracies into account is indicated by the uppermost thick black curve. It can be read off that a anti-neutrino fraction in between 0.3 and 0.85 is required to succeed in resolving the degeneracies at the 3σ confidence level. Pure anti-neutrino running on the other hand is clearly again lacking the opposed neutrino mode. However, the grey thick line represents the final sensitivity limit to $\sin^2 2\theta_{13}$ at the 4σ confidence level and it can be seen that the degeneracies cannot be resolved at this higher confidence level independent of the runtime fraction of the anti-neutrino running. If one considers the sensitivity to *any* CP violation and sensitivity to the mass hierarchy the first interesting aspect is that the sensitivity gap that can be observed at intermediate $\sin^2 2\theta_{13}$ cannot be covered independent of the runtime fractions and the sensitivities are spoiled by parameter degeneracies, *e.g.* by the "π-transit" in case of sensitivity to δ_{CP}. The middle plot suggests to keep the anti-neutrino running fraction in between 0.1 and 0.7 with slightly better performance for smaller runtime fractions. The same is true for the sensitivity to mass hierarchy and if also the sensitivity to θ_{13} is taken into account there appears no reason to depart from the standard assumption of using equally split runtime fractions for both, neutrinos and anti-neutrinos. So, in the next sections, where we will discuss the performances of the reference scenarios defined in the last subsection, we will stick to 4 years of anti-neutrino running and 4 years of neutrino running.

8.4 Matter Density Uncertainty

One of the main characteristics of a Neutrino Factory is the very long baseline of several thousands of kilometers. All discussed Neutrino Factory reference scenarios make use of the standard baseline $L = 4000$ km and the magic baseline $L = 7500$ km and matter effects along the baseline enter the oscillation probability in a sizeable manner which also allows for the determination of the mass hierarchy. Along these baselines the neutrinos travel through the mantle of the earth with an average matter density $\rho \sim 5$ g/cm^3. The outer core of the earth begins not until at a depth of 3000 km where the matter density instantly increases up to $\rho \sim 10$ g/cm^3. But to touch the outer core the baseline would be required to be larger than approximately 11000 km. So the assumption of an average matter density profile along the baseline is justified. However, the matter density is not exactly known and associated with a certain uncertainty of approximately 5%. All simulations in the previous and following sections are performed under the assumption of $\Delta\rho = 5\%$. The matter density ρ [g/cm^3] is treated as a free fit parameter and the uncertainty is introduced by adding a parabolic pull term $(\rho - \rho_0)^2/(0.05\rho_0)^2$ to keep the fit value near the incident true value ρ_0.

The quantitative effect of the matter density uncertainty is illustrated in Fig. 8.6 for $L = 4000$ km (NF50@4000km) in the upper row and $L = 7500$ km (NF50@7500km) in the lower row for the performance indicators discovery reach in $\sin^2 2\theta_{13}$ (left column), sensitivity to *any* CP violation (middle column), and sensitivity to mass hierarchy (right column). The band shows the effect of switching from an exactly known matter density uncertainty $\Delta\rho = 0$ to the standard assumption $\Delta\rho = 5\%$. The short-dashed curve shows the performance with a small matter density $\Delta\rho = 2.5\%$. Note, that the the NF50@7500km scenario does not show any sensitivity to CP violation since the baseline is approximately at the magic baseline. Furthermore, by comparing the upper and the lower row we can deduce that the effects of the matter density uncertainty is increasing with the baseline since it is affecting the longer baseline $L = 7500$ km to a larger extend in the left and right column. However, the most important observation in Fig. 8.6 is the sensitivity to *any* CP violation for the NF50@4000km scenario. At smaller $\sin^2 2\theta_{13}$ the matter density shows nearly no effect at all but for larger $\sin^2 2\theta_{13} \gtrsim 10^{-2}$ the matter density uncertainty turns out to be crucial. The reason is that matter effects are increasing with increasing $\sin^2 2\theta_{13}$. For $\sin^2 2\theta_{13} < 10^{-3}$ matter effects do not contribute significantly and consequently, the matter density uncertainty does also not give a significant effect. With an exactly known matter density this scenario can establish CP violation for slightly more than 80% of all possible true values for δ_{CP} in this range

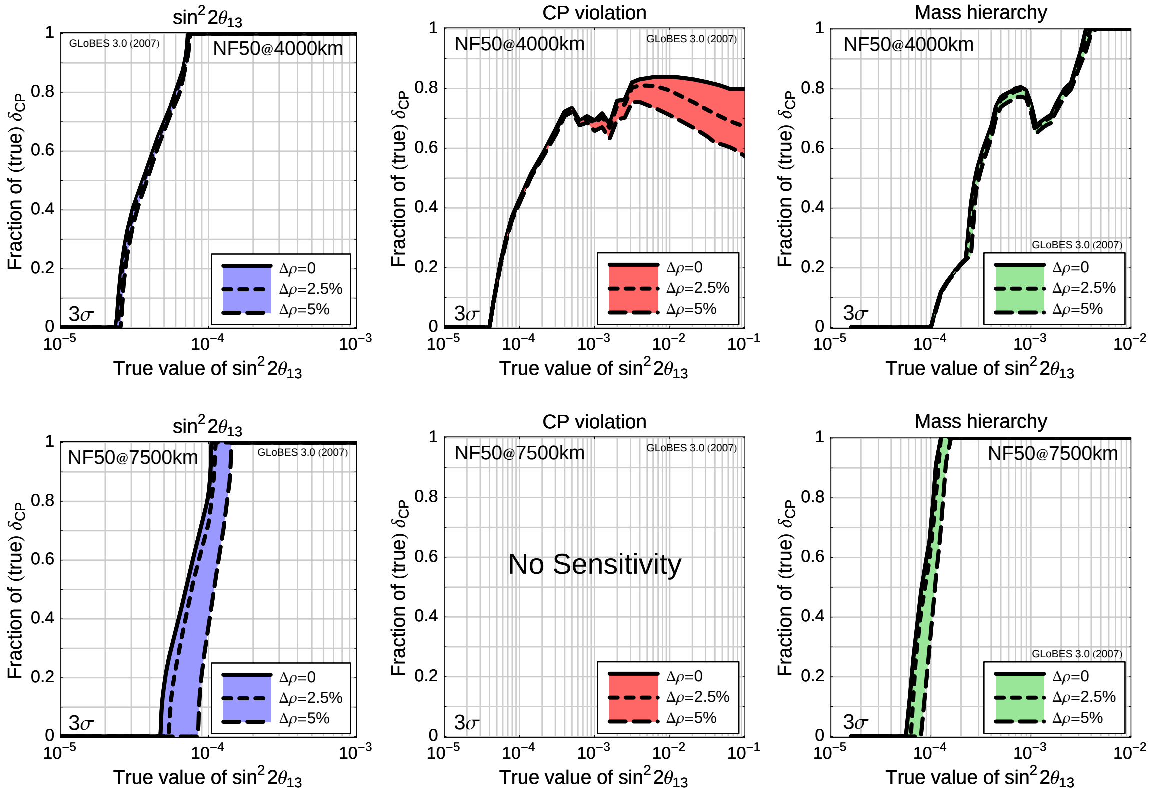

Figure 8.6: The impact of the matter density uncertainty at a Neutrino Factory on the $\sin^2 2\theta_{13}$ discovery reach (left), the sensitivity to *any* CP violation (middle), and sensitivity to the mass hierarchy (right). The fraction of the true values of δ_{CP} of all possible values in the interval $[0, 2\pi[$ where the respective sensitivity is given at the 3σ confidence level is displayed as a function of the true value of $\sin^2 2\theta_{13}$. The band indicates the impact of the matter density uncertainty $\Delta\rho$ along the baseline. It is varied from $\Delta\rho = 5\%$ (long-dashed line, standard assumption) over $\Delta\rho = 2.5\%$ (short-dashed line) to $\Delta\rho = 0$ (long-dashed line). The upper row is for the NF50@4000km scenario and the lower row is for the NF50@7500km scenario.

of true $\sin^2 2\theta_{13}$. If the 5% matter density uncertainty is considered the Neutrino Factory scenario looses this sensitivity for approximately 20% of all possible values of δ_{CP} and CP violation can only be established for the remaining 60%. So, although a Neutrino Factory is a very dedicated experimental setup that allows measurements of three-flavor effects down to extremely small values of $\sin^2 2\theta_{13}$ there appears a further problem besides resolving the degeneracy at intermediate $\sin^2 2\theta_{13}$, the matter density uncertainty along the baseline. We will see in the comparison with different technologies that the Neutrino Factory is the very promising candidate for small $\sin^2 2\theta_{13}$, but for large $\sin^2 2\theta_{13}$ also other technologies could turn out to be more promising because of the effect of the matter density uncertainty.

8.5 Inclusion of Different Channels

Besides the combination of neutrino and anti-neutrino data or using different baselines, the inclusion of additional channels offers a possibility to help resolve the parameter correlations and degeneracies that a Neutrino Factory is suffering from at intermediate $\sin^2 2\theta_{13}$. Additionally, the inclusion of the different channels can improve the performance of a Neutrino Factory at large $\sin^2 2\theta_{13}$. Alongside the golden $\nu_e \to \nu_\mu$ appearance, the silver $\nu_e \to \nu_\tau$ or the platinum $\nu_\mu \to \nu_e$ appearance measurement can offer promising improvement potential. However the inclusion of these additional channels is aligned with additional detector requirements. The silver channel requires the ability to detect, identify, and reconstruct the τ events. Since the OPERA experiment is planned to detect τ events that oscillate from the CNGS neutrino beam, the same detector technology, an Emulsion Cloud Chamber, is possible to perform the silver channel measurements at a Neutrino Factory [240, 241, 244, 245]. The inclusion of the platinum channel on the other hand requires the ability to detect and identify the electron/positron events of the platinum channel. However, the beam already contains a huge majority of electron/positrons from $\nu_e/\overline{\nu}_e$-disappearance. Comparable to the golden channel muons that have to be discriminated from the wrong-sign muons of the disappearance, the platinum appearance electrons/positrons have to be distinguished from the wrong-sign disappearance electrons/positrons. The separation by CID can be done at a magnetized detector by observing the track curvature. But since electrons tend to shower early, which means that the track is too short and the curvature is hardly measurable this CID is more difficult than the CID for muons of the golden channel. We will now address technical details and requirements of the inclusion of the silver channel and the platinum channel to the golden channel of a neutrino factory. Further details of the simulation of the silver and platinum channel can be found in Section 8.1.

Silver Channel

As already mentioned, the silver channel measurements require an OPERA-like Emulsion Cloud Chamber detector to allow for the detection of the τ events. The main limitation of the silver channel is the low event rate that is to be expected at the Emulsion Cloud detector, first because of the smaller size compared to the main detector and secondly because of the low detection efficiency. This additional detector is in principle independent of the main golden Magnetized Iron detector and can be located at various baselines. The main purpose is to help resolving the degeneracies at intermediate $\sin^2 2\theta_{13} \sim 10^{-3}$. From the optimization discussion of the Neutrino Factory scenarios it could be observed that the golden channel alone suffers from the degeneracies and sensitivity to CP violation and mass hierarchy is lost for true $\delta_{\rm CP} \sim 3\pi/2$. Although sensitivity could be established down to very small $\sin^2 2\theta_{13} \sim 10^{-4}$ at intermediate $\sin^2 2\theta_{13}$ the sensitivity absolutely was lost at the 3σ confidence level and a sensitivity gap occurred. We checked that the overall optimization discussion of the golden channel baseline from the previous sections does not get modified by the additional silver channel data and the optimal golden channel scenarios do not have to be reconsidered. Hence, the question arises if the additional silver channel data can cover the mentioned sensitivity gap, *i.e.* help to resolve the degeneracies, and which baseline for the silver channel detector is most appropriate. The achievable coverage of this sensitivity gap ($\delta_{\rm CP} = 3\pi/2$) for sensitivity to *maximal* CP violation (dashed-dotted curve) and sensitivity to mass hierarchy (dashed curve) is shown in Fig. 8.7 for the standard silver channel scenario assumptions as a function of the silver detector baseline $L_{\rm ECC}$. The golden channel is fixed to the 4000 km baseline and is corresponds to NF50@4000km. A coverage of 0% means that no improvement can be gained compared to the golden channel alone and 100% corresponds to a full resolving of the degeneracies and sensitivities can be restored in the full range of the original sensitivity gap. The coverage percentage is defined on a logarithmic scale in $\sin^2 2\theta_{13}$. Please note, that this figure is taken from [236] and was calculated for a slightly different set of true parameter

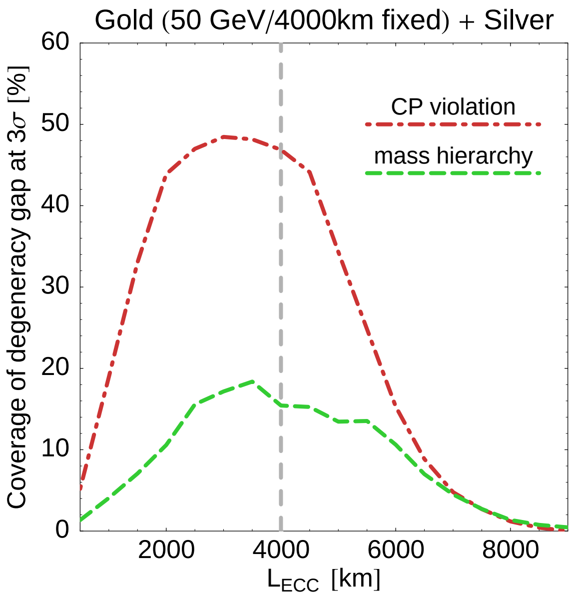

Figure 8.7: The improvement of the degeneracy resolution potential at intermediate $\sin^2 2\theta_{13}$ by including the standard silver channel to the golden channel as a function of the silver channel baseline L_{ECC}. The parent muon energy is 50 GeV and the golden channel detector is located at $L_{\mathrm{MID}} = 4000$ km. The curves show the coverage of the sensitivity gap at intermediate true $\sin^2 2\theta_{13} \sim 10^{-3}$ for sensitivity to *maximal* CP violation (dashed-dotted curve) and sensitivity to mass hierarchy (dashed curve) at the 3σ confidence level (true $\delta_{\mathrm{CP}} = 3\pi/2$ assumed). A coverage of 0% corresponds to the width of the sensitivity gap for golden channel only and 100% would correspond to a complete restoration of sensitivity for intermediate $\sin^2 2\theta_{13}$. The figure is taken from [236] and produced with the true parameter assumption of $\Delta m^2_{31} = 2.2 \cdot 10^{-3}$ eV^2.

values including a $\Delta m^2_{31} = 2.2 \cdot 10^{-3}$ eV^2. As can be read off from Fig. 8.7 the standard silver scenario cannot resolve the degeneracies completely independent of the silver baseline and a sensitivity gap still remains for the combination of golden and silver channel data at intermediate $\sin^2 2\theta_{13}$. However, in the silver baseline range from 2000 km to 5000 km the best performance can be observed where almost 50% of the original (golden channel only) sensitivity gap in CP violation measurements and almost 20% of the original sensitivity gap in mass hierarchy measurements can be covered by the inclusion of the silver channel data. The optimal silver baseline is approximately found at 3000 km however at 4000 km, which is the assumed baseline of the golden detector, the performance is very similar, so we will in the following only consider a silver detector at the same baseline as the main golden detector, since this is more cost effective because no further cavities at different baselines are required. It should be mentioned that the optimistic silver channel scenario with a doubled detector size and an improved signal detection can in principle cover 100% of the sensitivity gaps for both, CP violation and mass hierarchy measurements for $\delta_{\mathrm{CP}} = 3\pi/2$. The performance of the optimistic silver channel will be compared to the standard scenario in the next-to-next subsection.

Platinum Channel

The measurement of the platinum channel is very promising since an adequately high event rate as in the golden channel is in principle obtainable. Furthermore, this channel is the

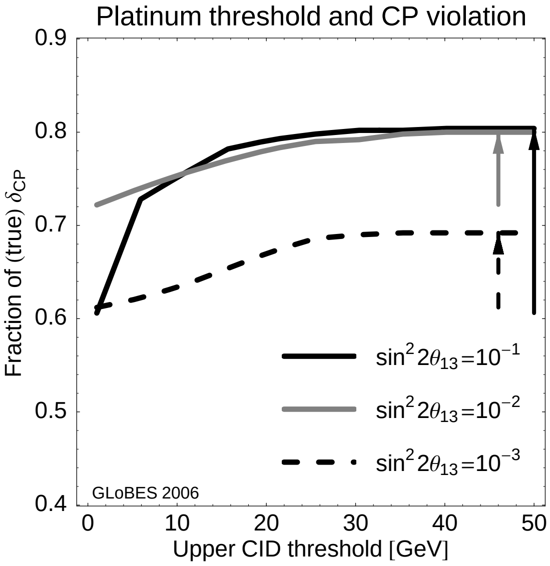

Figure 8.8: The impact of the upper platinum CID threshold to the sensitivity to *any* CP violation for $\sin^2 2\theta_{13} = 10^{-3}$ (dashed curve), $\sin^2 2\theta_{13} = 10^{-2}$ (grey curve), and $\sin^2 2\theta_{13} = 10^{-1}$ (black curve) for a combination of the golden and platinum channels. The fraction of (true) δ_{CP} for which CP violation can be discovered at the 3σ confidence level is shown as a function of the upper CID threshold and the arrows refer to the improvement in the physics potential by including the platinum channel. The figure is taken from [236] and produced with the true parameter assumption of $\Delta m^2_{31} = 2.2 \cdot 10^{-3}$ eV^2.

T-conjugated oscillation channel to the golden channel and hence corresponds to the CP-conjugated channel with different matter effect so a separation of intrinsic and extrinsic CP violating effects is in principle accessible. Consequently, this channel is also very promising to improve the potential of a Neutrino Factory at large $\sin^2 2\theta_{13}$ where the performance is mostly limited by uncertainties of the matter density along the baseline that affect the matter effect. However, the observation of the platinum electrons/positrons is hard to achieve since the CID to separate them from the disappearance electrons/positrons is challenging. The track length before the electrons/positrons tend to shower grows with energy and so the CID can only be possible up to a certain energy, this is called upper CID threshold in the following. The platinum channel simulations should be interpreted with care since it is based on assumptions, while the silver channel simulation is more reliable since it is based on detailed studies in the earlier literature. However, to push the upper CID threshold to higher energies is the most demanding detector requirement that is introduced with the additional platinum channel. For the optimistic platinum channel scenario we assume the 50 kt golden detector also to collect the platinum data so the baseline for both channels, golden and platinum channel is assumed to be equal. Considering the sensitivity gaps in sensitivity to *maximal* CP violation and to mass hierarchy at intermediate $\sin^2 2\theta_{13} \sim 10^{-3}$ and $\delta_{\mathrm{CP}} = 3\pi/2$ the optimistic scenario can cover the complete gap as also the optimistic silver scenario (assuming an upper CID threshold larger than 40 GeV) while the standard scenario (only a 15kt detector, upper CID threshold 7.5 GeV) can only cover 10% and does not affect the degeneracy resolving potential of the golden channel [236].

Here we will address the evolution of the potential in sensitivity to *any* CP violation of the optimistic platinum scenario added to the golden channel as a function of the upper CID threshold at the detector for $\sin^2 2\theta_{13} = 10^{-3}$, $\sin^2 2\theta_{13} = 10^{-2}$, and $\sin^2 2\theta_{13} = 10^{-1}$. This is shown in Fig. 8.8 as the fraction of true δ_{CP} where CP violation can be discovered at the 3σ confidence level. The left of the plot edge corresponds to the performance of the golden channel alone since a zero upper CID threshold means that CID for the platinum electrons/positrons is not possible at all. The right edge of the plot corresponds to the optimistic platinum channel scenario with an upper CID threshold of 50 GeV. The improvement is indicated by the vertical arrows. As can be seen in Fig. 8.8 the optimistic platinum channel scenario can add an improvement for all three choices of true $\sin^2 2\theta_{13}$. However, the improvement is most impressive for large $\sin^2 2\theta_{13} = 10^{-1}$ where the fraction of true δ_{CP} where CP violation can be discovered is extended from approximately 60% (golden only) to 80% while the improvement for the other choices of $\sin^2 2\theta_{13}$ is roughly 10% of all possible values of δ_{CP}. The most important result from Fig. 8.8 is the observation that the requirements to achieve this huge improvement in the performance for large $\sin^2 2\theta_{13}$ do not necessarily involve a too high upper CID threshold, but a lower threshold at about 20 GeV can already give a very good increase in the potential.

Standard vs. Optimistic Scenarios

The last subsections suggested that the inclusion of the silver channel and platinum indeed provides the possibility to improve the performance of a neutrino factory that only observes the golden appearance channel. The golden channel alone suffers from degeneracies at intermediate $\sin^2 2\theta_{13} \sim 10^{-3}$ and from the matter density uncertainty at large $\sin^2 2\theta_{13} \sim 10^{-1}$. However, the level of improvement depends crucially on the detection properties that can be achieved. In Section 8.1 we introduced the details of the simulation of the silver and the platinum channel and for each channel a standard scenario and a optimistic scenario was defined. Each standard scenario corresponds to a feasible set of detector requirements. The optimistic scenarios on the other hand describe a detector response that is very challenging and might not be achievable. For the silver channel that involved a very dedicated detector volume with the double size of the standard assumption and the increase of the signal efficiency by observing all leptonic and hadronic decay channels of the τ and not only the decays into muons as in the standard assumption. The optimistic scenario for the platinum channel involves the assumption that the platinum electrons/positrons can be observed at the same (modified) golden detector as the golden channel with a platinum CID possible up to neutrino energies of 50 GeV.

The contributions from the additional channels to the “golden channel only” performance in the two relevant regimes of intermediate $\sin^2 2\theta_{13} = 10^{-3}$ and large $\sin^2 2\theta_{13} = 10^{-1}$ are compared in Fig. 8.9 and the improvement going from the standard channel scenarios to the optimistic scenarios can be seen. for the sensitivity to *any* CP violation and to mass hierarchy at the 3σ confidence level. The x-axis gives the fraction of (true) δ_{CP} for which CP violation can be discovered or respectively the mass can be determined. First of all, at large $\sin^2 2\theta_{13}$ the golden channel alone already can observe the mass hierarchy for 100% of all possible true values of δ_{CP} and no further improvement is required by the inclusion of the additional channel data. Thus, in the large $\sin^2 2\theta_{13}$ regime only the performance in the δ_{CP} measurement determines the improvement[8]. The optimistic scenarios both improve the

---

[8] The sensitivity to θ_{13} is also not to be considered, since $\sin^2 2\theta_{13}$ can be measured by the golden channel alone for 100% of all possible true values of δ_{CP}.

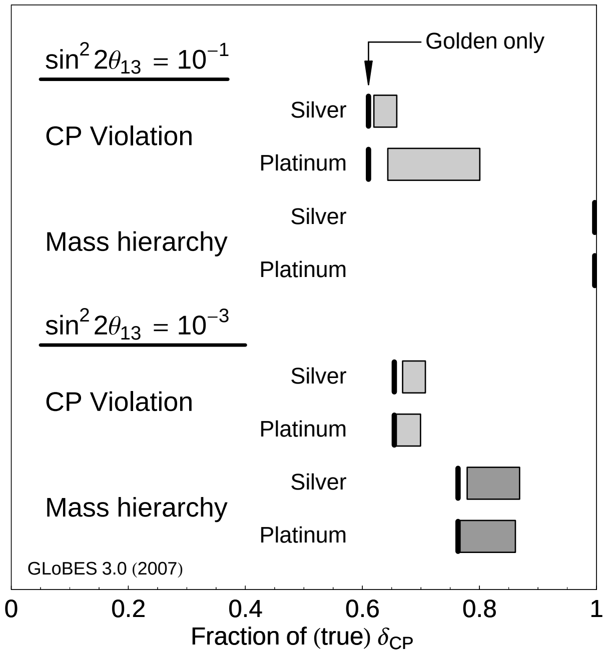

Figure 8.9: The comparison of the improvement of the standard and optimistic silver and platinum channel scenarios considering the sensitivity to *any* CP violation and the sensitivity to mass hierarchy sensitivity at the 3σ confidence level for large $\sin^2 2\theta_{13} = 10^{-1}$ and intermediate $\sin^2 2\theta_{13} = 10^{-3}$. The black lines refer to the performance of NF50@4000km with golden channel only. The grey bars refer to the improvement of the performance by inclusion of the silver or platinum channel whereas the left edges of the bars represent the standard channel scenarios and the right edges represent the optimistic scenarios NF50@2DGS or NF50@2DGP.

sensitivity to *any* CP violation but the impact of the platinum channel is more than twice as large as the impact of the silver channel which is due to the statistical difference in the two channels. At intermediate $\sin^2 2\theta_{13}$ the contribution of both channels to the sensitivity to CP violation is rather small however there is an improvement in the sensitivity to mass hierarchy. We observe that the inclusion of the silver and the platinum channel leads to very similar improvements in the potential. The negative outcome of Fig. 8.9 is that the possible improvement can only be achieved with the optimistic channel scenarios. The respective realistic scenarios do not affect the performance of the golden channel in a significant manner, neither at large nor at intermediate values of $\sin^2 2\theta_{13}$. So it has to be concluded that the detector response would have to be enhanced with respect to the standard assumed scenarios in order to allow the additional channels to contribute in a sizeable manner to the overall performance of the Neutrino Factory. Unless this cannot be achieved, the effort to introduce the additional channel to a Neutrino Factory experiment is not worthwhile. Consequently, the reference scenarios with additional channel data included, that will be discussed in the following, do only involve the optimistic silver and platinum channel assumptions.

8.6 Performance of the Neutrino Factory Reference Scenarios

This sections aims to compare the performances of all defined optimized Neutrino Factory reference scenarios that were introduced in Section 8.2. We will focus on the respective abilities to discover a non-zero θ_{13}, CP violation, and determine the mass hierarchy in the range from large $\sin^2 2\theta_{13}$ to very small $\sin^2 2\theta_{13}$. The goal is to find an optimized Neutrino Factory experiment. The different approaches to improve the performance of the Neutrino Factory, like data taking at different baselines, inclusion of different channels, or improving the detector response of the main detector with a lower threshold, are compared to find the most promising approach. The performances of the reference setups are shown in Fig. 8.10. The left column represents the discovery reach in $\sin^2 2\theta_{13}$, the middle column represents the sensitivity to *any* CP violation, and the right column represents the sensitivity to mass hierarchy, each at the 3σ confidence level. The rows indicate the detector effort by showing the single detector scenarios in the first row, the double detector scenarios in the middle row, and finally the triple detector scenario in the lowest row. The performance is furthermore compared with the performance of an upgraded Superbeam experiment T2HK*[9] that is indicated by the grey area in the plots.

First, we address the first row of Fig. 8.10 and the single detector scenarios NF50@4000km, NF30@4000km, and NF50@7500km. The standard scenario NF50@4000km has been optimized for δ_{CP}. All three single detector scenarios have the ability to discover $\sin^2 2\theta_{13}$ down to values of $\sin^2 2\theta_{13} \sim 10^{-4}$ for 100% of all possible values of δ_{CP}. The scenario NF50@7500km at the magic baseline looses the discovery potential for smaller values of $\sin^2 2\theta_{13}$ almost immediately, whereas the fraction of (true) δ_{CP} where a non-zero θ_{13} could be discovered decreases slightly slower for NF50@4000km and NF30@4000km, which is due to the correlation with δ_{CP}. So, whether a non-zero $3 \cdot 10^{-5} \lesssim \sin^2 2\theta_{13} \lesssim 10^{-4}$ can be discovered at NF50@4000km or NF30@4000km depends on the true value of δ_{CP}. The effect that the discovery reach for $\sin^2 2\theta_{13}$ at the scenario NF50@7500km does not drop as a vertical line is due to the fact that the 7500 km baseline is close, but not exactly located at the magic baseline at approximately 7250 km. When it comes to the sensitivity to *any* CP violation NF50@7500km shows no sensitivity at all. So clearly this scenario is not suitable as a single detector experiment and the magic baseline can only be considered for at least a double detector scenario. However, NF50@4000km and the lower energy scenario NF30@4000km share nearly the same sensitivity to *any* CP violation over the whole range from small to large $\sin^2 2\theta_{13}$. The reach to small $\sin^2 2\theta_{13}$ is rather impressive and at $\sin^2 2\theta_{13} \sim 10^{-4}$ CP violation can already be discovered for approximately 40% of all possible values of δ_{CP}. As already addressed in former sections the golden channel only suffers from parameter degeneracies at intermediate $\sin^2 2\theta_{13} \sim 10^{-3}$ which can be seen in the plot. The curve does not follow a smooth evolution since sensitivity to CP violation gets lost in some areas of parameter space because of the formerly discussed "π-transit" of the sign-degenerate solution. Additionally, it can be read off how the fraction of (true) δ_{CP} where CP violation can be established decreases again for increasing $\sin^2 2\theta_{13}$ towards 10^{-1} which is due to the matter density uncertainty. Because of these problems the single detector Neutrino Factory scenarios cannot establish CP violation in more than 75% of all possible values of δ_{CP} independent of $\sin^2 2\theta_{13}$. For large $\sin^2 2\theta_{13}$ the fraction even decreases down to approximately 60%. For large $\sin^2 2\theta_{13}$ also the impact of the correlation with the leading atmospheric parameters becomes more important. If the muon CID cut was also used for the disappearance data (as was done in older studies, *cf. e.g.* [246]), the fraction

---

[9] The simulation is performed with the GLoBES experiment file `T2HK.glb` provided with the GLoBES 3.0 package [220, 221] but the fiducial volume is modified to 500 kt instead of 440 kt to be comparable at a fair with the β-Beam scenarios that involve a Water Cherenkov detector. The modification is indicated by the star following the notation from [186] since this is the same scenario that was used there. Further details of the experiment description are given in the GLoBES manual [223].

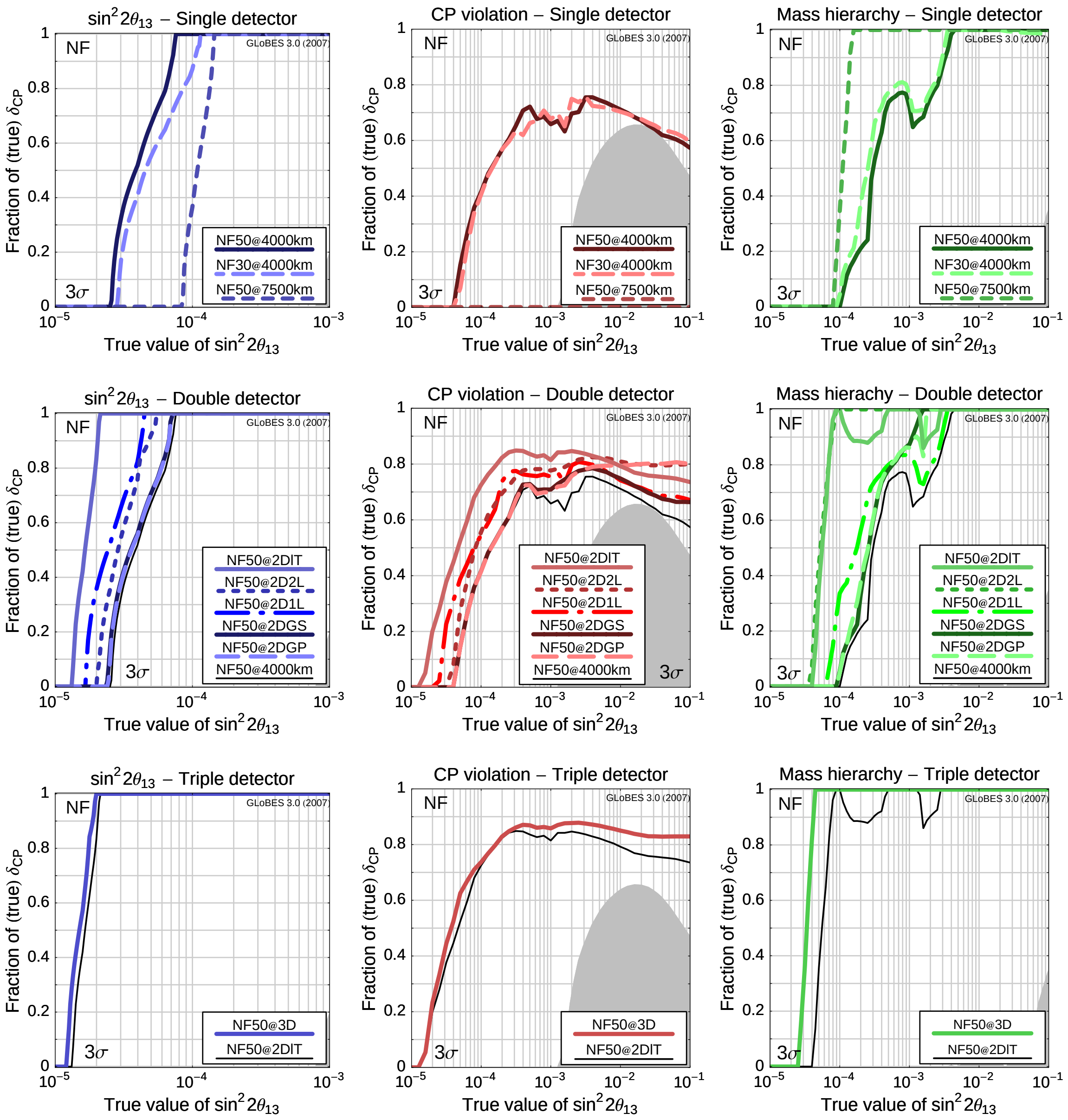

Figure 8.10: The comparison of the performance of all Neutrino Factory reference scenarios for the performance indicators $\sin^2 2\theta_{13}$ discovery reach (left column), sensitivity to *any* CP violation (middle column), and sensitivity to the mass hierarchy (right column). The fraction of the true values of δ_{CP} of all possible values in the interval $[0, 2\pi[$ where the respective sensitivity is given at the 3σ confidence level is displayed as a function of the true value of $\sin^2 2\theta_{13}$. The upper row is for the Neutrino Factory scenarios with a 50 kt Magnetized Iron detector, the middle row is for the Neutrino Factory scenarios with a double detector effort the lowest row is for the Neutrino Factory scenario with a triple detector effort: NF50@3D. The grey area indicates the respective performance of the upgraded Superbeam scenario T2HK* for reasons of comparison.

of (true) δ_{CP} where CP violation can be established at $\sin^2 2\theta_{13} = 10^{-1}$ decreases below 50%. All three considered single detector scenarios can determine normal mass hierarchy for 100% of all possible values of true δ_{CP} down to an intermediate $\sin^2 2\theta_{13} \sim 5 \cdot 10^{-3}$ but only the scenario at the magic baseline has excellent abilities to determine the mass hierarchy to very small $\sin^2 2\theta_{13} \sim 10^{-4}$. The $L = 4000$ km scenarios suffer from the $(\theta_{13}, \delta_{\rm CP})$-degeneracy at intermediate $\sin^2 2\theta_{13}$ and the baseline is too low to compete with the $L = 7500$ km scenario for smaller $\sin^2 2\theta_{13}$. A very important observation in the first row of Fig. 8.10 is that the low parent muon energy scenario NF30@4000km shows a very similar performance as the $E_\mu = 50$ GeV scenario and going to a lower parent muon energy seems well justified.

The second row of Fig. 8.10 increases in detector effort compared to the first row. All scenarios assume the combination of two detectors, either at the same baseline or a second baseline as the main golden detector. The scenario NF50@2D1L is only introduced to indicate the performance of a scenario for that the whole double detector effort is only put into a doubled statistics. So, wherever the double detector scenarios perform better than NF50@2D1L, the second detector adds complementary data, *i.e.* leads to a truly synergetical effect and is not only due to the increased statistics that is implied by the double detector effort. Furthermore the thin black line again shows the performance of NF50@4000km from the first row for reasons of comparison. First, we will consider the scenarios that include the silver and platinum channels, NF50@2DGS and NF50@2DGP. For small $\sin^2 2\theta_{13}$ the performance of the Neutrino Factory is not significantly improved by the additional channels. The θ_{13} discovery potential is not affected at all. For intermediate $\sin^2 2\theta_{13}$ we observe that the channels can help to partially resolve the degeneracies and improve the sensitivities to *any* CP violation and mass hierarchy but in case of sensitivity to $\delta_{\rm CP}$ this improvement is smaller than the improvement by just doubling the statistics. In the case of mass hierarchy sensitivity the silver channel can contribute in a sizeable manner and resolve the degenarcies at $\sin^2 2\theta_{13} \sim 10^{-3}$. There, the fraction of (true) $\delta_{\rm CP}$ where the mass hierarchy can be detected is increased from approximately 70% to about 100%. The platinum channel also helps to resolve the degeneracies in that regime but not as successful as the silver channel. The biggest improvement potential of the platinum channel lies at large $\sin^2 2\theta_{13} \sim 10^{-1}$ where CP violation can be established for 20% more of all possible values of $\delta_{\rm CP}$ than is possible with the golden channel only while the silver channel improvement is only 10% that also could be achieved with a doubled statistics in the golden channel. The addition of the magic baseline also provides a very good tool to counteract the matter density uncertainty at large $\sin^2 2\theta_{13}$ and NF50@2D2L provides the same improvement potential at large $\sin^2 2\theta_{13}$ than the platinum channel in CP violation sensitivity. Furthermore, the magic baseline improves the potential to determine the mass hierarchy. Degeneracies are completely resolved at intermediate $\sin^2 2\theta_{13}$ and also the sensitivity reach in the small $\sin^2 2\theta_{13}$ regime is improved. So, the combination of the golden channel data from $L = 4000$ km (CP optimized) and the magic baseline (mass hierarchy optimized) already provide excellent potential for all three parameters $\sin^2 2\theta_{13}$, $\delta_{\rm CP}$, and the sign of Δm^2_{31}. The last double detector scenario to be discussed is NF50@2DIT that should also provide an improved potential since the first oscillation maximum is directly accessible due to the lower energy threshold at the hybrid detector. The discovery potential for $\sin^2 2\theta_{13}$ is excellent down to extremely small values $\sin^2 2\theta_{13} \sim 2 \cdot 10^{-5}$ and thus all other double detector scenarios are outperformed. Also the reach in sensitivity to mass hierarchy is excellent but for intermediate $\sin^2 2\theta_{13}$ still some of the degenarcies remain to spoil the sensitivity for approximately 10% of all possible values of $\delta_{\rm CP}$ at $\sin^2 2\theta_{13} \sim 2 \cdot 10^{-3}$ and also at small $\sin^2 2\theta_{13} \sim 2 \cdot 10^{-4}$. Also the sensitivity to CP violation is best of all double detector scenarios with the hybrid detector at small and intermediate $\sin^2 2\theta_{13}$. Only for large $\sin^2 2\theta_{13}$ the matter density uncertainty still remains as a problem and the addition of the platinum channel or the magic baseline provides the better improvement potential.

Consequently, if the overall improvement should be optimized by going to a triple detector effort, the optimal combination should be a hybrid detector with a lower threshold at $L = 4000$ km combined with a detector at the magic baseline. So, the excellent abilities of the hybrid detector are synergetically combined with the degeneracy resolving potential at intermediate $\sin^2 2\theta_{13}$ at the magic baseline and the impact of the matter density uncertainty at large $\sin^2 2\theta_{13}$ is to be decreased. The performance of this triple detector combination NF50@3D is s given in the lowest row of Fig. 8.10. The thin black line indicates the performance of NF50@2DIT from the middle row and the improvement by the addition of the magic baseline can be read off. This scenario is providing excellent capabilities in all regimes of $\sin^2 2\theta_{13}$. A non-zero $\sin^2 2\theta_{13}$ can be discovered for 100% of all possible values of δ_{CP} for $\sin^2 2\theta_{13} > 2 \cdot 10^{-5}$ and likewise, mass hierarchy can be determined for $\sin^2 2\theta_{13} > 4 \cdot 10^{-5}$. CP violation can be established for more than 80% of all possible values of δ_{CP} for $\sin^2 2\theta_{13} > 2 \cdot 10^{-4}$. This scenario can only undergo a slight improvement for large $\sin^2 2\theta_{13}$ of a few percent if additionally the platinum channel could be utilized (see [236]). But since this would correspond to a quadruple detector effort, we do not discuss it here.

Chapter 9

The Global Picture

In this chapter we will review the global picture of the neutrino oscillation search beyond the precision measurements of the leading solar and atmospheric oscillation parameters towards three-flavor-effects. These include the search for the small mixing angle $\sin^2 2\theta_{13}$ that up to now remains undetermined. Besides the magnitude of $\sin^2 2\theta_{13}$ the value of the CP phase δ_{CP} and the mass hierarchy of the neutrino mass eigenstates remain unsolved puzzles in neutrino physics. The possibility to get insight to the latter is connected to the magnitude of $\sin^2 2\theta_{13}$ and if $\sin^2 2\theta_{13}$ turns out to be too small, it will be difficult, respectively impossible to gain information. However, the future experiments of neutrino physics provide various opportunities to solve the puzzles.

9.1 The Road Map of Neutrino Oscillation Experiments

There are plenty of different experiments planned or proposed for future measurements with increasing effort leading to an improving discovery reach of a non-zero $\sin^2 2\theta_{13}$. A possible road map for this evolution of the global neutrino oscillation program is given in Fig. 9.1 that is taken from [149]. The $\sin^2 2\theta_{13}$ discovery reach at the 3σ confidence level is illustrated for the future neutrino oscillation experiments in the next decades. The first generation are the conventional neutrino beams like MINOS or the CNGS experiments. The MINOS experiment is in the phase of data taking and has already published first results [120–123] and also the CNGS beam is operable and the first neutrinos have been observed [142]. The second step is the start of data taking at reactor experiments such as a 2nd generation reactor experiment like DoubleCHOOZ. From the year 2010 it is expected that the 1st generation of Superbeam experiments and the 3rd generation of reactor experiments like Daya Bay, RENO, or even a possible DoubleCHOOZ upgrade TripleCHOOZ (these are represented in Fig. 9.1 by the Reactor-II scenario defined in [155]) will start the operation. The shown Superbeam experiments are T2K in Japan and NOνA in the United States. The bands of the beam experiments in Fig. 9.1 represent the dependency that is introduced by the yet undetermined phase δ_{CP} meaning that at the upper edge of the bars a non-zero $\sin^2 2\theta_{13}$ can be discovered in parts of the δ_{CP} parameter space and not until the lower edge of the bars a $\sin^2 2\theta_{13}$ discovery is possible for 100% of all possible values of true δ_{CP}. The reactor experiments provide a definite discovery reach since θ_{13} measurements are independent of correlations with δ_{CP}. The mentioned experiments will be able to successively cover the $\sin^2 2\theta_{13}$ parameter space down to a value of $\sin^2 2\theta_{13} \sim 10^{-2}$, which is referred to as a branching point. Above the

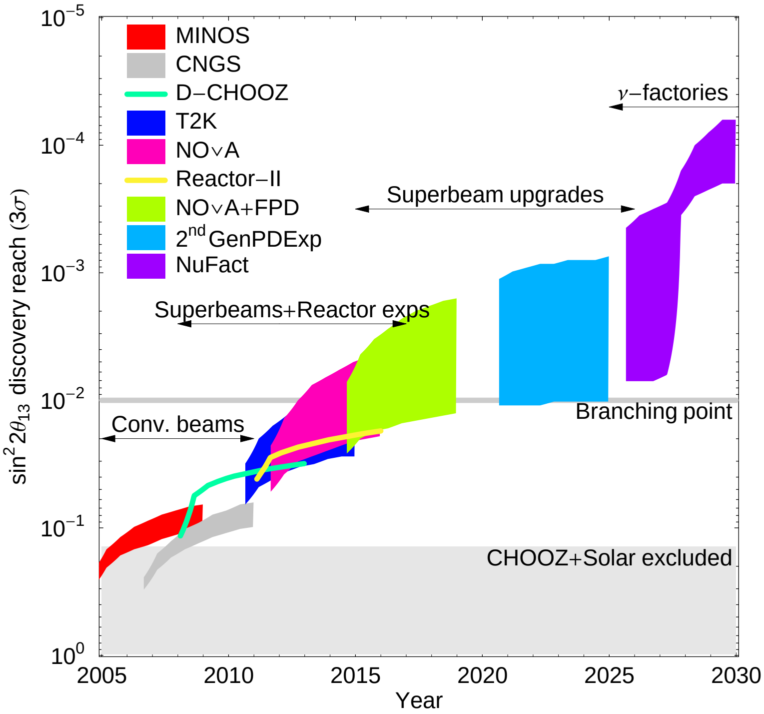

Figure 9.1: The possible global evolution of the $\sin^2 2\theta_{13}$ discovery reach at the 3σ confidence level as a function of time. The bands indicate the region where a non-zero true value of $\sin^2 2\theta_{13}$ could be established at the 3σ confidence level, *i.e.* $\sin^2 2\theta_{13} = 0$ can be excluded, depending on the actual true value of the phase $\delta_{\rm CP}$. Below the lower edge of the bands a non-zero true value of $\sin^2 2\theta_{13}$ could be established independent for 100% of the $\delta_{\rm CP}$ parameter space. The assumed true values for the other oscillation parameters are $\sin^2 2\theta_{12} = 0.83$, $\Delta m^2_{21} = 8.2 \cdot 10^{-5}$ eV^2, $\sin^2 2\theta_{23} = 1$, and $\Delta m^2_{31} = +2.5 \cdot 10^{-3}$ eV^2 (normal hierarchy assumed) very close to the true parameters assumed throughout the previous chapters of this work. Systematics, correlations and degeneracies are taken into account. This figure is taken from [149].

branching point the measurements are mainly affected by systematical uncertainties and the matter density uncertainty, while for values below the branching point reactor experiments get highly limited by the systematical uncertainties and the intrinsic beam background at Superbeam experiments starts to limit the potential. So, to reach for values of $\sin^2 2\theta_{13}$ below the branching point, upgrades of the Superbeam experiments with higher statistics or even better β-Beams or a Neutrino Factory are required. Additionally, the branching point approximately indicates the theoretical branching point, that separates the large $\sin^2 2\theta_{13}$ regime, where $\sin^2 2\theta_{13}$ still can be accidentally small compared to the other mixing angles, and the small $\sin^2 2\theta_{13}$ regime, where the smallness of $\sin^2 2\theta_{13}$ implies an underlying symmetry that suppresses $\sin^2 2\theta_{13}$. As can be read off from Fig. 9.1, this branching point should be reached within the next ten years. Beyond the year 2015 more dedicated experiments are required and the first step can be provided by an upgrade of the Superbeam experiments. Note, that Fig. 9.1 is taken from [149], a report for the Proton Driver at the FermiLab, so only US strategies are shown here. Note, that also the upgrade T2HK of the T2K Superbeam in Japan and the SPL Superbeam at CERN are planned to operate at the comparable magnitude of intermediate $\sin^2 2\theta_{13}$. These upgraded Superbeam experiments provide discovery potential below the branching point and even cover the parameter space partially down to $\sin^2 2\theta_{13} \sim 10^{-3}$. Further candidates for this regime are low γ β-Beams. However, for even smaller $\sin^2 2\theta_{13} < 10^{-3}$ flavor pure neutrino beam experiments as a medium to high γ β-Beam or a Neutrino Factory are required Here, only a standard Neutrino Factory is shown but we have demonstrated that also β-Beam are able to cover this regime in Chapter 7 and we will address this point in the next Sections. The intended time schedule as indicated in Fig. 9.1 for this kind of experiments is beyond 2025. The rapid increase of the Neutrino Factory discovery reach at mid time of data taking is due to the switching of beam polarities, *i.e.* between neutrino and anti-neutrino running which provides degeneracy resolving potential and thus improves the discovery reach immediately by one order of magnitude.

9.2 Promising Future Experiments

It should be kept in mind that the time-line evolution discussed in the last subsection assumes that no signal has been observed in between. Of course, the reactor experiments or 1st generation of Superbeams are possible to discover a large non-zero $\sin^2 2\theta_{13}$ during their runtime. This certainly would change the picture and one should aim for a precise measurement of $\sin^2 2\theta_{13}$ and also δ_{CP}. This is the reason why we will now discuss the performance of possible promising next generation future experiments in the regime of large $\sin^2 2\theta_{13} \sim 10^{-1}$. After that we will discuss different options for intermediate $\sin^2 2\theta_{13}$ where the resolving of the degeneracies has to be focused and finally we will address the reach in small $\sin^2 2\theta_{13}$.

Large $\sin^2 2\theta_{13}$

We will now focus on the scenario of large $\sin^2 2\theta_{13} = 10^{-1}$. Such a large value will be discovered at the 1st and 2nd generation of future reactor experiments and at the 1st generation of Superbeam experiments. The reactor experiments will provide a clean measurement of $\sin^2 2\theta_{13}$ without parameter correlations with δ_{CP}. The measurement at the 1st generation of Superbeam experiments will be correlated with the phase δ_{CP} but it is very unlikely that one can gain information on δ_{CP} due to the $(\sin^2 2\theta_{13}, \delta_{\mathrm{CP}})$-degeneracy. Still, the whole parameter space of δ_{CP} will be contained in the allowed region. However, the combination of the complementary data sets of reactor experiments and Superbeams start to disfavor some regions of the δ_{CP} parameter space to some extend. Still this effect will be also spoiled by the sign-degeneracy and it will not be possible to distinguish CP violation from CP conservation [140, 141]. So, also in this large $\sin^2 2\theta_{13}$ scenario more dedicated experiments like upgraded Superbeam experiments, β-Beams, or a Neutrino Factory will be required to shed light to the puzzle of δ_{CP} and the mass hierarchy of the neutrinos.

The performance of the defined β-Beam and Neutrino Factory scenarios and a representative of the upgraded Superbeam experiments T2HK* in terms of discovery potential of $\sin^2 2\theta_{13}$ (dark/blue bars), CP violation (red/medium grey bars), and the mass hierarchy (green/bright grey bars) is summarized in Fig. 9.2 for true $\sin^2 2\theta_{13} = 10^{-1}$. The bars indicate the fraction of (true) δ_{CP} where the respective parameter can be discovered at the 3σ confidence level. From top to bottom the detector effort is quantitatively increased from single detector scenarios to triple detector scenarios. As expected all experiment scenarios can discover the large $\sin^2 2\theta_{13}$ independent of δ_{CP}. Also, since $\sin^2 2\theta_{13}$ is large, most of the scenarios can determine the mass hierarchy in 100% of the δ_{CP} parameter space. Only the shorter baseline experiments are not able to observe matter effects and distinguish normal from inverted hierarchy in large

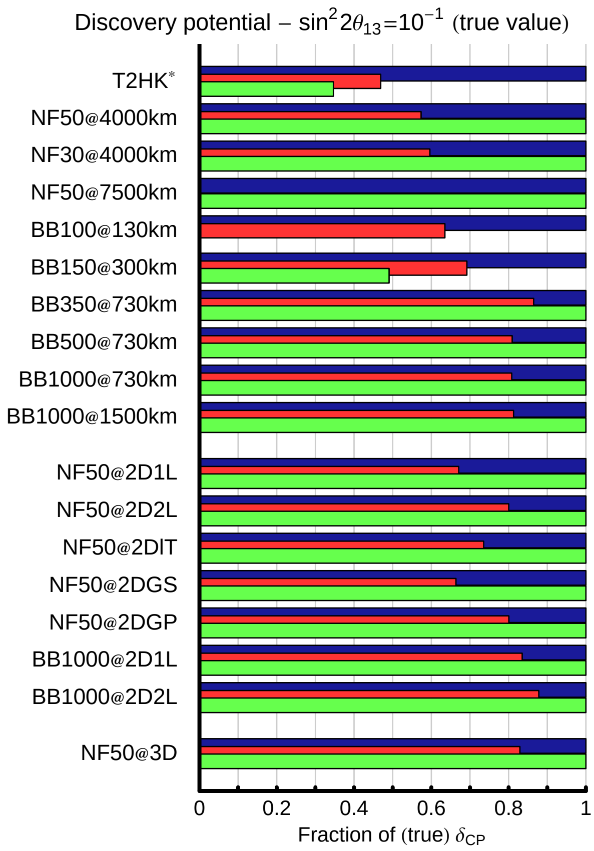

Figure 9.2: Summary of the performances of all β-Beam and Neutrino Factory reference scenarios for the performance indicators $\sin^2 2\theta_{13}$ discovery (dark/blue bars), sensitivity to *any* CP violation (middle grey/red bars), and sensitivity to the mass hierarchy (bright grey/green bars) at the true value $\sin^2 2\theta_{13} = 10^{-1}$. The fraction of the true values of $\delta_{\rm CP}$ of all possible values in the interval $[0, 2\pi[$ where the respective sensitivity is given at the 3σ confidence level is displayed. The respective scenarios are arranged from top to bottom with increasing detector effort (single, double and triple detector effort). For reasons of comparison also the performance of the upgraded Superbeam scenario T2HK* is given (upper-most bar).

parts of the $\delta_{\rm CP}$ parameter space. These are T2HK* and the low γ β-Beams BB100@130km and BB150@300km. The main performance indicator relevant for the large $\sin^2 2\theta_{13}$ scenario is the sensitivity to CP violation. If one only considers the scenarios with single detector effort, the medium γ β-Beam BB350@730km is very hard to beat. The very good performance of the medium γ β-Beams do not require to have a double detector effort or to push the isotope acceleration to high γ. The neutrino factory on the other hand is limited by the matter density uncertainty and so a multiple detector effort is required to improve the performance. For large $\sin^2 2\theta_{13}$ the most promising upgrade strategies are the installment of a second detector at the magic baseline and the utilization of the platinum channel. The charge identification of the platinum electrons/positrons to distinguish the disappearance wrong-sign electrons/positrons is not required up to the highest energies, an upper CID threshold of approximately 20 GeV is already sufficient to enable this improvement. In summary, a medium β-Beam is the optimal machine at large $\sin^2 2\theta_{13}$ with already superb performance on a single detector basis. However, the assumptions of the different technologies have only be estimated and considerable R&D is required before the final technology discussion can be made. Before a dedicated experiment like a Neutrino Factory or a medium γ β-Beam is to be installed the Superbeam experiments with possible upgrades are very likely to already constrain the δ_{CP} parameter space quite efficiently. Also low γ β-Beam scenarios such as the CERN-Frejus $\gamma = 100$ baseline scenario (similar to BB100@130km) are very promising candidates. The L=130 km baseline was also proposed to combine two experiment technologies, the SPL Superbeam and the $\gamma = 100$ β-Beam with the same megaton Water Cherenkov detector [247]. Then the CP and the T conjugate channels could be measured at one site and furthermore systematical uncertainties can be reduced since the β-Beam signal event type corresponds to the background at the Superbeam and vice versa. The potential of such a scenario was investigated in [187]. It was realized that the combination of T and CP conjugated channels at such a facility improve quite significantly the sensitivity to the mass hierarchy even at the very small baselines [248]. Another possibility with even more promising potential is implied by the combination of the T2HK Superbeam with a low γ β-Beam similar to BB150@300km.

Intermediate $\sin^2 2\theta_{13}$

If $\sin^2 2\theta_{13}$ is not discovered at the reactor experiments and first generation of Superbeam experiments the large $\sin^2 2\theta_{13}$ regime will be excluded and a new lower limit can be established with $\sin^2 2\theta_{13} \lesssim 10^{-2}$. Following the time schedule of Fig. 9.1 this could be the case approximately in the year 2015 (depending on the actual individual startup of the single experiments). Beyond this point more sophisticated experiments are required to take over. Superbeam upgrades, low γ β-Beam experiments or even combinations of these are thinkable to be candidates to start exploiting the next smaller regime of intermediate $10^{-3} < \sin^2 2\theta_{13} < 10^{-2}$, however not the complete parameter space can be covered and especially the determination of the mass hierarchy is difficult. Although the δ_{CP} parameter space can be well covered by a medium γ β-Beam sufficient potential to measure the sign of Δm^2_{31} is also difficult for such a scenario due to the still relative small baseline. Therefore, a Neutrino Factory experiment is most promising to provide excellent discovery potential for all three puzzles, $\sin^2 2\theta_{13}$, δ_{CP}, and the mass hierarchy, but the problems due to parameter correlations and the eight-fold degeneracy have to be addressed. This means that multiple detector scenarios have to be considered.

The performance of the defined β-Beam and Neutrino Factory scenarios and a representative of the upgraded Superbeam experiments T2HK* in terms of discovery potential of $\sin^2 2\theta_{13}$ (dark/blue bars), CP violation (red/medium grey bars), and the mass hierarchy (green/bright grey bars) is summarized in Fig. 9.3 for true $\sin^2 2\theta_{13} = 10^{-3}$. The bars indicate the fraction of (true) δ_{CP} where the respective parameter can be discovered at the 3σ confidence level. From top to bottom the detector effort is quantitatively increased from single detector scenarios to triple detector scenarios. The discovery of θ_{13} is only a problem for the Superbeam and the low γ β-Beam scenarios. Already medium γ β-Beams with a Water Cherenkov detector, high γ β-Beams and a Neutrino Factory can discover a non-zero $\sin^2 2\theta_{13} = 10^{-3}$ independent of the true δ_{CP}. However, already for intermediate $\sin^2 2\theta_{13}$ the performance of the β-Beams gets disadvantageous compared to the Neutrino Factory scenarios because the mass hierarchy determination potential is limited. This can only be restored by a high γ β-Beam with a double detector effort and a second baseline L$\sim$3000 km as BB1000@2D2L. The δ_{CP} discovery potential of the β-Beams and the Neutrino Factory scenarios is very similar with slight lead for the medium and high γ β-Beams. The degeneracy resolving at the Neutrino Factory can be facilitated by double detector effort and at intermediate $\sin^2 2\theta_{13}$ a second detector at

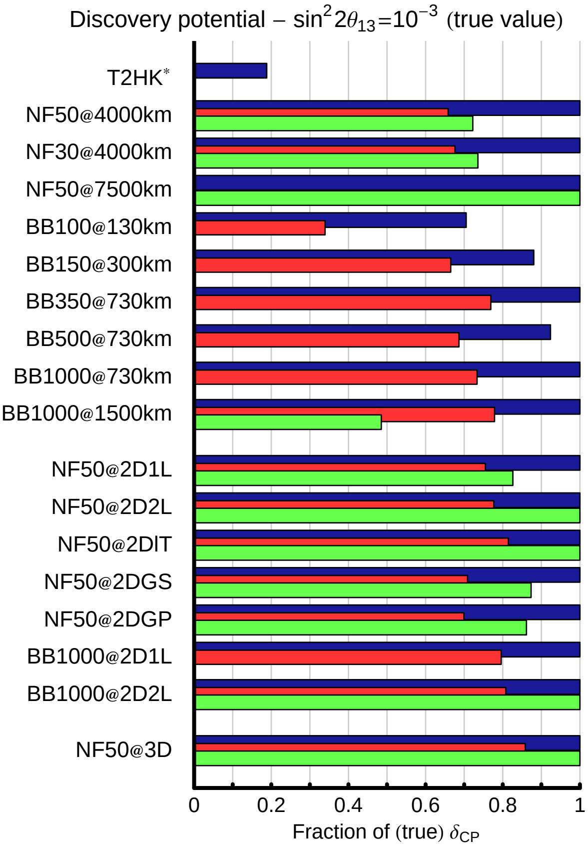

Figure 9.3: Summary of the performances of all β-Beam and Neutrino Factory reference scenarios for the performance indicators $\sin^2 2\theta_{13}$ discovery (dark/blue bars), sensitivity to *any* CP violation (middle grey/red bars), and sensitivity to the mass hierarchy (bright grey/green bars) at the true value $\sin^2 2\theta_{13} = 10^{-3}$. The fraction of the true values of δ_{CP} of all possible values in the interval $[0, 2\pi[$ where the respective sensitivity is given at the 3σ confidence level is displayed. The respective scenarios are arranged from top to bottom with increasing detector effort (single, double and triple detector effort). For reasons of comparison also the performance of the upgraded Superbeam scenario T2HK* is given (upper-most bar).

the magic baseline or a lower energy threshold at a Hybrid detector are the most promising scenarios. The inclusion of the additional channels, silver or platinum, only helps to some extend to resolve the degeneracies and if the assumptions of the optimistic scenarios cannot be achieved, the improvement cannot justify the detector effort that is involved with the inclusion. The combination of magic baseline and a Hybrid detector at L=4000 km is the ultimate optimized scenario at intermediate $\sin^2 2\theta_{13}$ and provides excellent discovery potential.

Small $\sin^2 2\theta_{13}$

From an experimental point of view, the worst case scenario is a very small $\sin^2 2\theta_{13}$ since additionally to the parameter correlations and degeneracies, the decreasing statistics in the appearance channel become a limiting factor. So, the reach of the experiment scenarios gets important, *i.e.* to which small values of $\sin^2 2\theta_{13} < 10^{-3}$ a reasonable discovery potential can be maintained.

The performance of the defined β-Beam and Neutrino Factory scenarios and a representative

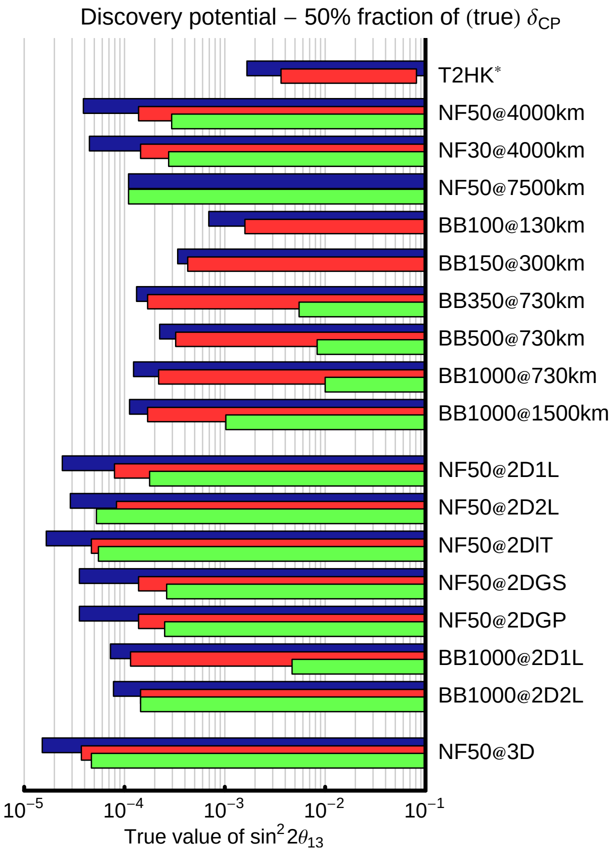

Figure 9.4: Summary of the performances of all β-Beam and Neutrino Factory reference scenarios for the $\sin^2 2\theta_{13}$ reach of the performance indicators $\sin^2 2\theta_{13}$ discovery (dark/blue bars), sensitivity to *any* CP violation (middle grey/red bars), and sensitivity to the mass hierarchy (bright grey/green bars). The bars indicate for which true values of $\sin^2 2\theta_{13}$ the respective sensitivities are given for at least 50% of all possible true values of δ_{CP} in the interval $[0, 2\pi[$at the 3σ confidence level. The respective scenarios are arranged from top to bottom with increasing detector effort (single, double and triple detector effort). For reasons of comparison also the performance of the upgraded Superbeam scenario T2HK* is given (upper-most bar).

of the upgraded Superbeam experiments T2HK* in terms of discovery potential of $\sin^2 2\theta_{13}$ (dark/blue bars), CP violation (red/medium grey bars), and the mass hierarchy (green/bright grey bars) is summarized in Fig. 9.4 considering the discovery reach to small $\sin^2 2\theta_{13}$. The bars indicate the $\sin^2 2\theta_{13}$ parameter space, where the respective parameters can be discovered for at least 50% of the δ_{CP} parameter space at the 3σ confidence level. Here, the main interest lies on those scenarios from Fig. 9.4 with a discovery potential that reaches to values of small $\sin^2 2\theta_{13} < 10^{-3}$. The most promising scenario is a Neutrino Factory since only the Neutrino Factory scenarios provide a θ_{13} discovery potential for values $\sin^2 2\theta_{13} < 10^{-4}$ already for the single detector effort setups. Additionally, at a Neutrino Factory the discovery potential to determine the neutrino mass hierarchy can be maintained to smallest $\sin^2 2\theta_{13} \sim 10^{-4}$. The best optimizing strategy to increase the discovery reach of a standard NF50@4000km turns out to be the Hybrid detector scenario with the lower threshold or even a combination with the magic baseline with a triple detector effort. The only optimizing strategy for β-Beams to remain competitive for small $\sin^2 2\theta_{13}$ in terms of all three performance indicators requires a high γ scenario with two Totally Active Scintillator detectors at two different baselines. One of these baselines at L$\sim$3000 km to improve the discovery reach for the determination of the mass hierarchy to $\sin^2 2\theta_{13} \sim 10^{-4}$. However, we summarize that the optimal technology for small $\sin^2 2\theta_{13}$ turns out to be a Neutrino Factory with a second detector at the magic baseline and possibly improved detector performance, *i.e.* a lower energy threshold.

Chapter 10

Summary and Conclusions

In this work, we have discussed the performance of the sophisticated neutrino oscillation long baseline scenarios of β-Beam experiments and Neutrino Factory experiments. The main focus was set on the investigation of the features of the possible optimization strategies and technical considerations of the respective experiment characteristics in the search for three-flavor effects in the observable appearance channels at the respective experiments and the implied sensitivities to the small mixing angle $\sin^2 2\theta_{13}$, the Dirac phase δ_{CP}, and the mass hierarchy of the neutrino mass eigenstates.

The optimization of the experiment scenarios was discussed in terms of the baseline L and the neutrino energy E_ν for single detector scenarios. In the simulations of the β-Beam experiments, two different detector technologies were considered, a Water Cherenkov detector and a Totally Active Scintillator detector. The Water Cherenkov detector is suitable for low and medium γ β-Beams, but for high γ scenarios a different detector technology is required because the Water Cherenkov detector is limited by the background from single pion production in neutral-current reactions and the pions can be misidentified as muons. Hence, for the high γ scenarios only the Totally Active Scintillator detector technology was considered, that provides excellent background rejection even at higher energies and additionally better energy resolution. The Totally Active Scintillator detector was also considered for medium γ scenarios to allow for a comparison of the detector technologies at intermediate neutrino energies. Similarly, the discussion of the optimization of a Neutrino Factory experiment involved the choice of the baseline L and the neutrino energy, controlled by the energy of the stored parent muons E_μ. This optimization was first performed for a single detector scenario focusing on the measurement of the so-called golden channel $\nu_e \rightarrow \nu_\mu$ that can be measured at a Magnetized Iron detector which allows for a separation of the so-called wrong sign muons coming from the dominating disappearance channel.

For both, the β-Beam and the Neutrino Factory scenarios, we found that the optimization in terms of sensitivity to $\sin^2 2\theta_{13}$ and sensitivity to CP violation is very similar since for optimal performance in both sensitivities, the $(\sin^2 2\theta_{13}, \delta_{\mathrm{CP}})$-degeneracy has to be resolved. Consequently, there has to be no trade-off for the optimization. However, if also a good ability to resolve the sign-degeneracy and determine the existing mass hierarchy of the neutrino mass eigenstates is requested, the situation becomes more complicated because optimal performance for sensitivity to CP violation and sensitivity to the mass hierarchy cannot be optimized simultaneously and multi-detector scenarios are required for an overall optimized performance. For the neutrino factory, this implies one detector at $L \sim 4000$ km for optimal CP sensitivity and one detector at the magic baseline $L \sim 7500$ km for excellent sign-degeneracy resolving potential. The β-Beam on the other hand is mainly a very powerful tool for measurements of $\sin^2 2\theta_{13}$ and $\delta_{\rm CP}$ and is less sensitive to the mass hierarchy because the baselines are smaller than Neutrino Factory baselines and matter effects do not play such an important role. However, the discussed high γ scenarios at relatively large baselines provided reasonable sensitivities to the mass hierarchy and also two-detector scenarios turned out to increase the potential enormously.

Beyond the elementary optimization strategies in terms of experiment baselines and neutrino energies, also different technical considerations of the β-Beam and Neutrino Factory scenarios were discussed. For both kinds of experiments we have shown that the actual ratio the neutrino and anti-neutrino runtime fractions does not play a very significant role and splitting the runtime in two equal phases of neutrino and anti-neutrino running is well justified.

Since the β-Beam experiments do not provide the possibility to measure the leading atmospheric parameters in the dominating disappearance channel, as is the case at a Neutrino Factory, it was expected that parameter correlations with the atmospheric parameters would heavily affect the sensitivities to $\sin^2 2\theta_{13}$, $\delta_{\rm CP}$, and the mass hierarchy at a the β-Beam scenarios. We have presented the impact of the inclusion of external disappearance data from the first generation Superbeam experiment T2K and it could be seen that the external information on the leading atmospheric parameters indeed gives a large impact in the performance. Hence, the disadvantage of a β-Beam compared to a Neutrino Factory is the dependency on external informations, whereas the Neutrino Factory is capable of measuring the leading atmospheric parameters in the disappearance channel. Note, that a β-Beam cannot participate in the search for deviations from maximal mixing $\sin^2 2\theta_{23}$ due the missing information on the leading atmospheric parameters.

Furthermore, we discussed the impact of a possible γ-scaling of the number of isotope decays at a β-Beam if higher γ accelerations are considered, since the usually discussed number of decays is treated constant for low, medium, and high γ scenarios. This of course requests an appropriate scaling of the storage ring and the sufficient injection of accelerated isotopes. It was observed that a possible γ-scaling can indeed destroy the excellent sensitivities that can be achieved at medium and high γ β-Beams and going to higher γ scenarios is only reasonable if the γ scaling of the number of isotope decays can be kept at a minimum.

For the optimization of the Neutrino Factory scenarios we have additionally discussed the possibility of an inclusion of secondary channels, the silver channel $\nu_e \rightarrow \nu_\tau$ and the platinum channel $\nu_\mu \rightarrow \nu_e$, to help resolving the degeneracies at intermediate $\sin^2 2\theta_{13}$ since the performance of the golden channel is to some extend limited due to the $(\sin^2 2\theta_{13}, \delta_{\rm CP})$- and sign-degeneracies. This effect is mainly observed at Neutrino Factory experiments since a Neutrino Factory is not operated at the oscillation maximum due to the CID cut that is required to identify the wrong-sign muons coming from the dominating disappearance channel. At β-Beam experiments the effects of the degeneracies are not as large as for Neutrino Factory experiments since the β-Beam beam neutrino spectrum perfectly covers the first oscillation maximum. It was shown that the standard assumptions about the included silver and platinum channels at a Neutrino Factory are not sufficient to significantly improve the resolving of the degeneracies and more optimistic assumptions have to be realized that are hardly feasible. For the silver channel a dedicated increase in the detector mass of the silver channel detector, an Emulsion Cloud Chamber detector, is required and also the detection of the τ decay in all decay channels and not only the leptonic decays as was assumed for the standard silver channel. The optimistic assumptions for the platinum channel involved the detector mass of

50 kt and the extremely optimistic assumption of a possible electron/positron discrimination up to the highest energies. Hence, we have to conclude that the usefulness of the additional channels for helping to resolve the degeneracies at intermediate $\sin^2 2\theta_{13}$ is questionable.

We have nevertheless observed that the platinum channel is very promising in the regime of large $\sin^2 2\theta_{13}$ where the main limiting factor at a Neutrino Factory is the matter density uncertainty along the baseline. This is due to the fact that the platinum channel is the T reversed channel of the golden channel, whereas switching from neutrino to anti-neutrino running compares the CP conjugated golden channels. In vacuum oscillations the T reversed and CP conjugated channels carry the same information and only statistics could be increased, however in oscillations in matter the platinum channel does not involve the reversed matter effect as the CP conjugated golden channel and the inclusion of the platinum channel gives the possibility to distinguish the intrinsic and extrinsic contributions to CP violation. So, the sensitivity to CP violation is significantly improved. We found that this effect does not require the very optimistic assumptions for the platinum channel detection and in this case it is sufficient to achieve an upper electron/positron CID threshold of about 15-20 GeV. However, this is still a demanding requirement since electrons tend to shower early in the detector and the observation of the track curvature is difficult. The CID is required to reduce the background in the platinum channel coming from the electrons/positrons from the disappearance channel $\nu_e \rightarrow \nu_e$ comparable to the requirement of the muon CID in the golden channel.

A very interesting observation for the Neutrino Factory scenarios was given when we discussed the performance potential of a Neutrino Factory scenario at $L \sim 4000$ km with a lower stored parent muons energy $E_\mu = 30$ GeV compared to the standard assumption of $E_\mu = 50$ GeV. We found that the lower neutrino energy Neutrino Factory scenario provides the very similar performance for all three performance indicators and it may not be necessary to accelerate the muons to the highest energies. This gives the interesting opportunity to economize the effort in the construction of the acceleration complex.

Furthermore, we have discussed an optimized golden channel detection with a lower energy threshold and better energy resolution. This could be achieved with an Hybrid detector, *i.e.* a combined detector technology for higher and lower energies. Due to the lower energy threshold the oscillation maximum at lower energies would become accessible and the potential to resolve the degeneracies is significantly improved. Such a scenario gives the best Neutrino Factory optimizing potential at intermediate and small $\sin^2 2\theta_{13}$ and can only be beaten for large $\sin^2 2\theta_{13}$ by the inclusion of an optimized platinum channel or a double detector scenario with a golden channel measurement at $L \sim 4000$ km combined with the golden channel measurement at the magic baseline.

We have analyzed the potential of a low γ β-Beam scenario comparable to the $\gamma = 100$ CERN-Frejus baseline scenario and it was shown that a low γ β-Beam cannot compete with higher γ β-Beams or Neutrino Factory experiments mainly due to the lack of sensitivity to the mass hierarchy even in the regime of large $\sin^2 2\theta_{13}$. However, it became apparent that low γ β-Beams can compete and even slightly outperform the second generation of Superbeam scenarios, in our discussions represented by the T2HK experiment. We proposed a low γ β-Beam at the baseline of $L \sim 300$ km and $\gamma = 150$ which is accessible at an accelerator complex of the size of the SPS that provides a considerably better performance as the $\gamma = 100$ β-Beam at the similar technical effort. Note, that the baseline of $L \sim 300$ km matches the baseline of the baseline between the J-PARC accelerator complex in Japan and the designated location of the Hyper-Kamiokande megaton Water Cherenkov detector. Just as the CERN-Frejus baseline, this baseline would also allow for a combination of a Superbeam and a β-Beam at the same baseline to improve the sensitivity to the mass hierarchy.

The discussion of the medium β-Beam scenarios indicated that in principle it is not required to aim for high γ scenarios since the sensitivity to CP violation is already excellent at medium γ β-Beams and the sensitivity to the mass hierarchy is only slightly improved. High γ scenarios are only interesting if two-detector scenarios are considered to impressively improve the $\sin^2 2\theta_{13}$ reach in the sensitivity to the mass hierarchy.

To summarize, in the regime of large $10^{-2} \lesssim \sin^2 2\theta_{13} \lesssim 10^{-1}$ the medium γ β-Beam scenarios give the best performance since mainly the sensitivity to CP violation discriminates the best experiment technology because θ_{13} and mass hierarchy discovery potential is excellent at Neutrino Factory experiments and higher γ β-Beam experiments. However, the combination of the data of upgraded Superbeam experiments, reactor experiments and possibly also low γ β-Beams already will give very good performances and higher γ β-Beams or Neutrino Factory scenarios are not necessarily required.

In the regime of intermediate $10^{-3} \lesssim \sin^2 2\theta_{13} \lesssim 10^{-2}$ the most promising candidates are medium γ β-Beams for measurements of $\sin^2 2\theta_{13}$ and δ_{CP}. Unfortunately, medium γ β-Beams loose the sensitivity to the mass hierarchy in this regime of $\sin^2 2\theta_{13}$ and high γ β-Beams and Neutrino Factory experiments at large baselines become preferable. However, the Neutrino Factory requires optimization of the golden channel, *i.e.* a detector at the magic baseline in order to successfully resolve the parameter degeneracies at intermediate $\sin^2 2\theta_{13}$. The aim for a lower threshold due to a Hybrid detector scenario is extremely promising to give further optimization of the Neutrino Factory performance.

Finally, if the regime of small $\sin^2 2\theta_{13} \lesssim 10^{-3}$ is considered, clearly the Neutrino Factory scenario is the ultimate machine because the discovery potential reaches to very small $\sin^2 2\theta_{13} \lesssim 10^{-4}$ for all three performance indicators sensitivity to $\sin^2 2\theta_{13}$, CP violation, and the sensitivity to the mass hierarchy. The best performance can be achieved if a lower threshold at a Hybrid detector scenario can be achieved and the sensitivity reach to the mass hierarchy is impressively improved with additional measurements at the magic baseline. The combination of the Hybrid detector at $L \sim 4000$ km and the magic baseline measurements give the ultimate optimized Neutrino Factory in the regime of small $\sin^2 2\theta_{13}$. β-Beam scenarios cannot compete with Neutrino Factory experiments in the regime of small $\sin^2 2\theta_{13}$, because even an ultimate two-detector high γ β-Beam cannot establish as good mass hierarchy sensitivities as a Neutrino Factory.

Appendix A

The General Long Baseline Experiment Simulator

The General Long Baseline Experiment Simulator GLoBES [220, 221, 249] is a software package that allows to simulate future neutrino oscillation long baseline experiments and analyze their potential to measure neutrino oscillation parameters. Within GLoBES the experiments are described in an Abstract Experiment Definition Language, so-called AEDL, that allows to simulate a variety of different detector technologies combined with point-like neutrino sources. Thus, besides beam-based experiments as conventional beam experiments, Superbeams, β-Beams or Neutrino Factory experiments also neutrino reactor experiments can be simulated. Additionally, very different kinds of systematical uncertainties, as *e.g.* normalization and energy calibration errors can be included to the simulation and the matter profile along the baseline can be treated accurately including uncertainties. GLoBES provides the calculation of the exact three-flavor oscillation probabilities, in vacuum and in matter and the calculation of event rates as well as simple Poisson χ^2 calculation. More sophisticated GLoBES functions allow to treat the full multi-parameter correlations and degeneracies by the $\Delta\chi^2$-projection of the six-dimensional parameter space to planes or axes in the parameter space.

The GLoBES software is available from the web and can be found at

`http://www.mpi-hd.mpg.de/lin/globes/`

in the newest version GLoBES 3.0. Together with the software, pre-defined experiment describing AEDL files are distributed, and some have been used in modified versions in the simulations throughout this work. The β-Beam simulations can be reproduced with the files `BBvar_WC.glb` that describes a variable β-Beam with a Water Cherenkov detector and `BBvar_TASD.glb` that describes a variable β-Beam with a Totally Active scintillator detector. The β-Beam fluxes are provided as built-in functions and only the γ,the endpoint energies of the considered isotopes, and the number of isotope decays per year have to be set. The Neutrino Factory simulations can be partially reproduced with the files `NFvar.glb` that describes a variable golden channel Neutrino Factory with a 50 kt Magnetized Iron detector, `NF_GoldSilver.glb` that describes the same golden channel as above in combination with the standard silver channel scenario, and the file `NF_hR_lT.glb` that describes an optimized golden channel with better energy resolution and lower energy threshold (in this work labeled as hybrid detector scenario). The description for the platinum channel and the optimistic silver channel are not distributed with GLoBES. The Neutrino Factory fluxes are provided as built-in functions and only the parent energy of the stored muons and the number of stored muons have to be set. Furthermore, the results for the Superbeam T2HK can be reproduced with the file `T2HK.glb`.

For performing simulations, the flux is mapped into an energy-binned event rate vector for different channels, signals and backgrounds. This mapping takes into account the oscillation probabilities (matter effects included accordingly to the respective baseline and neutrino energy), neutrino cross sections for the selected channels, and the AEDL described detector response that includes the fiducial detector mass, signal efficiencies, background rejection factors, energy dependent threshold functions, and the energy resolution of the detector. At the beginning of all simulations the event rate vector for an assumed set of so-called true oscillation parameter values is calculated. If not explicitely stated otherwise, the true parameter values for the leading oscillation parameters $\sin^2 2\theta_{12}$, Δm^2_{21}, $\sin^2 2\theta_{23}$, Δm^2_{31} used in the simulations throughout this work are the best-fit parameters given in Eq. (5.25). The true parameters of $\sin^2 2\theta_{13}$ and $\delta_{\rm CP}$ depend on the considered performance indicators. This event rate vector is then treated as the simulated data of the simulated experiments. The GLoBES functions are then used to fit the simulated data with fit values by using the same mapping function to calculate simulated expected rate vectors as described above and calculate the respective Poisson χ^2 value. Additionally the defined χ^2 function includes the systematical uncertainties like normalization errors, energy calibration errors, or the matter density uncertainty. The parameter space of fit values is effectively scanned by using the marginalization features of GLoBES by projecting the $\Delta\chi^2$ to the respective axes of the parameter space by including all possible degenerate solutions in the six-dimensional parameter space. Throughout this work only projections to the $\sin^2 2\theta_{13}$ and $\delta_{\rm CP}$ axis are required for the simulations while the sensitivities to mass hierarchy are calculated by marginalizing over all parameters to find the local minimum of the sign-degenerate solution in the six-dimensional parameters space.

Further details of simulations with the GLoBES software together with the detailed description of the event rate calculation, the implementation of systematical uncertainties, and the χ^2 calculation within GLoBES can be found in the GLoBES manual [223].

Appendix B

Performance Indicators

Throughout this work, we have made use of the so-called performance indicators to describe the physics potential of neutrino oscillation long baseline experiments, such as a β-Beam or a Neutrino Factory. The performance indicators were used to optimize different experiment scenarios in terms of baseline and neutrino energy, to describe the impact of different effects to the overall performance or to compare the performance of the different experiment and detector technologies. The performance indicators shall describe the potential of the considered experiments to make discoveries of three-flavor effects, *i.e.* measure a non-zero $\sin^2 2\theta_{13}$ or establish CP violation or the mass hierarchy of the neutrinos. In the following, all different discussed performance indicators are listed and a detailed definition is given.

Sensitivity limit to $\sin^2 2\theta_{13}$

The sensitivity limit to $\sin^2 2\theta_{13}$ is the largest fit value $\sin^2 2\theta_{13}^{\mathrm{fit}}$ that still fits an assumed true value $\sin^2 2\theta_{13}^{\mathrm{true}} = 0$ at the chosen confidence level after marginalization over all other oscillation parameters δ_{CP}, $\sin^2 2\theta_{12}$, Δm_{21}^2, $\sin^2 2\theta_{23}$, and Δm_{31}^2 where both degenerate fit solutions are considered: $\Delta m_{31}^2 > 0$ and $\Delta m_{31}^2 < 0$. Systematics are taken into account and the marginalization process also includes the matter density ρ to account for the matter density uncertainty $\Delta\rho$ (constrained by a pull term). For the set of assumed true parameters a normal mass hierarchy with $(\Delta m_{31}^2)^{\mathrm{true}} > 0$ is chosen only, since the assumption of inverted hierarchy gives essentially the same $\sin^2 2\theta_{13}$ sensitivity limit. This was demonstrated in the appendix of [140] where further details of the computation of the $\sin^2 2\theta_{13}$ sensitivity limit have been visualized. The sensitivity limit to $\sin^2 2\theta_{13}$ can be interpreted as the achievable lower bound on $\sin^2 2\theta_{13}$ at the considered experiment in case of a non-observation.

Discovery reach for $\sin^2 2\theta_{13}$

The discovery reach for $\sin^2 2\theta_{13}$ is the smallest true value $\sin^2 2\theta_{13}^{\mathrm{true}}$ for that the fit value $\sin^2 2\theta_{13}^{\mathrm{fit}} = 0$ could still be excluded at the chosen confidence level, *i.e.* a non-zero $\sin^2 2\theta_{13}$ could still be discovered. The discovery reach for $\sin^2 2\theta_{13}$ depends strongly on the true value of the phase δ_{CP}. As for the sensitivity limit, a marginalization over all other oscillation parameters δ_{CP}, $\sin^2 2\theta_{12}$, Δm_{21}^2, $\sin^2 2\theta_{23}$, and Δm_{31}^2 is performed. Systematics are taken into account and the marginalization process also includes the matter density ρ to account for the matter density uncertainty $\Delta\rho$ (constrained by a pull term).

Sensitivity to maximal CP violation

Sensitivity to *maximal* CP violation is given at the chosen confidence level for a true value of $\sin^2 2\theta_{13}^{\mathrm{true}}$ in case of maximal CP violation (either $\delta_{\mathrm{CP}}^{\mathrm{true}} = \pi/2$ or $\delta_{\mathrm{CP}}^{\mathrm{true}} = 3\pi/2$), if the CP conserving fit values $\delta_{\mathrm{CP}}^{\mathrm{fit}} = 0$ and $\delta_{\mathrm{CP}}^{\mathrm{fit}} = \pi$ can be excluded at this confidence level after marginalization over all other oscillation parameters $\sin^2 2\theta_{13}$, $\sin^2 2\theta_{12}$, Δm_{21}^2, $\sin^2 2\theta_{23}$, and Δm_{31}^2 where both degenerate fit solutions are considered: $\Delta m_{31}^2 > 0$ and $\Delta m_{31}^2 < 0$. Systematics are taken into account and the marginalization process also includes the matter density ρ to account for the matter density uncertainty $\Delta\rho$ (constrained by a pull term).

Sensitivity to any CP violation

Sensitivity to *any* CP violation is given at the chosen confidence level for a pair of true values $\sin^2 2\theta_{13}^{\mathrm{true}}$ and $\delta_{\mathrm{CP}}^{\mathrm{true}}$, if the CP conserving fit values $\delta_{\mathrm{CP}}^{\mathrm{fit}} = 0$ and $\delta_{\mathrm{CP}}^{\mathrm{fit}} = \pi$ can be excluded at this confidence level after marginalization over all other oscillation parameters $\sin^2 2\theta_{13}$, $\sin^2 2\theta_{12}$, Δm_{21}^2, $\sin^2 2\theta_{23}$, and Δm_{31}^2 where both degenerate fit solutions are considered: $\Delta m_{31}^2 > 0$ and $\Delta m_{31}^2 < 0$. Systematics are taken into account and the marginalization process also includes the matter density ρ to account for the matter density uncertainty $\Delta\rho$ (constrained by a pull term). Note that a sensitivity to *any* CP violation can never be established for fit values of δ_{CP} close to the CP conserving values because of systematical and statistical uncertainties, *i.e.* sensitivity to *any* CP violation is not achievable for a fraction of 100% of all possible true values $\delta_{\mathrm{CP}}^{\mathrm{true}}$ in the intervals $]0, \pi[$ and $]\pi, 2\pi[$.

Sensitivity to mass hierarchy

Sensitivity to mass hierarchy is given at the chosen confidence level for a pair of true values $\sin^2 2\theta_{13}^{\mathrm{true}}$ and $\delta_{\mathrm{CP}}^{\mathrm{true}}$ and the assumption of $(\Delta m_{31}^2)^{\mathrm{true}} > 0$ (normal hierarchy), if the degenerate solution with $(\Delta m_{31}^2)^{\mathrm{fit}} < 0$ (inverted hierarchy) can be excluded at this confidence level after marginalization over *all* oscillation parameters $\sin^2 2\theta_{13}$, δ_{CP}, $\sin^2 2\theta_{12}$, Δm_{21}^2, $\sin^2 2\theta_{23}$, and Δm_{31}^2. Systematics are taken into account and the marginalization process also includes the matter density ρ to account for the matter density uncertainty $\Delta\rho$ (constrained by a pull term).

Acknowledgments

First of all I want to express my sincere thanks to my supervisor Prof. Dr. Manfred Lindner who introduced me to the very interesting field of neutrino physics and increased my interest in astro-particle physics already during my studies. He gave me the opportunity to travel to conferences and summer schools and experience interesting topics and interesting places all over Europe including Stockholm, Paris, Krakow, and last but not least Heidelberg. I am especially grateful that he further supported my work after going to Heidelberg and hence making it possible that I could finish my thesis in Munich.

I want to thank my long-time collaborators Patrick Huber and Walter Winter who provided me with this nice powerful simulation tool and gave me the opportunity to be a part of the GLoBES team. Especially Patrick required some intense patience since he also shared the office with me in the early days and had to listen to all my lazy questions. Why look in the manual, when the guy who knows it all, sits right besides you? Walter kept motivating me with the deadlines he commonly brought up in collaborations and showed me in early stages how to organize team work. Furthermore, he always gave me insight to his simulation techniques in the days I had to get used to GLoBES.

Also my collaborator Thomas Schwetz deserves my thanks since it was always a pleasure to listen to his thoughts and further comments like “Ja, des is’ mühsam!”.

Of course it was also a great pleasure to collaborate with young guys who I could share some knowledge with. So, I really thank Joachim “F.” Kopp and Alex Merle for the discussions we shared before they left for Heidelberg.

Finally, I want to thank Prof. Dr. Joe Sato from Japan who was a guest in our group and introduced me to the phenomenologically very nice idea of “high γ” monobeam experiments and provided me with the demanding task to implement the idea into GLoBES. Especially I am grateful for his patience and very nice personality. “Hats off!” for the one and only professor who ever joined us in a Kart-Race.

Most of all, I wish to express great thanks to my Mom. She supported me like no one else over the last, well almost thirty years. Without her motivations I could never have come so far. Also, I want to thank my Dad who, like my Mom, supported my studies in Munich from the beginning and I still benefit from his support because if I look out of the window, then there doesn’t seem to be any subway going to Munich anymore.

Lots of incredible thanks to the computer administrators who always kept the computers going and provided immediate help if something went wrong: Herbert Müller, Markus Micheal Müller, and Stefan Recksiegel.

Furthermore, I want to thank our secretary Karin Ramm for keeping everything going and the very helpful discussions about the office furniture and the hints regarding the choice of the color of the carpet. Yet, I am still very glad that Mato and I did not follow your suggestions regarding the color of the walls.

Special thanks go out to Prof. Dr. Michael Ratz for providing a nice atmosphere in Munich over the last year and giving me the opportunity to stay in my old office, involving the whole “Pimp my Office” thing.

By any means I would like to thank any former members of our group or guests that contributed to the very nice atmosphere at T30d: Evgeny Akhmedov, Mathias Anderson, Stefan Antusch, Florian Bauer, Alexander Blum, Marc-Thomas Eisele, Mathias Garny, Srubabati Goswami, Naoyuki Haba, Claudia Hagedorn, Andreas Hohenegger, Patrick Huber, Jörn Kersten, Joachim Kopp, Alexander Merle, Markus Michael Müller, Tommy Ohlsson, Toshihiko Ota, Florian Plentiger, Karin Ramm, Michael Ratz, Werner Rodejohann, Joe Sato, Yoshio Sato, Michael Schmidt, Thomas Schwetz, Gerhart Seidl, Alexei Smirnov, and Walter Winter. And of course I also want to thank lots of members of the groups of Prof. Dr. Andrzej Buras and Prof. Dr. Wolfram Weise for contributing to the nice atmosphere.

And now to something completely different. Thanks go out to ...

- .... well, first of all, to all guys and the some girls who joined for having Kart-Races, gambling Poker, going to the cinema, playing Billiard, or going to the “Biergärten”. It was a pleasure! You are too many and I am too lazy to give all the names. You know who you are.
- .... Jörn, for somehow convincing me to watch movies in the original versions which had a huge impact in the following years.
- .... Tommy, for introducing me to the City of Stockholm and all the nice restaurants.
- .... Werner, for being a cool dude, sharing the passion about Lost with me, and giving away the hint with “House, M.D.”. See yah in anothah life, brotha!
- .... MMM, for organizing the Kart-Races including the nice web page and all the enjoyable discussions about comedians and cabaret artists.
- .... the Sneak-Crew Felix, Tobi, and Florian. ... and of course the Ladies.
- .... the whole Crew of the Office 1142 over all those years. Thanks for the patience and please don’t tell away all the secrets!
- .... Mathias Anderson, for sharing some of the same passions with me: Poker, watching Snooker, Wong Kar-Wai movies, and the Gilmore Girls.
- .... Damon Lindelof and Carlton Cuse!!!! Furthermore to Tim Kring, Gregory Thomas Garcia and David Shore.
- .... Felix, for listening to my strange theories and being the only guy, one can talk to without explaining all the mentioned names along the conversation. Come on, there are people out there, who refer to Giovanni Ribisi and Jon Favreau as some guys who were once guest-starring in “Friends”.
- .... Claudia, for some of the most enjoyable discussions I ever had with a woman and for reminding me to spend a cake and coffee.

- .... Anton, for nice breaks in our office and the lessons in History and Economics. By the way, I was never actually present when you indeed said something critical.
- .... Mato, for well everything, for being the cool office mate, for the discussions about Poker, movies, and all the other stuff, for the challenge of confronting me with views I would not ever think about, for having stopped tickling me, ...
- .... Elmar, for the "cigarette move", for the art of unsubstantial conversations, for calling in from time to time, and for the incredible stories you have to tell.
- .... Konstancja, for the very nice days in Krakow and the smilies in the subsequent e-mails.
- .... Desideria, for the support of my superstitious mind with the regular placing of the irregular TGiF content.
- .... Felix, Tobi, and Jana for having been there.

Bibliography

[1] S. L. Glashow, *Partial symmetries of weak interactions*, Nucl. Phys. **22** (1961), 579–588.

[2] A. Salam and J. C. Ward, *Electromagnetic and weak interactions*, Phys. Lett. **13** (1964), 168–171.

[3] S. Weinberg, *A model of leptons*, Phys. Rev. Lett. **19** (1967), 1264–1266.

[4] S. L. Glashow, J. Iliopoulos, and L. Maiani, *Weak interactions with lepton-hadron symmetry*, Phys. Rev. **D2** (1970), 1285–1292.

[5] P. W. Higgs, *Broken symmetries, massless particles and gauge fields*, Phys. Lett. **12** (1964), 132–133.

[6] P. W. Higgs, *Broken symmetries and the masses of gauge bosons*, Phys. Rev. Lett. **13** (1964), 508–509.

[7] P. W. Higgs, *Spontaneous symmetry breakdown without massless bosons*, Phys. Rev. **145** (1966), 1156–1163.

[8] F. Englert and R. Brout, *Broken symmetry and the mass of gauge vector mesons*, Phys. Rev. Lett. **13** (1964), 321–322.

[9] J. Erler and P. Langacker, *Electroweak model and constraints on new physics*, (2004), `hep-ph/0407097`.

[10] N. Cabibbo, *Unitary symmetry and leptonic decays*, Phys. Rev. Lett. **10** (1963), 531–532.

[11] M. Kobayashi and T. Maskawa, *CP violation in the renormalizable theory of weak interaction*, Prog. Theor. Phys. **49** (1973), 652–657.

[12] Z. Maki, M. Nakagawa, and S. Sakata, *Remarks on the unified model of elementary particles*, Prog. Theor. Phys. **28** (1962), 870.

[13] E. K. Akhmedov, private communications.

[14] B. Pontecorvo, *Inverse beta processes and nonconservation of lepton charge*, Sov. Phys. JETP **7** (1958), 172–173.

[15] B. Pontecorvo, *Neutrino experiments and the question of leptonic-charge conservation*, Sov. Phys. JETP **26** (1968), 984–988.

[16] V. N. Gribov and B. Pontecorvo, *Neutrino astronomy and lepton charge*, Phys. Lett. **B28** (1969), 493.

[17] J. F. Kopp, *Phenomenology of three-flavour neutrino oscillations*, Diploma Thesis, **TUM** (2006).

[18] M. Beuthe, *Oscillations of neutrinos and mesons in quantum field theory*, Phys. Rept. **375** (2003), 105–218, `hep-ph/0109119`.

[19] J. Schechter and J. W. F. Valle, *Neutrinoless double-beta decay in $SU(2) \times U(1)$ theories*, Phys. Rev. **D25** (1982), 2951.

[20] WMAP, D. N. Spergel et al., *Wilkinson Microwave Anisotropy Probe (WMAP) three year results: Implications for cosmology*, (2006), `astro-ph/0603449`.

[21] A. D. Sakharov, *Violation of CP invariance, C asymmetry, and baryon asymmetry of the universe*, Pisma Zh. Eksp. Teor. Fiz. **5** (1967), 32–35.

[22] M. Fukugita and T. Yanagida, *Baryogenesis without grand unification*, Phys. Lett. **B174** (1986), 45.

[23] V. A. Kuzmin, V. A. Rubakov, and M. E. Shaposhnikov, *On the anomalous electroweak baryon number nonconservation in the early universe*, Phys. Lett. **B155** (1985), 36.

[24] A. Abada, S. Davidson, F.-X. Josse-Michaux, M. Losada, and A. Riotto, *Flavour issues in leptogenesis*, JCAP **0604** (2006), 004, `hep-ph/0601083`.

[25] E. Nardi, Y. Nir, E. Roulet, and J. Racker, *The importance of flavor in leptogenesis*, JHEP **01** (2006), 164, `hep-ph/0601084`.

[26] A. Abada et al., *Flavour matters in leptogenesis*, JHEP **09** (2006), 010, `hep-ph/0605281`.

[27] S. Blanchet and P. Di Bari, *Flavor effects on leptogenesis predictions*, JCAP **0703** (2007), 018, `hep-ph/0607330`.

[28] S. Pascoli, S. T. Petcov, and A. Riotto, *Connecting low energy leptonic CP-violation to leptogenesis*, Phys. Rev. **D75** (2007), 083511, `hep-ph/0609125`.

[29] G. C. Branco, R. Gonzalez Felipe, and F. R. Joaquim, *A new bridge between leptonic CP violation and leptogenesis*, Phys. Lett. **B645** (2007), 432–436, `hep-ph/0609297`.

[30] S. Antusch and A. M. Teixeira, *Towards constraints on the SUSY seesaw from flavour-dependent leptogenesis*, JCAP **0702** (2007), 024, `hep-ph/0611232`.

[31] S. Pascoli, S. T. Petcov, and A. Riotto, *Leptogenesis and low energy CP violation in neutrino physics*, (2006), `hep-ph/0611338`.

[32] S. Blanchet and P. Di Bari, *Flavor effects in thermal leptogenesis*, (2007), `hep-ph/0702089`.

[33] E. K. Akhmedov, *Neutrino physics*, (1999), `hep-ph/0001264`.

[34] L.-L. Chau and W.-Y. Keung, *Comments on the parametrization of the Kobayashi-Maskawa matrix*, Phys. Rev. Lett. **53** (1984), 1802.

[35] C. Jarlskog, *A basis independent formulation of the connection between quark mass matrices, CP violation and experiment*, Z. Phys. **C29** (1985), 491–497.

[36] C. Jarlskog, *Matrix representation of symmetries in flavor space, invariant functions of mass matrices and applications*, Phys. Rev. **D35** (1987), 1685.

[37] V. D. Barger, K. Whisnant, S. Pakvasa, and R. J. N. Phillips, *Matter effects on three-neutrino oscillations*, Phys. Rev. **D22** (1980), 2718.

[38] T. Ohlsson and H. Snellman, *Three flavor neutrino oscillations in matter*, J. Math. Phys. **41** (2000), 2768–2788, `hep-ph/9910546`.

[39] M. Freund, *Analytic approximations for three neutrino oscillation parameters and probabilities in matter*, Phys. Rev. **D64** (2001), 053003, `hep-ph/0103300`.

[40] E. K. Akhmedov, R. Johansson, M. Lindner, T. Ohlsson, and T. Schwetz, *Series expansions for three-flavor neutrino oscillation probabilities in matter*, JHEP **04** (2004), 078, `hep-ph/0402175`.

[41] V. Barger, D. Marfatia, and K. Whisnant, *Breaking eight-fold degeneracies in neutrino CP violation, mixing, and mass hierarchy*, Phys. Rev. **D65** (2002), 073023, `hep-ph/0112119`.

[42] J. Burguet-Castell, M. B. Gavela, J. J. Gomez-Cadenas, P. Hernandez, and O. Mena, *On the measurement of leptonic CP violation*, Nucl. Phys. **B608** (2001), 301–318, `hep-ph/0103258`.

[43] H. Minakata and H. Nunokawa, *Exploring neutrino mixing with low energy Superbeams*, JHEP **10** (2001), 001, `hep-ph/0108085`.

[44] G. L. Fogli and E. Lisi, *Tests of three-flavor mixing in long-baseline neutrino oscillation experiments*, Phys. Rev. **D54** (1996), 3667–3670, `hep-ph/9604415`.

[45] P. Huber and W. Winter, *Neutrino Factories and the 'magic' baseline*, Phys. Rev. **D68** (2003), 037301, `hep-ph/0301257`.

[46] Particle Data Group, W. M. Yao et al., *Review of particle physics*, J. Phys. **G33** (2006), 1–1232.

[47] DELPHI, P. Abreu et al., *Photon events with missing energy at* $\sqrt{s}$ *= 183 to 189 GeV*, Eur. Phys. J. **C17** (2000), 53–65, `hep-ex/0103044`.

[48] OPAL, G. Abbiendi et al., *Photonic events with missing energy in* $e^+ e^-$ *collisions at* $\sqrt{s}$ *= 189 GeV*, Eur. Phys. J. **C18** (2000), 253–272, `hep-ex/0005002`.

[49] ALEPH, A. Heister et al., *Single- and multi-photon production in* $e^+ e^-$ *collisions at* $\sqrt{s}$ *up to 209 GeV*, Eur. Phys. J. **C28** (2003), 1–13.

[50] L3, P. Achard et al., *Single- and multi-photon events with missing energy in* $e^+ e^-$ *collisions at LEP*, Phys. Lett. **B587** (2004), 16–32, `hep-ex/0402002`.

[51] V. Barger, J. P. Kneller, H.-S. Lee, D. Marfatia, and G. Steigman, *Effective number of neutrinos and baryon asymmetry from BBN and WMAP*, Phys. Lett. **B566** (2003), 8–18, `hep-ph/0305075`.

[52] R. H. Cyburt, B. D. Fields, K. A. Olive, and E. Skillman, *New BBN limits on physics beyond the standard model from* ^4He, Astropart. Phys. **23** (2005), 313–323, `astro-ph/0408033`.

[53] K. A. Olive and E. D. Skillman, *A realistic determination of the error on the primordial Helium abundance: Steps toward non-parametric nebular helium abundances*, Astrophys. J. **617** (2004), 29, `astro-ph/0405588`.

[54] C. Kraus et al., *Final results from phase II of the MAINZ neutrino mass search in tritium beta decay*, Eur. Phys. J. **C40** (2005), 447–468, `hep-ex/0412056`.

[55] V. M. Lobashev et al., *Direct search for mass of neutrino and anomaly in the tritium beta-spectrum*, Phys. Lett. **B460** (1999), 227–235.

[56] KATRIN, A. Osipowicz et al., *KATRIN: A next generation tritium beta decay experiment with sub-eV sensitivity for the electron neutrino mass*, (2001), `hep-ex/0109033`.

[57] K. Assamagan et al., *Upper limit of the muon-neutrino mass and charged pion mass from momentum analysis of a surface muon beam*, Phys. Rev. **D53** (1996), 6065–6077.

[58] ALEPH, R. Barate et al., *An upper limit on the tau neutrino mass from three- and five-prong tau decays*, Eur. Phys. J. **C2** (1998), 395–406.

[59] E. W. Kolb and M. S. Turner, *The early universe*, Front. Phys. **69** (1990), 1–547.

[60] A. A. Penzias and R. W. Wilson, *A measurement of excess antenna temperature at 4080-mc/s*, Astrophys. J. **142** (1965), 419–421.

[61] R. Dicke, P. Peebles, P. Roll, and D. Wilkinson, *Cosmic black-body radiation*, Astrophys. J. **142** (1965), 414–419.

[62] G. F. Smoot et al., *Structure in the COBE differential microwave radiometer first year maps*, Astrophys. J. **396** (1992), L1–L5.

[63] J. C. Mather, D. J. Fixsen, R. A. Shafer, C. Mosier, and D. T. Wilkinson, *Calibrator design for the COBE far infrared absolute spectrophotometer (firas)*, Astrophys. J. **512** (1999), 511–520, `astro-ph/9810373`.

[64] S. S. Gershtein and Y. B. Zeldovich, *Rest mass of muonic neutrino and cosmology*, JETP Lett. **4** (1966), 120–122.

[65] R. Cowsik and J. McClelland, *An upper limit on the neutrino rest mass*, Phys. Rev. Lett. **29** (1972), 669–670.

[66] W. L. Freedman et al., *Final results from the Hubble Space Telescope Key project to measure the hubble constant*, Astrophys. J. **553** (2001), 47–72, `astro-ph/0012376`.

[67] WMAP, C. L. Bennett et al., *First year wilkinson microwave anisotropy probe (WMAP) observations: Preliminary maps and basic results*, Astrophys. J. Suppl. **148** (2003), 1, `astro-ph/0302207`.

[68] WMAP, D. N. Spergel et al., *First year wilkinson microwave anisotropy probe (WMAP) observations: Determination of cosmological parameters*, Astrophys. J. Suppl. **148** (2003), 175, `astro-ph/0302209`.

[69] J. A. Peacock et al., *A measurement of the cosmological mass density from clustering in the 2dF Galaxy Redshift Survey*, Nature **410** (2001), 169–173, `astro-ph/0103143`.

[70] O. Elgaroy et al., *A new limit on the total neutrino mass from the 2dF Galaxy Redshift Survey*, Phys. Rev. Lett. **89** (2002), 061301, `astro-ph/0204152`.

[71] S. Hannestad, *Neutrino masses and the number of neutrino species from WMAP and 2DfGRS*, JCAP **0305** (2003), 004, `astro-ph/0303076`.

[72] U. Seljak, P. McDonald, and A. Makarov, *Cosmological constraints from the CMB and Ly-alpha forest revisited*, Mon. Not. Roy. Astron. Soc. **342** (2003), L79, `astro-ph/0302571`.

[73] S. Hannestad and Y. Y. Y. Wong, *Neutrino mass from future high redshift galaxy surveys: Sensitivity and detection threshold*, (2007), `astro-ph/0703031`.

[74] L. Baudis et al., *Limits on the majorana neutrino mass in the 0.1-eV range*, Phys. Rev. Lett. **83** (1999), 41–44, `hep-ex/9902014`.

[75] H. V. Klapdor-Kleingrothaus et al., *Latest results from the Heidelberg-Moscow double-beta-decay experiment*, Eur. Phys. J. **A12** (2001), 147–154, `hep-ph/0103062`.

[76] A. Staudt, K. Muto, and H. V. Klapdor-Kleingrothaus, *Calculation of 2ν and 0ν double-beta decay rates*, Europhys. Lett. **13** (1990), 31–36.

[77] IGEX, C. E. Aalseth et al., *The IGEX Ge-76 neutrinoless double-beta decay experiment: Prospects for next generation experiments*, Phys. Rev. **D65** (2002), 092007, `hep-ex/0202026`.

[78] H. V. Klapdor-Kleingrothaus, I. V. Krivosheina, A. Dietz, and O. Chkvorets, *Search for neutrinoless double beta decay with enriched ^{76}Ge in Gran Sasso 1990-2003*, Phys. Lett. **B586** (2004), 198–212, `hep-ph/0404088`.

[79] H. V. Klapdor-Kleingrothaus, A. Dietz, H. L. Harney, and I. V. Krivosheina, *Evidence for neutrinoless double beta decay*, Mod. Phys. Lett. **A16** (2001), 2409–2420, `hep-ph/0201231`.

[80] F. Feruglio, A. Strumia, and F. Vissani, *Neutrino oscillations and signals in beta and $0\nu\beta\beta$ experiments*, Nucl. Phys. **B637** (2002), 345–377, `hep-ph/0201291`.

[81] C. E. Aalseth et al., *Comment on 'Evidence for neutrinoless double beta decay'*, Mod. Phys. Lett. **A17** (2002), 1475–1478, `hep-ex/0202018`.

[82] H. V. Klapdor-Kleingrothaus, *Reply to a comment of article 'Evidence for neutrinoless double beta decay'*, (2002), `hep-ph/0205228`.

[83] H. L. Harney, *Reply to the comment on 'Evidence for neutrinoless double beta decay'. (mod. phys. lett. a16(2001) 2409)*, (2001), `hep-ph/0205293`.

[84] Y. G. Zdesenko, F. A. Danevich, and V. I. Tretyak, *Has neutrinoless double beta decay of* ^{76}*Ge been really observed?*, Phys. Lett. **B546** (2002), 206–215.

[85] CUORE, C. Arnaboldi et al., *Cuore: A cryogenic underground observatory for rare events*, Nucl. Instrum. Meth. **A518** (2004), 775–798, `hep-ex/0212053`.

[86] I. Abt et al., *A new* ^{76}*Ge double beta decay experiment at LNGS*, (2004), `hep-ex/0404039`.

[87] GERDA, S. Schonert et al., *The Germanium detector array (GERDA) for the search of neutrinoless beta beta decays of* ^{76}*Ge at LNGS*, Nucl. Phys. Proc. Suppl. **145** (2005), 242–245.

[88] Majorana, R. Gaitskell et al., *White paper on the majorana zero-neutrino double-beta decay experiment*, (2003), `nucl-ex/0311013`.

[89] S. R. Elliott and J. Engel, *Double beta decay*, J. Phys. **G30** (2004), R183, `hep-ph/0405078`.

[90] J. N. Bahcall, M. H. Pinsonneault, and S. Basu, *Solar models: Current epoch and time dependences, neutrinos, and helioseismological properties*, Astrophys. J. **555** (2001), 990–1012, `astro-ph/0010346`.

[91] J. N. Bahcall and M. H. Pinsonneault, *What do we (not) know theoretically about solar neutrino fluxes?*, Phys. Rev. Lett. **92** (2004), 121301, `astro-ph/0402114`.

[92] J. N. Bahcall, Web page, `http://www.sns.ias.edu/∼jnb/`.

[93] J. Davis, Raymond, D. S. Harmer, and K. C. Hoffman, *Search for neutrinos from the sun*, Phys. Rev. Lett. **20** (1968), 1205–1209.

[94] SAGE, J. N. Abdurashitov et al., *Measurement of the solar neutrino capture rate with Gallium metal*, Phys. Rev. **C60** (1999), 055801, `astro-ph/9907113`.

[95] GALLEX, W. Hampel et al., *GALLEX solar neutrino observations: Results for gallex iv*, Phys. Lett. **B447** (1999), 127–133.

[96] GNO, M. Altmann et al., *GNO solar neutrino observations: Results for GNO I*, Phys. Lett. **B490** (2000), 16–26, `hep-ex/0006034`.

[97] R. Davis, *A review of the Homestake solar neutrino experiment*, Prog. Part. Nucl. Phys. **32** (1994), 13–32.

[98] B. T. Cleveland et al., *Measurement of the solar electron neutrino flux with the Homestake Chlorine detector*, Astrophys. J. **496** (1998), 505–526.

[99] SAGE, J. N. Abdurashitov et al., *Measurement of the solar neutrino capture rate by the russian-american Gallium solar neutrino experiment during one half of the 22-year cycle of solar activity*, J. Exp. Theor. Phys. **95** (2002), 181–193, `astro-ph/0204245`.

[100] GNO, C. M. Cattadori, *Update of solar neutrino interaction rate measurements from GNO at LNGS*, Nucl. Phys. Proc. Suppl. **110** (2002), 311–314.

[101] Super-Kamiokande, S. Fukuda et al., *Determination of solar neutrino oscillation parameters using 1496 days of Super-Kamiokande-I data*, Phys. Lett. **B539** (2002), 179–187, `hep-ex/0205075`.

[102] SNO, Q. R. Ahmad et al., *Direct evidence for neutrino flavor transformation from neutral-current interactions in the Sudbury Neutrino Observatory*, Phys. Rev. Lett. **89** (2002), 011301, `nucl-ex/0204008`.

[103] SNO, Q. R. Ahmad et al., *Measurement of day and night neutrino energy spectra at sno and constraints on neutrino mixing parameters*, Phys. Rev. Lett. **89** (2002), 011302, `nucl-ex/0204009`.

[104] SNO, S. N. Ahmed et al., *Measurement of the total active* ^{8}B *solar neutrino flux at the Sudbury Neutrino Observatory with enhanced neutral current sensitivity*, Phys. Rev. Lett. **92** (2004), 181301, `nucl-ex/0309004`.

[105] KamLAND, K. Eguchi et al., *First results from KamLAND: Evidence for reactor anti-neutrino disappearance*, Phys. Rev. Lett. **90** (2003), 021802, `hep-ex/0212021`.

[106] KamLAND, T. Araki et al., *Measurement of neutrino oscillation with KamLAND: Evidence of spectral distortion*, Phys. Rev. Lett. **94** (2005), 081801, `hep-ex/0406035`.

[107] M. Maltoni, T. Schwetz, M. A. Tortola, and J. W. F. Valle, *Status of global fits to neutrino oscillations*, New J. Phys. **6** (2004), 122, `hep-ph/0405172`.

[108] Super-Kamiokande, Y. Fukuda et al., *Evidence for oscillation of atmospheric neutrinos*, Phys. Rev. Lett. **81** (1998), 1562–1567, `hep-ex/9807003`.

[109] Soudan 2, M. C. Sanchez et al., *Observation of atmospheric neutrino oscillations in Soudan 2*, Phys. Rev. **D68** (2003), 113004, `hep-ex/0307069`.

[110] MACRO, F. Ronga et al., *Atmospheric neutrino induced muons in the MACRO detector*, Nucl. Phys. Proc. Suppl. **77** (1999), 117–122, `hep-ex/9810008`.

[111] MACRO, G. Giacomelli and A. Margiotta, *New MACRO results on atmospheric neutrino oscillations*, Phys. Atom. Nucl. **67** (2004), 1139–1146, `hep-ex/0407023`.

[112] Super-Kamiokande, Y. Ashie et al., *Evidence for an oscillatory signature in atmospheric neutrino oscillation*, Phys. Rev. Lett. **93** (2004), 101801, `hep-ex/0404034`.

[113] CHOOZ, M. Apollonio et al., *Search for neutrino oscillations on a long base-line at the CHOOZ nuclear power station*, Eur. Phys. J. **C27** (2003), 331–374, `hep-ex/0301017`.

[114] CHOOZ, M. Apollonio et al., *Limits on neutrino oscillations from the CHOOZ experiment*, Phys. Lett. **B466** (1999), 415–430, `hep-ex/9907037`.

[115] M. Maltoni, T. Schwetz, M. A. Tortola, and J. W. F. Valle, *Status of three-neutrino oscillations after the SNO-salt data*, Phys. Rev. **D68** (2003), 113010, `hep-ph/0309130`.

[116] K2K, M. H. Ahn et al., *Indications of neutrino oscillation in a 250-km long- baseline experiment*, Phys. Rev. Lett. **90** (2003), 041801, `hep-ex/0212007`.

[117] Y. Oyama, *Results from K2K and status of T2K*, (2005), `hep-ex/0512041`.

[118] K2K, M. H. Ahn et al., *Measurement of neutrino oscillation by the K2K experiment*, Phys. Rev. **D74** (2006), 072003, `hep-ex/0606032`.

[119] MINOS, E. Ables et al., *P-875: A long baseline neutrino oscillation experiment at Fermilab*, FERMILAB-PROPOSAL-P-875.

[120] MINOS, D. G. Michael et al., *Observation of muon neutrino disappearance with the MINOS detectors and the NuMI neutrino beam*, Phys. Rev. Lett. **97** (2006), 191801, `hep-ex/0607088`.

[121] MINOS, F. Yumiceva, *Recent results from the MINOS experiment*, AIP Conf. Proc. **870** (2006), 540–543.

[122] MINOS, D. E. Jaffe, *Latest results from MINOS*, In the Proceedings of International Conference on Heavy Quarks and Leptons (HQL 06), Munich, Germany, 16-20 Oct 2006.

[123] MINOS, B. J. Rebel, *First MINOS results with the NuMI beam*, (2007), `hep-ex/0701049`.

[124] MINOS, *Proposal for a five year run plan for MINOS*, NuMI-930.

[125] G. L. Fogli, E. Lisi, A. Marrone, and D. Montanino, *Status of atmospheric* $\nu_\mu \to \nu\_\tau$ *oscillations and decoherence after the first K2K spectral data*, Phys. Rev. **D67** (2003), 093006, `hep-ph/0303064`.

[126] J. N. Bahcall, M. C. Gonzalez-Garcia, and C. Pena-Garay, *Solar neutrinos before and after Neutrino 2004*, JHEP **08** (2004), 016, `hep-ph/0406294`.

[127] A. Bandyopadhyay, S. Choubey, S. Goswami, S. T. Petcov, and D. P. Roy, *Update of the solar neutrino oscillation analysis with the 766-ty KamLAND spectrum*, (2004), `hep-ph/0406328`.

[128] LSND, A. Aguilar et al., *Evidence for neutrino oscillations from the observation of* $\overline{\nu}_e$ *appearance in a* $\overline{\nu}_\mu$ *beam*, Phys. Rev. **D64** (2001), 112007, `hep-ex/0104049`.

[129] LSND, C. Athanassopoulos et al., *The Liquid Scintillator Neutrino Detector and LAMPF neutrino source*, Nucl. Instrum. Meth. **A388** (1997), 149–172, `nucl-ex/9605002`.

[130] KARMEN, B. Armbruster et al., *Upper limits for neutrino oscillations* $\overline{\nu}_\mu \to \overline{\nu}_e$ *from muon decay at rest*, Phys. Rev. **D65** (2002), 112001, `hep-ex/0203021`.

[131] H. Murayama and T. Yanagida, *LSND, SN1987a, and CPT violation*, Phys. Lett. **B520** (2001), 263–268, `hep-ph/0010178`.

[132] G. Barenboim, L. Borissov, and J. D. Lykken, *CPT violating neutrinos in the light of KamLAND*, (2002), `hep-ph/0212116`.

[133] BooNE, E. D. Zimmerman, *BooNE has begun*, eConf **C0209101** (2002), TH05, `hep-ex/0211039`.

[134] The MiniBooNE, A. A. Aguilar-Arevalo et al., *A search for electron neutrino appearance at the* $\Delta m^2 \sim 1eV^2$ *scale*, (2007), `arXiv:0704.1500 [hep-ex]`.

[135] M. Maltoni and T. Schwetz, *Sterile neutrino oscillations after first MiniBooNE results*, (2007), `arXiv:0705.0107 [hep-ph]`.

[136] MINOS, M. Diwan et al., *A study of* $\nu_\mu \to \nu_e$ *sensitivity in MINOS*, Tech. Report NuMI-L-714, 2001.

[137] V. D. Barger et al., *Neutrino oscillation parameters from MINOS, ICARUS and OPERA combined*, Phys. Rev. **D65** (2002), 053016, `hep-ph/0110393`.

[138] M. Komatsu, P. Migliozzi, and F. Terranova, *Sensitivity to* θ_{13} *of the CERN to Gran Sasso neutrino beam*, J. Phys. **G29** (2003), 443, `hep-ph/0210043`.

[139] P. Migliozzi and F. Terranova, *Next generation long baseline experiments on the path to leptonic CP violation*, Phys. Lett. **B563** (2003), 73–82, `hep-ph/0302274`.

[140] P. Huber, M. Lindner, M. Rolinec, T. Schwetz, and W. Winter, *Prospects of accelerator and reactor neutrino oscillation experiments for the coming ten years*, Phys. Rev. **D70** (2004), 073014, `hep-ph/0403068`.

[141] P. Huber, M. Lindner, M. Rolinec, T. Schwetz, and W. Winter, *Combined potential of future long-baseline and reactor experiments*, Nucl. Phys. Proc. Suppl. **145** (2005), 190–193, `hep-ph/0412133`.

[142] OPERA, R. Acquafredda et al., *First events from the CNGS neutrino beam detected in the OPERA experiment*, New J. Phys. **8** (2006), 303, `hep-ex/0611023`.

[143] OPERA, D. Duchesneau, *The CERN-Gran Sasso neutrino program*, eConf **C0209101** (2002), TH09, `hep-ex/0209082`.

[144] ICARUS, P. Aprili et al., *The ICARUS experiment: A second-generation proton decay experiment and neutrino observatory at the Gran Sasso laboratory. Cloning of T600 modules to reach the design sensitive mass. (addendum)*, CERN-SPSC-2002-027.

[145] NOvA, I. Ambats et al., *NOvA: Proposal to build an off-axis detector to study* $\nu_\mu \to \nu_e$ *oscillations in the NuMI beamline*, FERMILAB-PROPOSAL-0929.

[146] Y. Itow et al., *The JHF-Kamioka neutrino project*, Nucl. Phys. Proc. Suppl. **111** (2001), 146–151, `hep-ex/0106019`.

[147] A. de Bellefon et al., *MEMPHYS: A large scale Water Cerenkov detector at frejus*, (2006), `hep-ex/0607026`.

[148] J. E. Campagne and A. Cazes, *The θ_{13} and δ_{CP} sensitivities of the SPL-Frejus project revisited*, Eur. Phys. J. **C45** (2006), 643–657, `hep-ex/0411062`.

[149] M. Albrow et al., *Physics at a Fermilab Proton Driver*, (2005), `hep-ex/0509019`.

[150] CALTECH-SIN-TUM, G. Zacek et al., *Neutrino oscillation experiments at the Gösgen nuclear power reactor*, Phys. Rev. **D34** (1986), 2621–2636.

[151] Y. Declais et al., *Search for neutrino oscillations at 15-meters, 40-meters, and 95-meters from a nuclear power reactor at Bugey*, Nucl. Phys. **B434** (1995), 503–534.

[152] F. Boehm et al., *Final results from the Palo Verde neutrino oscillation experiment*, Phys. Rev. **D64** (2001), 112001, `hep-ex/0107009`.

[153] L. Oberauer, F. von Feilitzsch, and W. Potzel, *A large liquid scintillator detector for low-energy neutrino astronomy*, Nucl. Phys. Proc. Suppl. **138** (2005), 108–111.

[154] T. M. Undagoitia et al., *Search for the proton decay $p \to \pi^+\overline{\nu}$ in the large liquid scintillator low energy neutrino astronomy detector LENA*, Phys. Rev. **D72** (2005), 075014, `hep-ph/0511230`.

[155] P. Huber, M. Lindner, T. Schwetz, and W. Winter, *Reactor neutrino experiments compared to Superbeams*, Nucl. Phys. **B665** (2003), 487–519, `hep-ph/0303232`.

[156] Double Chooz, M. . Ardellier et al., *DoubleCHOOZ: A search for the neutrino mixing angle θ_{13}*, (2006), `hep-ex/0606025`.

[157] M. Anderson et al., *White paper report on using nuclear reactors to search for a value of θ_{13}*, (2004), `hep-ex/0402041`.

[158] Daya Bay, X. Guo et al., *A precision measurement of the neutrino mixing angle θ_{13} using reactor antineutrinos at Daya Bay*, (2007), `hep-ex/0701029`.

[159] RENO, Web page, `http://neutrino.snu.ac.kr/RENO/`.

[160] M. Aoki et al., *Letter of Intent for Kaska: High accuracy neutrino oscillation measurements with $\overline{\nu}_e$'s from Kashiwazaki-Kariwa nuclear power station*, (2006), `hep-ex/0607013`.

[161] P. Huber, J. Kopp, M. Lindner, M. Rolinec, and W. Winter, *From Double Chooz to Triple Chooz: Neutrino physics at the Chooz reactor complex*, JHEP **05** (2006), 072, `hep-ph/0601266`.

[162] J. Sato, *Monoenergetic neutrino beam for long baseline experiments*, Phys. Rev. Lett. **95** (2005), 131804, `hep-ph/0503144`.

[163] J. Sato, *Monoenergetic neutrino beam for long baseline experiments*, Nucl. Phys. Proc. Suppl. **155** (2006), 180–181.

[164] J. Bernabeu, J. Burguet-Castell, C. Espinoza, and M. Lindroos, *Monochromatic neutrino beams*, JHEP **12** (2005), 014, `hep-ph/0505054`.

[165] M. Lindroos, J. Bernabeu, J. Burguet-Castell, and C. Espinoza, *A monochromatic electron neutrino beam*, PoS **HEP2005** (2006), 365.

[166] J. Bernabeu, J. Burguet-Castell, C. Espinoza, and M. Lindroos, *Perspectives in neutrino physics: Monochromatic neutrino beams*, (2005), `hep-ph/0512299`.

[167] J. Bernabeu, J. Burguet-Castell, and C. Espinoza, *Physics reach with a monochromatic neutrino beam from electron capture*, Pos **HEP2005** (2006), 182, `hep-ph/0512297`.

[168] J. Bernabeu, J. Burguet-Castell, C. Espinoza, and M. Lindroos, *Physics reach of electron-capture neutrino beams*, Nucl. Phys. Proc. Suppl. **155** (2006), 222–224, `hep-ph/0510278`.

[169] C. Volpe, *Topical review on 'Beta-Beams'*, J. Phys. **G34** (2007), R1–R44, `hep-ph/0605033`.

[170] M. Rolinec and J. Sato, *Neutrino beams from electron capture at high gamma*, to be published in JHEP (2006), `hep-ph/0612148`.

[171] Super-Kamiokande, Y. Ashie et al., *A measurement of atmospheric neutrino oscillation parameters by Super-Kamiokande I*, Phys. Rev. **D71** (2005), 112005, `hep-ex/0501064`.

[172] M. Ikeda, I. Nakano, M. Sakuda, R. Tanaka, and M. Yoshimura, *New method of enhancing lepton number nonconservation*, (2005), `hep-ph/0506062`.

[173] M. Yoshimura, *Photon irradiated compression as a tool of investigating fundamental physics beyond standard model*, (2005), `hep-ph/0507248`.

[174] T. Nomura, J. Sato, and T. Shimomura, *Laser irradiated enhancement of atomic electron capture rate for new physics search*, (2006), `hep-ph/0605031`.

[175] P. Zucchelli, *A novel concept for a $\overline{\nu_e}/\nu_e$ neutrino factory: The Beta Beam*, Phys. Lett. **B532** (2002), 166–172.

[176] M. Mezzetto, *Physics reach of the Beta Beam*, J. Phys. **G29** (2003), 1771–1776, `hep-ex/0302007`.

[177] J. Bouchez, M. Lindroos, and M. Mezzetto, *Beta Beams: Present design and expected performances*, AIP Conf. Proc. **721** (2004), 37–47, `hep-ex/0310059`.

[178] M. Mezzetto, *Beta Beams*, Nucl. Phys. Proc. Suppl. **143** (2005), 309–316, `hep-ex/0410083`.

[179] J. Burguet-Castell, D. Casper, J. J. Gomez-Cadenas, P. Hernandez, and F. Sanchez, *Neutrino oscillation physics with a higher gamma Beta-Beam*, Nucl. Phys. **B695** (2004), 217–240, `hep-ph/0312068`.

[180] J. Burguet-Castell, D. Casper, E. Couce, J. J. Gomez-Cadenas, and P. Hernandez, *Optimal Beta-Beam at the CERN-SPS*, Nucl. Phys. **B725** (2005), 306–326, `hep-ph/0503021`.

[181] F. Terranova, A. Marotta, P. Migliozzi, and M. Spinetti, *High energy Beta Beams without massive detectors*, Eur. Phys. J. **C38** (2004), 69–77, `hep-ph/0405081`.

[182] A. Donini, E. Fernandez-Martinez, P. Migliozzi, S. Rigolin, and L. Scotto Lavina, *Study of the eightfold degeneracy with a standard Beta-Beam and a Superbeam facility*, Nucl. Phys. **B710** (2005), 402–424, `hep-ph/0406132`.

[183] A. Donini, E. Fernandez-Martinez, and S. Rigolin, *Appearance and disappearance signals at a Beta-Beam and a Superbeam facility*, Phys. Lett. **B621** (2005), 276–287, `hep-ph/0411402`.

[184] A. Donini and E. Fernandez-Martinez, *Alternating ions in a Beta-Beam to solve degeneracies*, Phys. Lett. **B641** (2006), 432–439, `hep-ph/0603261`.

[185] A. Donini et al., *A Beta Beam complex based on the machine upgrades of the LHC*, (2006), `hep-ph/0604229`.

[186] P. Huber, M. Lindner, M. Rolinec, and W. Winter, *Physics and optimization of Beta-Beams: From low to very high gamma*, Phys. Rev. **D73** (2006), 053002, `hep-ph/0506237`.

[187] J. E. Campagne, M. Maltoni, M. Mezzetto, and T. Schwetz, *Physics potential of the CERN-MEMPHYS neutrino oscillation project*, JHEP **04** (2007), 003, `hep-ph/0603172`.

[188] S. K. Agarwalla, S. Choubey, and A. Raychaudhuri, *Neutrino mass hierarchy and θ_{13} with a magic baseline Beta-Beam experiment*, Nucl. Phys. **B771** (2007), 1–27, `hep-ph/0610333`.

[189] S. Geer, *Neutrino beams from muon storage rings: Characteristics and physics potential*, Phys. Rev. **D57** (1998), 6989–6997, `hep-ph/9712290`.

[190] S. Geer, *Neutrino beams from muon storage rings: Characteristics and physics potential*, Phys. Rev. **D57** (1998), 6989–6997, `hep-ph/9712290`.

[191] A. De Rujula, M. B. Gavela, and P. Hernandez, *Neutrino oscillation physics with a Neutrino Factory*, Nucl. Phys. **B547** (1999), 21–38, `hep-ph/9811390`.

[192] C. Albright et al., *Physics at a Neutrino Factory*, Nucl. Phys. **B547** (2000), 21–38, `hep-ex/0008064`.

[193] M. Apollonio et al., *Oscillation physics with a Neutrino Factory.*, (2002), `hep-ph/0210192`.

[194] V. Barger, S. Geer, and K. Whisnant, *Long baseline neutrino physics with a muon storage ring neutrino source*, Phys. Rev. **D61** (2000), 053004, `hep-ph/9906487`.

[195] A. Cervera et al., *Golden measurements at a Neutrino Factory*, Nucl. Phys. **B579** (2000), 17–55, `hep-ph/0002108`.

[196] M. Freund, P. Huber, and M. Lindner, *Systematic exploration of the Neutrino Factory parameter space including errors and correlations*, Nucl. Phys. **B615** (2001), 331–357, `hep-ph/0105071`.

[197] A. Blondel et al., *The Neutrino Factory: beam and experiments*, Nucl. Instrum. Meth. **A451** (2000), 102–122.

[198] P. Huber, M. Lindner, and W. Winter, *Superbeams versus Neutrino Factories*, Nucl. Phys. **B645** (2002), 3–48, `hep-ph/0204352`.

[199] MONOLITH Collab., N. Y. Agafonova et al., *MONOLITH: A massive magnetized iron detector for neutrino oscillation studies*, LNGS-P26-2000.

[200] N. Holtkamp and S. Geer, *Feasibility study of neutrino source based on muon storage ring*, ICFA Beam Dyn. Newslett. **21** (2000), 37–51.

[201] S. Ozaki et al., *Feasibility Study II of a muon-based neutrino source*, BNL-52623.

[202] Muon Collider/Neutrino Factory, M. M. Alsharoa et al., *Recent progress in Neutrino Factory and Muon Collider research within the muon collaboration*, Phys. Rev. ST Accel. Beams **6** (2003), 081001, `hep-ex/0207031`.

[203] P. Gruber et al., *The study of a European Neutrino Factory Complex*, CERN-PS-2002-080-PP.

[204] A. Blondel et al., *ECFA/CERN studies of a European Neutrino Factory Complex*, CERN-2004-002.

[205] P. Gruber, *Ionisation cooling for a Neutrino Factory*, CERN-THESIS-2001-029.

[206] H. Schonauer, *Ionisation cooling in FFAG Neutrino Factories*, Nucl. Instrum. Meth. **A503** (2003), 318–321.

[207] R. Edgecock, *The MICE experiment*, ICFA Beam Dyn. Newslett. **29** (2002), 43–57.

[208] R. Edgecock, *The MICE experiment*, J. Phys. **G29** (2003), 1601–1611.

[209] E. Radicioni, *MICE: the international muon ionization cooling experiment*, Eur. Phys. J. **C33** (2004), s1056–s1058.

[210] S. Dawson, *Precision measurements at a Muon Collider*, AIP Conf. Proc. **372** (1996), 285–292, `hep-ph/9512260`.

[211] J. F. Gunion, *Physics motivations for a Muon Collider*, (1996), `hep-ph/9605396`.

[212] M. C. Gonzalez-Garcia, Y. Grossman, A. Gusso, and Y. Nir, *New CP violation in neutrino oscillations*, Phys. Rev. **D64** (2001), 096006, `hep-ph/0105159`.

[213] A. M. Gago, M. M. Guzzo, H. Nunokawa, W. J. C. Teves, and R. Zukanovich Funchal, *Probing flavor changing neutrino interactions using neutrino beams from a muon storage ring*, Phys. Rev. **D64** (2001), 073003, `hep-ph/0105196`.

[214] P. Huber and J. W. F. Valle, *Non-standard interactions: Atmospheric versus Neutrino Factory experiments*, Phys. Lett. **B523** (2001), 151–160, `hep-ph/0108193`.

[215] T. Ota, J. Sato, and N.-a. Yamashita, *Oscillation enhanced search for new interaction with neutrinos*, Phys. Rev. **D65** (2002), 093015, `hep-ph/0112329`.

[216] P. Huber, T. Schwetz, and J. W. F. Valle, *Confusing non-standard neutrino interactions with oscillations at a Neutrino Factory*, Phys. Rev. **D66** (2002), 013006, `hep-ph/0202048`.

[217] M. Campanelli and A. Romanino, *Effects of new physics in neutrino oscillations in matter*, Phys. Rev. **D66** (2002), 113001, `hep-ph/0207350`.

[218] M. Blennow, T. Ohlsson, and W. Winter, *Non-standard hamiltonian effects on neutrino oscillations*, Eur. Phys. J. **C49** (2007), 1023–1039, `hep-ph/0508175`.

[219] J. Kopp, M. Lindner, and T. Ota, *Discovery reach for non-standard interactions in a Neutrino Factory*, (2007), `hep-ph/0702269`.

[220] P. Huber, M. Lindner, and W. Winter, *Simulation of long-baseline neutrino oscillation experiments with GLoBES*, Comput. Phys. Commun. **167** (2005), 195, `hep-ph/0407333`.

[221] P. Huber, J. Kopp, M. Lindner, M. Rolinec, and W. Winter, *New features in the simulation of neutrino oscillation experiments with GLoBES 3.0*, (2007), `hep-ph/0701187`.

[222] P. Huber, M. Lindner, and W. Winter, *Synergies between the first-generation JHF-SK and NuMI Superbeam experiments*, Nucl. Phys. **B654** (2003), 3–29, `hep-ph/0211300`.

[223] GLoBES 3.0, *Globes manual*, manual (2004, 2007), `http://www.mpi-hd.mpg.de/lin/globes/`.

[224] R. J. Geller and T. Hara, *Geophysical aspects of very long baseline neutrino experiments*, Phys. Rev. Lett. **49** (2001), 98–101, `hep-ph/0111342`.

[225] T. Ohlsson and W. Winter, *The role of matter density uncertainties in the analysis of future Neutrino Factory experiments*, Phys. Rev. **D68** (2003), 073007, `hep-ph/0307178`.

[226] S. V. Panasyuk, *REM (Reference Earth Model) web page* , `http://cfauvcs5.harvard.edu/lana/rem/index.htm`, 2000.

[227] A. Ereditato and A. Rubbia, *Ideas for future Liquid Argon detectors*, Nucl. Phys. Proc. Suppl. **139** (2005), 301–310, `hep-ph/0409143`.

[228] Y. Kozlov, L. Mikaelyan, and V. Sinev, *Two detector reactor neutrino oscillation experiment KR2DET at Krasnoyarsk: Status report*, Phys. Atom. Nucl. **66** (2003), 469–471, `hep-ph/0109277`.

[229] H. Minakata, H. Sugiyama, O. Yasuda, K. Inoue, and F. Suekane, *Reactor measurement of θ_{13} and its complementarity to long-baseline experiments*, Phys. Rev. **D68** (2003), 033017, `hep-ph/0211111`.

[230] NOvA, D. S. Ayres et al., *NOvA proposal to build a 30-kiloton off-axis detector to study neutrino oscillations in the fermilab numi beamline*, (2004), `hep-ex/0503053`.

[231] P. Litchfield and L. Mualem, *Results of simulations of the Liquid Scintillator detector*, Tech. Report Nova-NOTE-SIM-42, NOvA, June 2004.

[232] P. Litchfield and L. Mualem, *Comparison of the energy resolution of the standard and Totally Active Scintillator detectors*, Tech. Report Nova-NOTE-SIM-48, NOvA, August 2004.

[233] P. Litchfield, private communication.

[234] T. Schwetz, *Comparison of the CERN-MEMPHYS and T2HK neutrino oscillation experiments*, (2006), `hep-ph/0611261`.

[235] M. Lindroos, *Flux at a Beta Beam facility*, (2005), Talk given at the joint ECFA/BENE meeting, March 16, 2005, CERN, `http://nuspp.in2p3.fr/Bene/BENEWeekMarch05/`.

[236] P. Huber, M. Lindner, M. Rolinec, and W. Winter, *Optimization of a Neutrino Factory oscillation experiment*, Phys. Rev. **D74** (2006), 073003, `hep-ph/0606119`.

[237] S. Antusch, P. Huber, J. Kersten, T. Schwetz, and W. Winter, *Is there maximal mixing in the lepton sector?*, Phys. Rev. **D70** (2004), 097302, `hep-ph/0404268`.

[238] A. de Gouvea and W. Winter, *What would it take to determine the neutrino mass hierarchy if* θ_{13} *were too small?*, Phys. Rev. **D73** (2006), 033003, `hep-ph/0509359`.

[239] M. Freund, P. Huber, and M. Lindner, *Extracting matter effects, masses and mixings at a Neutrino Factory*, Nucl. Phys. **B585** (2000), 105–123, `hep-ph/0004085`.

[240] A. Donini, D. Meloni, and P. Migliozzi, *The Silver Channel at the Neutrino Factory*, Nucl. Phys. **B646** (2002), 321–349, `hep-ph/0206034`.

[241] D. Autiero et al., *The synergy of the Golden and Silver Channels at the Neutrino Factory*, Eur. Phys. J. **C33** (2004), 243–260, `hep-ph/0305185`.

[242] A. Rubbia, *Neutrino Factories: Detector concepts for studies of CP and T violation effects in neutrino oscillations*, (2001), `hep-ph/0106088`.

[243] A. Cervera, F. Dydak, and J. Gomez Cadenas, *A large magnetic detector for the Neutrino Factory*, Nucl. Instrum. Meth. **A451** (2000), 123–130.

[244] A. Donini, *Using* $\nu_e \rightarrow \nu_\tau$*: Golden and Silver Channels at the Neutrino Factory*, (2003), `hep-ph/0305247`.

[245] P. Migliozzi, *The synergy of the Golden and Silver Channels at the Neutrino Factory*, AIP Conf. Proc. **721** (2004), 223–226.

[246] P. Huber, M. Lindner, and W. Winter, *From parameter space constraints to the precision determination of the leptonic dirac CP phase*, JHEP **05** (2005), 020, `hep-ph/0412199`.

[247] M. Mezzetto, *SPL and Beta Beams to the Frejus*, Nucl. Phys. Proc. Suppl. **149** (2005), 179–181.

[248] T. Schwetz, *Determination of the neutrino mass hierarchy in the regime of small matter effect*, (2007), `hep-ph/0703279`.

[249] M. Rolinec, *GLoBES and its application to neutrino physics*, Acta Phys. Polon. **B37** (2006), 2049–2057.